Morphology-Structural Change of Calcium Silicate Hydrates

Xiaohong Zhu

Supervisors:

Professor Ian G. Richardson

Professor Phil Purnell

A thesis submitted in accordance with the requirements for the degree of

Doctor of Philosophy

The University of Leeds

School of Civil Engineering

June 2021

The candidate confirms that the work submitted is his own and that appropriate credit has been given where reference has been made to the work of others.

Acknowledgements

First and foremost, I would like to give my most sincere thanks to my primary supervisor, Prof. Ian G. Richardson, who gives me support and encouragement all the way through my PhD period. Additional thanks should be given to my co-supervisor, Prof. Phil Purnell, who gives me suggestions and supports for my PhD project.

Acknowledges are given to Leeds-CSC (China Scholarship Council) joint scholarship for sponsoring my PhD studies in Leeds. Also, thanks to the UKCRIC (UK Collaboratorium for Research on Infrastructure and Cities) for providing the access to some facilities and to the all the members in Structural Materials Group for the supports and help.

Many thanks should be given to the technician team of cementitious materials group, Karen, Vicky, Lucy, Les, Emma, Dave, and Morgen, without whose help and support I would not be able to finish these experiments. Also thanks to Dr. Zabeada Aslam and Dr. Stuart Micklethwaite from LEMAS, who helped me with the PIPS and TEM experiments. Thanks for the support given by Dr. Kai Yang, Prof. Changhui Yang, and Prof. Chong Wang from Chongqing University, who provides the access to the facilities in Chongqing University that helped partial experiments in this thesis. Additional thanks should be given to Ms Xiaojuan Kang (and Prof. Jiaping Liu), who helped me with the experiments in Chapter 6 and also for the access to the facilities in State (China) Key Laboratory of High Performance Civil Engineering Materials.

I would like to give my special thanks to Victoria Leadley (Vicky), who helped me greatly with her knowledge in NMR. Additional thanks to Sumanjani, who helped me with her experimental skills. I would like to extend my thanks to all the colleagues: Haoqi, Ali, Yue, Mubarak, Sam, Joe, Alastair, JP, James, Ahmad, Zengliang, and Yuyan for your company and all the valuable discussions.

I wish to express my gratitude to my family, who unconditionally support me throughout my entire life.

Abstract

Calcium silicate hydrates (C-S-H), which is the main binding phase in concrete, shows variable compositions and physicochemical properties that define the service life of structures. The morphology of the outer product (OP) C-S-H gel directly affects the shape of capillary pores and further, partially determines the transport properties in hardened pastes. Eventually, the morphology of OP C-S-H gel is linked with the durability of cementitious materials.

The morphological changes in C-S-H (gels) in blended cement systems, the synthetic alite system, and the synthetic C-S-H systems are examined through multiple techniques such as TEM-EDX, ^{29}Si, ^{27}Al, ^{23}Na MAS NMR, and ICP-OES. Other techniques such as ICC, XRF, XRD, STA and FTIR are also used to get full information. A more comprehensive understanding of the morphology-change of C-S-H together with the dependent factors are proposed.

The OP C-(A)-S-H gel in SCMs-blended cements change its morphology from fibrillar-like to mixed fine-fibrillar/foil-like when it shows the following characteristics: Ca/(Si+Al) ratio < 1.30 and Al/Si ratio > 0.15; MCL ≈ 7~8; SOF_{BT} > 0.6 or SOF_{BT}(Al) > 0.3; the proportion of Q^2(1Al) > 30%; Q^2(total)/Q^1 ratio > 2.0; Q^2(1Al)/ Q^2(total) ratio > 0.45; Q^2(1Al)/ Q^2(0Al) ratio > 0.80. Meanwhile, the pore solutions show the characteristics of effective saturation indices (ESI) of CH < -0.15 and ESI of J-based C-S-H gel < 0.10.

The morphology of OP C-S-H gel changes from foil-like at 2 h to fibrillar-like at 6 h when CH and Q^2 tetrahedra (in C-S-H gel) initially appear in alite system (w/s=10). The C-S-H at 2 h can be explained as the tobermorite-like dimer (T2) with minimum protonation; and that at 6 h can be explained as a mixture of minimum protonated 43.3% T5, 23.7% T2, and 33.0% J2 (T/J model). The foil-like C-S-H gel may be related to the tobermorite-like structure.

The single-phase C-S-H with a Ca/Si ratio of ~1.86 shows fibrillar-like morphology, which is a mixture of ~83% dimer and ~17% pentamer jennite-based units (J2/J5) with maximum protonation levels. The addition of either sodium hydroxide (NaOH) or aluminium nitrate ($Al(NO_3)_3$) solution during synthesis will change the fibrillar-like morphology to foil-like, which

is related to the reduction of Ca/Si ratio and the increased proportions of tobermorite units. C-S-H that equilibrates in deionised water (DIW), NaOH, or $Al(NO_3)_3$ solutions changes its morphology from fibrillar to foil-like by breaking the original jennite-based structure (i.e. omitting Ca-OH or breaking the longer chains). Only the C-S-H that is a mixture of integrated J2/J5 units show fibrillar-like morphology and others that are composed of either T/J units or incomplete jennite-based units show foil-like morphology.

The metastable C-S-H (gels) presented in blended wPC or synthetic C-S-H systems are observed on the equilibrium Curve A (Jennings), whilst those equilibrated on Curve B are supposed to be instable C-S-H gels that are present in PC < 1 d or alite hydrated in high w/s ratio (continuously dissolution and precipitation happens). The main difference between the two Curves may link with the insufficient diffusion barrier (stable C-S-H).

Keywords:

Calcium silicate hydrates (C-S-H); Morphology; Pore Solution Composition; Nanostructure.

Table of Contents

List of Figures

List of Tables

List of abbreviations

AFm: Monosulphoaluminate

AFt: Tri-sulphoaluminate or Ettringite

Al[IV]: Tetrahedral coordinated aluminium

Al[V]: Pentahedral coordinated aluminium

Al[VI]: Octahedral coordinated aluminium

AR-C-S-H: C-S-H synthesised by 'Auto-reactor method'

BO: Bridging oxygen

BSE: Back scattered electron

C-(A)-S-H: Calcium (aluminium) silicate hydrates

C-S-H: Calcium silicate hydrates

CH: Calcium hydroxide

CP NMR: Cross polarization nuclear magnetic resonance

DP MAS NMR: Direct pulse magic angle spinning nuclear magnetic resonance

DSC: Differential scanning calorimetry

DTA: Differential thermal analysis

EDX: Energy dispersive X-ray analysis

ESI: Effective saturation indices

FTIR: Fourier transform infrared spectroscopy

GGBS: Ground granulated blast-furnace slag

HRTEM: High resolution transmission electron microscopy

IP C-S-H: Inner product C-S-H

IC: Ion Chromatography

ICP-MS: Inductively coupled plasma-mass spectrometry

ICP-OES: Inductively coupled plasma-optical emission spectrometry

ICC: Isothermal conduction calorimetry

MCL: Mean chain length

NBO: Non-bridging oxygen

OP C-S-H: Outer product C-S-H

PFA: Pulverised fuel ash

PTFE: Polytetrafluoroethylene

RH: Relative humidity

SAED: Selected area electron diffraction

SANS: Small angle neutron scattering

SCM: Supplementary cementitious materials

SEM: Scanning electron microscopy

STA: Simultaneous thermal analysis

SI: Saturation indices

T/CH: Tobermorite/Calcium hydroxide

TEM: Transmission electron microscopy

TGA: Thermogravimetry analysis

T/J: Tobermorite/Jennite

TMS-GPC: trimethylsilylation gel permeation chromatography

VD: Vacuum drying

w/b: water to binder ratio

w/s: water to solid ratio

wPC: white Portland cement

XRD: X-ray diffraction

XRF: X-ray fluorescence

Cement chemistry terminology

A: Al_2O_3

C: CaO

F: Fe_2O_3

H: H_2O

K: K_2O

M: MgO

N: N_2O

S: SiO_2

C_3A: Tricalcium aluminate

C_4AF: Calcium aluminate ferrite

C_2S: Dicalcium silicate

C_3S: Tricalcium silicate

Ca/Si: Calcium to silicon atomic ratio

Al/Si: Aluminium to silicon atomic ratio

Chapter 1

Introduction

Reinforced concrete provides the construction basis for modern skyscrapers, dams, harbours and infrastructure of cities. However, the uninterrupted repairing of concrete reminds the engineers and scientists that many problems relevant to concrete durability are still unsolved. In Europe, approximately 40-60% of the construction budget is used for the maintenance and repair of the living concrete structures. Solely in the UK, the toll of this repair and maintenance of concrete is around £550 million per year, which makes "low-cost" concrete become expensive. Undoubtedly, there are continuous improvements that needs to be promoted in the concrete engineering area. Among which, the materials science can offer a clearer understanding of the nature behind the degradation of concrete and further seek for the suitable way to improve concrete durability.

1.1 Project framework and mind mapping

Concrete is a surprisingly complex composite, which normally consists of cement, aggregate, water, and other chemical admixtures. Cement is also called "binder" in concrete matrix because it can adhere all the aggregates and rebars to form "reinforced concrete". When hydraulic cement is encountered with water, the chemical reaction that occurs between cement and water results in the hydration products such like C-S-H gel, calcium hydroxide, sulphate (carbonate) aluminate (ferrite) [1]. Unlike crystal phases, C-S-H gel is the principal binding phase (~50-65% of final cement paste) which has a variable structure and composition at both atomic and mesostructured levels [2]. These variable properties of C-S-H gel require more attention towards the studies of its nanostructure, which will be a guidance to the changes of properties of concrete at the macro level. This motivation drives our group to put large efforts on understanding the nature of C-S-H gel for the last 30 years as shown in review papers presented by Richardson [3-7].

Despite many direct factors that affect the composition of C-S-H gel, including temperature [8], curing age [9, 10], and aggressive environment [11, 12], have been taken into consideration and studied, lots of questions still remain open. Recently, Rodriguez [13] tried to build the relationships between composition, structure and morphology of C-S-H, which aimed to declare that the morphology of C-S-H gel are subjected to its chemical composition or changed by the kinetic drive. The results from synthetic C-S-H experiments showed that the morphology of C-S-H is composition dependent, which was evidenced from the unchanged morphology compared between acceleration (fast growth) and deceleration period (slow growth) in different controlled lime concentrations. However, an interesting link between lime concentrations and morphology of C-S-H was also established. To be specific, the C-S-H with foils-like, mixture of foils/fibrils-like or fibrils-like morphology was connected with a lime concentration of 12-22 mmol/L, 22 mmol/L or ≥ 25 mmol/L. This result arouses the consideration of what happens to the C-S-H gel in hardened cement paste that has a variable pore solution composition? Richardson [14] analysed the relationships of morphology, composition and nanostructure of C-S-H gel both in KOH- and water-activated low calcium SCMs-containing white Portland cement (wPC). It was found that the morphology of OP C-A-S-H was connected with the CH content in samples, which started to appear as foil-like when the sample has %CH ≈ 8~13 (the Ca/(Si+Al) will simultaneously decrease from the original 1.75 to 1.2~1.3). More interestingly, links between pore solution composition and morphology of C-S-H were also proposed based on literature data (details are available in Ref. [14]). Three indications from pore solution were summarised in association with the change from fibrillar- to foil-like C-A-S-H gel: a). the decreasing pH of pore solution, b). the pore solution undersaturated with respect to CH, and c). the pore solution has a [Si] concentration > ≈ 0.35 mmol/L.

Based on the analysis above, it is clear that the equilibrium of solid and liquid phases in hardened cement results in some inter-relationships. Hence, a question is proposed whether these relationships can be verified in the same samples or not? This question is answered in the first part of this PhD project. To conduct this project, different kinds of SCMs (GGBS and PFA) are selected as a partial replacement of cement powder to investigate the changes in pore solution

composition and nanostructure of C-S-H gel. The results of pore solution are compared to extensive results adapted from literature, while, the saturation conditions based on the pore solution composition are calculated by thermodynamic modelling [15]. Then, the pH values, ions concentrations and saturation indices with respect to specific solid phases are obtained and compared. For the C-(A)-S-H gel, techniques such as XRD, STA-MS, TEM-EDX, and ^{29}Si MAS NMR are used for characterisation, followed by analysis using Richardson and Groves' Model [5] to obtain the nanostructure of C-S-H gel. The relationships (discussed in Ref. [14]) between the solid C-S-H phase and pore solution may be developed.

The second part of this project is the investigation of changes in the morphology of C-S-H gel during the hydration of synthetic pure alite phase, which aims to clarify whether this phenomenon is present in silicate minerals in cements at early-age. Also, similar methodology is used in this section but with a w/s ratio of 10. Additional information on the dissolution behaviours of alite and precipitation rate of C-S-H are also modelled, which attempts to link the hydration and morphological changes of C-S-H gel in alite system.

The third part of this project is to study the change in morphology of single-phase C-S-H, that synthesised via high lime (CH) concentration method, which is an extension of the methodology developed by Richardson and Vinnakota [16]. The additional information of chemical composition of filtrates is analysed by ICP-OES. The leaching behaviours of these C-S-H phases are investigated by statistic leaching in DI water, NaOH solution, and $Al(NO_3)_3$ solution. Further, the effects of Na and Al ions on the changes of morphology, composition, and nanostructure of this C-S-H are also studied through NMR and ICP-OES techniques.

Overall, a brief mind mapping is shown in Figure 1-1 in relation to the topic “The morphological change of C-S-H”.

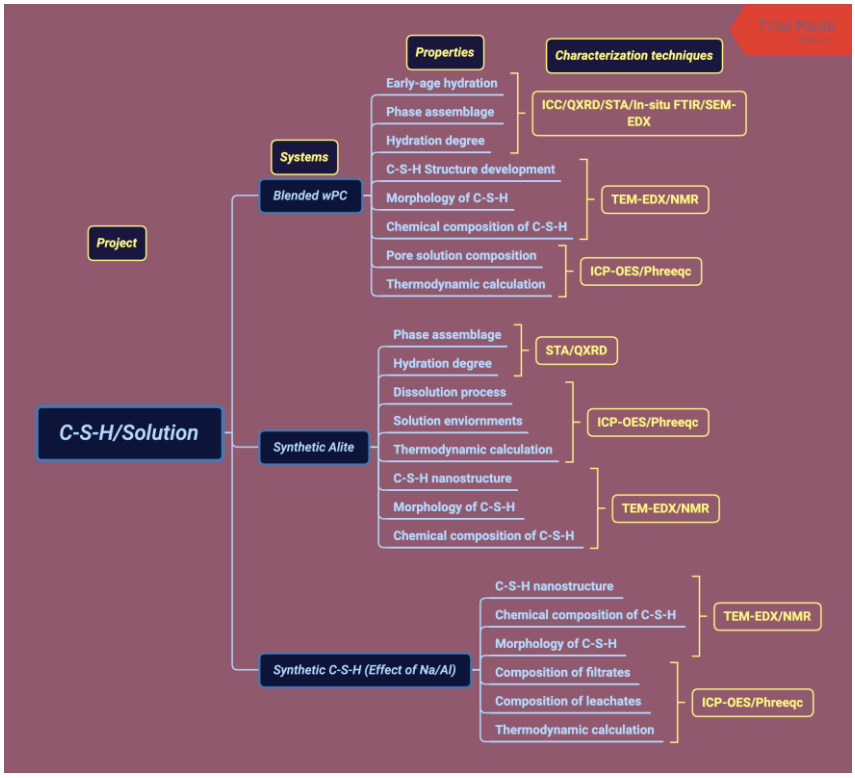

Figure 1-1 Mind mapping of the complete project.

1.2 Thesis outline

The thesis is divided into 8 chapters, Introduction, Literature review, Characterisation techniques, Experimental details, three chapters of results and discussion, and one chapter of summary.

Chapter 2 presents a literature review related to this project, including the hydration of cement, the development of C-S-H nanostructure, the pore solution composition of hardened cement, and the equilibrium of solution environment of C-S-H gel.

Chapter 3 includes the introduction of techniques and modelling methodology used in this study. The working principles of isothermal conduction calorimetry (ICC), quantitative-X-Ray diffraction (QXRD), simultaneous thermal analysis (STA), Fourier transform infrared spectroscopy (FTIR), nuclear magnetic resonance (NMR), inductively coupled plasma optical emission spectrometer (ICP-OES), and transmission electron microscopy-energy dispersive X-ray detector (TEM-EDX). In addition, the methodology of thermodynamic model is given in this Chapter.

Chapter 4 presents the details of experiments, which describes the identification of SCMs content and expected age of testing; the arrangement, preparation, and conditioning of samples. Also, the details of equipment and related testing parameters are also given in this Chapter.

Chapter 5 is the experimental results and discussion of the relationships between C-S-H gel and solution environment in different blended cements. The nano-structural development of C-S-H gel and the changes of solution environment are the main topics discussed. In the discussion section, data collected from literature are also interpreted and compared to the current study.

Chapter 6 gives the details of the hydration process of the main constituent part, alite, of Portland cement combined with its solution changes and C-S-H gel nano-structural development. Alite is synthesised in order to identify whether the changing of solution will change the morphology of OP C-S-H gel in an open space.

Chapter 7 discusses the synthesis of the fibrillar-like C-S-H with a high Ca/Si ratio and its solution composition. The effects of Na and Al ions on the morphology and C-S-H nanostructure are also discussed based on ^{29}Si, ^{23}Na, and ^{27}Al NMR results. In addition, the chemical compositions of leachates in different solutions and the nanostructure of the solid residual C-S-H are also discussed.

Chapter 8 summarises the main findings in Chapters 4-7, with an extension of further considerations and recommendations.

Chapter 2

A review on nanostructure, morphology, and chemical composition of C-S-H gels

2.1 Hydration of Portland cement

When the cement mixes with water, the dissolution of ions leads to a series of complex reactions in the pore solution which further precipitates to form hydration products. Hence, the hydration of cement is considered firmly a dissolution-precipitation process since it was first experimentally shown by Henri Le Chatelier in the 19th century. The hydration of cement is significantly important and can provide basic information for the activities conducted by the reactive binders, which will also link to the macro properties of concrete. Understanding the hydration mechanism is naturally the fundamental problem that needs to be addressed. In this section, the hydration of Portland cement is reviewed in view of composition, hydration kinetics, hydration products and related thermodynamic modelling studies.

2.1.1 Composition of Portland cement

When calcareous, siliceous and aluminous (sometimes including ferruginous) materials are mixed, followed by heating at 1450 ℃, a clinker is formed. This spherical clinker is further milled to powder which constitutes the basic components of Portland cement. The clinker normally contains four major mineralogical phases, including alite (impure C_3S), belite (impure β-C_2S), aluminate (impure C_3A) and ferrite (impure C_4AF) [1]. Alite is the main component of clinker (50%~70%), which has a relatively quick reaction with water and contributes to the main strength development up to 28 days. Whereas, Belite (15%~30%) shows a slower hydraulic reaction and contributes in an increase in strength at later age. The impure orthorhombic and cubic tricalcium aluminate (commonly less than 10%) rapidly reacts with water and cause the “fast-setting” of Portland cement paste [17]. Gypsum ($CaSO_4·2H_2O$) is normally added to cement to control the setting problem. Hence, tricalcium aluminate phase eventually reacts with sulphate phases to further form AFm and AFt. Ferrite makes up around 5%~15% of clinker and its reaction with

water depends on ionic substitutions and other characteristics. It is noticed that excessive contents of ferrite in clinker can cause rough background peaks in NMR analysis, therefore white Portland cement (which contains much less ferrite in clinker) is usually selected as a substitute for NMR analysis.

For a combined purpose of energy-saving, emission-reducing and durability-enhancing, SCMs, such as slag, fly ash, metakaolin and silica fume, are normally added into clinker to form different types of Portland cement with specific aims in constructional use. Among all the SCMs, fly ash and slag are most commonly used in cement system, which offers concrete an increase in strength at later age due to the so-called "pozzolanic reaction" [14]. The application of SCMs also improve the durability of concrete due to the changes in the nature of C-S-H gel and decrease in the hardened concrete's porosity [14].

Other than SCMs, the inert fillers including limestone, quartz powder are also used for partial replacement of clinker. These fillers are believed to have "filler effect" to increase the hydration degree of clinker, which is attributed to the dilution of effective water to cement ratios [18, 19]. Furthermore, some fillers, like limestone, are also identified to provide more nucleation and more space for the growth of hydration products [20].

2.1.2 Hydration mechanism of Portland cement

Hydration kinetics

The hydration of Portland cement is a simultaneous multifarious exothermic reactions process (heat-releasing), which can be monitored by the isothermal calorimetry analysis. As the dominant reaction in cement hydration, the reaction between C_3S and water attracts special attention. A typical hydration rate curve of alite (governing reaction) is shown in Figure 2-1 [21] and it can be divided into five stages. Stage 1 shows the highest heat-released peak mainly due to the wetting and partial dissolution of clinker grains, which is a non-steady state step [22]. Stage 2 is named as "induction or dormant period", which makes a trough in this hydration curve. The induction period is very important because it enables a time for concrete to be transferred and placed before hardening. The mechanism of the appearance of induction period remains debatable. Although

theories such as the formation of hydrate or precipitation of first C-S-H gel are widely accepted as the reasons for hydration delay, no direct evidence supports these theories [23]. Instead, some etch pits on the surface of grains are observed, which have sharp edges and may inhibit the formation of such layers [23]. Scrivener and Nonat [21] explained this phenomenon from geochemistry point of view, the formation of first etch pit on a smooth grain surface requires extra energy and hence delays the hydration. Stage 3 is the accelerating period, which is responsible for the fast crystal growth of hydration products after the setting of pastes [24]. Stage 4 can be regarded as decelerating period. According to Nicoleau [22], movement of ion concentrations towards C-S-H solubility and deviation from C_3S are observed at the transition between Stage 3 and 4. Stage 5 is the continuous hydration of C_3S and will last until the end of the hydration process and this stage is mainly controlled by interaction at phase boundaries process [25].

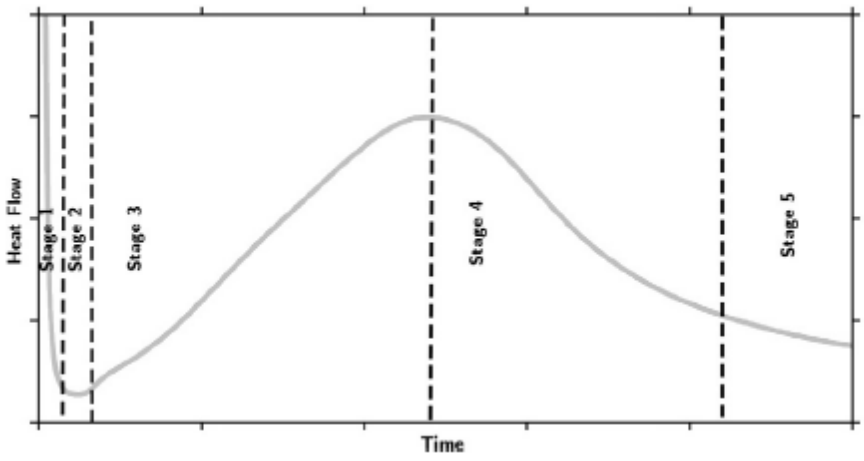

Figure 2-1 A typical 5-stages hydration curve of C_3S. Taken from [21].

For the hydration of Portland cement, it is clearly observed from Figure 2-2 that a small shoulder peak is found at around 20 hours. This peak is identified as the secondary formation of ettringite [26]. Moreover, a subsequent broad peak should also appear at the hydration curve generated by the formation of AFm phase as shown in Figure 11 in Ref. [26]. Figure 2-2 also shows the effect of SCMs (takes slag as an example) and inert fillers (takes quartz as an example) on the hydration of Portland cement. The addition of SCMs or inert fillers increases the heat flow of the main peak, which is attributed to the “filler effect”. The “filler effect” is mainly caused by two reasons. Firstly, increasing of water to cement ratio due to the dilution of cement which

further increases the hydration degree of clinker. Secondly, either slag or quartz can provide additional nucleation sites which is beneficial for the growth of C-S-H gel [19, 27]. The cross point of S-40Quartz and S-40Slag groups in Figure 2-2 implies the hydration of slag starts between 26 h and 28 h.

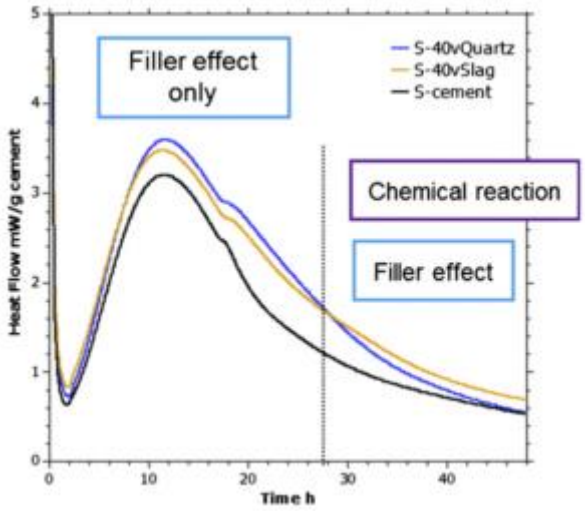

Figure 2-2 Effect of 40% quartz powder and 40% slag on the hydration of cement illustrated by normalized heat-released rate. Taken from [28].

Hydration kinetics are theoretically described using three basic processes: nucleation and crystal growth (NG), interactions at phase boundaries (I) and diffusion (D) [29]. It is assumed all three processes happen simultaneously while the controlled kinetics should be the slowest one [29]. When assuming that clinker powders are small particles, the three-hydration process can be mathematically described as shown in the following Equations 1 - 3 or other formats [25, 29, 30].

$$[\frac{d\alpha}{dt}]_{NG} = K_{NG} n(1-\alpha)[-ln\,(1-\alpha)]^{\frac{(n-1)}{n}} \qquad \textit{Equation 1}$$

$$[\frac{d\alpha}{dt}]_{I} = 3K_I(1-\alpha)^{\frac{2}{3}} \qquad \textit{Equation 2}$$

$$[\frac{d\alpha}{dt}]_{D} = \frac{3}{2}K_D(1-\alpha)^{\frac{2}{3}}/[1-(1-\alpha)^{\frac{1}{3}}] \qquad \textit{Equation 3}$$

Where α is the hydration degree at time t (days). The exponent n describes the geometrical crystal growth and the value usually ranges from 1 to 3. K_{NG}, K_I and K_D are the hydration rate constant for NG, I and D process respectively.

Although equation model can in such extent reflect the hydration of cement particles, a realistic simulation of hydration is also required to perform phenomena like porosity, heterogeneous distribution of unreacted particles and formation of hydration products. Based on these

requirements, the Jennings and Johnson microstructure simulation model, the HymoStruc model, CHMHYD3D, the HydratiCA simulation model and the µic microstructural modelling platform are developed and applied for the purposes of reflecting the real hydration. The details of these models are reviewed by J. Thomas *et. al* [30].

Hydration products

As stated in Section 2.1.1, clinker consists of four major phases and gypsum is always added when using as commercial cement. Hence, the following hydration for four mineral phases is presented separately in reaction formulas [31].

Hydration of siliceous phases (C_3S and C_2S):

$$C_3S + (3 - x + y)H \rightarrow C_x - S - H_y + (3 - x)CH \quad \textit{Equation 4}$$

$$C_2S + (2 - x + y)H \rightarrow C_x - S - H_y + (2 - x)CH \quad \textit{Equation 5}$$

Hydration of pure aluminate phase (C_3A) in presence of calcium sulphate:

$$C_3A + 3C\hat{S} + 32H \rightarrow C_6A_2\hat{S}_3H_{32} \ (ettrigite) \quad \textit{Equation 6}$$

or

$$C_3A + 3C\hat{S}H_2 + 26H \rightarrow C_6A_2\hat{S}_3H_{32} \ (ettrigite) \quad \textit{Equation 7}$$

$$2C_3A + C_6A\hat{S}_3H_{32} + 4H \rightarrow C_4A\hat{S}H_{12} \ (monosulphoaluminate) \quad \textit{Equation 8}$$

$$C_3A + 6H \rightarrow C_3AH_6 \quad \textit{Equation 9}$$

Hydration of aluminoferrite phase (C_4AF):

$$C_4AF + 3C\hat{S}H_2 + 30H \rightarrow C_6A_2\hat{S}_3H_{32} \ (ettrigite) + CH + FH_3 \quad \textit{Equation 10}$$

$$C_6A_2\hat{S}_3H_{32} + 2C_4AF + 12H \rightarrow 3C_4A\hat{S}H_{12} + 2CH + 2FH_3 \quad \textit{Equation 11}$$

$$C_4AF + 10H \rightarrow C_3AH_6 + CH + FH_3 \quad \textit{Equation 12}$$

The main reactions during the hydration of cement are expressed as Equations 4 and 5, which implies the main hydration products of hydration are C-S-H phase and CH. The values *x* (defined as Ca/Si molar ratio) and *y* (bounded water molecule of specific C-S-H) vary with different factors like relative humidity (RH) [32], temperature (T) [33], and solution environment [34]. Due to the non-stoichiometry, the calcium silicate hydrate phase is normally abbreviated as C-S-H, which is also the main binding phase in concrete. CH is also one of the dominant hydration products and takes up to around 20 wt. % of hydration products in ordinary Portland cement [14, 20, 35]. This hexagonal platelet crystal is also crucial for the secondary hydration of pozzolanic

powders such as PFA and slag, which is also named as “pozzolanic effect” [36]. Other than siliceous reactions, aluminate reactions are also confirmed as exhibited by Equations 6 – 9. It is noticed that gypsum is always present as $CaSO_4 \cdot 2H_2O$ in reactions shown in Equation 7, however, $CaSO_4$ (no chemical combined water, i.e. anhydrite) will be form due to the high temperature in the kiln or milling process, which will react with C_3A according to Equation 6. Ettringite and monosulphoaluminate are no doubt the main hydration products due to the aluminate reactions. Further, some C_3A can directly react with water to form C_3AH_6. The ettringite, CH and some FH_3 are the main hydration products as shown in the reactions of C_4AF (Equations 10-12). Under some circumstances, the presence of other negative ions, like chloride and carbonate, can easily replace the sulphate ions to form phases like Friedel’s salt, mono-(hemi-)carboaluminate [20]. These phenomena are attributed to the ions exchangeable property of layered double hydroxides (LDHs) phases, as which monosulphoaluminate and C_3AH_6 can be classified [37, 38]. Also, the presence of ions, like selenite and chromate will also replace sulphate ions in ettringite to further form Se- or Cr-ettringite [39, 40]. Although other phases may also be present, the main hydration products well accepted are as C-S-H gel, CH, ettringite, monosulphoaluminate, C_3AH_6 and FH_3.

When SCMs are added into neat cement, the subsequent reaction unquestionably depends on the composition of SCMs. The hydration process will also be different even for an SCM in the same classification. Section 2.1.1 states that the most commonly used SCMs are fly ash and slag, which will also be used in this investigation. Hence, effects of the addition of fly ash and slag on the products of cement hydration are briefly reviewed. Fly ash and slag are both high in silica content, which will decrease the Ca/Si ratio of original C-S-H gel [36]. The differences between these two SCMs are fly ash contains more Al_2O_3 but slag contains significantly high CaO. For fly ash blended cement, strätlingite (C_2SAH_8), which is normally formed in high alumina cement [41], is identified due to the presence of significantly high alumina content [42]. In addition, slag also contains 7%-15% MgO, which will further form another Mg-Al LHDs phase named as hydrotalcite-like crystal [4, 10, 36, 43]. Besides, strätlingite will also form at a high slag replacement level [10, 44].

2.1.3 Thermodynamic modelling study

Thermodynamic modelling derives from a view of energy and mass conservation [45], which provides us with an understanding from atom-scale rearrangement of chemical reactions. In the cementitious system, thermodynamic equilibrium modelling can be used for the prediction of solid and pore solution chemistry composition of cement as a function of time or as a function of chemical components [15, 36, 46-48]. Thermodynamic modelling provides a tool that can quickly and easily calculate the composition of stable blended pastes and further avoid massive experimental work.

The thermodynamic modelling is achieved normally by one of the two basic approaches: a) solving the law of mass action (LAW) equations, and b) minimizing the Gibbs free energy to a stable status of system (as shown in equation 13 and can be specifically calculated for a reaction as shown in equation 14) [15, 45, 49]. Both the approaches are written into codes: for LAW method, PHREEQC, MINEQL, EQ3/6 and CHESS are available, and for Gibbs free energy method, GEMS is one of the most common approaches in cement equilibrium [15, 50].

$$G = H - TS = \sum_i n_i \mu_i \qquad \textit{Equation 13}$$

$$\Delta_r G^0 = \sum_i v_i \Delta_f G^0 = -RT ln\, K \qquad \textit{Equation 14}$$

Where G stands for Gibbs free energy, H is the function of enthalpy and S is the function of entropy. n_i is the number of moles of the one compound and μ_i is the partial molar Gibbs free energy. $\Delta_r G^0$ is the Gibbs free energy of reaction, v_i stands for the stoichiometric coefficients of the reaction, $\Delta_f G^0$ is the Gibbs free energy of formation of the specific compound. R = 8.31451 J/mol/K is the universal gas constant and T is the temperature (K). K stands for the equilibrium constant.

Gibbs free energy is a state function, which is deeply affected by pressure and temperature but finally depends on the initial and final state of the system and independent with the process [15, 48]. For an equilibrium between solid and liquid phases, the equilibrium constant K can connect the system balance information to the Gibbs free energy. Based on this, Equation 14 is extremely important in the thermodynamic study of cement composites because the cement system is the balance between solid (hydration products or residual clinker phase) and liquid (pore solution)

phases. As clearly defined in many textbooks [45, 51, 52], the equilibrium constant K for reaction shown in Equation 15 can be expressed as equation 16.

$$aA + bB \rightleftharpoons mM + nN \qquad \textit{Equation 15}$$

$$K = \frac{[M]^m[N]^n}{[A]^a[B]^b} \qquad \textit{Equation 16}$$

Where *A* and *B* are reactants, *M* and *N* are products. *a*, *b*, *m*, and *n* are stoichiometric for these stable phases respectively. *[M]*, *[N]*, *[A]*, and *[B]* stands for the activity of ions in pore solution.

Under this circumstance, the solution concentration plays an important role in the thermodynamic study. However, the ion concentration cannot be used directly for the equilibrium constant calculation. The activity corrections should be taken for all the aqueous species based on the ion concentration. Specifically, Davies equation is used for the solution that have an ionic strength of 0.1 to 0.5 molal (mol/kg) and Extended Debye-Hückel equation is used for the solution that have an ionic strength of 1 to 2 molal. For even higher up to 6 molal, the use of specific ion interaction term or Pitzer model is necessary [15].

Moreover, some solid phases in Portland cement are not stoichiometrically certain, for example, the C-(A)-S-H gel phase, should use solid solution method to determine the dissolution properties for a purpose of involving this phase into the thermodynamic model. Solid solution model with mixing of two sub-lattice sites which built from a structural model (for example, Richardson-Groves' model [5, 53, 54]) is always selected as the basic thermodynamic structure of C-S-H phases [55-57]. Hence, a proper C-S-H solid solution model requires further efforts in increasing structural consistency with a more accurate structural model for C-S-H phase [57].

The thermodynamic modelling can be used for: a) the simulation of stable phase assemblage based on the composition, b) modelling the hydrated systems: for high alumina cement system [58], when incorporating different SCMs [25, 36, 59, 60], at different hydration environment [47], and with the presence of some difficult detective phases (for example, thaumasite) [61], c) coupling with hydration kinetics model (Section 2.1.2), and d) coupling with transport models [62]. Some typical results related to this study are presented in Figure 2-3. For PC-fly ash system, strätlingite is found when the fly ash content increased to approximately 35% or more, which is mainly due to the increasing alumina content in the system. For PC-slag system, a large number

of hydrotalcite-like phases increased because of the introduction of magnesium by slag. Meanwhile, the portlandite is consumed with the loading of both fly ash and slag. These results are all in good consistency with other techniques detected as discussed in Section 2.1.2.

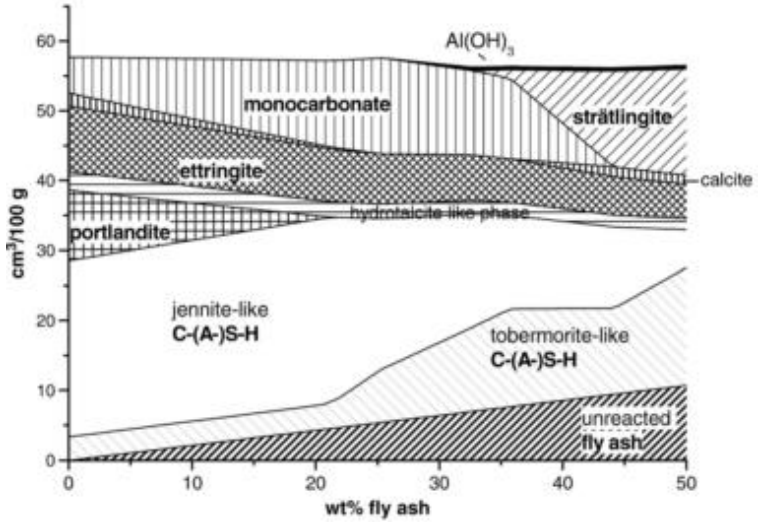

(a) PC-fly ash system

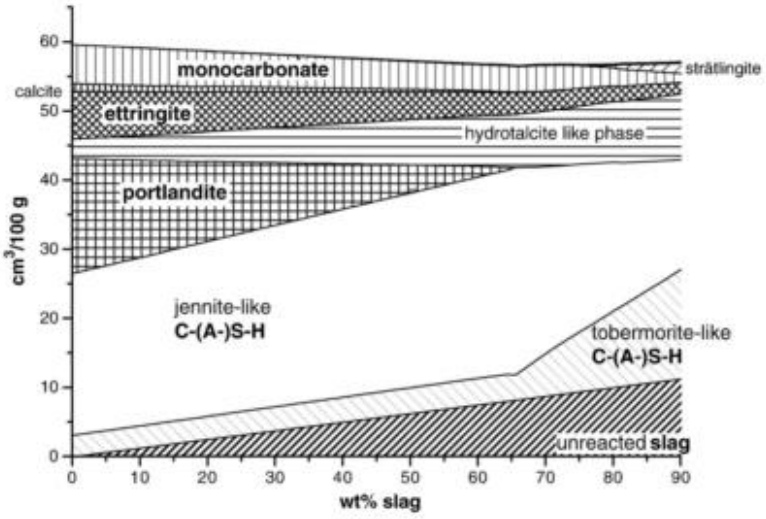

(b) PC-slag system

Figure 2-3 Modelled hydrated phases of Portland cement incorporating with (a) fly ash and (b) slag. Taken from Ref. [36], where provides the raw materials composition.

2.2 Main binding phase of hardened cement paste: Calcium silicate hydrate (C-S-H) gel

As mentioned previously, C-S-H gel consists of nearly 70% of hydration products in neat Portland cement and is mainly responsible for the binding properties Understanding the nature of C-S-H gel is the key to understand the degradation of concrete and further, find the solutions for

the improvement of durability of concrete. The generic terminology, calcium silicate hydrate (C-S-H), stands for a category of mineral which has over 30 kinds of crystalline structural minerals [63]. However, the C-S-H gel generated from the hydration of either C_3S or C_2S in cement system is surprisingly disordered and compositionally variable [6]. Hence, the C-S-H gel particularly refers to the C-S-H mixtures in cement system to distinguish it from crystals or synthetic ones. This section will give a brief review of the studies of basic properties of C-S-H gel and synthetic C-S-H.

2.2.1 Techniques used in the study of C-S-H gel

Chemical method

Using the chemical method for the determination of C-S-H structure is the first ever insightful investigation of local silicate anions in C-S-H gel. Molybdate complexing [64, 65] and trimethylsilylation gel permeation chromatography (TMS-GPC) [66, 67] are the two most commonly used methods in silicate anion detection. The basis of using molybdate complexing is the formation of β-molybdosilicic acid when adding an acidified solution of ammonium paramolybdate to monomeric silicic acid (converted from C-S-H), followed by studying the kinetics of Si-O-Si bond rupture and formation during this process to give the information of silicates proportion [64]. For TMS-GMS method, silicate anions are converted to silicic acids and then react with TMS to form $Si\text{-}OSi(CH_3)_3$ [66], GPC method is applied to measure the so-called "polysilicate" fraction.

Although the chemical method is not such accurate because of the possibility of condensation reactions or other side reactions taking place before the silicic acid forms molybdenum-/TMS products, it still provides some important information [63]. The most precious result provided by TMS is that the silicate anions presented in hydration products follow a 2, 5, 8 … (3n-1) sequence, where n is integer [14].

Powder X-ray diffraction (XRD)

Due to the high complexity of C-S-H gel, advanced techniques need to be used in order to get the accurate information. XRD is the most common method in crystal structure study, which is

also applied for the study of C-S-H phases despite it being structurally disordered and virtually X-ray amorphous [7]. The XRD patterns for synthetic C-S-H consists of few broad and weak diffraction maxima, normally appearing at (2θ Cu Kα) ~ 7.4° (12.0 Å), ~ 16.7° (5.3 Å), ~ 29.1° (3.1 Å), ~ 32.0° (2.8 Å), ~ 49.8° (1.8 Å), ~ 55.0° (1.7 Å), and ~ 66.8° (1.4 Å) [68], and they only appears at 2.6~3.2 Å (broad band) and 1.82 Å (sharp peak). Although the spacing at different 2θ angles corresponds to the presence of Ca-O of C-S-H phases, the structural information cannot be easily concluded from the XRD pattern due to the uncertainly in the location of Ca-O [63]. However, a general principle is observed from XRD that the basal spacing decreases with increasing Ca/Si ratio [7]. The basal spacing at the low angle peak of XRD patterns corresponds to the layer thickness of mineral in C-S-H gel. Although C-S-H has a less ordered structure, the Rietveld refinement of the structure of synthetic C-S-H can also be fitted based on introducing "fragments" constraints to study the C-S-H structure [69]. Also, quantitative X-ray pair distribution function analysis is also used along with synchrotron X-ray scatting data for the investigation of C-S-H structure [70-72].

Nuclear magnetic resonance (NMR)

NMR spectroscopy is one of the most powerful tools in the elucidation of C-S-H gel structure, which can probe the local atomic structure of a material in a short-range order [73, 74]. Solid-state NMR was not widely used until the technique of spinning the sample at the magic angle (i.e. 54.7356°) to the axis of the applied magnetic field appeared [73, 75], known as magic angle spinning (MAS) NMR. The reason for the selection of the magic angle is because the solid materials signal oriented at the magic angle may appear hyperintense. NMR experiments are conducted in a high magnetic field and the spinning of a positively charged nuclei can generate a magnetic moment, which is the same as a charge moving in a circle creates a magnetic field [76]. The spinning properties of an atom's nuclei also depend on protons and neutrons, the nuclei have no magnetic properties if the atomic number (protons) and the atomic mass (the sum of protons and neutrons) are even [76]. Hence, when the atomic number or atomic mass is odd, the nuclei are said to be resonance-responded. For specific nuclei, the spin quantum number can only take on certain values, for spherical nuclei this is 1/2 and for non-spherical nuclei is 1 or more (in

increments of 1/2). When the sample is exposed to an electromagnetic radiation environment, energy is absorbed at specific resonance frequencies. These frequencies are specific to the chemical environment of the nuclei being observed and are converted by Fourier transform into chemical shift values.[77]. ^{29}Si, and ^{27}Al are the two most commonly observed nuclei in cementitious materials [78-82], others like ^{1}H, ^{13}C, and ^{17}O are also used in cement research [63, 74, 83]. Many valuable results are given by the deconvolution of solid-state MAS NMR spectra [5, 6, 84].

The accurate analysis of the silicate structure in cement systems is to a great extent attributed to the application of ^{29}Si MAS NMR since it was first used in cement systems in 1982 [85]. The peak intensity of a pattern obtained from ^{29}Si single-pulse MAS NMR can be calculated through a deconvolution process and denoted as $Q^n(m\text{Al})$ [14]. Where, Q, is connected via oxygen bridges to *m* Al and *n-m* other Si atoms, with *n* ranges from 0 to 4 and *m* ranges from 0 to *n* [14]. In other words, for silicate tetrahedron itself, Q^0 is the monomer, Q^1 is the dimer, Q^3 is the cross-linking sites and Q^4 is the network tetrahedron (as shown in Figure 2-4) [72].

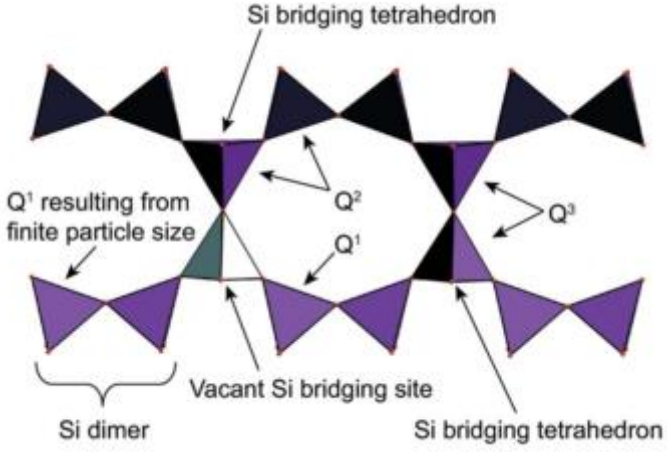

Figure 2-4 A wollastonite-like chains showed the different silicate tetrahedron, adapted from [72].

As stated before, [SiO_4]-contained C_3S and β-C_2S are present in unreacted cement. In ^{29}Si MAS NMR spectra, there are up to 9 Q^0 peaks in the range of -67 to -74 ppm can be attributed to C_3S. However, for β-C_2S there is only one peak at -71 ppm [85]. The C-S-H gel generally gives the Q^1 and Q^2 peaks at around -79 and -85 ppm, respectively, indicating that the presence of dimer and pentamer tetrahedra. Although Q^0 sites are negligible in ^{29}Si MAS NMR spectrum of C-S-H, a

small amount of monomer in C-S-H (up to 2% of total Si) was still proven to be present by using ^{29}Si-^{1}H cross polarization (CP) MAS NMR [86]. (The application of this double resonance NMR is to avoid the ^{29}Si that solely comes from Si-OH in anhydrous materials so that the tetrahedron in anhydrous phases are eliminated [8, 80, 82, 86, 87]). The Q^3 peak, which sometimes appears at -96 ppm of low Ca/Si ratio C-S-H gel, indicates the presence of cross-linking sites [56]. Q^4 sites are due to the network of silicate tetrahedron, which is normally found in silica gel, quartz or silica fume at a position of -112 to -113 ppm. The results obtained from NMR are also consistent with the results given by chemical methods. When assuming Q^3 is absent, the mean silicate chain length and hydration degree can be calculated as shown in Equations 17 and 18, respectively [7, 14, 53].

$$Mean\ silicate\ chain\ length\ (MCL_{Si}) = 2(1 + Q^2/Q^1) \qquad Equation\ 17$$

$$Degree\ of\ hydration = \frac{Q^1+Q^2}{Q^0+Q^1+Q^2} \qquad Equation\ 18$$

Results from NMR give a MCL_{Si} of approximately 4.8 of C-S-H in a 26 years hydrated C_3S, which is quite close to the MCL_{Si} of ~ 5 given by TMS method for the C-S-H in 22-30 years hydrated C_3S [63]. The MCL_{Si} of C-S-H gel generally increases with the age or degree of hydration [63] and decreases with the increasing Ca/Si ratio [88]. Moreover, when C-S-H containing some Al^{3+}, the Al/Si ratio and total MCL can be calculated using Equations 19 and 20.

$$MCL = 2(1 + \frac{Q^2}{Q^1} + \frac{3}{2}\frac{Q^2(1Al)}{Q^1}) \qquad Equation\ 19$$

$$\frac{Al}{Si} = \frac{1/2\ Q^2(1Al)}{Q^1+Q^2+Q^2(1Al)} \qquad Equation\ 20$$

^{27}Al MAS NMR is extremely useful in distinguishing the coordination of alumina in cement systems containing SCMs, in which the tri-positive cations Al^{3+} can substitute the Si^{4+} to form C-A-S-H [7, 14, 54, 55, 78, 89]. An important finding from combined use of ^{27}Al and ^{29}Si NMR, energy loss spectroscopy, and TEM-EDX is that Al^{3+} only substitutes at the bridging tetrahedral of dreierketten [7, 54, 78, 79, 89]. More importantly, the ratio of octahedral Al (Al[6]) to tetrahedral Al (Al[4]) can be detected through ^{27}Al MAS NMR. The Al[6] is generally attributed to the Mg-Al LDHs phases, AFt phase, and TAH at 13.3, 9.9, and 4.5 ppm respectively [7, 35, 90]. Sometimes, minor Al[5] signals can be observed due to the uptake for interlayer Ca^{2+} by Al^{3+} in

C-A-S-H at about 35 ppm [35]. The chemical shift of substituted Al[4] is located near 69 ppm, and this peak sometimes contains the Al[4] in raw materials (for example, the PFA) [35]. In addition, the ratio of Al[6] to Al[4] is proven to increase with Ca/Si ratio [91], which may also relate to the decreasing MCL with increased Ca/Si ratio [7].

Other nuclei used in NMR C-S-H gel studies include ^{17}O MAS NMR and ^{1}H MAS NMR, which are believed to have the potential power to distinguish the different sites of oxygen or hydrogen atoms in C-S-H gel. Compared to ^{29}Si MAS NMR and ^{27}Al MAS NMR, ^{17}O MAS NMR and ^{1}H MAS NMR are scarcely applied in cement systems due to some technological problems.

For ^{17}O nuclei, the interactions of quadrupole moments (nuclei spin equal to 5/2) during NMR tests result in excessive broadening of the lines in the spectrum [77]. In addition, the natural abundance of ^{17}O nuclei is only 0.037% (^{29}Si has a value of 4.68% and ^{27}Al has a value of 100%), which may involve a lengthy exchange process that requires longer testing time. Although some signals from ^{17}O NMR spectra remain uncertain, six explicit oxygen sites in synthetic C-S-H, or C-S-H formed from β-C_2S, are deconvoluted from peaks between 80-110 ppm [92]. These oxygen sites specifically include two non-bonding oxygen sites (NBO, Si-O-), one bonding oxygen site (BO, Si-O-Si), silica hydroxyl site (Si-OH), calcium hydroxyl site (Ca-OH) and H_2O molecules [92]. J Chen [63] speculated the erratically distributed chemical shifts of Si-OH (normally between -15 to 13 ppm, sometimes less than 37 ppm) was attributed to the prominence of Si-OH sites at the surface of silica particles. ^{17}O MAS NMR spectra can provide the proportion of oxygen-sites in C-S-H gel, which is important for the understanding of C-S-H structure.

^{1}H nuclei have a natural abundance of 99.99% and a nuclei spin value of 1/2, hence, ^{1}H NMR is widely used for analysing organic materials in solution. However, due to the fixed position of protons in C-S-H gel, very broad signals are seen in ^{1}H MAS NMR spectra because of the dipolar coupling effect [77]. A technique called combined rotation and multi-pulse spectroscopy (CRMPS) was applied to ^{1}H NMR in order to obtain the high-resolution spectra of protons in solids. By applying this method, the ^{1}H NMR spectrum showed peaks at 3-6 ppm, 7-13 ppm, and -3 to 3 ppm which were attributed to H_2O, Si-OH and Ca-OH, respectively [93]. Therefore, ^{1}H NMR is

very powerful in deconvolution of the nanostructure of C-S-H gel, especially for the presence of the hydroxylated layer (Si-OH) [63].

Transmission electron microscopy combined energy dispersion X-ray analysis (TEM-EDX)

The microscope is designed to transform an "object" into an "image" by using the optical system, from which up to nanometre or even Angstrom-unit information can be observed [94-96]. Electron microscopy combined with EDX technique is principally used in the study of morphology and chemical composition of C-S-H gel or other related crystal phases in cement system. The historical timeline of how electron microscopy techniques developed in cement-based materials since the firstly recorded in 1939 was completely tabulated by Richardson [75] (See table 22.1 in Ref. [75]). Among all the electron microscopy techniques, TEM is believed to be the most suitable one for the structure and composition study of poorly crystalline C-S-H gel phase [75, 84]. By a combined analysis of TEM morphology and EDX results, the intermixed phases in C-S-H gel can be easily identified [84, 97]. More importantly, the EDX provides the chemical composition of C-S-H, for example, Ca/Si ratio and Al/Si ratio, which provide the basis for the understanding of the atomic structure of C-S-H [7, 53, 88, 98, 99].

Vibrational spectroscopy

Vibrational spectroscopy, including Infrared (IR) and Raman, is an essential tool in the study of molecular structures of either organic or inorganic materials. The theory behind the vibrational test is based on the vibration of atoms in a molecule within a few definite distances and these vibrational frequencies occur in the region of electromagnetic spectrum 13333 cm^{-1} to 50 cm^{-1} and beyond [100]. Only molecules vibrated to produce dipole-moment changes are IR active, while others vibrated to produce polarization of the electron are Raman active [100]. Both IR and Raman spectroscopy are useful for the understanding of the structure of C-S-H gel [101, 102]. An advanced understanding of how Ca/Si ratio increases up to 1.3 of tobermorite-like C-S-H gel was possibly explained by near-IR infrared spectroscopy [103]. It is found that the Ca ions can also substitute for protons in Si-OH groups as the Ca/Si ratio of C-S-H increases, which provides a suitable explanation for additional Ca in C-S-H gel [103]. Raman spectra in the range of 3100-

3900 cm^{-1} were normally used for analysis of the hydrogen bond network [102], Si-O stretching region is at 950-1000 cm^{-1} [104], and doubtful Ca-OH bonds at 180 cm^{-1}, which provided additional evidence in resolving the structure of C-S-H [63].

Other advanced techniques

Many other advanced techniques have also been developed since 20th century, including inelastic neutron spectroscopy (INS) for detecting the structural environments of protons, extended X-ray absorption fine structure (EXAFS) for the interatomic spacing and coordination information of a specific atom, atomic force microscopy (AFM) for the topography of surface atom, and Small-angle scattering (SAS) for illustrating the structure of C-S-H from particle level, which were specifically reviewed by J. Chen [63]. Especially the SAS technique, the studies on decalcification process and physical properties of C-S-H have relied on this technique [105-108].

2.2.2 Mineral basis for C-S-H

Although the C-S-H gel is amorphous and disordered, studies also show that it still has local short-range structural order. Due to the similarity between crystalline C-S-H and C-S-H gel, the understanding of nanostructure of C-S-H gel is beneficial from the insights in natural calcium silicate crystals [109, 110]. Figure 2-5 shows 11 different one-dimensional infinite tetrahedral structures among the silicates and all these structures are based on the infinite chains of tetrahedral configuration with [SiO_4] units. All these presented in Figure 2-5 are also based on well-known minerals as details given in figure captions. Except (e), all these infinite tetrahedral structures confirm $[X_nO_{3n}]_\infty$ periodicity, which means the silicate chain repeat every *n* tetrahedra. Another difference should be noticed that is the steric characteristic of this tetrahedron even with the same periodicity. For example, when compared (c) and (j) with the same periodicity in Figure 2-5, a typical fourfold helix axis can be found in (j) which also appears in natural mineral neptunite.

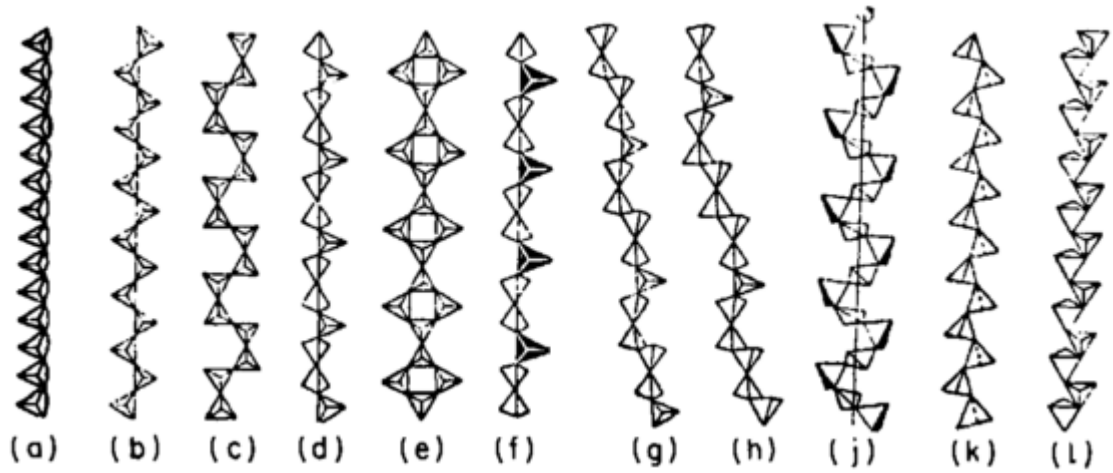

Figure 2-5 Various single chains of tetrahedral. (a) Ideal metasilicates $[Si_1O_3]_\infty$; (b) pyroxene, $[Si_2O_6]_\infty$; (c) batisite $[Si_4O_{12}]_\infty$; (d) wollastonite $[Si_3O_9]_\infty$; (e) vlasovite $[Si_4O_{11}]_\infty$; (f) melilite $[Si_2ZnO_9]_\infty$; (g) rhodonite, $[Si_5O_{15}]_\infty$; (h) pyroxmangite, $[Si_7O_{21}]_\infty$; (j) metaphosphate, $[P_4O_{12}]_\infty$; (k) fluoroberyllate, $[Be_2F_6]_\infty$; (l) beryllite, $[Be_2O_6]_\infty$; Firstly summarized by Belov, taken from [109].

The mineral basis of C-S-H was inspired by the structure of Maddrell's salt, a polymorph of $NaAsSO_3$, which shows to be isostructural with β-wollastonite (β-$CaSiO_3$) [63]. The wollastonite structure is clearly shown in Figure 2-5 (d), which contains infinite metasilicate chains kinked so at to repeat at intervals of three tetrahedra. More specifically, it can also be described that one tetrahedral bridge the gap between two consecutive Si_2O_7 groups [109]. This kind of silicate chain can be named as "dreierketten", a word came from German, which means "three-membered chains" [63]. The other terminologies include zweierketten $[Si_2O_6]_\infty$ as shown in Figure 2-5 (b), fünferketten $[Si_5O_{15}]_\infty$ as shown in Figure 2-5 (g), and siebenerketten $[Si_7O_{21}]_\infty$ as shown in Figure 2-5 (h). The reason that is behind the formation of unique dreierketten also depends on the nature of the cation that the Si shares oxygen atoms with. When the small cations such as Mg^{2+}, Fe^{3+}, and Al^{3+} in the metal-oxygen layer, the silicate chain is easy to form zweierketten $[Si_2O_6]_\infty$ and these can either remain single-chain as in pyroxene (Figure 2-5(b)) or condense into double-chains presented in amphiboles or the sheets of clay minerals [63]. For the larger cations such as Ca^{2+} and Na^+, the silicate chain prefers to form dreierketten $[Si_3O_9]_\infty$ and the dreierketten can either keep single-chain as in wollastonite (Figure 2-5(d)) and 1.4-nm tobermorite or condense into double-chains presented in xonotlite and 1.1-nm tobermorite [63]. This is vital for

understanding the structure of amorphous C-S-H gel and the presence of Ca-O interlayer also confirms “dreierketten” unit in C-S-H gel.

Tobermorite and Jennite groups

Figure 2-6 gives the schematic diagrams structure of 1.4-nm tobermorite (only shows one layer), among which, ‘paired tetrahedral’ shares two oxygen with Ca-O layer while ‘bridging tetrahedral’ only shares one. The 1.4-nm tobermorite has a general formula of $Ca_5Si_6O_{16}(OH)_2 \cdot 8H_2O$, which is the most hydrated member in tobermorite group. Meanwhile, the prefixes of tobermorite stands for the interlayer spacing along (002). When heating 1.4-nm tobermorite, this compound will transfer to 1.1-nm [$Ca_5Si_6O_{16}(OH)_2 \cdot 5H_2O$] (which is also named as clinotobermorite) or 0.9-nm tobermorite [$Ca_5Si_6O_{16}(OH)_2$] through a way of directly losing water molecules at 55 ℃ or 300 ℃, respectively. It is clear to see that the presence of water molecules shows a direct effect on the interlayer spacing of tobermorite mineral. However, there is another type of 1.1-nm tobermorite named as ‘anomalous’ type [$Ca_{4+x}Si_6O_{15+2x}(OH)_{2-2x} \cdot 5H_2O$], which will not shrink to 0.9-nm tobermorite when the temperature exceeds 300 ℃ and is noted by Mitsuda and Taylor [63]. When observing two 1.1-nm tobermorite, it is easy to found that the biggest difference is the absence of interlayer Ca in ‘anomalous’ type from the formula point of view.

1.4-nm tobermorite is a natural mineral and has an ideal Ca/Si ratio of 0.83 [111]. However, the Ca/Si ratio of tobermorite can be as low as 0.67 if all the Si-O-X positions are protonated instead of connecting to Ca polyhedral. Moreover, the 1.4-nm tobermorite can also be synthesized through a reaction between $Ca(OH)_2$ and hydrous silica at 60-100 ℃ by starting with initial Ca/Si ratio of 0.9 [112]. Many evidences have shown that the structure of 1.4-nm tobermorite is suitable for C-S-H gel at low Ca/Si ratios [6], although C-S-H possesses only single-chain dreierketten and limited chain length.

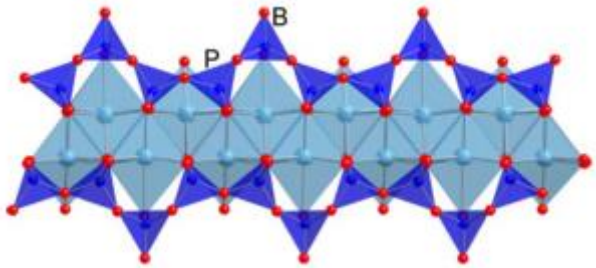

Figure 2-6 Schematic diagrams of 1.4-nm tobermorite projected along [210], taken from [5]. In which, it includes dreierketten (blue tetrahedral) consists of two 'paired tetrahedral' (denoted as P) and one 'bridging tetrahedral' (denoted as B). Two infinite dreierketten are connected by the linked CaO_6 (light green), which based on the coordination requirements.

Figure 2-7 shows the structure of jennite, which has a general formula of $Ca_9(Si_6O_{18})(OH)_6{\cdot}8H_2O$. Like tobermorite, jennite can occur as a natural mineral [113] or be synthesized through the similar reaction as the synthetic tobermorite but with higher starting Ca/Si ratios ranging from 1.2 to 1.5 [112]. The structure of jennite, as shown in Figure 2-7, can also be similarly described as a central Ca-O corrugated sheet is flanked by rows of dreierketten and OH groups [113]. However, the biggest differences between tobermorite and jennite is attributed to the differences in Ca-O layers. As clearly shown in the simplified structure of both 1.4-nm tobermorite and jennite in Figure 2-8, the first different should be that every other dreierketten is replaced by a row of OH groups which makes the Ca-O layer in jennite hold an empirical formula of Ca_2O_5. The other significant difference is that partial O atoms in a sublayer of jennite shared with the dreierketten, the paired tetrahedral of which are inset within the corrugations and the other O atoms form OH groups linking with Ca atom. Hence Ca-OH is one of the significant different group between jennite and tobermorite, which was investigated by J Chen [63] using INS method to explain the structural changes of C-S-H with increasing Ca/Si ratio. Due to the difference in Ca-O sublayer, jennite has an obvious lager ideal Ca/Si ratio of 1.5. Meanwhile, the jennite structure is more suitable for C-S-H gel at high Ca/Si ratios [1, 6, 13, 63].

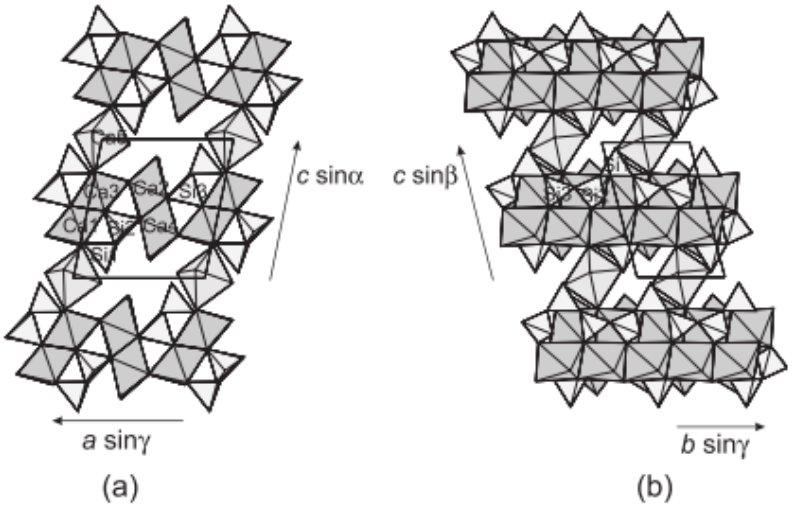

Figure 2-7 Projections of crystal structure of jennite from (a) [010] and (b) [100], taken from Ref. [113]. Light grey is the silicon tetrahedral and dark grey stands for Ca polyhedral, also bonds from interlayer Ca cations to water molecules and hydroxyl groups are shown.

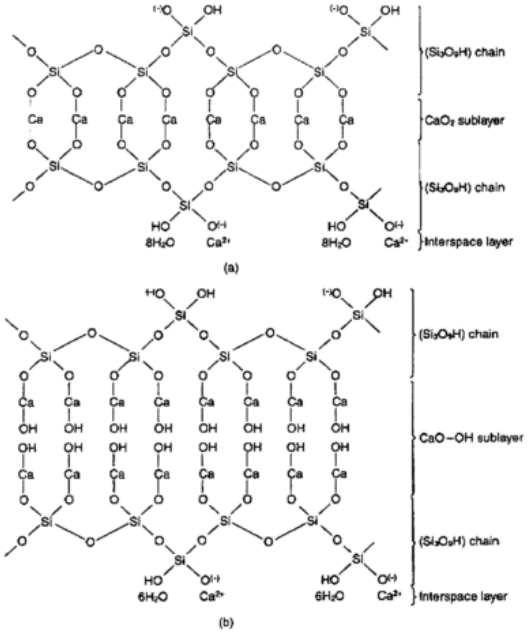

Figure 2-8 Idealised chemical structure (one layer) of (a) 1.4 nm tobermorite and (b) jennite, taken from Ref. [8].

Difference between C-S-H (I) and C-S-H (II), and C-S-H gel

The classification of C-S-H in a way of C-S-H (I) and C-S-H (II) is given by Taylor in a 1950 paper and further summarised in the classic book *Cement Chemistry* [1]. Reactions between CaO and SiO_2, or alkali silicate and a Ca-salt, or a C_3S hydrated under certain conditions, in aqueous suspension at normal temperature give a hydration product named C-S-H (I) [1, 8, 63]. C-S-H (I) can be regarded as an imperfect version of 1.4-nm tobermorite and lots of understanding of the nanostructure of C-S-H gel starts from this assumption [5, 13, 63]. The evidence from XRD

shows that C-S-H (I) has reflections of *hk0* bands (or *hk* band heads) of 1.4-nm tobermorite together with sometimes a broad basal reflection. The broad basal reflection at the low angle is related to the mean layer thickness of C-S-H (I), but this basal signal is absent if the structure is less ordered. Due to the variation of 1.4-nm tobermorite as stated above, C-S-H (I) has a Ca/Si ratio as low as 0.67. Similarly, some defects like the omission of bridging tetrahedral and the content of interlayer Ca give C-S-H (I) a Ca/Si ratio as high as 1.50. Meanwhile, a difference between ideal 1.4-nm tobermorite and C-S-H (I) is that the latter has the single-chain dreierketten structure which is confirmed by TMS and ^{29}Si NMR results as discussed in Section 2.2.1.

Unlike C-S-H (I), C-S-H (II) is normally regarded as an imperfect version of jennite which is produced from a prolonged hydration of C_3S or β-C_2S with excess water at room temperature [1]. Evidence from TEM show that the C-S-H (II) has a morphology of bundles of fibres. The connection of C-S-H (II) and jennite are based on the unit-cell parameters determined by electron diffraction, XRD and IR [1]. Also, C-S-H (II) possesses a higher Ca/Si ratio of 1.50-2.0 when compared to that of C-S-H (I). However, the synthetic of C-S-H (II) remains absent in previous studies and still will be a research direction.

C-S-H gel is a word specifically used to describe the hydration products of cement or the hydration products of C_3S or β-C_2S with limited water (water to binder ratio equal to or less than 0.50). C-S-H gel has an average Ca/Si ratio of 1.7-1.8, which also shows a less ordered structure than either C-S-H (I) or C-S-H (II) [63]. The broadband of C-S-H gel always occurs in XRD pattern at 0.26-0.32 nm and a sharper band occurs at 0.182 nm, which correspond the repeated structure of Ca-O layers in C-S-H gel.

2.2.3 Synthetic C-S-H phases

The C-S-H phases can be synthesised either through a reaction of $Ca(OH)_2$/CaO and silica or a Ca-salt and an alkali silicate (double decomposition) [13, 63, 114, 115]. These reactions can take place at a room temperature and normal pressure as performed by Cong [92, 116]. Otherwise, a hydrothermal treatment (high temperature and high vapour pressure) is a better choice, which offers a wide range of synthetic products as shown in Figure 2-9. Normally, C-S-H (I) can be

synthesised under a room temperature [92], while those C-S-H (II) are hardly formed in this way. A higher temperature (120 to 210 °C) accompanying with extremely high initial Ca/Si ratio (2-3) are required for the C-S-H with Ca/Si of 1.59 to 1.75 [13]. Moreover, the mechanochemical method is also a good way to synthesise the C-S-H and Rodriguez provided an optimized synthesis route in ref. [13]. It should be noticed that all the synthetic procedure should be carried out under an N_2 atmosphere to avoid the potential carbonation [117]. For the synthetic C-A-S-H, the tricalcium aluminate ($Ca_3Al_2O_6$) [118] and calcium aluminate ($CaAl_2O_4$) [13] are normally chosen as the alumina precursors.

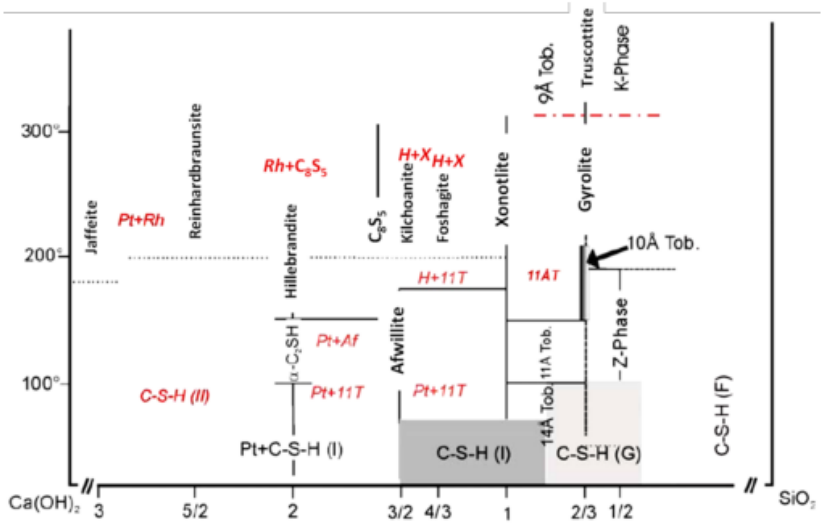

Figure 2-9 Diagram of the synthetic products from $Ca(OH)_2$-Slica reaction under hydrothermal treatment. The abbreviation Pt, Rh, Af, 11T, H and X stand for Portlandite, Reinhardbraunsite, Afwillite, 11 Å tobermorite, Hillebrandite and Xonotlite respectively. C-S-H (I) and C-S-H (II) are defined in Section 2.2.2. C-S-H (G) and C-S-H (F) are Gyrolite and Faujasite. Taken from Ref. [13].

2.2.4 Morphology of C-S-H gel

The morphology of hardened cement pastes, especially the main binder (C-S-H) gel, attracts particular interest in cement research, which is believed to have an important influence on the capillary pores and further affect the long-term properties of concrete [119]. Since the first observation of microstructure of cement clinker by La Chatelier in 1882, researchers continuously developed the applications of the electron microscopy techniques in cement science. Richardson (Table 22.1 in Ref. [75]) summarised the timeline of electron microscopy studies in cement area.

Generally, the hydration products of a cement particle can be divided into the inner product (IP) and outer product (OP), which have totally different morphology [5]. Other terminologies to

describe this phenomenon includes phenograins and groundmass or high density and low-density C-S-H [119]. Zhang [119] summarised five main factors that affect the morphology of C-S-H, which specifically includes curing temperature [8], admixtures [120-123], sample preparation procedure [124, 125], water to solid ratio [126], and the Ca/Si ratio of C-S-H [13, 127-129]. The incorporation of SCMs can change the morphology of C-S-H, which is undoubtedly related to the changes in its chemical composition [9, 14, 130]. Table 2-1 to 2-3 summarized the characteristics and compositions of inner and outer products in OPC and blended cements. As expected, the inner products of either pure OPC paste or blended cement have a compact and fine-scale morphology, whilst that of the outer product changes as the loading of SCMs accompanying with the changed chemical composition.

Table 2-1 Summary of TEM morphology of Inner and outer C-S-H gel in hydrates C_3S or OPC [5].

C-S-H gel type	Morphology	Description of composition
Inner product	Compact, fine-scale and homogeneous; Fan-like texture.	Consists of aggregates of small (3 ~ 8 nm) globular particle; The particle formed under higher temperature is smaller; Pores are less than ≈10 nm.
Outer product	Fibrillar, directional morphology; A function of space strain.	Consists of a large number of long thin particles aligned along its length; The particles have a variable length from a few nanometres to many tens of nanometres; Pore scale depends on the space strain: lager when coarse fibrillar forms whilst smaller when fine fibrillar forms.

Table 2-2 Summary of TEM morphology of Inner and outer C-S-H gel in GGBS blended cement [4, 5, 131].

C-S-H gel type	Morphology	Description of composition
Inner product	Compact, fine-scale and homogeneous;	Intermixes with Mg-bearing phase; Consists of 4 ~ 8 nm globules.
Outer product	Depends on the slag content (chemical composition); 50% slag-blend: fine fibrillar; 75% slag-blend: a very linear, directional (fanned-out crepe paper); 90% slag-blend: crumpled sheet-like foils.	The mean Ca/Si ratio decrease whilst the mean Al/Ca increase; Si/Ca = 0.4277 + 4.732(Al/Si) r^2=0.98 50%-slag blend: Consists of agglomerations of 3-6 nm (thicker) long thin particles; Ca/Si ≈ 1.5 and Al/Ca ≈ 0.07 to 0.10; 75%-slag blend: Ca/Si ≈ 1.34 and Al/Ca ≈ 0.13; 90%-slag blend: Ca/Si ≈ 1.18 and Al/Ca ≈ 0.19; One- to two- dimensional growth; Long thin particles to thin foils.

Table 2-3 Summary of TEM morphology of Inner and outer C-S-H in PFA blended cement [8, 14, 35, 98].

C-S-H gel type	Morphology	Description of composition
Inner product	Fine scale, dense, and homogeneous;	At 30% replacement level, the IP C-S-H had a mean Ca/Si ratio of 1.34 and Al/Si ratio of 0.113.
Outer product	Changes from fibrillar morphology to foil-like morphology with ageing and chemical composition; Coarser at evaluated temperature.	The mean Ca/Si ratio decrease whilst the mean Al/Ca increase; Si/Ca = 0.451 + 2.220(Al/Si) r^2=0.90 The composition clanged from high Ca/(Si+Al) (1.7~1.8) to Ca/(Si+Al) ≈ 0.9 ~ 1.0. The foil-like morphology appears at Ca/(Si+Al) ≈ 1.2 ~ 1.3.

2.3 Models development of C-S-H

For a better understanding of C-S-H gel, several models at different dimensions are built in order to link to the structure or performance of the hardened cementitious materials. The C-S-H models at atom level provide a strong basis for the further stoichiometry model [132, 133], thermodynamic calculation [57], and other hydration prediction models [134], whilst the models at particle level are normally accepted for the explanation of extremely complex engineering properties of concrete [107]. It is no doubt that the changes at atom level will affect the performance of C-S-H at the particle level, however, the links between these models at two levels are still not clear. Recently, Chen [63] linked the relationship between Ca/Si ratio of C-S-H to its morphologies (high density (HD) or low density (LD)) by using SANS techniques. The surface area tested by SANS during the decalcification of C-S-H provides the evidence for the explanation for the transformation between HD and LD morphologies [63].

2.3.1 C-S-H models at atom level

At atom scale, the C-S-H varies in Ca/Si ratio, mean chain length, Si-OH, and Ca-OH contents and models at this level should explain these related variations. At the early-age, the tobermorite-like structure is used as the basis for the models, which can explain the structure of C-S-H with lower Ca/Si ratio by creating defects [135]. However, some experimental findings suggest that the C-S-H gel in Portland cement varies from 1.3 to 2.1 with a mean value of approximately 1.75 [14]. The latter researches try to explain this phenomenon by introducing jennite structure as a more appropriate model. It is also argued that the results from spectroscopic studies supported the 1.4-

nm tobermorite more than jennite, however, these studies are analysed by synthetic C-S-H (I) instead of using C-S-H gel formed in cement [63].

Taylor's model

This model in 1986 [2] is an extension of his earlier model for C-S-H (I) published in 1956 [135], in which the C-S-H model is developed based on structurally imperfect jennite ($Ca_9Si_6O_{32}H_{22}$) and 1.4-nm tobermorite ($Ca_5Si_6O_{26}H_{18}$) modified by omission of silicate tetrahedra. By this way, the maximum and minimum values of Ca/Si in this model are 2.25 and 0.83. Finite silicate chain with a chain length of 3n-1 (where n is an integer) is used in this model, which is consistent with the observation from the chemical method (Section 2.2.1). Meanwhile, Taylor assumed that each bridging tetrahedra carry only one H atom and that when one of these tetrahedra is missing only one of the broken ends of the chain is terminated by an H atom. Therefore, no charge balance required from the interlayer Ca atoms [2]. Based on these assumptions, Taylor linked the Ca/Si ratio to reciprocal MCL of jennite or 1.4-nm tobermorite and found a linear relationship between the aforesaid parameters as shown in Figure 2-10. At a young age, the Ca/Si ratio is achieved by J2 or T2 and J5 or T5 may be the main composites of more mature pastes [2]. This model can be considered as a special case of Richardson and Groves' model [5].

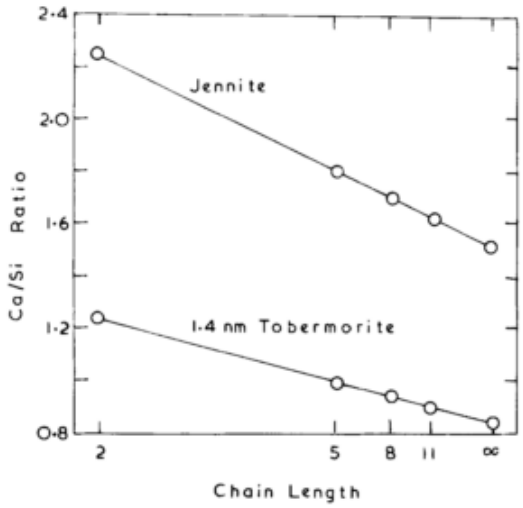

Figure 2-10 Calculated Ca/Si ratio against the reciprocal MCL of jennite or 1.4-nm tobermorite, proposed by Taylor [2].

Richardson and Groves' model

Richardson and Groves' model was initially proposed in 1992 based on the observation of C-S-H gel in C_3S paste [53] and further widely applied and accepted in different cement system [5, 14, 88], thermodynamic modelling [57] and stoichiometry modelling [132, 133]. They describe the C-S-H from both tobermorite-jennite (T/J) and tobermorite-'solid solution' calcium hydroxide (T/CH) point of views and this model provides a more flexible Ca/Si ratio (0.67 and 2.5 for minimum and maximum respectively) than Taylor's model (0.83 and 2.25) [5, 13]. The biggest difference between T/J and T/CH point of views is the position of Ca^{2+} ions, which is in the CH layer of tobermorite-like structure for T/CH point of view or linked to jennite dreierketten as the formation of Si-O-Ca-OH [5]. That is also the reason that why Ca-OH is the key parameter for the resolve of the C-S-H structure as discussed by Chen [63]. The structural chemical formula of T/J viewpoint can be expressed as Equation 21.

$$[Ca_{2n}H_wSi_{(3n-1)}O_{(9n-2)}] \cdot (OH)_{w+n(y-2)} \cdot Ca_{\frac{n\cdot y}{2}} \cdot mH_2O \qquad \textit{Equation 21}$$

Where w is the number of silanol groups (Si-OH), w/n is the degree of the protonation of the silicate chain and n is an integer (1, 2, 3…). Since then, the silicate tetrahedra are arranged in dimers (n=1), pentamers (n=2), octamers (n=3), and so on.

The solid solution T/CH viewpoint can be expressed as Equation 22 by adding additional $Ca(OH)_2$ to the tobermorite-based C-S-H.

$$[Ca_XH_{(6n-2X)}Si_{(3n-1)}O_{(9n-2)}] \cdot zCa(OH)_2 \cdot mH_2O \qquad \textit{Equation 22}$$

Where $X = (6n - w)/2$, $z = (w + n(y - 2))/2$ and n, w, y refers to the same physical significance as Equation 21.

The parameters in the T/J and T/CH models can be determined by experimental results. The silicate mean chain length (expressed as 3n-1) can be detected by NMR, from which the n is calculated. The y is a parameter related to Ca/Si ratio, which can be obtained through the TEM-EDX results by a combination with n. For the protonation ratio w, which is limited by restrictions to maintain the layer structure and neutrality, as defined by Equations. 23-25.

$$0 \le y \le 2 \ \rightarrow n(2 - y) \le w \le 2n \qquad \textit{Equation 23}$$

$$2 \le y \le 4 \ \rightarrow 0 \le w \le 2n \qquad \textit{Equation 24}$$

$$4 \le y \le 6 \ \rightarrow 0 \le w \le n(6-y) \qquad \textit{Equation 25}$$

When some substitution ions take the position of Si ions in C-S-H gel, the T/J and T/CH viewpoints can be modified to incorporate the other elements, as expressed in Equations. 26 and 27, respectively [89].

$$[Ca_{2n}H_w(Si_{1-a}R_a^{[4]})_{(3n-1)}O_{(9n-2)}]I_{\frac{a}{c}(3n-1)}^{c+} \cdot (OH)_{w+n(y-2)} \cdot Ca_{\frac{n\cdot y}{2}} \cdot mH_2O \qquad \textit{Equation 26}$$

$$[Ca_XH_{(6n-2X)}(Si_{1-a}R_a^{[4]})_{(3n-1)}O_{(9n-2)}]I_{\frac{a}{c}(3n-1)}^{c+} \cdot zCa(OH)_2 \cdot mH_2O \qquad \textit{Equation 27}$$

Where, $R_a^{[4]}$ is the trivalent cation (Al^{3+} or Fe^{3+}) substituted the Si in silicate chains and I^{c+} is the monovalent alkali cation (K^+ or Na^+) or bivalent (Ca^{2+} or Mg^{2+} [115]) needed for charge-balance. The replacement ratio R/Si is expressed as $\frac{a}{1-a}$, which can be determined by TEM-EDX. The other parameters remain same as Equations 21-22. This phenomenon is very common in SCMs-containing cement samples, in which the Al ions provided by SCMs can replace the Si in the silicate chain of C-S-H to form C-A-S-H.

Richardson's C-(A)-S-H(I) model

A new model structure for C-(A)-S-H based on clinotobermorite was recently (2014) proposed by Richardson [7]. Normally, the model structure of C-S-H starts from orthotobermorite which has an orthorhombic sub-cell [5, 53, 89, 111], however, Richardson found that it is not possible to generate a structural model for a dimer which is crystal-chemically consistent with known C-S-H if the starting structure is an orthotobermorite [7]. Therefore, a more plausible model based on clinotobermorite instead of orthotobermorite was developed. In this model, the C-S-H structure is derived from single-chain clinotobermorite as shown by a general expression in Equation 28.

$$Ca_4[Si_{1-f-v}Al_f\blacksquare_vO_{3-2v}]_6H_{2i}Ca_{2-i}(Ca, Na_2, K_2)_{3f} \cdot mH_2O \qquad \textit{Equation 28}$$

Where f is the fraction of tetrahedral sites substituted by Al, v is the fraction of vacant tetrahedral sites (represented by "■"), and i (in the range of 0 to 2) is the negatively charge that can balance this formula. When i=0, it means that the charge is balanced by entirely Ca. In the same way, for i=1, by Ca and protons equally; for i=2, by entire protons.

Pellenq's molecular model

In 2009, Pellenq and co-workers [136] proposed a realistic molecular model for C-S-H based on bottom-up atomistic simulation approach with the considerations on the chemical specificity of the systems. This model gives a chemical composition of $(CaO)_{1.65}(SiO_2)(H_2O)_{1.75}$ for C-S-H gel and predicts the essential structural features, fundamental physical properties, and some mechanical properties of C-S-H. The results of this model suggest that C-S-H gel is consist of both glass-like short-range order and crystalline features of mineral tobermorite. This model was then widely used in the explanation of C-S-H morphology [129, 137] and interactions between nanocomposites and C-S-H gel [138, 139].

Despite this molecular model can well fit the experimental results of C-S-H gel, some unrealistic structures in this model were also pointed out from crystal-chemical and geometrical reasoning [7, 37]. The first mistake (or unrealistic result) is that some of Ca-O distance in their model are shorter or longer than the minimum or maximum distances that are known for crystalline C-S-H [7, 37]. The second one is that more than half of the Ca atoms in this model are coordinated to fewer than six O atoms. Their model has Ca in five-, four- or even threefold coordination Ca as calculated by Richardson [7, 37].

2.3.2 C-S-H models at particle level

At particle level, the C-S-H gel contains pores with diameters from several to tens of nanometres, which further forms interfacial surface area and also becomes more disordered in vision. Thus, the models for C-S-H gel at this level are always built concerning with its surface area, pore structure, density and morphology observation [107]. These models are important for the interrelated properties, such as deformation and mechanical properties, of C-S-H gel at macro level [140]. Unfortunately, the links between atomic and particle models are not well explored.

Powers model [141] (Colloidal model)

In this model, the particulate colloid is assumed to be the basic unit of C-S-H gel, which has an average diameter of 10 nm based on the calculation results from water vapour adsorption isotherms. The porosity of C-S-H gel is estimated as 28% and the mean diameter of the pores is

about 1.8 nm or approximately 5 times of the diameter of an unbounded oxygen atom. This value (1.8/5) is about 0.36 nm, which is also the same as that of an N_2 molecule. The original Ref. [141] uses 0.36 nm as the diameter of a water molecule, which is not right and the diameter of a water molecule should be 0.275 nm. It is to say the mean diameter of pore size should be approximately 6.5 times of a water molecule. It is also pointed out that only water molecule can complete access these pores and nitrogen can only access a fraction of gel pores due to the "ink-bottle" effect. The 'ink-bottle' geometry pores will keep part of adsorbent in the main body of pores after desorption, which is due to the 'neck' of the 'ink-bottle'-like pores.

Further, Powers connected this model to the freezing of evaporable water and attributed the destructive effect of frost is not due to the lack of space in concrete for expansion of water. Powers also implemented this concept model for the explanation of deformation (such as drying shrinkage), mechanical properties, and permeability of saturated pastes to water. In this model, Powers speculated that the main strength in C-S-H gels arose from physical bonds between particles. Meanwhile, the chemical bonds were also important due to the limited swell performance in water.

Feldman-Sereda model (Layered structure model)

It was pointed out by Feldman and Sereda [142] that Powers model is very similar to the model for wood or other cellulosic materials. In which, a linear decrease in strength with the increasing amount of water adsorbed should exist due to the attenuated number of hydrogen bonds. However, in Powers model, the decreasing in strength is not due to a change in state of the solid or to modification of bonding between units when the concentration of water molecules is enough to maintain the rate of diffusion in the cracks. Thus, Feldman-Sereda model is modified based on the foundation of Powers' model. A layered structure of C-S-H gel was proposed and the surface area, density and porosity of C-S-H gel were accurately measured at 11% RH. This experiment was based on the assumption that the water in the interlayer spaces was considered as an integral part of the solid. The authors also linked the specific surface area to Ca/Si ratio of C-S-H gel by assuming that the water did not penetrate the interlayer space, which was later questioned [63].

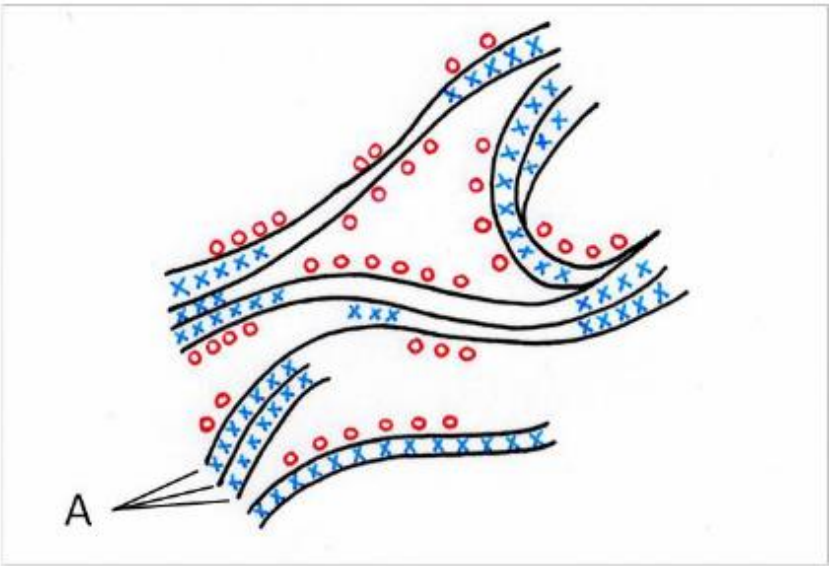

Figure 2-11. Feldman-Sereda model for C-S-H gel. A stands for the tobermorite sheets, (×) is the interlayer water molecules, and (o) is the physically adsorbed water molecules. Figure was originally proposed in [142], but taken from [143].

Jennings model (CM-II) [107]

This model was modified from model CM-I, in which, the low density (LD) and high density (HD) C-S-H with different morphologies were proposed and supported by statistical analysis, SANS data and nitrogen sorption results [144]. The CM-II model assumes that the C-S-H gel is comprised of globules that are not spherical and have a cross-section of 5 nm. The water-filled spaces in C-S-H gel are well interpreted by a combination of physical properties. These spaces are divided into interlayer spaces, the intralobular spaces (IGP), the small gel pores (SGP), and the large gel pores (LGP) as shown in Figure 2-12. It is also proposed that the globules can deform slowly and the deformation is recoverably reversible. These globules are particles that can rearrange under stress, which can be used for the interpretation of viscous flow and irreversible deformation of concrete. This model was used for the explanation of some shrinkage properties, for example, the shrinkage in alkali-activated slag mortars [145].

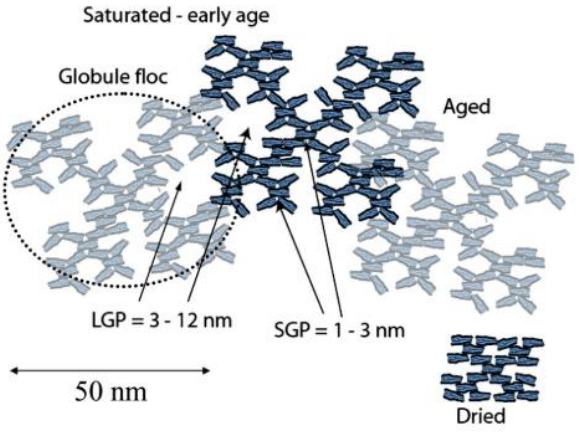

Figure 2-12. The schematic drawing of the water spaces in the C-S-H gel in CM-II model. From the left to right, the ageing and drying process was also presented.

2.4 Pore solution composition of hardened cement pastes

The hardened paste contains solid, liquid, and gas phases, which make it ultra-heterogeneous. By using a pressure device, pore solution can be expressed from hardened cement pastes and mortars [146]. An extensive study was carried out on the analysis of pore solution since the application of such a device [147]. This section briefly reviewes the terminologies used in pore solution study and the pore solution composition.

2.4.1 Nomenclature in pore solution study

For a reaction shown in Equation 15, the equilibrium constant can be expressed as Equation 16. Similarly, for a dissolution process of a solid product, the equilibrium constant is called the solubility product (*Ks* or *Ksp*). For example, the solubility product of gypsum (the activity of pure solid phase and water are all defined as one) can be written as Equation 29. Meanwhile, the ion activity products (IAP) can also be calculated using Equation 29 at non-equilibrium.

$$K_s = \{SO_4^{2-}\}\{Ca^{2+}\} = IAP \qquad \textit{Equation 29}$$

In Equation 29, the brace stands for the activity for specific ions, which is different from ion concentration (in mol/kg H_2O). The activity for an ion is corrected by the activity coefficient, γ, as expressed in Equation 30.

$$\{Ca^{2+}\} = \gamma \frac{[Ca^{2+}]}{[Ca^{2+0}]} \qquad \textit{Equation 30}$$

Where the $[Ca^{2+0}]$ stands for the molar concentration in standard state and equals to 1 mol/kg H_2O. Further for the γ, which stands for the deviations of an ion in solution from the ideal

condition, as defined by several models satisfied with different ionic strengths. The most common models used in cement pore solution calculations are Davies (Equation 31) and Extended Deby-Hückel (Equation 32) equations [15, 48, 148].

$$log\,\gamma_i = -A_\gamma z_i^2 (\frac{\sqrt{I_m}}{1+\sqrt{I_m}} - 0.3I_m) \quad \textit{Equation 31}$$

$$log\,\gamma_i = \frac{-A_\gamma z_i^2 \sqrt{I_m}}{1+ \dot{a}B_\gamma \sqrt{I_m}} + b_\gamma I_m \quad \textit{Equation 32}$$

$$I_m = \frac{1}{2}\sum m_i z_i^2 \quad \textit{Equation 33}$$

Where, I_m is the effective molal ionic strength (mol/kg), which is defined in Equation 33. Z_i is the charge of the ion i, Aγ and Bγ are two constants related to the temperature and pressure, which have values of 0.51 and 0.33 at 25 °C and standard atmospheric pressure (1 atm). ȧ and bγ are two parameters individually for different ions by measuring and fitting with the activity of pure salt solutions. For some ions that the fitting parameters are not known, Davies equation is normally implemented. Both of equations are written in Phreeqc and GEMS, which can be used directly. It should be noticed that, these equations only suitable for the solutions with ionic strength in the range of 0.1 to 0.5 molal. When ionic strength is larger than 1.0, specific ion interaction term (SIT) or Pitzer model should be considered. The ionic strength of pore solution in cement samples normally within 0.5 according to the calculations from J. Thomas and co-workers [33, 148].

The Gibbs free energy of a solid phase can be calculated with Equation 34, which will be useful for further thermodynamic study [149].

$$\Delta G - \Delta G^0 = RTln\,K_s \quad \textit{Equation 34}$$

Where, ΔG is the Gibbs free energy at a specific condition, ΔG^0 is the standard Gibbs free energy.

By a combination of IAP and solubility product of solid, saturation indices (SI) can be calculated for a disequilibrium solution-solid system (Equation35) [150, 151].

$$SI = log\,\frac{IAP}{K_s} \quad \textit{Equation 35}$$

A positive SI indicates that the solution is oversaturation to the respective solid, while a negative SI means an undersaturation condition. The “effective” saturation index is defined by dividing the saturation indices by the number of ions participating in the reactions to form solids.

The number for gypsum, Portlandite, ettringite, and monosulphate are 2, 3, 15, and 11 respectively [15, 25, 48].

2.4.2 Dissolution of clinker phases of Portland cement

The dissolution kinetics of cement clinker can demonstrate its reaction and precipitation process. From the geochemical point of view, the dissolution dynamics in minerals are due to the presence of surface defects [152]. As reviewed by Gallucci et. al [152], the previous opinion insists that etch pits are formed as a result of the releasing of ions from these defects and are regarded as the obvious centres of all dissolution activity, while the other areas of the crystal surface are assumed to be passive and dormant. However, a step wave model [153] was proposed and verified to refute the previously mentioned opinion. This model emanates from etch pits and proposes a general dependence of crystal dissolution rate on free energy:

$$Rate = A\left(1 - e^{\Delta G/kT}\right) tanh\left[\frac{B}{f(\Delta G)}\right] f(\Delta G) \qquad \textit{Equation 36}$$

Where A and B are constants and where

$$f(\Delta G) \equiv \left(1 - \frac{1-e^{\frac{\Delta G_{crit}}{kT}}}{1-e^{\frac{\Delta G}{kT}}}\right) \qquad \textit{Equation 37}$$

$$\Delta G_{crit} = \frac{2\pi^2\gamma^2\kappa\bar{V}}{\mu b^2} \qquad \textit{Equation 38}$$

Where b is the numerical modulus of the Burgers vector b, γ is the surface energy, μ is the shear modulus, $\bar{V}$ is the molar volume of the crystal, κ is a parameter (function) describing the contribution of dislocation defects. The application of this model is shown in Figure 2-13.

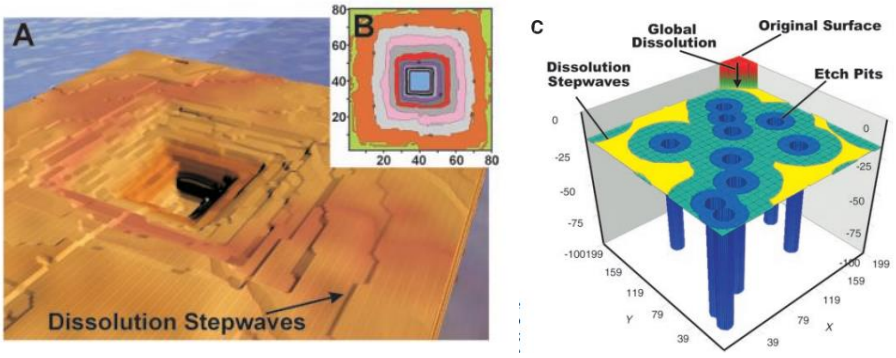

Figure 2-13 (A) Monte Carlo simulation for the formation of an etch pit at the site of dislocation defect and the generated dissolution step waves, (B) Plot of topography showing the steep waves, and (C) dissolution model shows the far-reaching dissolution steep waves. These graphs are taken from [153].

Dissolution of C_3S or C_2S

As stated above, C_3S and C_2S are the main components (70-90%) in cement clinker and their reactions with water through a dissolution-precipitation process [154]. It is found that the dissolution of C_3S seems to be similar to other natural silicates [154]. The aforementioned model was also applied in the explanation of the dissolution of C_3S (Figure 2-14) in cement clinker [152].

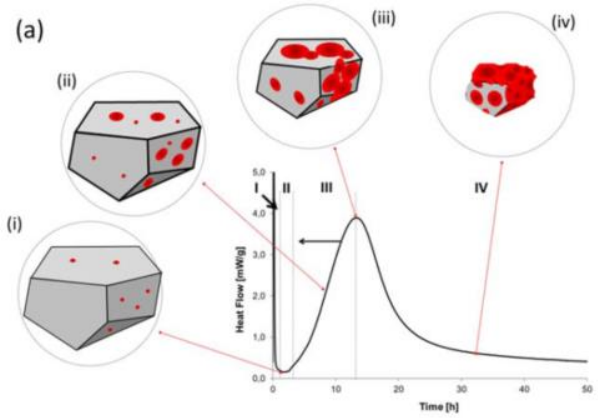

Figure 2-14 A typical dissolution process at different hydration stages: i pure dissolution; ii the low activity period; iii the accelerating steps; iv the decelerating period.

The dissolution process of C_3S can be expressed as Equation 39, which further associates with the Gibbs free energy (Equation 40) of C_3S dissolution.

$$Ca_3SiO_5 + 5H_2O \rightarrow 3Ca^{2+} + H_4SiO_4 + 6OH^- \quad \textit{Equation 39}$$

$$\Delta_{diss}G_{C_3S} = -RTln\,K_{c_3s} + RTln\,IAP_{C_3S} = RT\,ln\frac{IAP_{C_3S}}{K_{c_3s}} = 10RTlnSI \quad \textit{Equation 40}$$

$$IAP_{C_3S} = (Ca^{2+})^3(H_4SiO_4)(OH^-)^6 \quad \textit{Equation 41}$$

The dissolution of C_3S in solution will result in calcium, hydroxide and silicate ions groups and the dissolution rate is controlled by the deviation from equilibrium condition. Nicoleau and other co-workers [154] designed a special ICP-equipment for monitoring the ions concentrations in a dilution environment (devoid of participation of C-S-H gel). Further, the effects of different ions on the dissolution of C_3S were also investigated [149, 155]. Specifically, caesium and sulphate ions are found to adsorb on silicates and further tend to reduce the dissolution of C_3S. Contrary to the monovalent anions or ions, aluminate ions (sourced from $AlCl_3$) undergo covalent bonding (Si-O-Al) especially at moderate alkaline conditions, which further inhibit the dissolution of C_3S. This conclusion is also supported by Bellmann [156], both the C_3A and ettringite were used as the source of aluminate ions and it was also found a reduction in the dissolution of C_3S, however, the

reduction in reactivity is not due to elevated aluminium concentrations in the pore solution. The calcium ions seem to delay the dissolution of C_3S as evidenced both from Bellmann [157, 158] and Nicoleau.[155] The micro-reactor was also introduced in a study of C_3S dissolution by Suraneni [159]. It is found that the defects caused by polishing do not affect the dissolution extent in this study, which is not consistent with the theory mentioned above. This study also pointed out that the effect of aluminium on the dissolution of C_3S depended on the pH of solution environment. A strong reduction was found between pH of 8 and 12, however, there is the very little effect of aluminium when pH was above 13, regardless of Al concentration. In addition, the dissolution of C_3S is not limited by the introduction of alditols whereas the inhabited precipitation of C-S-H is the reason for the retardation as shown by a study carried out by Nalet [160, 161].

Dissolution of C_3A

The setting behaviour of Portland cement is controlled by the kinetics of C_3A hydration. so it is important to understand its dissolution. The effects of some chemical additives, for example, superplasticisers and retarders, on the dissolution behaviour of C_3A were widely studied. It is [162] reported that the addition of polycarboxylate-based superplasticiser can increase the aluminium, iron and magnesium ion concentrations during hydration, which is suspected that this polymer perturbs the initial dissolution of C_3A or nucleation of ettringite. The effects of different alditols on the hydration of aluminate-sulphate mixture were also investigated by Nalet [163]. The formation of ettringite is affected differently by the type of alditols, whereas the formation of AFm phase slowed down by adding either type of alditols. The explanation of this phenomenon is attributed to the stereochemistry of their hydroxyl groups. A study [17] on the dissolution of cubic (cub-) and orthorhombic (orth-) C_3A shows that the adsorption of chemical additives on the surface of C_3A can only be investigated through solution chemistry because no new solid hydration products can be identified through XRD analysis.

2.4.3 Pore solution changes due to the presence of SCMs

Pure cement system

The compositions of pore solution in Portland cement are widely investigated. It normally consists of alkali ions (K and Na), calcium, silicon, aluminium, sulphate and hydroxide ions, which is consistent with its bulk chemical composition. The dissolution of alite and belite will result in alkali, calcium, silicon, and hydroxide ions. The aluminium ions are mainly due to the dissolution of aluminate and ferrite, which may also result in some iron ions. The sulphate ions mainly come from the dissolution of gypsum, which is used to control the setting time of cement. In addition, the dissolution of clinker will also result in some Mg, sulphate, K and Na as summarised by Taylor (Ref. [1], Table 1.3). Due to the extremely low solubility products of related hydration products, the concentrations of aluminium, silicon, and calcium are really low and hard to detect [25]. In contrast, the concentrations of K, Na, and hydroxides takes the dominate positions in the composition of pore solution due to the high solubility product of the related phases and activity of ions. A statistical review of the composition of pore solution in Portland cement containing SCMs was done by Vollparacht [147].

Blended with GGBS or PFA [147, 151]

It is found that the replacement of GGBS shows the limited effect on the calcium ions in pore solution whereas the alkali ions concentrations drop significantly. The main reason should be the replacement of clinker by GGBS decreases the total alkali in the system. The calcium ions concentration in blended cement pore solution seems to be similar to that of Portland cement, which may be due to the slag also contains high calcium oxide content (even it is much lower than cement). The effect on aluminium and silicon ions seems to be small. It should be noticed that, due to the reduction reaction for the production of GGBS, the presence of sulphur always performs as sulphide instead of sulphate. The test of sulphide should be determined in joint with ion chromatography (IC)[1] while the test for total sulphur should be carried out by inductively coupled plasma (ICP) instruments.

[1] The amount of sulphate ions can be determined by IC and the total of sulphur element can be detected by ICP-OES/MS/AES, therefore, the difference can be roughly regarded as sulphide content.

For the PFA replacement, the K ions concentration in the pore solution of PFA blended cement is lower than that of Portland cement, as shown by the statistical results. However, the Na concentration seems to behave similarly. It is pointed out that the formation of C-A-S-H contributes to the binding of alkali ions. Meanwhile, the calcium and sulphate concentration remain in the same range of CEM I pore solution. The main reason may attribute the extremely lower solubility of related hydration products, which needs to be balanced in the pore solution environment. Meanwhile, due to the hydration of PFA, the concentration of aluminium increased while that of silicon remain quite similar range. However, some researches pointed out that the incorporation of PFA will increase the silicon concentration up to 0.35 mmol/L as summarised by Richardson [14].

Table 2-4 Possible changes in ions concentration in pore solutions of blended (GGBS/PFA) cement compared to that of CEM I.

Ions type	Blended with GGBS	Blended with PFA
Potassium	Lower	Lower
Sodium	Lower	Remains the same range
Calcium	Remains the same range	Remains the same range
pH value	Lower	Lower
Silicon	Remains the same range	Remains the same range (or increase)
Aluminium	Remains the same range	Higher
Sulphur	Higher sulphide	Remains the same range

2.5 Equilibrium of pore solution and C-S-H gel

A widely acceptable equilibrium curve of C-S-H gel was built by Jennings in 1986 and reproduced in Figure 2-15, which was based on the collection of the silicon and calcium ions concentrations at different equilibrium conditions [164]. It is explained that Curve A is the metastable solubility curve of C-S-H (I), or of the material of similar structure type (tobermorite) but with lower crystallinity. In contrast, Curve B is produced from the experiment results of C_3S hydration in a long range of reaction times and w/b ratios. Therefore, Curve B most probably the metastable solubility curve of a modification of C-S-H distinct from Curve A. It is also suspected that Curve B is a mixture of tobermorite-like and jennite-like for C-S-H (I)-C-S-H (II) forms of C-S-H. These curves (or theory) were further used in the explanation in alkali-activated slag system

[165], construction of C-S-H sub-particle model [107, 144], solubility behaviours of solid phases in cement paste [33, 105, 148].

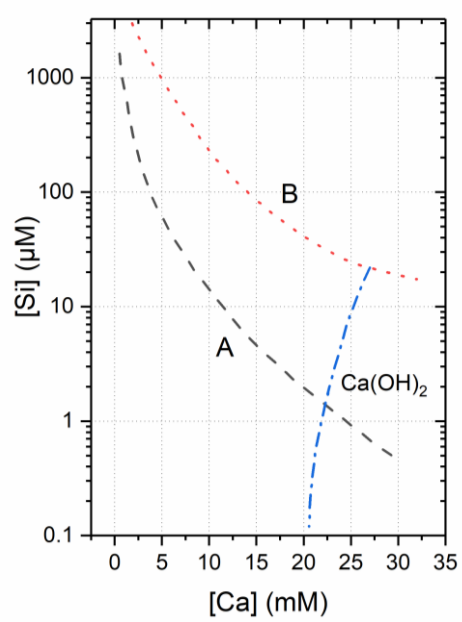

Figure 2-15 Two smooth equilibrium curves of C-S-H gel proposed by Jennings. This figure is reproduced from Ref. [164].

2.5.1 Decalcification and re-calcification procedure of C-S-H

The calcium position and content in C-S-H gel is really important for the understanding of its structure due to the unique Ca-OH bond in pure jennite sub-layer (sometimes in tobermorite and surface site of C-S-H gel, see discussion in Ref. [105]). Therefore, the decalcification and re-calcification procedure enable a clear observation of how Ca content affect the solubility and structure of C-S-H gel [63, 105, 106, 166].

A decalcification experiment of synthetic C-S-H was carried out by Chen [63] in 6 M ammonium nitrate solution. It is found that a two-step linear relationship between Ca/Si ratios to weight loss leaching existing in such a system, further the Ca/Si was controlled by monitoring the weight loss of samples. After removing the calcium, the re-calcification experiment was done in a CH solution. A possible change of Ca/Si ratio due the increase of [Ca] concentration was plotted by using the results from de-/re-calcification experiments as shown in Figure 2-16. This experiment directly correlated the changes in Ca/Si ratio in CH saturation with the Ca-OH content in C-S-H. In solids lacking Ca-OH, the structure is purely tobermorite-like, whilst more resemblance to jennite with increasing Ca-OH in C-S-H gel [105].

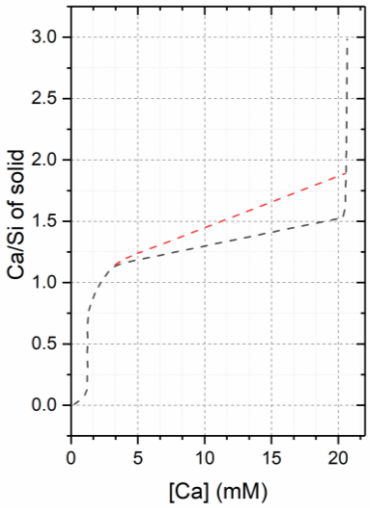

Figure 2-16 Plot of [Ca] concentration to Ca/Si of C-S-H gel. (Reproduced from [105]).

2.5.2 Equilibrium in the presence of aluminates

The aluminium is present in C-S-H gels by substituting the central silicon ions, which was evident from the ^{27}Al NMR analysis of synthetic slag [78] and further verified in different SCMs-containing systems [5, 8]. Thus, the presence of aluminium shows vital influence on the formation and structure of C-S-H. As reviewed in Section 2.4.2, the presence of any kind of aluminium shows a slower dissolution rate compared to the pure CaO-SiO_2 system. A recent study taken by Frank [156] pointed out that the detection of aluminium is really difficult in the samples independent of the presence of aluminium in tricalcium silicate or the addition of extra Al-phases. The only elevated concentrations occur in the presence of C_3A. The delay role of aluminium was also confirmed in Begarin's study [167], in which the results also indicate that alumiocalcium silicate hydrates precipitate instead of C-S-H in the pore solution environment. However, most of these research focus on the hydration behaviour of clinker phase in the presence of aluminium without deep concerning on the effect of aluminium on the structure of C-S-H.

2.5.3 Possible morphological changes due to the changes in pore solution

It was pointed out that the morphology of OP C-A-S-H gel in blended (GGBS or PFA) cements changes from fibrillar at higher Ca/Si and Ca/Al ratios to foil-like at lower values [9, 10, 14]. Although the morphology of C-S-H gel is also influenced by the space constraints and other factors (as reviewed in 2.2.4), the changes of fibrillar to foil-like C-A-S-H in water activated

cement system appears at a Ca/(Si+Al) ratio at around 1.2-1.3 [14]. However, the morphology of C-A-S-H remains foil-like regardless of its chemical composition in alkali (KOH) activated wPC pastes. Since Rodriguez et al. [13] studied the relationship between the chemical composition, silica anion structure and morphology of C-S-H using either synthetic method or hydration-controlled C_3S, it was found that the samples under a Ca/Si of 1.5 was totally foil-like morphology; a sample with a Ca/Si ratio of 1.58 was a mixture morphology of foil and fibrillar; a sample with a Ca/Si ratio of 1.61 to 1.63 had entirely fibrillar-like morphology. It is interesting that these Ca/Si ratios were achieved under different [CaO] concentrations from 22 to 27 mmol/L. Further, an extend relationship was applied to the cement system. It was pointed out that the morphology changes of C-A-S-H in blended cement system is related to a pore solution: i) reducing in pH; ii) undersaturated with respect to CH; and iii) has a concentration of Si that is $>\approx$ 0.35 mmol/L. In addition, the results from chemical composition analysis of C-A-S-H prove that the foil-like morphology cannot be directly linked to tobermorite-based structures [14].

2.6 Summary and outlook

The hydration process, morphology/chemical composition of C-S-H gel, and the composition of pore solution in blended cement systems or synthetic C-S-H systems are reviewed. The results from the literature indicate that a possible relationship between solution environment and C-S-H may exist. The understanding of this relationship can partially explain whether the formation of C-S-H is chemically defined or kinetically driven. With these considerations, the following questions will be answered in this thesis.

1. Will the pore solution affect the morphology and the chemical composition of C-S-H gel in cement pastes? And hence, will this relationship be a universal law? (Chapters 5 and 6)
2. If there exists such a relationship, will the morphology change due to the changes happened in an aqueous environment? (Chapter 7)
3. Will some specific ions (for example, Na and Al ions) affect the morphology and chemical composition of C-S-H gel? (Chapter 7)

Chapter 3

Characterisation techniques and modelling methodologies

3.1 The principles of characterisation techniques and experimental setup

3.1.1 Isothermal conduction calorimetry (ICC)

Principle of ICC

As reviewed in Section 2.1.3, the hydration kinetics of cement exhibit an exothermic nature, which can be recorded by a heat flow sensor configured in an ICC equipment (Figure 3-1). Both reference and sample were put into a thermostatic environment and the difference between the thermal signal from the sample and the reference was recorded as the exothermic behaviour of cement. The purpose of using a reference was to remove the potential effect brought by external factors, hence, a reference with similar properties (especially the same heat capacity) but without any thermal production was required. For cement experiments, quartz is a good reference because it has a similar specific heat capacity as cement (0.75 J/g/k for cement and 0.8 J/g/k for quartz).

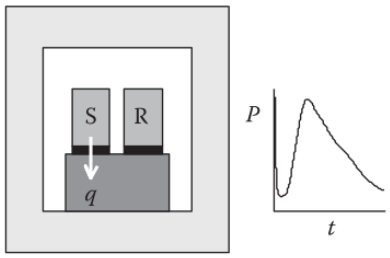

Figure 3-1 Schematic illustration of an ICC equipment (taken from [168]). S: Sample; R: Reference; P: Thermal power; t: time.

ICC experimental setup

The equipment used in this investigation was a TAM-Air (TA Instruments, U.S.) with 8 twin-channels equipped with quartz as the reference. The heat production rate of both sample and reference was parallelly recorded by the computer and 20 ºC was used throughout this experiment. Before ICC experiments, all the raw materials including DI water were placed in a room with constant temperature of 20 ºC for around 3 hours. 9 g of paste (6 g of binder and 3 g of DI water) was placed

into a 20 ml ampoule. External mixing method [14] (2 min shaken on an orbital shaker) was used and the ampoules were immediately moved to the equipment. Around 20 min was used for the equilibrium of the background, needed due to opening the sample chamber. The measurements were carried out for 3 days. The paste weight (including water) was used to calculate the normalised heat release. Table 4-2 shows the slurry arrangement for ICC experiments. Two replacement levels for slag, PFA and anatase were selected for comparison.

Table 3-1 Paste arrangement for ICC tests.

No.	Description	wPC	TiO_2	GGBS	PFA	water	w/binder	w/cement
1	Neat 0.50 wPC	6g				3g	0.50	0.50
2	30PFA-70wPC	4.2g			1.8g	3g	0.50	0.71
3	30GGBS-70wPC	4.2g		1.8g		3g	0.50	0.71
4	30Ti-70wPC	4.2g	1.8g			3g	0.50	0.71
5	60PFA-40wPC	2.4g			3.6g	3g	0.50	1.25
6	60GGBS-40wPC	2.4g		3.6g		3g	0.50	1.25
7	60Ti-40wPC	2.4g	3.6g			3g	0.50	1.25

Note: wPC stands for white Portland cement; PFA is pulverized fly ash; Ti stands for TiO_2 (anatase); Reference: 6g Quartz and 3g water; temperature: 20 °C.

3.1.2 Simultaneous thermal analysis (STA)

Principle of STA

STA is combined techniques of thermogravimetric analysis (TGA) and differential thermal analysis (DTA) or differential scanning calorimetry (DSC). Both DTA and DSC record the temperature difference between a sample and the reference in thermal voltage (μV). However, DSC can convert the temperature difference into a heat-flux difference (mW) by using proper sensitivity calibration method, which does not happen in DTA equipment.

As shown in the left of Figure 3-2, a STA measuring set consists of a furnace and the integrated sensors for both sample and reference crucibles, which allows for recording both temperature changes. The reference is normally an empty pan of the same material. Due to the heat capacity of the sample, the reference crucible will heat faster than the sample side as described in the right of Figure 3-2 (i.e. the linear line stands for the reference and the line with a step stands for sample signal). The two lines exhibit parallel behaviour in the furnace until a reaction happens (i.e. the Point t_1 shown in Figure 3-2), which will be further recorded as the DSC signal. This signal indicates melting, decomposition or re-

crystallisation is happening in this system. The temperature difference (ΔT) is recorded and then the integration (Area A in blue) is calculated as the transition enthalpy (J/g).

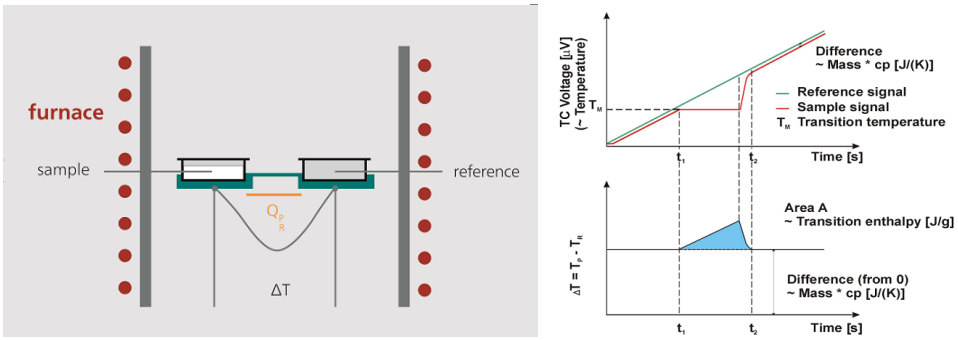

Figure 3-2 Schematic illustration of an STA equipment (Left) and the principle for DSC calculation (https://www.netzsch-thermal-analysis.com).

For cement paste samples, the mass loss occurs when the temperature increases in the furnace. Water firstly decomposes from hydrated phases such like C-S-H, gypsum, AFt and AFm as shown in Figure 3-3. The temperature range for water loss in above phases is always up to 350 ºC [169]. However, it is also argued that a larger temperature range of 50-600 ºC is attributed to the dehydration of C-S-H gel, which is used as the theoretical basis for applying the tangential method in calculation of CH and carbonates content in cement pastes [168]. The tangential method assumes that the weight loss of C-S-H and other hydrates will be linearly before and after the Portlandite decomposition peak. The carbonates are a series of compounds that are present in hydrated cement due to either carbonation or from raw materials. Normally, three decomposition regions range from 550-680 ºC, 680-780 ºC, and 780-990 ºC represent different kinds of calcium carbonates. Crystalline polymorphs $CaCO_3$ (CC) (calcite, vaterite and aragonite) decomposes at higher temperature (680-780 ºC) and amorphous $CaCO_3$ decomposes at lower temperature (550-680 ºC). In addition, the crystalline size also affects the decomposition temperature.

STA measurement is a precise process. The influencing factors include heating rete, open and closed vessels, gas flow (type), samples weight, organic solvents, drying procedures and carbonation during storage and testing, which are summarised in Ref [168].

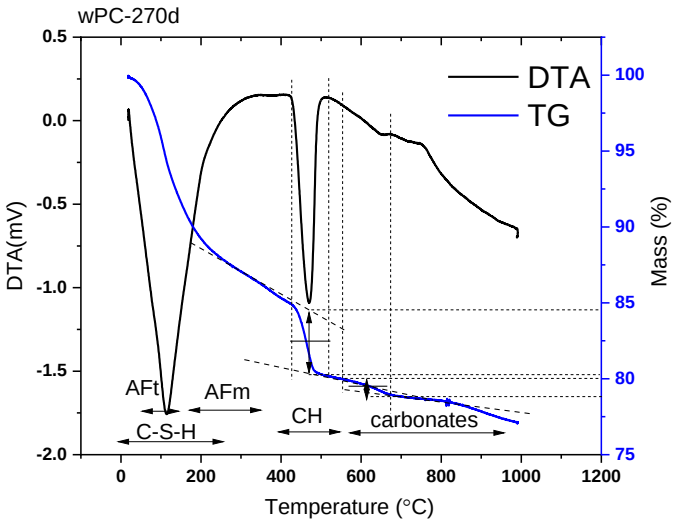

Figure 3-3 An example showing the TG and DTA plots for 270d hydrated wPC. The dash lines indicted the tangential method used for confirming CH contents.

STA experimental setup and data processing

The hydrated wPC and alite samples (15-18 mg each) in this investigation were analysed by the Stanton Redcroft Simultaneous Thermal Analyser STA 780 (UK) under N_2 atmosphere with a heating rate of 20 ºC/min. An empty platinum crucible was used as the reference and the testing temperature ranges from room temperature (20 ºC) to 1000 ºC. The raw materials and synthetic C-S-H samples (20-40 mg) were analysed by the Netzsch Simultaneous Thermal Analyser 449 F5 Jupiter (Germany) under same conditions as wPC/Alite samples.

The CH content was calculated based on Equations 42-47 using the tangential method after calibration. The calculation included the subtraction of mass loss (in the same temperature range) of raw materials according to their proportions in the paste.

$$CH\% = \frac{CH_{cal}\% \times {}^{74}/_{18}}{M_{550}} \times 100 \qquad \textit{Equation 42}$$

$$CH_{cal}\% = CH_{TG}\% - \sum(CH_{RAW}\% \times wt._{RAW}\%) \qquad \textit{Equation 43}$$

$$CC\% = \frac{CC_{cal}\,(\%) \times {}^{100}/_{44}}{M_{550}} \times 100 \qquad \textit{Equation 44}$$

$$CC_{cal}\% = CC_{TG}\% - \sum(CC_{RAW}\% \times wt._{RAW}\%) \qquad \textit{Equation 45}$$

$$CH_{eq}\% = CC\% \times \frac{74}{44} \qquad \textit{Equation 46}$$

$$CH_{total} = CH\% + CH_{eq}\% \qquad \textit{Equation 47}$$

Where, CH% is the CH content calculated from the mass loss of calibrated CH peak; CH_{cal}% stands for the CH mass loss after the subtraction of the mass loss from raw materials (sum of wPC, PFA, and

GGBS) according to their weight percentage; CH_{TG}% and CH_{RAW}% are mass loss from TG experiments for samples and raw materials respectively; similarly, CC%, CC_{cal}%, CC_{TG}%, and CC_{RAW}% stand for the same physical significances but for CC. Finally, CH_{eq}% stands for the equivalent CH calibrated from carbonation and CH_{total}% is the original CH content formed in wPC systems.

In addition, the chemically bound water was also calculated from TG data according to Equation 48.

$$H_2O_{bound}\% = \frac{M_{50}-M_{550}}{M_{550}} \times 100 \qquad \textit{Equation 48}$$

Where, H_2O_{bound}% is the chemically bounded water in hydrated phase; M_{50} and M_{550} stand for the mass percentage at 50 and 550 ºC.

3.1.3 Attenuated total reflection – Fourier transform infrared spectroscopy (ATR-FTIR)

Principle of ATR-FTIR

ATR is a sampling technique used in combined with FTIR which enables the paste powder samples to be tested directly without further preparation. In this case, the ATR-FTIR technique can be also used for in-situ test of non-hydration stopping samples, which illustrates the hydration characterisations continuously. Figure 3-4 shows the principle of ATR, which uses the property of total reflection resulting in an evanescent wave. The IR beam passes through the ATR crystal with a relatively higher refractive index (mostly between 2.38 to 4.01 at 2000 cm^{-1}) and directly penetrates into the sample (~0.5-2 μm). Then the beam reflects from the internal surface of the sample and generates the evanescent wave which projects orthogonally in to the sample that contact with the ATR crystal. After several reflections (varies by the angle of incidence), the beam will be collected by the detector. The optical path difference signal will be recorded and then translated by Fourier Transform in conjunction with the subtraction of background. The final ATR-FTIR spectrum will show the peaks due to the adsorption of IR beam, which related to the characteristic vibrations (natural frequency of vibration) of different chemical bonds.

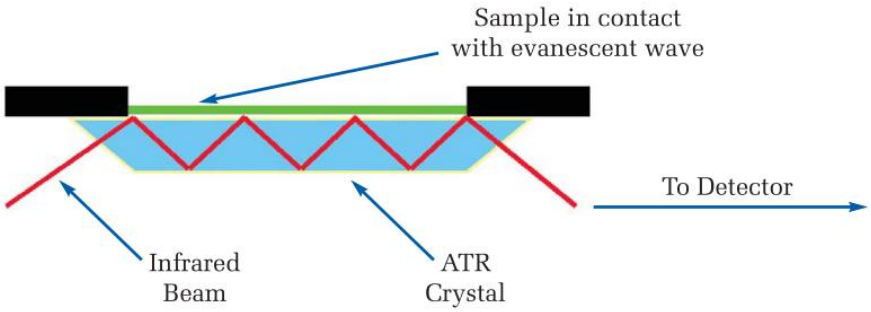

Figure 3-4 The multiple ATR system that shows the reflection principle and the position of samples. (Taken from https://www.perkinelmer.com/uk/).

ATR-FTIR experimental setup

All ATR-FTIR data were collected by the PerkinElmer PolymerID-Analyser with ATR (Diamond, refractive index=2.41) spectrometer over 400-4000 cm^{-1} wavenumber range. A pressure arm was used to help to generate close contact between the sample and ATR crystal. To achieve a comparable spectrum, the applied force was controlled the same. Before experiments, the background spectrum was collected by only use the ATR crystal without any sample on. The in-situ samples were externally mixed and filled into a small metal holder which was fitted with foot of force arm. The powder samples were hydration stopped and placed between the force arm and ATR crystal. 32 scans with a resolution of 4 cm^{-1} were used for all samples.

3.1.4 X-ray diffraction (XRD)

Principle of XRD

XRD is a powerful tool for the detection of identity parameters and atomic structures for crystalline phases. X-rays are high energy light with a repeating wavelength which is similar to the distance between atoms in a crystal. When X-ray absorbed by electrons surrounds atoms, elastic scattering allows the energy being readmitted in the form of new X-ray with the same energy. The constructive interference happened at when the waves are in alignment (i. e. diffraction) can be used to measure the well-defined distances between the atom planes in the crystal. Strong diffraction only happens at specific angles, which requires the second wave must travel a whole number of wavelengths (i. e. half on the incident side and half on the scattered side). Therefore, the following X-ray travels integral multiples in a defined crystal lattice. The diffraction phenomenon is perfectly described by Bragg's Law (by Lawrence Bragg & Henry Bragg in 11/11/1912) as expressed in Equation 49.

$$n\lambda = 2d\sin\theta \qquad \textit{Equation 49}$$

Where, n is a positive integer or named the order of reflection; λ is the X-ray wavelength; d is the distance between lattice planes; θ is the incidence angle.

The XRD is always used for the qualitative and quantitative analysis of clinker phases and hydration products in hydrated pastes. Four main components in clinker (impure C_3S, C_2S, C_3A, and C_4AF) are crystalline, which can be quantitative analysed by XRD. Some hydration products, such as CH, AFt, AFm phases, are also crystalline, however, the main hydration product (i. e. C-S-H gels) is amorphous. The application of XRD on C-S-H gel is summarised in Section 2.2.1.

XRD experimental setup

Quantitative XRD (QXRD), focusing on crystal phases, was used for the analysis of CH content evaluation in wPC and alite samples. External standard (corundum, α-Al_2O_3) method, namely G-factor method, was used to wPC, GGBS/wPC, PFA/wPC, and alite samples. Internal standard method was used for anatase (TiO_2) containing samples for all ages. Hydration stopped samples were ground into fine powder and back-loaded into the sample holder, which was further placed in the middle of XRD equipment. All data except those for 270 d blended wPC samples were collected by a Bruker D2 Phaser (CuKα radiation source) under the operation conditions at 30kV and 10mA. A step size of 0.01with a dwell time of 1.0 s and the rotation of 15º rot/min were applied in the range of 5-70º 2θ. The 270 d samples were operated with XRD Philips X'Pert equipped with the same radiation source. The same conditions were used except the scanning angles were between 5-80º 2θ. The corundum was running simultaneously during the tests of samples to acquire the radiation/equipment conditions (G-factor). The modelling methodology of Rietveld refinement QXRD is given in Section 3.2.1.

3.1.5 Magic angle spinning nuclear magnetic resonance (MAS NMR)

Principle of MAS NMR

The 'Spin' is an intrinsic property of an atomic nuclei due to the presence of angular momentum. All the nuclei (or other atoms) possess a spin quantum number (S) of 0, 1/2, 1, 3/2…. (increase by 1/2). If the nuclei with a spin number that not equal to 0, Zeeman splitting will happen when they are placed in a strong magnetic field. Zeeman splitting results in a splitting of energy states that corresponding to (2S+1) energy levels. If the sample is exposed to a radiofrequency pulse, resonance

(i.e. all nuclei have the same phase position in the precession movement) will happen when the energy of radiation frequency equals to the energy difference (refer to Larmor frequency), which allows the transitions (i.e. absorption of photons) occur between different energy levels (according to selection rule if more than 2 energy levels present, i.e. S > 1/2). If a 90-degree radiofrequency was applied, all precession movement happened at the x-y plane. Once the radiofrequency is turned off, all the nuclei relax back to their original positions [170]. The net magnetization vector along z direction will be recorded and forms a Free Induction Decay (FID) signal. The FID signal (time-domain signal) then will be transferred by Fourier Transform to give a frequency spectrum. The chemical shift is usually expressed in ppm, which is related to the local structural environment and can be calculated from frequency with the standard reference compound. The most important application of NMR in cement science area is ^{29}Si MAS NMR, which is a powerful tool for uncovering the nature of C-S-H gel. The details of application of this technique are given in Section 2.2.1 in Literature review.

MAS NMR experimental setup

^{29}Si, ^{23}Na and ^{27}Al MAS NMR data were collected by a Bruker Avance III HD with a 9.4 T WB magnetic field. The operating Larmor frequencies of ^{29}Si, ^{23}Na and ^{27}Al were 74.48, 105.84 and 104.26 MHz respectively. The samples that used for MAS NMR experiments were hydration stopped and ground into fine powder. 7 mm zirconia rotors with KEL-F caps were used for ^{29}Si MAS NMR and 2.5 mm zirconia rotors with Vespel caps were used for ^{23}Na and ^{27}Al MAS NMR. All the experiments run at the magic angle of 57.4º. The magic angle was set by observation of ^{79}Br resonance in KBr standard.

Since the nature abundance of ^{29}Si is only 4.67%, longer scans are normally required to achieve a quantitative spectrum. All ^{29}Si MAS NMR for blended wPC or alite samples were acquired for 2048 scans and those contains PFA were acquired for 4096 scans, at a spin rate of 6 kHz used an excitation with a pulse duration (width) of 5.5 μs. An acquisition time of 40 ms and the 40 s recycle time were used for all samples. The ^{29}Si CP MAS NMR were acquired for 2048 scans with the decoupling of the effect of ^{1}H, which was operated at a frequency of 400.13 MHz. An acquisition time of 40 ms, a contact time of 2 ms and a recycle time of 10 s were used for the CP NMR experiments. TMS (Tetramethylsilane) was used as the reference for all ^{29}Si NMR samples. Deconvolutions of blended

wPC pastes ^{29}Si MAS NMR spectra were performed using a user made procedure for Igor Pro (WaveMetrics, USA) initially developed by Brough [87]. The Voigt line shape (mixture of Cacuchy-Lorentz and Gaussian line shapes) was used for all peaks fitting. Deconvolutions of hydrated alite samples were performed by a commercial software Peakfit V4.0. The Voigt line shape was also used during deconvolution. The peak positions and peak fitting profiles were acquired from the spectra of raw material and long-term (around 3 months) hydrated alite.

^{27}Al MAS NMR of synthetic samples were acquired for between 12500 and 65500 scans at a spin rate of 12 kHz used an excitation with a pulse duration of 0.23-0.33 μs. The acquisition time and recycle time were 10 ms and 0.5 s respectively. 1 *M* $Al(NO_3)_3 \cdot 6H_2O$ solution was used as the reference.

^{23}Na MAS NMR of synthetic samples were acquired for between 1214 and 4096 scans at a spin rate of 12.5 kHz used an excitation with a pulse duration of 0.33 μs. The acquisition time and recycle time were 17 ms and 1.0 s respectively. 1 *M* NaCl solution was used as the reference.

3.1.6 Analytical transmission electron microscopy-Energy dispersive X-ray (TEM-EDX)

Principle of TEM-EDX

Figure 3-6 shows the electron microscopy family and illustrates the essential parts for different EMs. Analytical TEM normally contains: an electron gun to generate medium (300-400 kV) or high (600-3000 kV) voltage to accelerate the electron; the condenser system to control the convergence angle; the scan coils allow the electron beam to across the sample; detectors (for example, X-ray detector or Electron detector) to analysis the chemical composition of area of interest; the objective and intermediate lenses to form and enlarge the image to be shown on the screen or obtained by a CCD camera [94, 95]. The TEM-EDX allows the morphology and chemical composition of C-S-H gel to be detected. More importantly, the high resolution and smaller interaction volume (between electron beams and samples) in TEM-EDX result a more accurate analysis than SEM-EDX. Some highlights and history of using TEM in cement science are reviewed in Section 2.2.1.

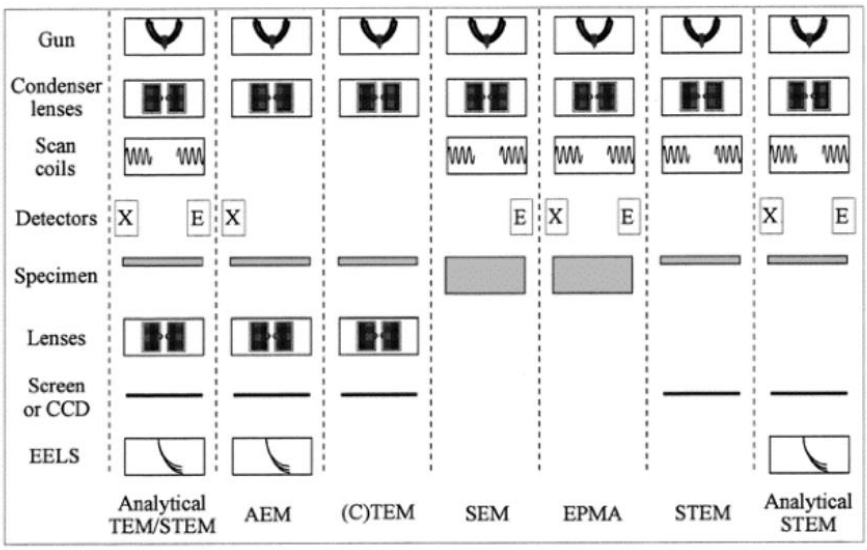

Figure 3-5 Electron microscopy family illustrates the essential components in different equipment. (Taken from [95], some unmentioned acronyms here: AEM: Analytical electron microscopy; EPMA: Electron probe microanalysis; EELS: Electron energy loss spectrometry.)

TEM-EDX experimental setup

Samples used for TEM-EDX analysis require to be thin enough to let the electron beam transmit through the sample. Slices (around 1-2 mm thick) were cut from blended cement paste cylinders using a Bucheler Isomet low-speed saw with a diamond blade. The slices were hydration stopped using isopropanol and dried in the desiccator. The dried slice was then attached to a clean glass slide with cyanoacrylate glue and thinned by hand using progressively finer SiC papers (#500, #800, #1200, and #2000, corresponding to the grain size of 30, 22, 15, and 10 µm) until a thickness of approximately 30 µm. The thinned slice was removed by immersion into acetone and glued between two 3 mm diameter copper TEM grids using epoxy. The grid had a hole with dimensions of 2 × 1 mm, which allowed the sample to be argon ion-beam milled in Gatan Precision Ion Polishing System (PIPS). The aim of doing PIPS is to form a hole in the centre of the sample, which allows the electron to transmit through the sample.

The Gatan PIPS was vacuum-worked at 3-4 keV with a milling angle in the range of 4-6º. The lower milling angle (glancing incidence) vastly reduced the input energy, preventing damage due to thermal affects. The whole PIPS process for each sample lasts for around 40 ~ 50 hours. Samples were then stored under vacuum condition and carbon-coated using Agar Turbo Carbon Coater to prevent charging affect before putting into TEM equipment.

The powder samples (including C_3S and synthetic C-S-H) were ground into fine powder and dispersed into ethanol. The obtained sample-containing solution was sonicated for around 15 min in an ultrasonic bath. Several drops of solution were deposited over a 200-mesh copper grid with carbon film.

The TEM experiments were carried out with a FEI Titan Themis 300 microscope operating at 300 kV with a windowless 4-detector. Images at a magnification with a range from 5k to 20k were taken. EDX analysis were performed at ≈ 20k with a spot size of 3 and live time of 10 s. The outer products in blended wPC or alite systems are the main areas of interest. In addition, thinner part was chosen when examining EDX analysis, which aimed to avoid the absorption of emitted X-rays from samples.

3.1.7 Inductively coupled plasma optical emission spectrometer (ICP-OES)

Principle of ICP-OES

Figure 3-7 gives the essential components of ICP-OES. Normally, before starting ICP tests, a stable plasma is required, which is generated by the inductively coupled effect. The ICP is formed by seeding ions in a stream of argon which is flowing through radio frequency (RF) and magnetic field in the induction coil (Figure 3-7 right). By subjecting argon gas to a high voltage spark, small amounts of argon will be ionized. These electrons and ions are then accelerated by the magnetic field and collide with other argon atoms, causing further ionization. The plasma is subsequently formed and the transfer of energy is named inductive coupling. After the stable ICP formed, the liquid sample will be finely divided into aerosols and transferred into the ICP torch (the area of plasma). The aerosols are then passed firstly through the most energetic and hottest area (10k ºC, induction zone in Figure 3-7), where the liquid evaporates and completely dissociates into atoms and ions within milliseconds. Further, a powerful RF generator will sustain the plasma, which will reduce all the oxide formation and other chemical interferences to a minimum. The ionized sample will transfer to analytical zone of plasma (60–70k ºC). The ions or atoms in the sample will be able to absorb the energy from the surrounding plasma and will emit light at the characteristic wavelengths. The wavelengths are then split by a polychromator system as shown in left in Figure 3-7, which are further recorded by the detector.

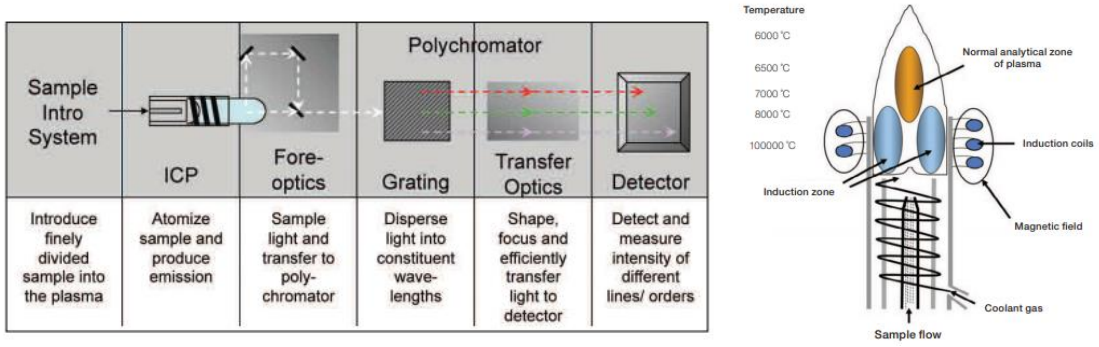

Figure 3-6 Schematic illustrates the main components of ICP-OES instrument (left) and a close look at the ICP torch (right), it should be stressed that the induction zone is about 10k ºC instead of 100k ºC. (https://www.thermofisher.com/uk).

The problems that related to the accuracy of elements concentration measurement in cement solution are summarized as follows [171, 172]: 1. High alkali concentrations vs. low Si/Al/Ca concentrations (salt effect). Three parts of ICP equipment will be affected by high concentration of alkali (salt) ions (mainly precipitated here): a. the rubber tubes for solution transport; b. the nebulizer; c. two cones (sampling cone and skimmer cone, connects between ICP part to Mass Spectroscopy or OES part); The Ion Chromatography (IC) was also tried to use for the characterisation of the Ca^{2+} concentration, however, similar problem also happens (all elements should be diluted under 20 ppm, higher concentration will result a contamination of column, further generate memory effect). Furthermore, the higher salt will affect the viscosity of solution, which will decrease the intensity of trace ions due to background problem. 2. The plasma torch is made of quartz; thus, the reactions will occur between some ions (typically Al) and SiO_2 under 10k ºC, (for Al ions, the product will be $3Al_2O_3 \cdot 2SiO_2$). 3. The interactions between different ions will also shift the signal of ions.

ICP-OES experimental setup

The element concentrations of cement pore solutions and filtrates of synthetic C-S-H were tested by an ICP-OES (Perkin Elmer optima 8000) using argon plasma. The equipment was pre-heated for around 30 min to achieve a stable plasma condition as stated above. The filtrated samples (0.45 µm PTFE Springe Filter) were acidified with proper levels of 5 mol/L HNO_3 and diluted with deionized water to end up with a pH value of around 1.0 (as shown in Figure 3-8). The ICP-OES equipment is really sensitive to total solids and the alkali ions in the solution. Some important issues were summarised by Vollpracht et al. [147] and Dean [172]. Other parameters that related to equipment set up were summarised in Table 3-2.

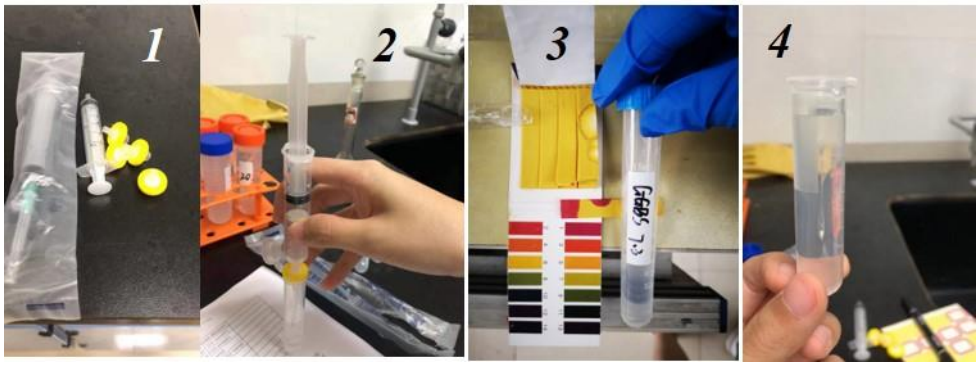

Figure 3-7. The preparation process of ICP-OES test: 1. the 0.45 μm PTFE Springe Filter and springe; 2. filtration of obtained solution samples; 3. dilution and acidified to suitable pH≈1.0; 4. samples in the tubes ready for test and will be further stored in the fridge at 5 ºC.

Table 3-2 Operating conditions for ICP-OES equipment.

Operating conditions	Value/type
Nebulizer	Concentric glass
Spray chamber	Glass cyclone
Number of replicates per sample	Three
Spectral range	163-900 nm
Plasma power	1300 W
Pump speed	30 rpm
Coolant flow	12 L/min
Auxiliary gas flow	0.65 L/min
Nebulizing gas flow	0.3 L/min

3.2 Modelling and methodologies

3.2.1 Rietveld Refinement XRD methodology

Rietveld Refined XRD provides a quantitatively analysis of XRD results, which is widely used in cement science [168, 173, 174]. Two methods, namely internal and external method, are always used for Rietveld QXRD analysis. Either method requires the use of standard materials. Since anatase (TiO_2) is one of these standard materials [174], the QXRD of wPC pastes with replacement of 30% and 60% anatase samples were performed with internal method. However, external method was applied for all other samples and the corundum (α-Al_2O_3) was used as the external standard. Since external method is more complex, the following QXRD method mainly focus on the methodology of external method QXRD [173].

General equation for determination of the phase fractions in hydrated cement samples is shown as follows (Equation 50):

$$C_j = \frac{S_j(ZMV)_j}{\sum_{i=1}^{n} S_i(ZMV)_i} \qquad \textit{Equation 50}$$

Where, C_j is the weight fraction of phase j; S_j is the scale factor of phase j; Z is the number of formula units per unit cell; M is the mass of the formula unit; V is the unit-cell volume..

We use corundum (Al_2O_3) as external standard, which generates a G factor as calculated below (Equation 51):

$$G = S_{cor} \frac{\rho_{cor} V_{cor}^2 \mu_{cor}}{w_{cor}} \qquad \textit{Equation 51}$$

Where, S_{cor} is the Rietveld scale factor of corundum; ρ_{cor} is the density of corundum; V_{cor} is the unit-cell volume of corundum; W_{cor} is weight fraction of corundum (which is 100% and equals to 1); μ_{cor} is the mass attenuation coefficient (MAC) of corundum. In addition, the product of density and unit-cell volume square should theoretically equal to ZMV (Equation 52) and the ZMV values used in this study are given in **Appendix A**.

$$ZMV = \rho V^2 \qquad \textit{Equation 52}$$

By using G factor, the phase fraction of cement can be expressed as (Equation 53):

$$C_j = s_j \frac{ZMV\mu_{sample}}{G} \qquad \textit{Equation 53}$$

The μ_{sample} was calculated based on Equation 54 in conjunction with chemically bound water from TG calculation using Equation 48. All the calculated MAC results can be found in **Appendix A**.

$$\mu_{sample} = \sum_i W_i \mu_i \qquad \textit{Equation 54}$$

Based on the theories above, the steps that using TOPAS V4.2 (https://www.bruker.com/products/x-ray-diffraction-and-elemental-analysis/x-ray-diffraction/xrd-software/topas.html) to quantitatively calculate the crystal phase are summarised below. It should be noticed that, the external method is coded in TOPAS V5.0 or higher version.

a. Calculate the scale factor of corundum from TOPAS;
b. Identify the MAC of corundum;
c. Calculate the G factor of corundum;
d. Calculate the scale factor of phase j;
e. Calculate the MAC (μ) of each sample (Equation 54);
f. Calculate the phase content (C_j or W_j) using Equation 53.
g. Rescale of phase fraction into paste or anhydrous using the following equations [168].

Fresh specimen:

Per 100g paste: $W_{j,rescaled} = W_{j,Rietveld}$

Per 100g anhydrous: $W_{j,rescaled} = W_{j,Rietveld}(1 + w/c)$

Dried specimen:

Per 100g paste: $W_{j,rescaled} = W_{j,Rietveld}/[(1 - H_2O_{bound})\left(1 + \frac{w}{c}\right)]$

Per 100g anhydrous: $W_{j,rescaled} = W_{j,Rietveld}/(1 - H_2O_{bound})$

3.2.2 Thermodynamic modelling

The basic theory and applications of thermodynamic modelling in cement science are reviewed in Section 2.1.3, here, the further introduction and implement of thermodynamic modelling using PHREEQC Interactive V3.4.0 are given. The thermodynamic modelling is useful for explaining the experimental data from solution chemistry point of view and provides insights of understanding the interactions between solid phases and its solution environments. The similar calculation process was also used by the author in Refs. [175-177].

Thermodynamic modelling of saturation levels in respect to solid phases through the pore solution composition requires the assumption of local equilibrium condition, which means the ionic transport is negligible when compares to the dissolution and precipitation process. The determination of the thermodynamic activity of each ion in the complex solution environment is the first step towards to the calculation of relevant equilibria. In classic analytical chemistry, the ion activity of individual species (a_i) is defined as its molality (m_i, mol/kg) multiply by the activity coefficient (γ_i), which can be expressed by Equation 55.

$$a_i = m_i\gamma_i \qquad \textit{Equation 55}$$

The activity of ion is affected by the formation of complexes in the system, which will reduce its value. Take the [Ca^{2+}] ions as an example, the formation of $CaOH^+$, $CaSO_4^0$ will reduce its activity. Therefore, it is important to have a complete testing of the ions presented in the pore solution in order to improve the accuracy in thermodynamic calculations.

The most common models used in cement pore solution for determination of activity coefficient are Davies (Equation 56) and Extended Deby-Hückel (Equation 57) equations.

$$log\,\gamma_i = -A_\gamma z_i^2 (\frac{\sqrt{I_m}}{1+\sqrt{I_m}} - 0.3I_m) \qquad \textit{Equation 56}$$

$$log\,\gamma_i = \frac{-A_\gamma z_i^2 \sqrt{I_m}}{1+ \dot{a}B_\gamma \sqrt{I_m}} + b_\gamma I_m \qquad \textit{Equation 57}$$

$$I_m = \frac{1}{2}\sum m_i z_i^2 \qquad \textit{Equation 58}$$

Where, I_m is the effective molal ionic strength, which is defined in Equation 58. Z_i is the charge of the ion i, $A\gamma$ and $B\gamma$ are two constants related to the temperature and pressure, which have values of 0.51 and 0.33 at 25 °C and standard atmospheric pressure. $\dot{a}$ and $b\gamma$ are two parameters (those used for this study are given in **Appendix C**) individually for different ions by measuring and fitting with pure salt solution activity. For some ions that the fitting parameters are not known, Davies equation is normally implemented. Both of equations are written in PHREEQC and GEMS, which can be used directly. It should be noticed that, these equations are only suitable for the solutions with ionic strength in range of 0.1 to 0.5 molal. When ionic strength is larger than 1.0, specific ion interaction term (SIT) or Pitzer model should be considered. The ionic strength of pore solution in cement samples normally within 0.5 according to the calculations from Thomas and co-workers [33, 148].

The ions activity products (IAP) equations and the solubility products (K_{sp}) values (25 °C) at equilibrium condition used in this study are given in **Appendix C**. These values are collected from the previous works [15, 33, 148, 178] and specifically coded into Phreeqc database. In addition, Lothenbach et al. [179] provide the state-of-art thermodynamic database named Cemdata18. The temperature dependence of the K_{sp} is defined by van Hoff equation (Equation 59), which extends the standard K_{sp} to be used at different temperature.

$$ln(K_{sp}) = ln(K_{sp25c}) + \frac{\Delta H_r}{R}(\frac{1}{298} - \frac{1}{T}) \qquad \textit{Equation 59}$$

Where ΔH_r stands for the enthalpy of reaction (kJ/mol, which is defined in Equation 60 and also provided in **Appendix C**), R is the gas constant (8.314 J·mol^{-1}·K^{-1}) and T is the temperature (K).

$$\Delta H_r = \sum \Delta H_{f,products} - \sum \Delta H_{f,reactants} \qquad \textit{Equation 60}$$

Where, ΔH_f is the standard formation enthalpy (kJ/mol).

With the definitions above, the saturation indices (SI) can be expressed as follows:

$$SI = log\,\frac{IAP}{K_{sp}} \qquad \textit{Equation 61}$$

The equilibrium condition is reached when IAP equals to K_{sp}, which means that the SI equals to 0. A SI > 0 indicates that the solution is supersaturated with the respective solid phase and the related solid phase is possibly precipitated. For a SI < 0, which means that the solution is undersaturated with the relevant solid phases. In order to compare the results with the existing literatures, the effective SI (ESI) was used. ESI is defined as dividing the SI by the number of ions participating in the reactions. For example, these numbers in gypsum, Portlandite, and ettringite are 2, 3, and 15, respectively [25, 47]. The verification of this model was given in **Appendix B** with original data and results taken from Rothstein et al. [148].

Chapter 4

Experimental scope and details

4.1 Identification of the replacement ratio of SCMs and related testing procedures

4.1.1 Pulverized fuel ash (PFA) replacement ratio

For PFA, the key factors that affect the "switch point" of morphology-change (i.e. transfer from fibrillar-like to foil-like) of C-S-H gel is fully discussed by Richardson [14] and summarised in Table 4-1. According to that study, the fuel ash content can be set as 30% with the expected changing point at 50-70 days.

Table 4-1 Expected ages for the "switch point" of PFA-PC paste.

Conditions	Ages expected
Starting age for CH decreasing	At 14 days (depends on PFA composition)
1. Age for $CH^{act}/CH^{exp} < 0.85$ (morphological change point); 2.Pore solution undersaturated (to CH) point; 3. [Si] > 0.35 mmol/L.	At 50-70 days (up to 1 year)
1.Ca/(Si+Al) = 1.2~1.3 (C-S-H); 2. Consumption of CH to 8%~13%.	At 50-70 days (up to 1 year)

4.1.2 GGBS replacement ratio

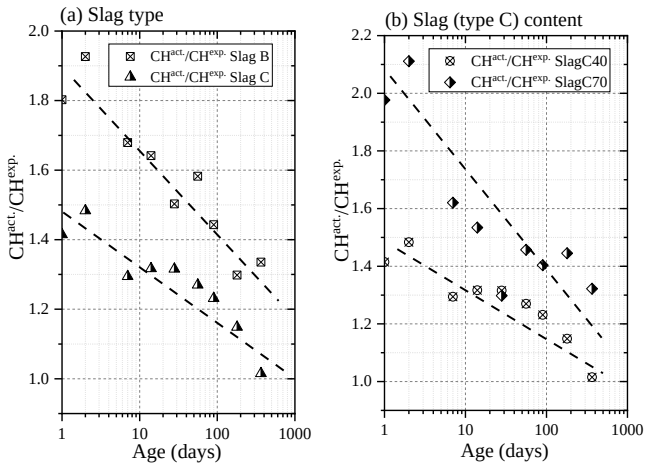

Figure 4-1 Effect of slag type (left) and slag content (right) on $CH^{act.}/CH^{exp.}$ of blended cement pastes, data were taken and recalculated from J. Whittaker [180].

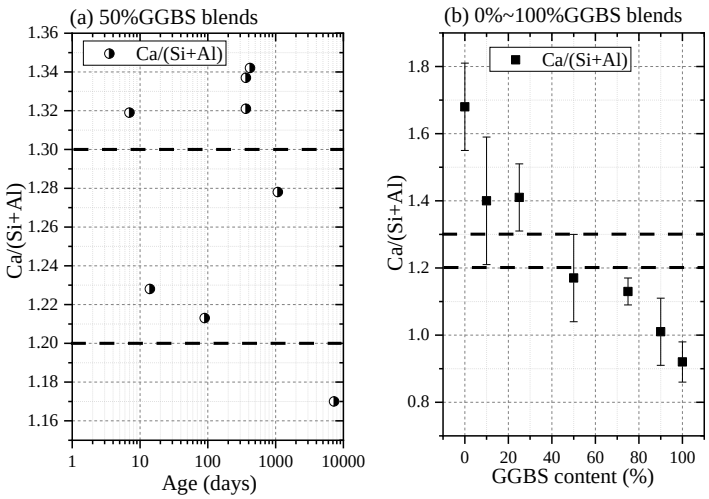

Figure 4-2 Ca/(Si+Al) ratios of outer C-S-H gel(left) in 50% slag:50% OPC sample, data are taken and recalculated from Ref. [43]; (Right) 0%-100% slag blended wPC hydrated for 20-years, data taken and reproduced from R. Taylor [10].

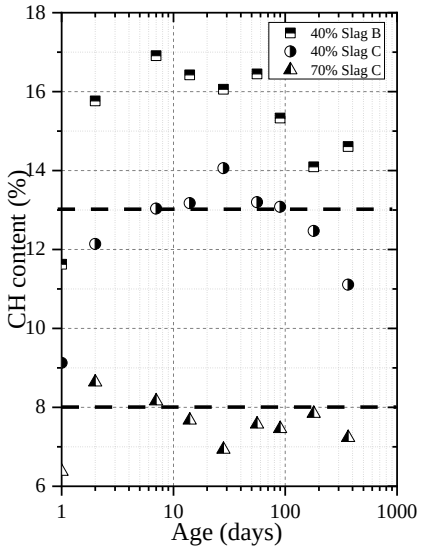

Figure 4-3 CH content development in 40%-70% blended cement, data taken from J. Whittaker [180].

The situation of slag (GGBS) is different from that of PFA mainly due to its hydraulic activity and the higher CaO content. Figure 4-1 shows a general decreasing trend of CH content against the hydration age of slag samples, which results from the secondary pozzolanic hydration. However, the value ($CH^{act.}/CH^{exp.}$) cannot reach 0.85 in GGBS blended samples. This may be attributed to the cement type used in the research (CEM I), which is finer and gives a higher hydration degree at the certain age. For the Ca/(Si+Al) ratio (Figure 4-2), this value will be lower than 1.2 when the slag replacement ratio is larger than 50%. Assuming the "switch point" of CH content is 8% to 13% [14], as shown in Figure 4-3, this threshold value is not easy to achieve in 40% slag blended sample but easy to reach in 70%-slag samples. Therefore, the GGBS

replacement ratio is selected as 60% in order to achieve the requirements of the "switch point". The critical conditions summarised from literature are given in Table 4-2.

Table 4-2 Expected ages for the "switch point" of GGBS-PC paste.

Conditions	Ages expected
Starting age for CH decreasing	At 7 days
1. Ages for CH^{act}/CH^{exp} < 0.85 (morphology change point); 2.Pore solution undersaturated to CH; 3. [Si] > 0.35 mmol/L.	1. CH^{act}/CH^{exp} < 0.85 is difficult to achieve (Figure 4-1); Hence the 'switch point' may not at 0.85, this parameter may be 1.2-1.4 according to the morphology in [43] at 14 months. 2. & 3. Remains to be confirmed.
1.Ca/(Si+Al) = 1.2~1.3; 2. Consumption of CH to 8%~13%.	1. Ca/(Si+Al) = 1.2~1.3: After 14 days at a replacement level of 50% (Figure 4-2); 2. CH to 8%~13%: If the replacement level at 40%, happened at 90 days; or the replacement level at 70%, happened at 14 days.

4.1.3 Raw materials characterisations and paste samples array

Raw materials characterisations

Table 4-3 Chemical composition of GGBS, PFA and wPC (% by mass).

Composition	SiO_2	Al_2O_3	Fe_2O_3	MgO	CaO	Na_2O	K_2O	SO_3	LOI
GGBS	35.07	12.43	0.41	8.41	40.67	0.38	0.58	0.78	-0.15
PFA	50.65	25.54	10.18	1.59	2.35	0.92	3.39	<0.10	--
Fe-Remove PFA	51.26	25.27	6.80	1.78	2.47	1.98	3.57	0.48	4.03
Residual PFA	49.02	24.38	10.92	1.59	2.43	1.42	3.46	0.47	4.07
wPC	24.49	2.09	0.30	0.59	68.08	0.25	0.09	1.95	0.95

As shown in Table 4-3, the bulk chemical composition of starting materials is characterised by XRF method. The mineralogy phase composition of wPC according to modified Bogue method (Taylor's re-interpretation of the Bogue equation) [181] (the MATLAB code is given in **Appendix B**) is 77.8% C_3S, 15.5% C_2S, 5.3% C_3A, 3.3% gypsum. Figure 4-4 shows the mineralogy characteristics of raw wPC by XRD, from which, Alite (M3), Belite (β and γ), cubic aluminate and gypsum are identified. The QXRD analysis indicates the phases present as: C_3S: 75.22%, C_2S: 17.30%, C_3A:2.43%, gypsum: 5.05%, which are close to those from Bogue method calculated with bulk chemical composition.

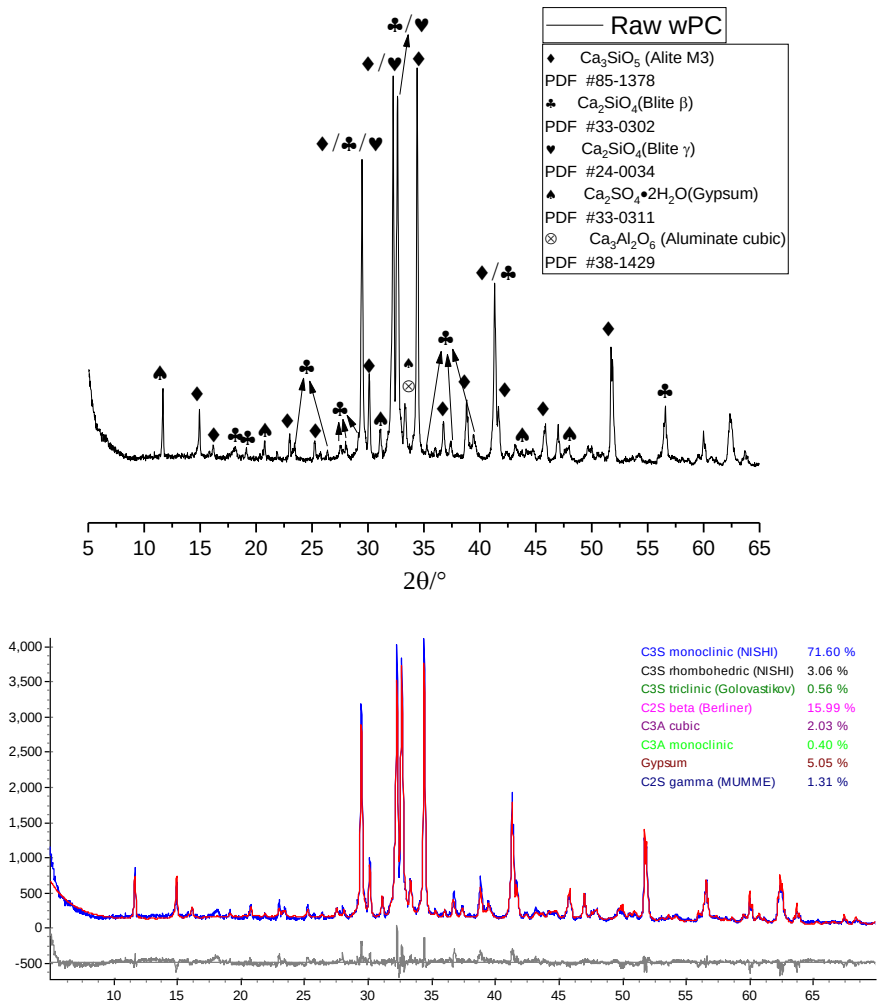

Figure 4-4 XRD patterns of raw wPC: phase identification (upper) and Quantitative XRD fitting (lower).

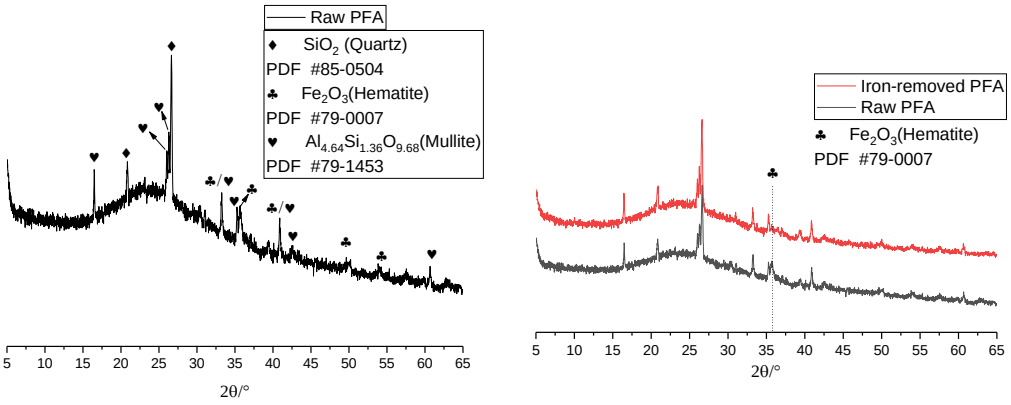

Figure 4-5 XRD patterns of raw PFA (left) and iron-removed PFA (right).

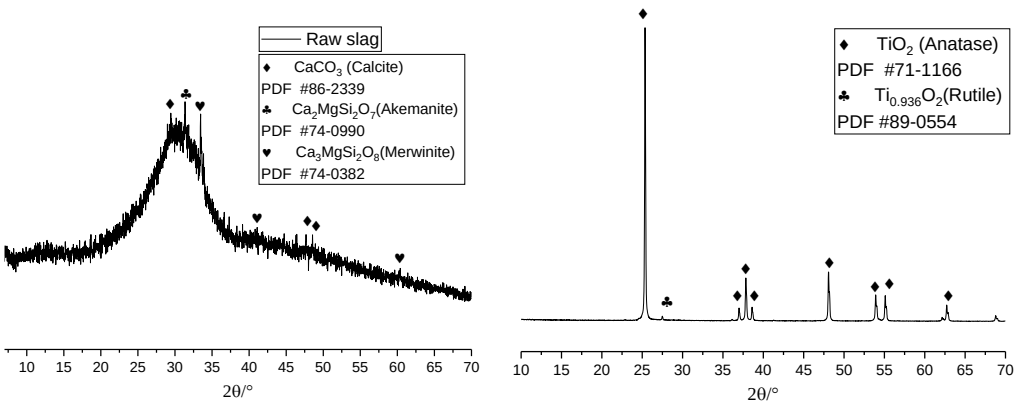

Figure 4-6 XRD patterns of raw slag (left) and raw anatase (right).

Figure 4-5 gives the XRD patterns of raw and iron-removed PFA. The PFA that used in this study is Fe-removed by magnet (metallic iron, instead of the iron in glassy phase) to reduce the paramagnetic effect in NMR experiments. The broad peak around 25 degrees indicates that the presence of glassy phase in PFA, while the sharp peaks are associated with quartz, hematite, and mullite. However, in the iron-removed sample, the hematite peak is significantly reduced, which is the main iron content removed by magnet (FTIR characterisations can be found in **Appendix E**). Figure 4-6 is corresponding to the XRD patterns of raw slag and anatase. It is found that some calcite, akermanite, and merwinite are present in the glassy slag phase. The XRD also confirms that the TiO_2 has the anatase crystal type with very little rutile intermixed.

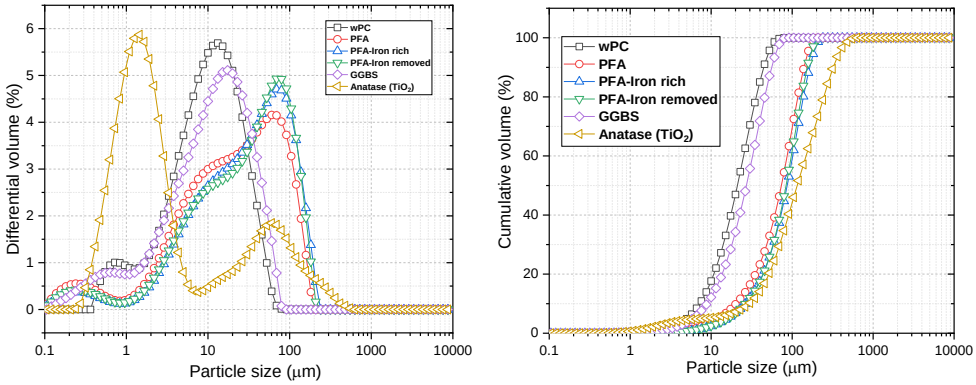

Figure 4-7 Particle size distribution of raw materials used in this study: differential (left) and cumulative (right) volume.

The particle size distribution of raw materials, determined by laser granulometry, is given in Figure 4-7. Compared to wPC, GGBS has a comparable size distribution, whilst PFA is coarser and TiO_2 is finer.

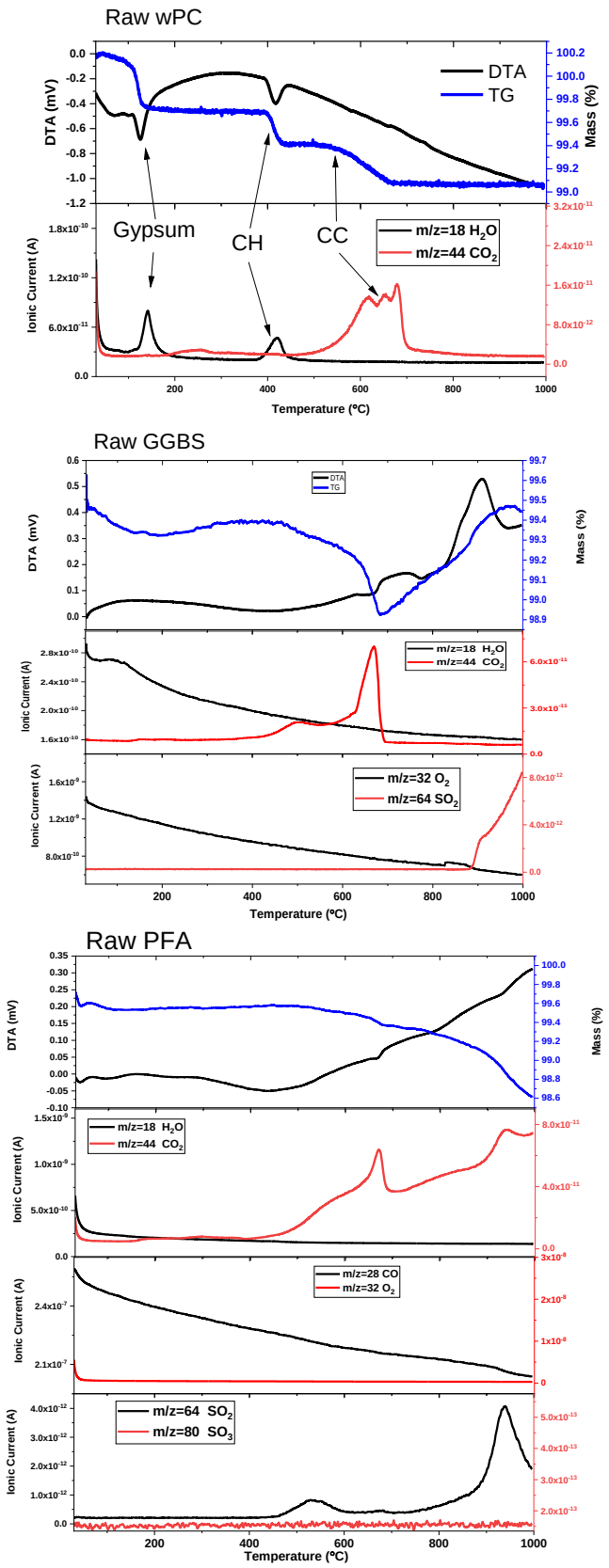

Figure 4-8 TG-DSC-MS characterisations of raw materials (wPC, GGBS, and PFA).

Figure 4-8 shows the TG-DSC-MS plots of starting materials, which can be used for the subtractions of corresponding peaks that may affect CH content evaluations (Section 3.1.2). The

MS spectra show the signals of matching gases that escaped from the sample during heating. For raw wPC, two peaks assigned to H_2O (m/z=18) and three peaks assigned to CO_2 (m/z=44) can be identified. The first H_2O mass loss at around 150 ºC illustrates the presence of gypsum and the shape of the peak is affected by the heating rate [182]. The second H_2O loss peak (0.28%) at around 400-450 ºC corresponds to the decomposition of CH, which indicates that the cement is slightly wetted during storage. Three peaks of CO_2 loss (0.32%) appear within 600-700 ºC corresponds to the decomposition of polymorphic calcium carbonate [183], which means that small amount calcium carbonate may originally be present in raw cement. For GGBS, peaks related to the release of CO_2 and SO_2 (m/z=64) are found in MS spectra. Small amount of calcite, as confirmed by XRD (Figure 4-6), decomposed during heating is responsible for CO_2 release. The recrystallization process of gehlenite ($Ca_2Al[AlSiO_7]$) and decomposition of sulphur-containing mineral phase at high temperature [31] may release some SO_2 gas. Evident mass loss peaks of CO (m/z=28), CO_2, and SO_2 are found in PFA sample. The unburned carbon is mainly responsible for carbon containing gases [184], which are not due to the reaction with the atmosphere gas (N_2). Furthermore, the decomposition of sulphur-containing phase also releases SO_2. All these decomposition peaks are subtracted according to their weight percentage in the matrixes during the calculation of CH using TG curves (**Appendix D**).

Paste sample arrangements

Table 4-4 Mix proportions of paste samples used in this investigation.

Groups	wPC content (wt.%)	SCMs content (wt.%)	w/b ratio	Remarks
wPC	100	0	0.50	Reference
wPC-30PFA	70	30	0.50	High alumina
wPC-30TiO_2	70	30	0.50	Dilution effect
wPC-60GGBS	30	60	0.50	Low alumina
wPC-60TiO_2	30	60	0.50	Dilution effect

PFA, GGBS and TiO_2 are selected to equally replace wPC by weight and the mix proportions of pastes containing different SCMs/filler are shown in Table 4-4. Three types of SCMs/filler are used mainly due to their different effects on the hydration of cement, which will further influence the phase assemblage of C-S-H gel. PFA usually has around 20.0% ~ 30.0% Al_2O_3 in bulk oxide compositions while GGBS has only around 7.0% ~ 14.0%, which will affect the formation of C-

S-H with higher Al [5, 14]. For TiO_2 powder, it is believed that it shows limited effect on the phase assemblage of C-S-H gel [185].

4.1.4 Testing procedures

Hydration stopping and drying method (Vacuum vs N_2 gas flowing)

Hydration arrest is vital for reservation of the microstructure features of cementitious materials as summarised by Zhang et al. [186]. Oven-, microwave-, perchlorate-, dry-ice-, vacuum-, freeze-, N_2-flowing-, and supercritical-drying are methods that can be applied in cementitious materials, of which, oven-, vacuum-, and N_2-flowing drying are most widely used [124]. Since oven-drying generates significant damage to microstructure of cementitious materials [186], vacuum- and N_2-flowing are selected for comparison. Before drying, isopropanol exchange is used to stop the hydration [186], which is proved to be one of the best methods that can reserve the microstructures. Figure 4-9 presents the TG-DSC results of two samples arrested by two drying methods. No obvious difference can be identified from mass loss curves; however, some differences are found in DTA curves. The positions (temperature) of phase-change remained exactly the same, which means the drying method will not affect the quantitative analysis of CH content under this situation.

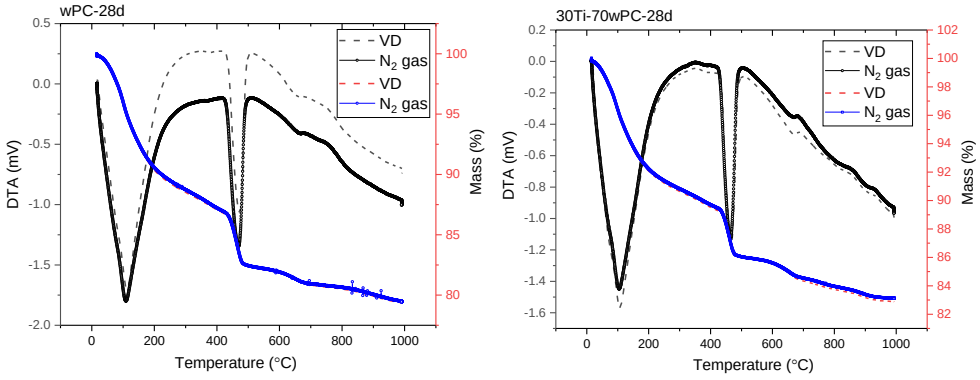

Figure 4-9 TG-DSC analysis of wPC samples arrested by VD (vacuum-drying) and N_2 gas flow drying.

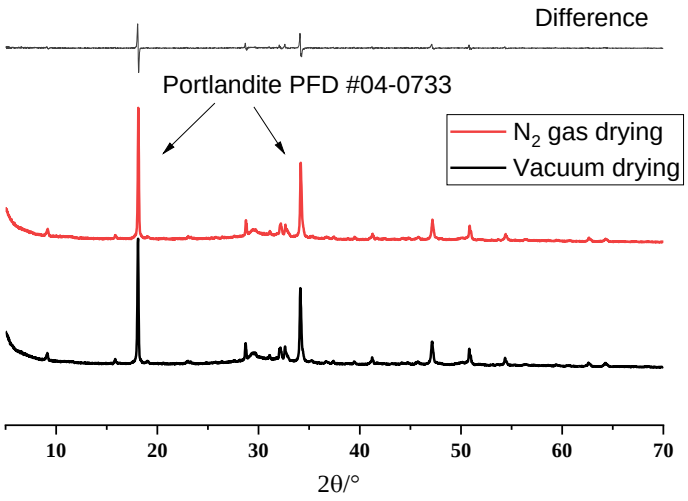

Figure 4-10 XRD analysis of wPC samples arrested by VD (vacuum-drying) and N_2 gas flow drying.

Figure 4-10 shows the XRD patterns of two wPC samples arrested by both VD and N_2 gas drying. From the differences shown above, only slight peak shifting can be confirmed. Therefore, vacuum drying is applied for all samples as the hydration-stopping methodology.

Acquisition of pore solutions from hardened cement pastes

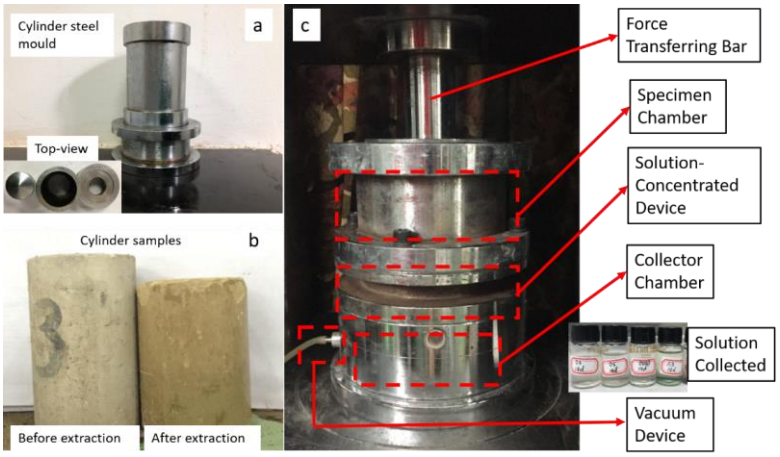

Figure 4-11 (a) Casting mould, (b) cylindrical samples and (c) pore solution extraction device (SBT, Co., Ltd)[175].

Figure 4-11 gives the pore solution extraction equipment (first used by Longuet et al. [187]), which was also used in previous studies [175, 188]. The pore solution of cylindrical paste samples is extracted under a constant pressure of 407.6 MPa (800 kN over 1962.5 mm^2) for 45 min. A vacuum pump is used to avoid the carbonation of collected solution. Since it is very difficult to extract the solution from mature paste samples, more than 2 cylindrical pastes should be used to acquire enough solution for analysis. The analysis of solution by ICP-OES is given in Section 3.1.8.

Samples used for XRD analysis (the choice of slice or powder sample)

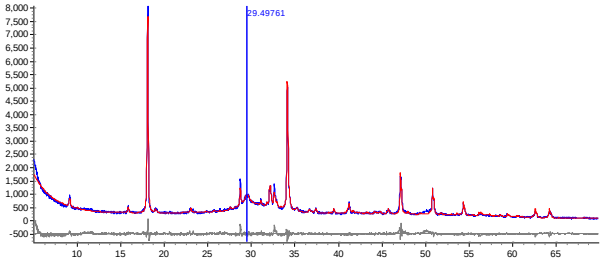

(a) Powder sample—vacuum drying (28d wPC, Rwp: 8.923).

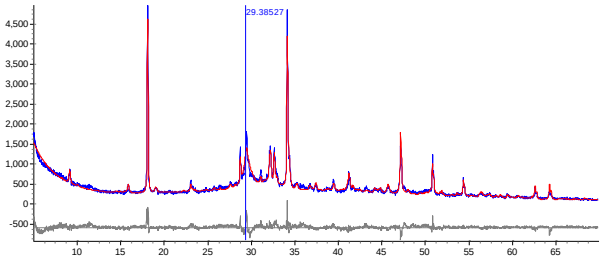

(b) Hydration-stopped slice wPC sample (7d, Rwp: 9.739) shows obvious carbonate peak.

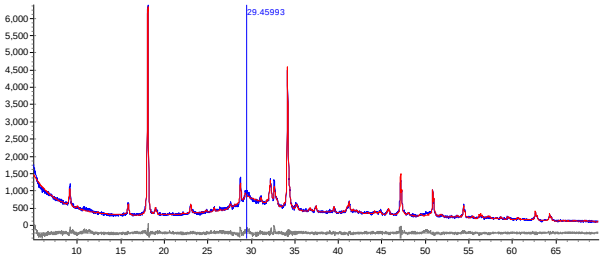

(c) Non-hydration stopped slice wPC sample (14d, Rwp=6.892).

Figure 4-12 The QXRD simulation of representative samples (a) powder sample (b) hydration-stopped slice wPC sample (c) non-hydration stopped slice sample.

Figure 4-12 shows QXRD results of 3 different wPC paste samples: one conventional powder sample and two slice samples. It is obvious that all peaks using SPVII function for fitting C-S-H gel appears at around 29.4° 2θ and other peaks associated to crystal peaks are quite close. In addition, the carbonation of surface for slice sample is also evident as shown in Figure 4-12(b), while the non-hydration stopped slice sample shows comparative less calcium carbonate peak. However, the non-hydration samples do not show obvious advantages on XRD spectrum when compared to that of powder sample. Since all samples for STA, NMR, and FTIR are powder samples, QXRD analysis is also done on the powder samples to make the characterization clear and even.

Overall experimental procedures

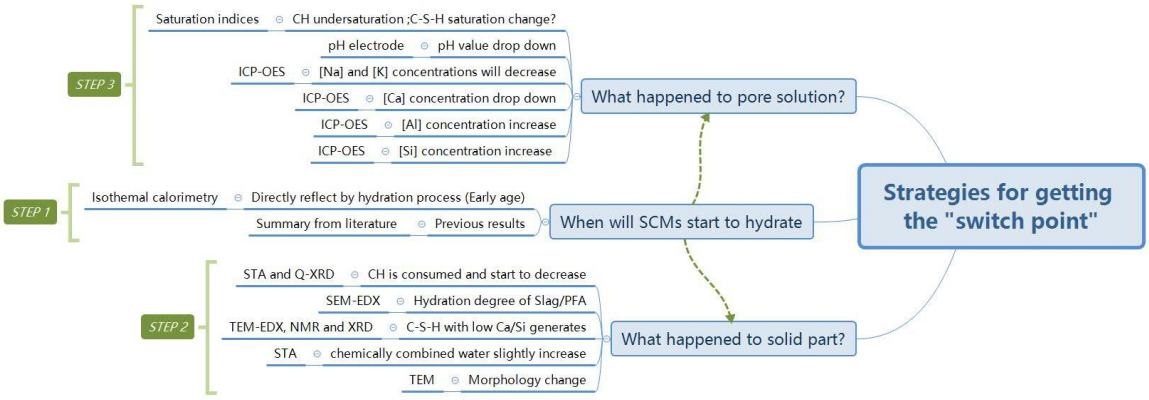

Figure 4-13 Strategies for getting the "Switch point" for blended cements.

Figure 4-13 gives the strategies for getting the "switch point" of C-S-H morphology-change in blended cements. In order to firstly analyse the composition of hardened wPC pates, QXRD and STA-MS (CH content) characterizations were performed. Moreover, the chemical compositions and nanostructure of C-S-H (mostly) were obtained from a combination of MAS NMR (nanostructure) and TEM-EDX (morphology and chemical composition) methods. Meanwhile, the C-S-H phase was analysed through Richardson and Groves' model [53].

For the composition of pore solution, ICP-OES was the main method in this project Si, Al, Ca, Na, and K elemental concentrations were tested and pH values of extracted pore solution were determined by electrode method. It should be noticed that the concentrations of aluminium and silicon are less than 1 mmol/L in OPC system [20, 156, 159].

4.2 Synthesis of alite and related testing procedures

4.2.1 Synthesis of alite and characterisation

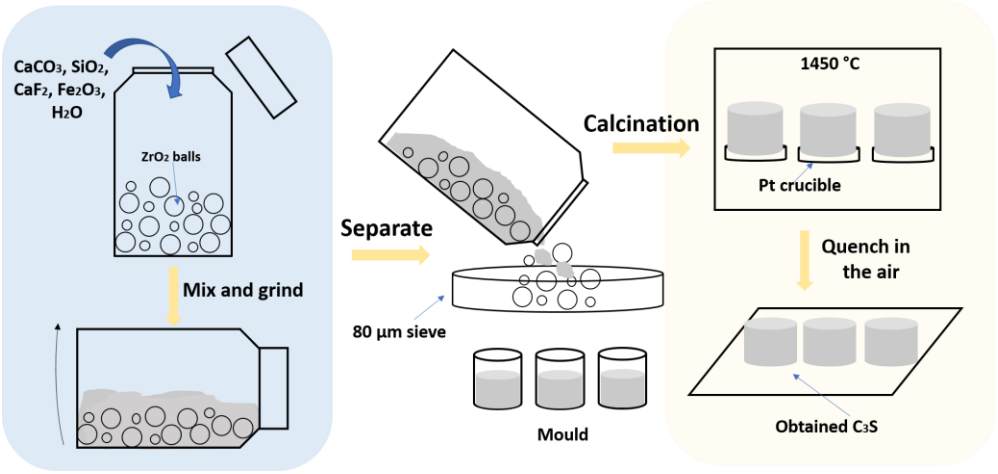

Figure 4-14 Synthetic process of alite.

Reagent-grade $CaCO_3$ and SiO_2 were used to synthesise alite together with CaF_2 (0.5 wt.%) and Fe_2O_3 (0.5 wt.%) as mineralizers (which were additives that aid the solubilization of the crystal). The entire procedure was carried out according to Figure 4-14 at the University of Jinan. All starting materials were mixed and ground in a milling machine to obtain uniform mixture. The as-prepared samples were put into a platinum mould for further calcination. The regime of calcination can be divided into following steps: a. initially up to 900 °C (5 °C/min) and kept for 30 min; b. then continuously rose up to 1550 °C (5 °C/min) and kept for 6 h; c. the samples were only removed from the furnace when the temperature cooled down to about 1000 °C and followed by quenching in the air. The calcination should ensure the free-CaO was lower than 0.8 wt. %. The final product (alite) was ground to pass a 32 μm sieve. The obtained samples were characterised by XRF, XRD, and nitrogen adsorption method (Figure 4-15). The chemical composition (XRF) of obtained alite is CaO 73.4%, SiO_2 25.7%, F 0.251 % Fe_2O_3 0.329%. XRD result confirmed the monoclinic C_3S (Fe-, F-doped) was synthesised with a specific surface area of 0.870 m^2/g as determined by Brunauer-Emmett-Teller (BET) method.

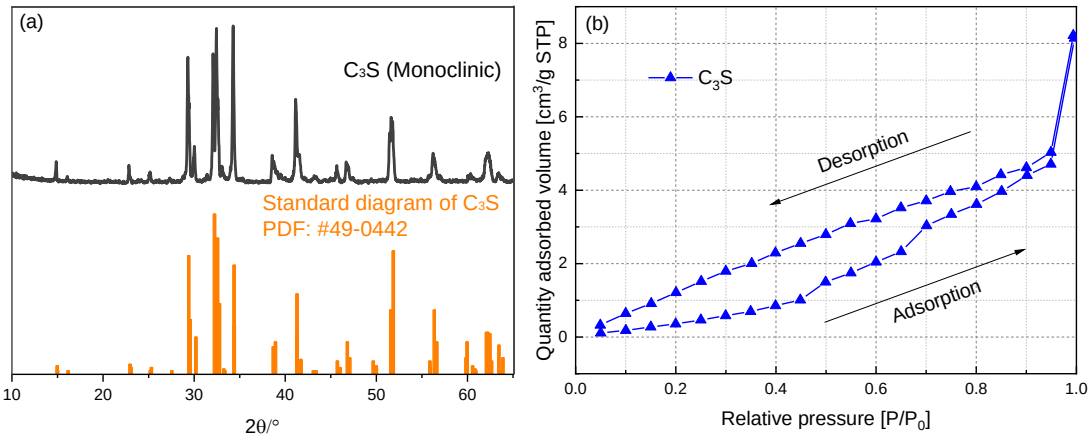

Figure 4-15 Characterisation of obtained alite: XRD (left) and nitrogen adsorption test (right).

4.2.2 Experimental details

A constant water (ultrapure, 18.2×10^6 Ω·cm) to solid ratio of 10 was used for the hydration of alite in order to have a better dissolution and sufficient water throughout hydration [177, 189]. The experiments were conducted (under 25±1 °C) in a sealed polypropylene vessel. The solution was obtained by filtration using a 0.45 µm nylon filter, followed by ICP-OES, pH, and conductivity tests. The solid phases were hydration-stopped by isopropanol and then vacuum-dried at 35 °C for XRD, STA, BET, NMR and TEM-EDS analyses. The testing ages were 5 min, 30 min, 2 h, 6 h, 12 h, and 24 h.

4.3 Autoreactor C-(N, A)-S-H synthetic and testing procedures

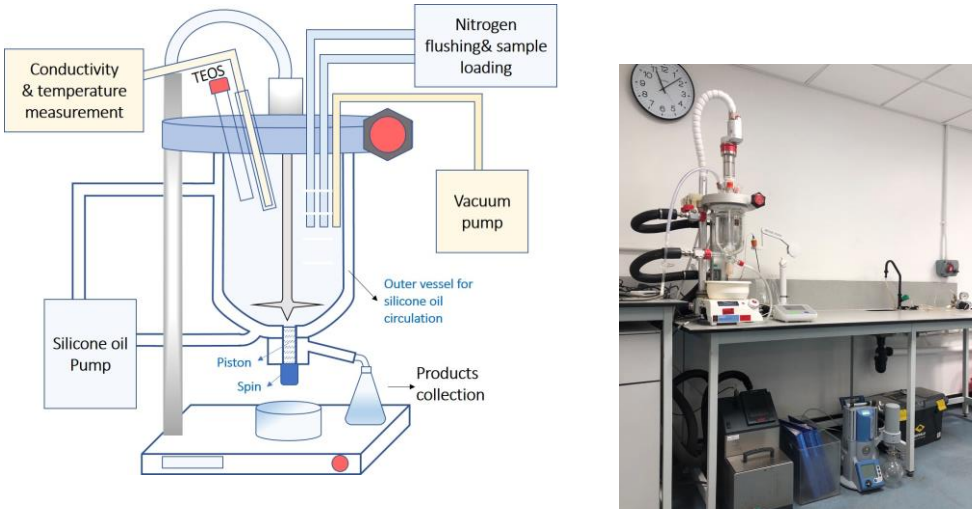

Figure 4-16 Sketch diagram (left) and equipment (right) of experimental setup for autoreactor synthesised C-S-H.

The 'autoreactor' method was firstly described by Grudemo and modified by Richardson and Vinnakota [16]. The basic principle of this method was to keep the lime concentration constant in

solution throughout the formation of C-S-H gel, which was also applied by Rodriguez for providing a constant lime solution for C_3S hydration [13]. It is well known that the concentration of CH (C, in mmol/L) shows inverse correlation to the temperature (T, in °C), which was calibrated for this equipment as expressed in Equation 62 [16].

$$C = 26.145 - 0.1954T \ (r^2 = 0.995) \qquad \textit{Equation 62}$$

Conductivity (mS/cm) is the parameter for monitoring the lime concentrations during the reaction, which was calibrated and shown in Equation 63.

$$C = 2.5661 \times Conductivity - 0.0925T + 1.09 \qquad \textit{Equation 63}$$

A silicone oil pump was used to maintain a constant temperature by circulation of oil. A vacuum pump was used for continuously sucking water during the reaction, which allows the increase of CH concentration. N_2 gas was used to maintain a normal pressure (and an inert atmosphere) during the process of adding solutions (a specific 1 mL/min was used throughout experiments), which aims to avoid carbonation. Also, degassing processing by using a vacuum pump (30 min) was applied for the deionized water before the dissolution of CH.

The TEOS ($(C_2H_5O)_4Si$) - Ethanol (C_2H_5OH) solution (4% TEOS dispersed in ethyl alcohol) was used as the silica resource based on the repaid hydrolyzation of TEOS (i.e. forms SiO_2 and ethyl alcohol). Supersaturated CH solution was prepared by dissolving 3 g CH in 1 L deionized water in a conical flask which was placed into a bucket containing enough ice to maintain a low temperature (1 ± 1 °C). The solution was continuously stirring for 48 hours in a glovebox. The obtained mixture was passed through a 13 μm qualitative filter paper (Fisher scientific) to obtain pure and clear CH solution and immediately transferred to the jacketed vessel shown in Figure 4-16. The constant temperature of 5 °C controlled by the circulated silicone oil was used throughout for all the synthetic procedures. The conductivity was recorded for every synthetic step. Finally, the product was collected in a conical flask with N_2 gas flushed during collection. The obtained solution was filtered and separated into filtrates and solid C-S-H. The filtrates were filtered with 0.45 μm nylon film and acidified with a concentrated 50% nitric acid at a ratio of 6:1 (filtrate: acid) for ICP-OES test. The solid C-S-H was washed (i.e. hydration-stopped) by 50% ethanol-50% water (v/v) solvent followed by pure ethanol and then dried in a glovebox with flushing N_2.

4.3.1 Synthesis of C-S-H using autoreactor

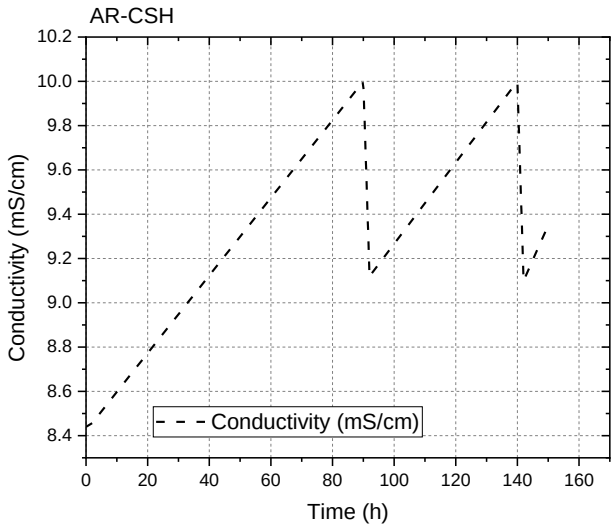

Figure 4-17 Synthetic process of C-S-H using autoreactor.

Figure 4-17 combined with Table 4-5 describe the complete procedure of synthesis of C-S-H using Syrris Atalas autoractor (Syrris Ltd, UK). The initial distillation process allowed a high CH concentration to achieve. Two-cycle steps were repeated in order to have more C-S-H product. The details of dosage and rate of addition of TEOS are given in Table 4-5. Minimum conductivity value was controlled at 8.44 mS/cm, which corresponds to around 22.29 mmol/L Ca^{2+} concentration.

Table 4-5 Summary of actions during C-S-H synthetic process.

Time (h) (±0.5)	**Conductivity(mS/cm) (±0.02)**	**Actions**
0	~8.44	Keep stable for around 1 hour (it normally takes 2-3 hours to reach stable);
1	8.44 (22.29 mmol/L)	Start the distillation;
90±0.5	10.00 (26.29 mmol/L)	Stop the distillation and start the injection; Adding 8ml 4% TEOS solution @ 1mL/min;
92±0.5	9.12 (24.03 mmol/L)	Starts the distillation;
140±2	10.00 (26.29 mmol/L)	Stop the distillation and start the injection; Adding 8ml 4% TEOS solution @ 1mL/min;
142±0.5	9.10 (23.98 mmol/L)	Start the distillation;
150	9.35 (24.62 mmol/L)	Collect the solution and start filtration under ice-bath pH of leachate solution is 12.70

4.3.2 Synthesis of C-A-S-H using autoreactor

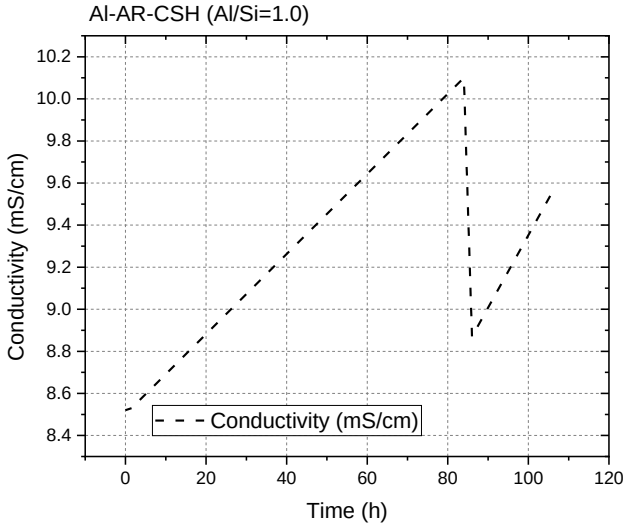

Figure 4-18 Synthetic process of C-(A)-S-H using autoreactor.

The Al/Si ratio (bulk) of 1.0 was used during synthetic process and the detailed calculations can be found in **Appendix F**. Figure 4-18 and Table 4-6 summarise the synthetic process of C-A-S-H phase. $Al(NO_3)_3 \cdot 9H_2O$ (Sigma-Aldrich, CAS7784-27-2) was used as the additional Al source, which was added together with 4% TEOS at a certain ratio. Meanwhile, only one-cycle process was implemented because the conductivity was not exactly corresponding to Ca^{2+} concentration. Therefore, for the purpose of accurately controlling the amount of Al, only one step corresponding to the addition of Si and Al was applied.

Table 4-6 Summary of actions during C-(A)-S-H synthetic process.

Time (h)	**Conductivity (mS/cm) (±0.02)**	**Actions**
0	~ 8.52	Keep stable for around 1 hour;
1	8.52 (22.49 mmol/L)	Start the distillation;
84	10.10 (26.55 mmol/L)	Stop the distillation and start the injection; Adding 10ml 4% TEOS solution @ 1mL/min; Adding 6 ml 0.01 M $Al(NO_3)_3$ solution @ 1mL/min;
86	8.87	Start the distillation (Assuming that the differences of conductivity were caused by the adding $Al(NO_3)_3$ solution, 0.35 was reduced) (9.22 mS/cm should be shown if nothing added.);
106	9.56	Collect the solution and start filtration under ice-bath pH of leachate solution is 12.80.

4.3.3 Synthesis of (C, Na)-S-H using autoreactor

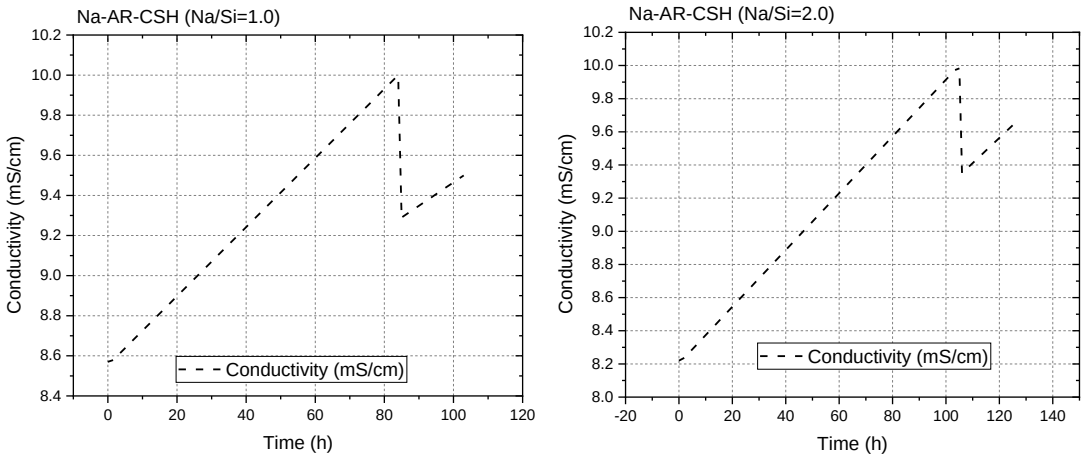

Figure 4-19 Synthetic process of (C, Na)-S-H using autoreactor: Na/Si=1.0 (left) and Na/Si=2.0 (right).

The synthetic (C, Na)-S-H was synthesised based on controlled Na/Si bulk ratio of 1.0 and 2.0 (**Appendix F**). Figure 4-19 and Tables 4-7, 4-8 summarise the assemblage process of (Ca, Na)-S-H. NaOH (Sigma-Aldrich, CAS1310-73-2) solution (0.1 *M*) was used as the additional Na source. Similarly, only one one-cycle process of adding Na was implemented during the synthesis in order to control the similar Ca^{2+} concentration as the C-S-H group.

Table 4-7 Summary of actions during (C, Na)-S-H (Na/Si=1.0) synthetic process.

Time (h)	Conductivity (mS/cm) (±0.02)	Actions
0	~ 8.57	Keep stable for around 1 hour;
1	8.57 (22.62 mmol/L)	Start the distillation;
84	10.00 (26.29 mmol/L)	Stop the distillation and start the injection; Adding 8ml 4% TEOS solution @ 1mL/min; Adding 14.4 ml 0.1 *M* NaOH solution @ 1mL/min;
85	9.29	Start the distillation (Assuming that the differences of conductivity were caused by the adding NaOH, 0.17 mS/cm was increased);
103	9.50	Collect the solution and start filtration under ice-bath pH of leachate solution is 12.85.

Table 4-8 Summary of actions during (C, Na)-S-H (Na/Si=2.0) synthetic process.

Time (h)	Conductivity (mS/cm) (±0.02)	Actions
0	~ 8.22	Keep stable for around 1 hour;
1	8.22 (21.72 mmol/L)	Start the distillation;
105	10.00 (26.29 mmol/L)	Stop the distillation and start the injection; Adding 8ml 4% TEOS solution @ 1mL/min; Adding 28.8 ml 0.1 *M* NaOH solution @ 2mL/min;
106	9.35	Start the distillation (Assuming that the differences

		of conductivity were caused by the adding NaOH, 0.25 mS/cm was increased);
135	9.64	Collect the solution and start filtration under ice-bath pH of leachate solution is 12.80.

4.3.4 Leaching tests of C-S-H in NaOH/Al(NO$_3$)$_3$ solutions

The static leaching tests of C-S-H (the C-S-H used here is from that synthesised in Section 4.3.1) in different solutions are conducted in order to verify the change in C-S-H morphology under different solution environments. Deionized water, NaOH solutions (0.01 *M*, 0.1 *M*, and 0.5 *M*), and Al(NO$_3$)$_3$·9H$_2$O solutions (0.01 *M* and 0.1 *M*) were used as the media of leaching. The deionized water or solutions used for leaching were degassed for around 30 min and a solid to liquid ratio of 150 was used for leaching. The leaching process was performed under N_2 atmosphere for 28 days. The filtrates (leachates) and solids (residues) were acidified and hydration-stopped respectively using the same methods as those for synthetic C-S-H (Section 4.3) for further characterisations.

4.3.5 ICP-OES and TEM-EDX calibrations

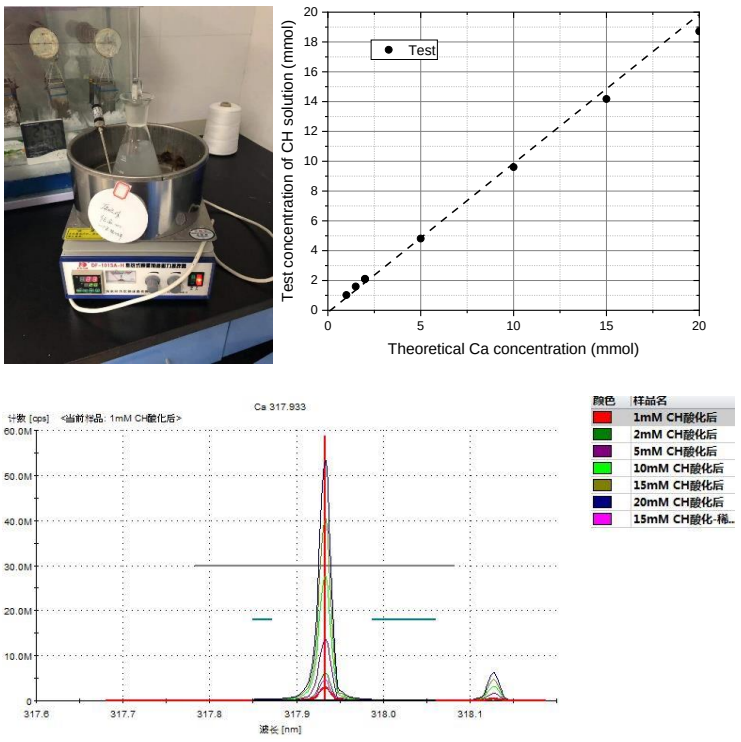

Figure 4-20 Calibration of ICP-OES before testing: dissolution of CH in conical flask (upper left); relationships between theoretical Ca ions and tested Ca concentration by ICP-OES (upper right, the dash line is y=x); ICP-OES spectra of different solutions show the position of Ca element.

Other than the standard elements calibration, the ICP-OES was calibrated by using solutions that dissolved the CH under 20 °C as shown in Figure 4-20. The reason for using CH is that the solution environment that are present in paste pore solution or in synthetic systems are similar with CH solutions. A specific amount of CH is dissolved in water-bath with constant 20 °C to make the CH solutions with Ca concentrations of 1, 2, 5, 10, 15, and 20 *mM* (i.e. mmol/L). The ICP-OES spectra show the main adsorption peak of Ca (element) at 317.933 nm with a small additional peak at ~318.125 nm. The calibration generally shows a good relationship between the theoretical and testing concentrations; however, the testing value is slightly lower when Ca concentration is higher than 15 *mM*.

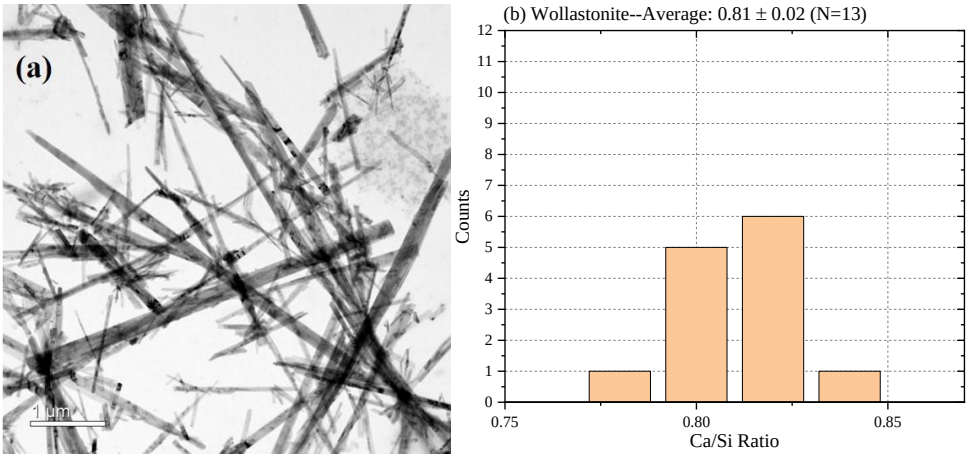

Figure 4-21 Calibration of TEM-EDX before testing: (a) morphology of wollastonite; (b) Ca/Si ratio distribution of wollastonite. The calibration factor is 1.23 in this case.

TEM-EDX calibration with a correction factor of 1.23 is used only for synthetic C-S-H in line with the previous studies [13, 16]. The average Ca/Si ratio and the distribution frequency histogram of wollastonite are given in Figure 4-21(b). In addition, the mineralogy information of wollastonite is also provided by Rodriguez (Figure 4.6 in [13]) to confirm the purity. This calibration factor is not applied in alite or cement samples [13, 16].

Chapter 5

Morphology-structural change of C-S-H gel in blended cements

5.1 Hydration process of blended wPC

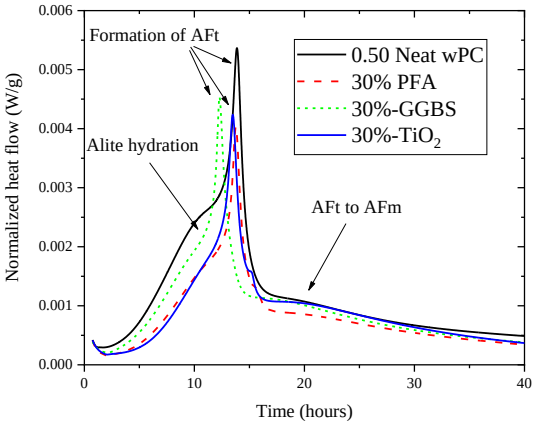

Figure 5-1 Hydration rate of neat wPC, 30%PFA-wPC, 30% slag-wPC, and 30%TiO_2-wPC samples.

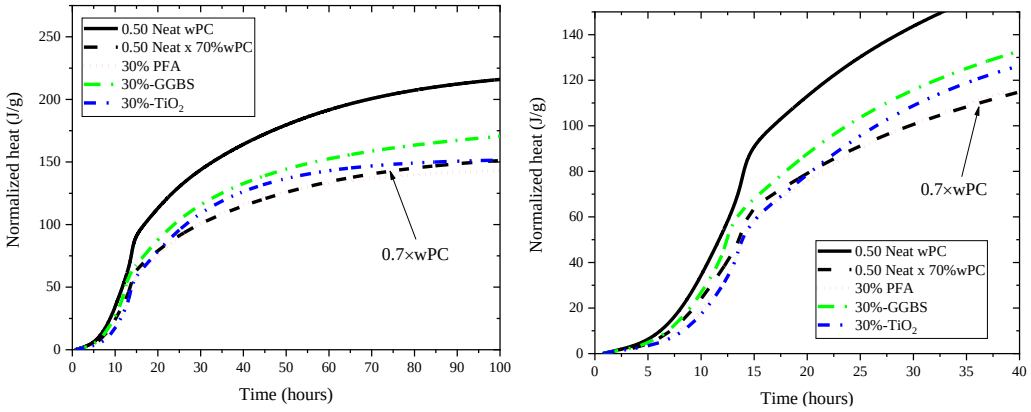

Figure 5-2 Hydration heat of neat wPC, 30%PFA-wPC, 30% slag-wPC, and 30%TiO_2-wPC samples, 0-100 hours (left) and 0-40 hours (right).

Figures 5-1 and 5-2 show the effect of 30% filler or SCMs on hydration process of wPC. In Figure 5-2, the black dash line represents the hydration heat of neat wPC multiplied by 0.7. In the heat flow spectrum, it is very clear that the three hydration peaks occur during 5 to 24 h. The alite hydration peaks are the dominant peaks during hydration with additional first shoulder peak representing AFt formation and second shoulder peak indicating AFm formation [28, 168, 190]. For all the samples with SCMs or filler replacement, both the first and second hydration peaks are

reduced dramatically. This is due to the initial lower hydraulic properties of these fillers. Besides, the AFt formation peak is accelerated by the addition of GGBS, but no obvious change can be noticed in PFA/TiO_2 containing samples. It is noted that the GGBS gives a higher and faster hydration curve when compared to that of PFA and anatase added samples, which is attributed to the self-hydraulic nature of GGBS [43, 131, 191]. The cumulated hydration heat in Figure 5-2 shows that the initial heat accumulation (within 20 hours) of 30% PFA or TiO_2 is the same, which is lower than the 0.7 wPC group (based on simple dilution effect). This result is opposite to the theory 'filler effect' during the early age hydration of cement [19], however, it is the same as Richardson's results [14]. This may indicate that the PFA or TiO_2 have an initial retarder effect on wPC hydration. In contrast, GGBS has a totally different hydration curve compared to that of PFA or TiO_2, which gives a much higher cumulated heat than the reference group. The main reason is also due to the self-hydraulic property of GGBS [43]. The curves passed the reference group at around 20 h for TiO_2 sample and at around 30 h for PFA sample, which indicate the start of 'filler effect'. Richardson [14] summarised three conduction calorimetry results of PFA-OPC samples, the cumulative heat curves of two PFA-containing samples surpassed the reference at around 25 h.

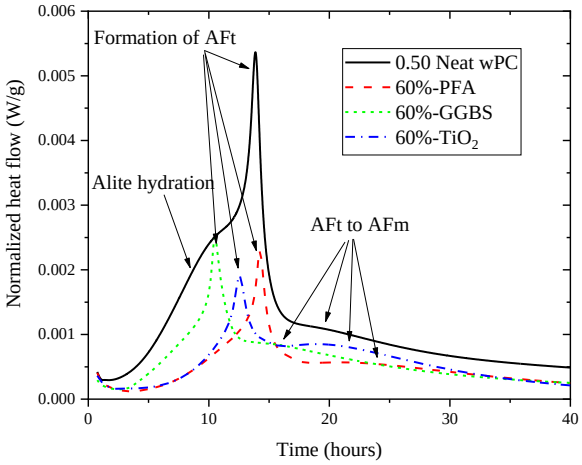

Figure 5-3 Hydration rate of neat wPC, 60%PFA-wPC, 60% slag-wPC, and 60%TiO_2-wPC samples.

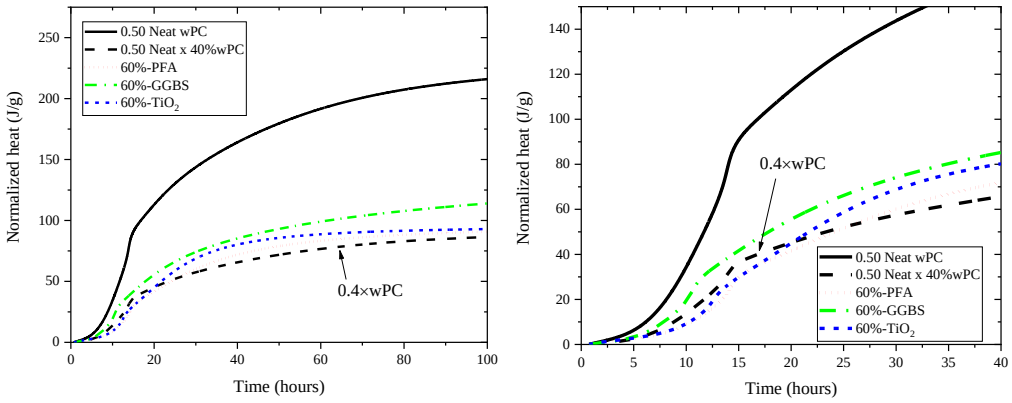

Figure 5-4 Hydration heat of neat wPC, 60%PFA-wPC, 60% slag-wPC, and 60%TiO_2-wPC samples, 0-100 hours (left) and 0-40 hours (right) specifically for 40% × neat wPC, 60%-PFA and 60%-TiO_2 samples.

Figures 5-3 to 5-4 give the same information as Figures 5-1 and 5-2 but for 60% fillers/SCMs added samples. Not surprisingly, the main hydration peaks are much lower than those of 30% groups. A more obvious retarder on alite hydration peak in PFA and TiO_2 containing samples can be identified. However, TiO_2 accelerated the formation of AFt, which is also delayed by adding PFA. Again, the cumulative heat of PFA and TiO_2 added samples are lower than reference group (wPC multiply by 0.4 as shown in black dash line in Figure 5-4) at very early age (within 24 h), whereas that of GGBS added samples stays higher. The results are not changed as the loading of 'fillers' content increases. Interestingly, the cumulated heat curve of 60% PFA and TiO_2 groups surpasses that of the reference group at around 18 h and 25 h, which is faster than the changing points in 30% replacement groups. As TiO_2 is inert in this system, the increase in hydration heat can be attributed to the 'filler effect'. Thus, the same situation happened to PFA-containing samples, which means the increase of cumulative heat after 24 h is attributed to the 'filler effect' instead of PFA hydration.

5.2 Phases present in blended wPC

The crystalline phases against time development of all blends are determined by XRD as shown in Figures 5-5 to 5-9. The results include the XRD patterns from 5 h to 91 d at the left side of each figure and the right side shows a closer look at the 270-d result.

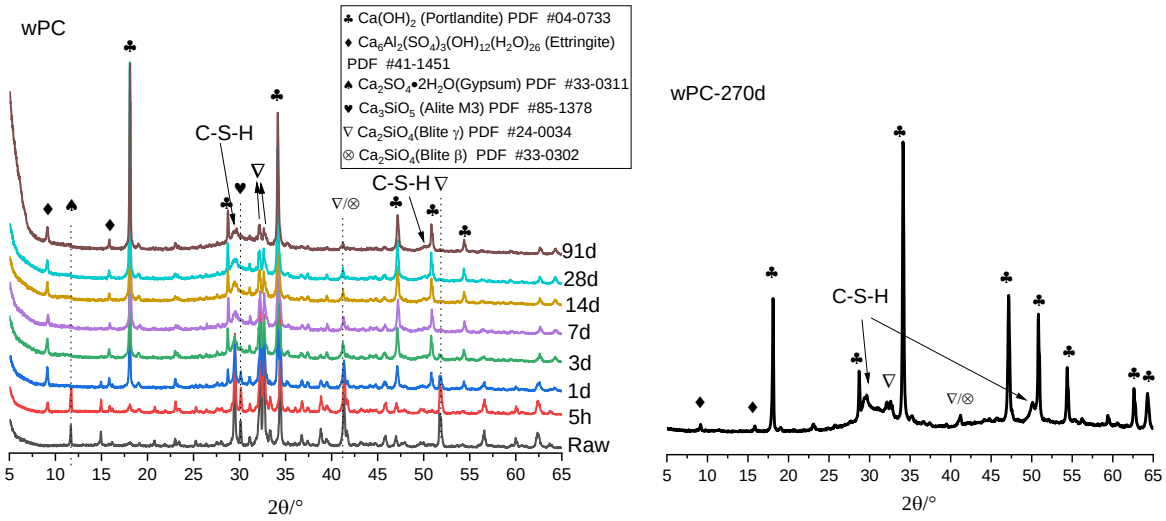

Figure 5-5 XRD analysis of wPC samples.

The XRD results of neat wPC hydrated up to 270 days are shown in Figure 5-5. Residual cement phases (alite and belite) continuously reduces but are present throughout the ages. The main hydration products are C-S-H gel, Portlandite, and ettringite. The gypsum disappeared at 1 d after the formation of AFt, which is consistent with that of conduction calorimetry results in Section 5.1. Some monosulphate phases (AFm) may be present after 3 d, however, no obvious peak is detected in all age XRD patterns. The reason may be attributed to its small amount or a small crystal size [14]. The AFm-type phases could be determined by ^{27}Al NMR at a chemical shift of ≈ 9 ppm [35].

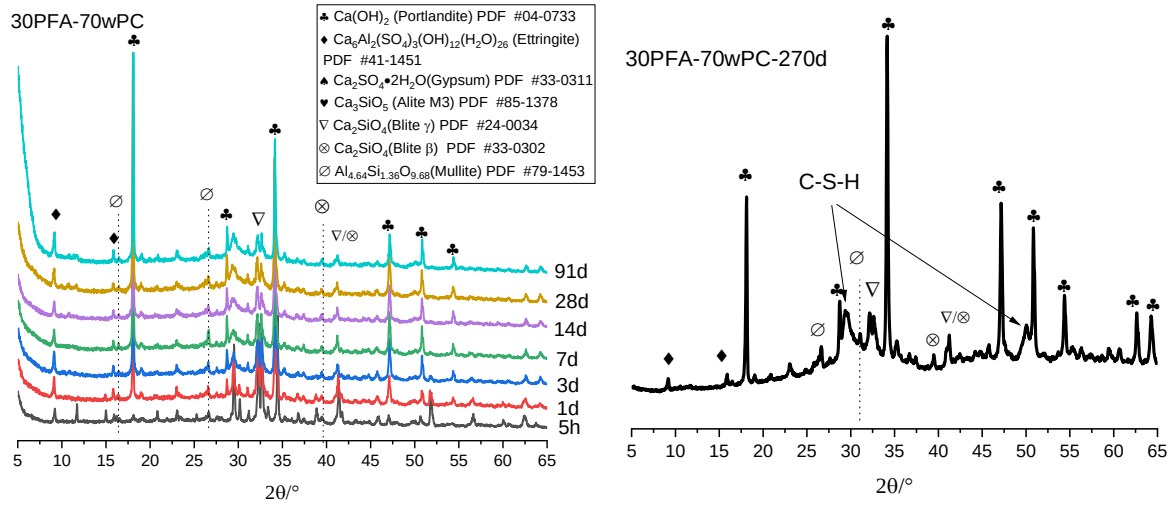

Figure 5-6 XRD analysis of 30PFA-70wPC samples.

Figures 5-6 gives the XRD patterns of 30PFA-70wPC samples hydrated for same ages. The main hydration products include C-S-H gel, Portlandite and ettringite, which remain similar to

those in neat wPC. A broad peak can be identified at around 25° 2θ, which is due to the raw PFA at small replacement level. Some mullite and quartz originally from PFA can be hardly recognised but are still present in all 30PFA-70wPC samples.

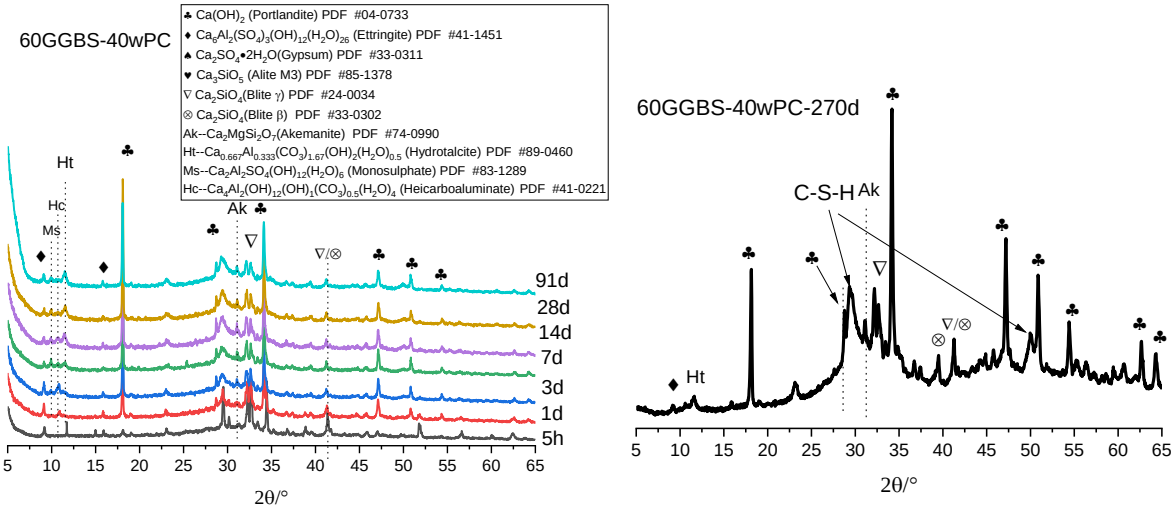

Figure 5-7 XRD analysis of 60GGBS-40wPC samples.

Figures 5-7 is the XRD results of 60% GGBS replaced wPC samples. Again, the ettringite, Portlandite and C-S-H gel are the principal hydration products for every group hydrated for more than 1 d. Some LDHs phases (hydrotalcite and monosulphate phases) are identified in GGBS-containing wPC samples after 7-day hydration. The hydrotalcite is often found in pure slag or slag-containing samples due to the presence of Mg and Al phases in GGBS [97, 132]. The monosulphate appears mainly due to the higher alumina and sulphate source from GGBS, although only around 20% sulphur in GGBS exists as sulphate [192, 193]. The hump phase in the range of 25 to 35° 2θ is present all throughout the age, which is brought by GGBS. Interestingly, the peaks of residual cement in PFA and GGBS blended cements are higher than those in neat wPC paste after long-term hydration, which indicate a lower hydration degree of clinker phases are identified in SCMs blends.

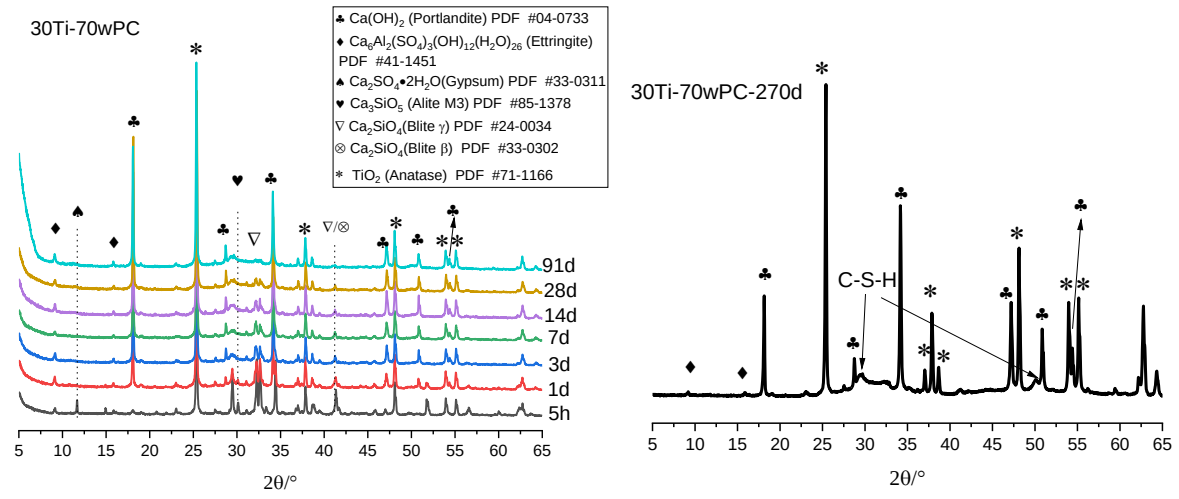

Figure 5-8 XRD analysis of 30TiO₂-70wPC samples.

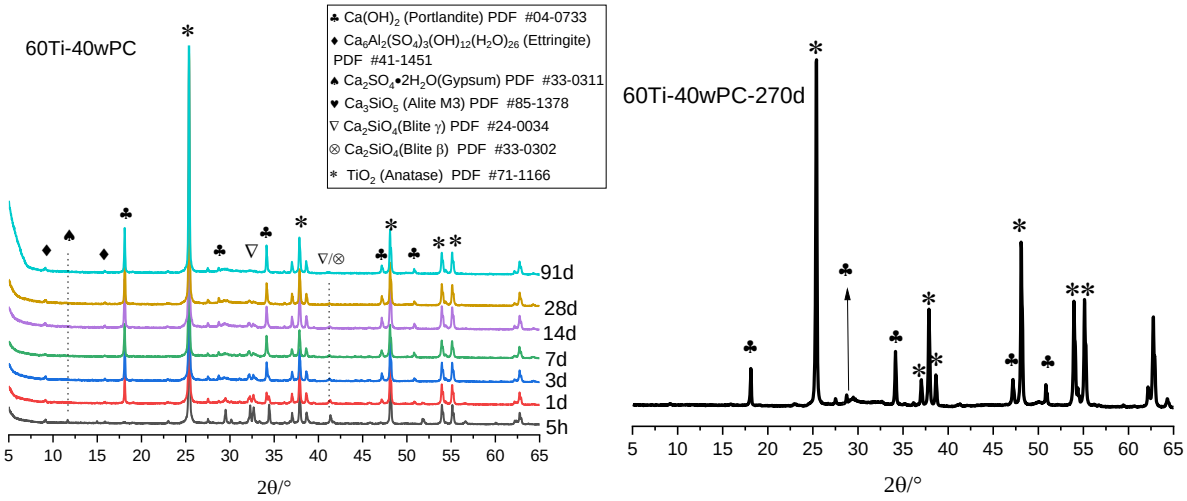

Figure 5-9 XRD analysis of 60TiO₂-40wPC samples.

The same hydration products are also found in 30% and 60% TiO_2 containing samples as shown in Figures 5-8 and 5-9. The diffraction peaks of anatase remain same regardless of hydration time, which indicates that anatase is totally inert in this system. Meanwhile, the peaks of residual cement phases are extremely tiny and can hardly be detectable at 270 d, which means that TiO_2 promotes the hydration degree of clinker phases in anatase blends.

In addition, most Al-bearing crystalline phases are hard to detect by XRD, but give signals on ^{27}Al NMR spectrum, including ≈ 5 ppm for 'third aluminate hydrate' (TAH), ≈ 9 ppm for AFm phase (also possibly ≈ 62 ppm for the interlayer of AFm), ≈ 13 ppm AFt phase, and ≈ 61 ppm for strätlingite [14, 35].

5.3 Calcium hydroxide/chemically bound water evaluation of blended wPC samples

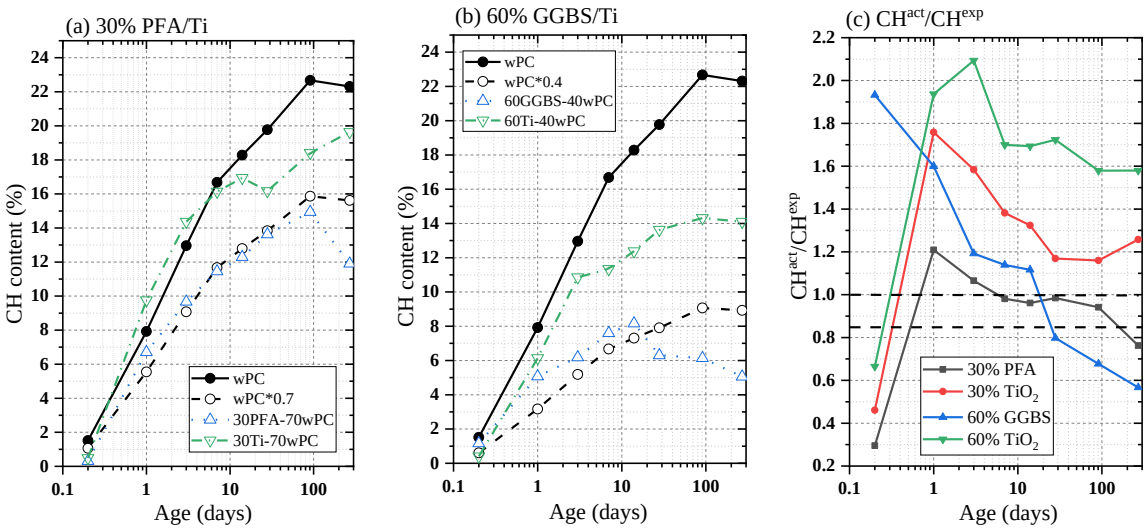

Figure 5-10 CH content evaluation from QXRD: (a) at 30% replacement level; (b) at 60% replacement level; (c) calculated parameter CH^{act}/CH^{exp}, where CH^{act} is the actual CH content in blended cement and CH^{exp} is the expected CH content calculated by the percentage of wPC.

Figures 5-10(a) and (b) gives the CH content development of both 30% and 60% replacement level systems determined by QXRD analysis. There is no doubt that the CH content increased over hydration time. The unfilled circles in these two graphs stand for the CH of neat wPC multiplied by 0.7 or 0.4 for the purpose of comparison, which can be therefore regarded as the reference groups (denoted as CH^{exp}) for the SCMs/filler added samples based on simple dilution [10, 14]. The measured CH contents in the blended system are denoted as CH^{act}. The ratios of CH^{act} to CH^{exp} are calculated for each blend and plotted in Figure 5-10(c).

The ratios shown in Figure 5-10(c) clearly exhibit that the PFA or TiO_2 samples has a lower CH content when compared to neat wPC at 5 h, which can be explained as initial retardation that occurred in such systems. Whereas, the GGBS increases the CH content initially. These results are consistent with conduction calorimetry results as shown in Figures 5-1 to 5-4. The initial 'retarder effect' of PFA (the delay of the hydration process of cement) was also pointed out and discussed by Richardson et al. [14]. As reviewed and summarised by Richardson [14], the effect of PFA on early age hydration of cement is controversial when comparing some publications in 1980s: some studies reported the hydration of aluminate phase was retarded, some supported the hydration of silicate phases was retarded, and some considered both aluminate and silicate

hydration were retarded; on the other hand, some studies held a totally opposite view. There are no doubts that the mechanism regarding the effects of PFA particles on the hydration of cement is complex, which depends on both ingredients' compositions and the hydration environment. The results in current study support that the aluminate reaction is not significantly affected by 30% PFA but slightly retarded by 60% PFA; whereas silicate reactions are significantly initially retarded by replacing 30%-60% PFA (see Figures 5-1 and 5-3). These results are also supported by the quantity of CH data, which gives a CH^{act}/CH^{exp} ratio lower than 1 at early age. The less CH that initially generated in PFA/TiO_2 blends is obviously resulted from the retarded silicate reactions.

However, the CH^{act}/CH^{exp} ratio rose at intermediate ages for TiO_2/PFA containing samples, which indicates that an acceleration happened during this period (the so-called 'filler effect'). After around 1 d hydration, the CH^{act}/CH^{exp} ratio of PFA blends dropped down, which indicates the starting of secondary hydration; whereas the TiO_2 blends remained higher CH^{act}/CH^{exp} ratios until 270 d, which means TiO_2 does not consume CH and a higher hydration degree is achieved. This result is also supported by the lower residual cement peaks of TiO_2 blends in XRD patterns (Figures 5-8 and 5-9). As expected, the PFA and GGBS consumes CH and CH^{act}/CH^{exp} ratios in these two systems gradually decreased to lower than 1. The 'changing ages' (from >1 to <1) from QXRD for 30% PFA and 60% GGBS blends are around 7 d and 20 d, respectively. However, the CH^{act}/CH^{exp} ratio of PFA blends stays stable at around 1 until 28 d and then decreased significantly since then, which indicates the consumption of CH mainly happened after 28 d.

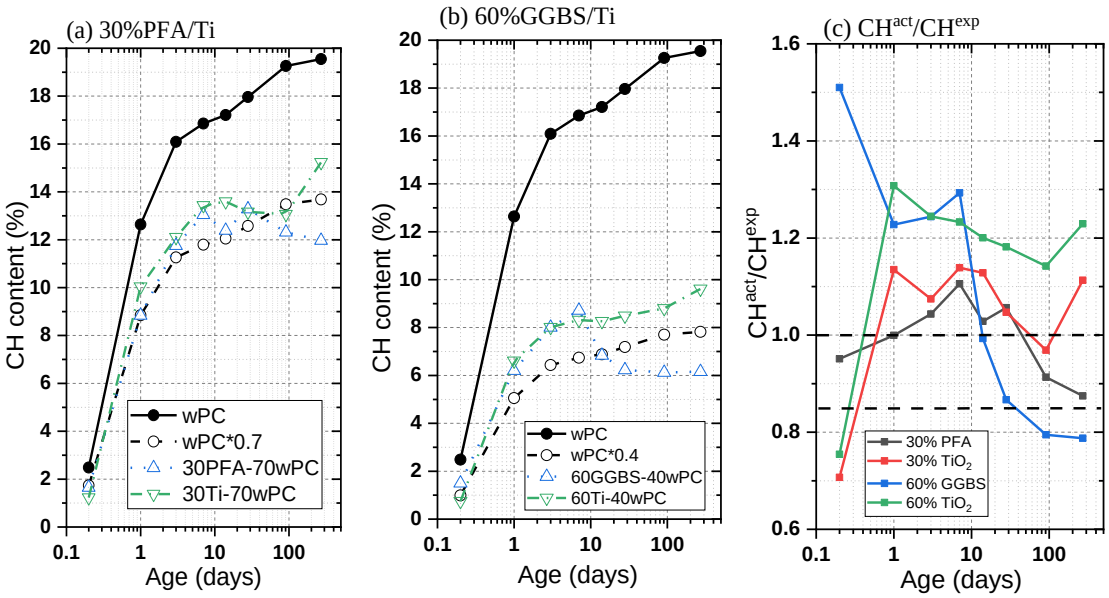

Figure 5-11. CH content evaluation from TG-DSC: (a) at 30% replacement level; (b) at 60% replacement level; (c) calculated parameter CH^{act}/CH^{exp}.

The same information but obtained from TG-DSC analysis regarding CH^{act}/CH^{exp} ratios is given in Figure 5-11. Again, the unfilled circles represent the expected CH content on the basis of simple dilution. Similar results are obtained from TG-DSC calculations expressed as a percentage of ignited mass. Both PFA and TiO_2 initially retarded the hydration and then accelerated the hydration after 1 d. Since then, the TiO_2 blends keep a CH^{act}/CH^{exp} ratio higher than 1, which again supports the higher hydration degrees are achieved in these blends. The PFA blends give a close developing trend as compared to that obtained by Richardson et al. [14]: the CH^{act}/CH^{exp} ratio rose up to higher than 1 until 28 d and then dropped down to lower than 1 at the age of 91 d. The 'changing ages' (from >1 to <1) from TG-DSC for 30% PFA and 60% GGBS blends are around 40 d and 14 d, respectively.

Comparison with the changing ages from QXRD, the result for GGBS blends are quite close, which happens at around 14-20 d. But for PFA blends, the QXRD results indicate that the decrease happens at the age of 1 d and the CH^{act}/CH^{exp} ratio keeps around 1 until 28 d, while those from TG-DSC show that the CH^{act}/CH^{exp} ratio keeps higher than 1 until 28 d. As lots of studies [10, 36, 43, 98, 194, 195] show that the reactivity of GGBS is higher than that of PFA in most cases, thus the consumption of CH in GGBS blends is expected to be higher and quicker than that of PFA blends. These evidences suggest that the TG-DSC results are more accurate than those

from QXRD. Meanwhile, a CH^{act}/CH^{exp} ratio closer to 1 until 28 d also indicate that the PFA is not sufficiently hydrated until 28 d.

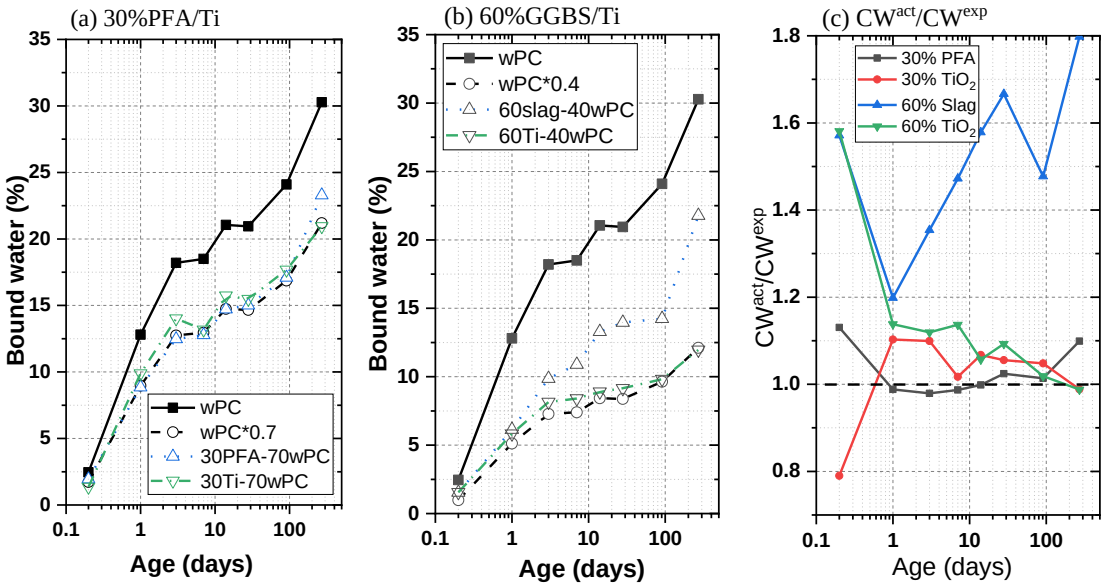

Figure 5-12. Chemically bounded water determined by TG-DSC: (a) at 30% replacement level; (b) at 60% replacement level; (c) calculated parameter CW^{act}/CW^{exp}.

More information on the bound water in hydrates calculated from TG-DSC analysis are also plotted in Figure 5-12. Similarly, the unfilled circles stand for the expected chemically combined water (CW^{exp}) multiply by the wPC content (i. e. 0.7 and 0.4) based on the simple dilution. The measured bound water in blends is denoted as actual bound water (CW^{act}). The ratio of CW^{act} /CW^{exp} is calculated and given in Figure 5-12(c). The chemically bound water is present in both C-S-H gels and crystalline phases. It is notable that the CW^{act} /CW^{exp} ratio of GGBS blends is always higher than 1, which supports the acceleration of hydration of cement. This value is much higher than those for TiO_2 and PFA blends. This is due to the self-hydraulic property and higher reactivity of GGBS that can generate more crystalline phases (see XRD results in Figure 5-7) and that can maintain more water molecules [36, 195]. An extreme high CW value of 60% TiO_2 blend is found at 5 h, this is probably because the nano-scaled particles can preserve some water molecules between the particles, which is hard to remove from hydration stopping process.

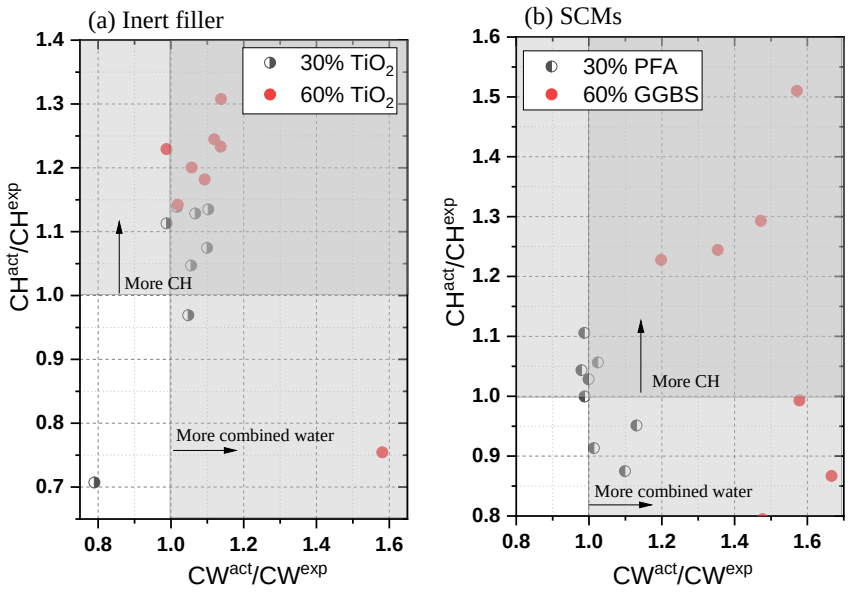

Figure 5-13. Relationships between CW^{act}/CW^{exp} and CH^{act}/CH^{exp} in inert filler (TiO_2) and SCMs-blended wPC systems.

Comparison between CW^{act}/CW^{exp} and CH^{act}/CH^{exp} is given in Figure 5-13 for a purpose of identifying the reason of the increasing CW^{act}/CW^{exp} ratio. Figure 5-13 (a) shows the relationship of these two ratios in TiO_2 (inert filler) blends and the same information but for SCMs (GGBS and PFA) is given in Figure 5-13 (b). As confirmed by XRD in Figures 5-5 to 5-9 that the hydration products remain same in TiO_2 blends, thus only CH and C-S-H gel resulted from silicate reactions can maintain more water molecules.

A good correlation between CW^{act}/CW^{exp} and CH^{act}/CH^{exp} is observed in TiO_2 blends as shown in Figure 5-13 (a), which means TiO_2 accelerates the hydration degree at the later age and generates more hydration products (i. e. CH and C-S-H gel). In comparison to TiO_2 blends, SCMs blends give a totally different relationship of CW^{act}/CW^{exp} and CH^{act}/CH^{exp}. GGBS generates more CH and more bound water than 'expected' and the bound water is far more than that solely brought by the more CH. This observation is supported by conduction calorimetry and XRD results in Section 5.1 and 5.2. More CH results from the accelerated hydration process and the extra bound water (other than taken by the more CH and C-S-H gels as compared to the slope of this relationship in TiO_2 blends) is held by more AFm type phase as shown in XRD patterns. More CH and bound water are also found in PFA blends, which is much lower than other groups. This observation is consistent with the value of both CW^{act}/CW^{exp} and CH^{act}/CH^{exp} around 1 at

intermediate ages, which illustrates a slight acceleration effect of PFA particles. After the consumption of CH, both PFA and GGBS blends have a CH^{act}/CH^{exp} value lower than 1, but a CW^{act}/CW^{exp} value higher than 1. The more bound water is confidently assigned to that the C-S-H gel resulted from the secondary reactions between CH and glassy phases in SCMs.

5.4 ^{29}Si NMR analysis of blended wPC samples

5.4.1 Experimental observations

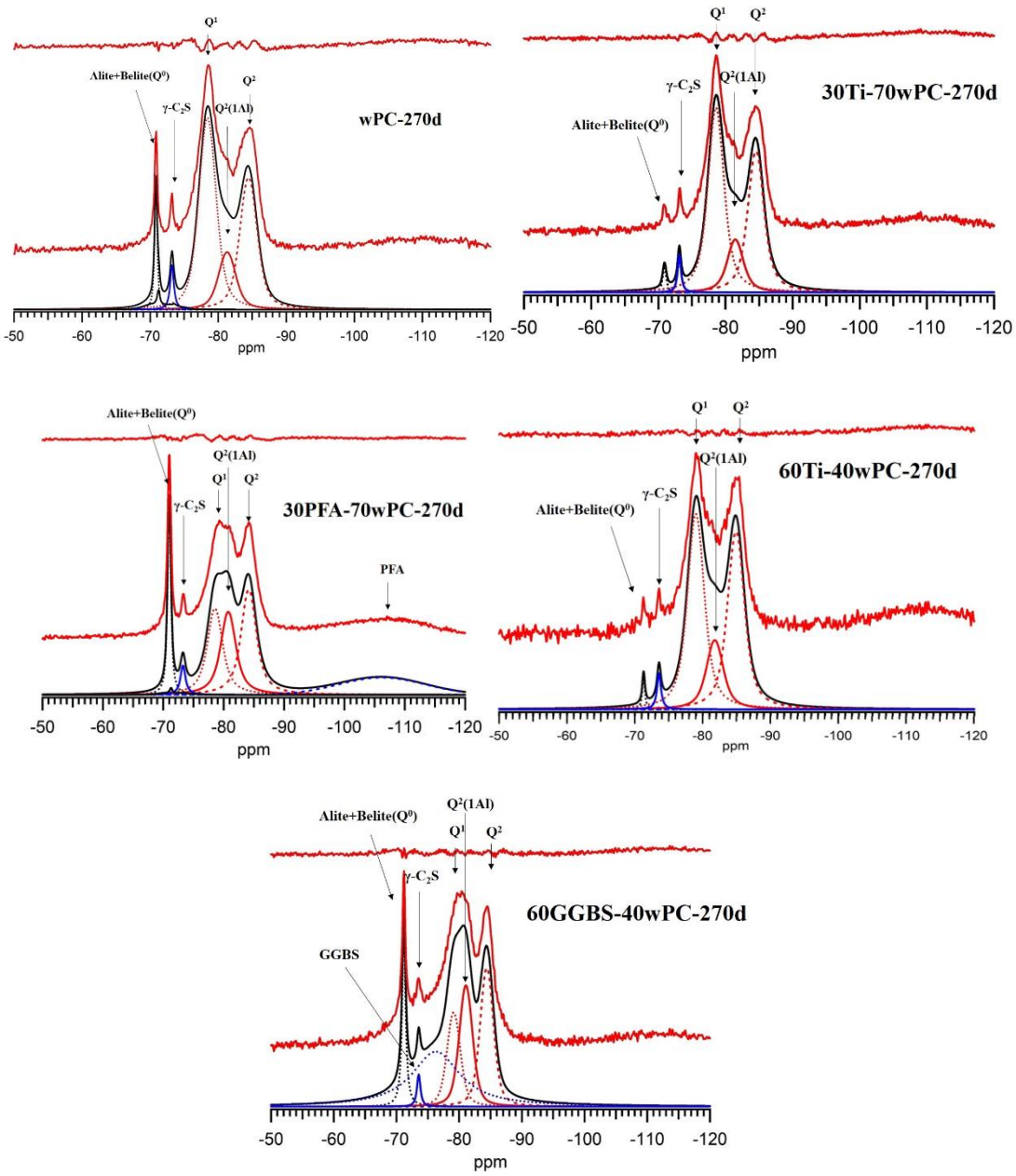

Figure 5-14 Examples of ^{29}Si MAS NMR results of blended cements: (a) 270d wPC; (b) 270d 30Ti-70wPC; (c) 270d 30PFA-70wPC; (d) 270d 60Ti-40wPC; (e) 270d 60GGBS-40wPC. The deconvolution of other-age samples can be found in ***Appendix G****.*

Figure 5-14 shows the ^{29}Si MAS NMR spectra and the deconvolution of all blends hydrated for 270 d. The same information of other ages (7, 14, 28, 91 d) are given in **Appendix G**. The results from deconvolution are shown in Figures 5-15 to 5-19. The same peaks related to the possible structural silicate units but with different intensities are assigned to these blended cements, which include monomers (belite, Q^0) at ≈ -71.3, dimers (Q^1) at ≈ -79.2, and middle chains at ≈ -81.5 for Q^2(1Al) or ≈ -85.2 ppm for Q^2(0Al) [5, 6, 131]. In addition, a small peak related to monomers in γ-C_2S are present throughout all blends and samples, which originates from raw wPC. For GGBS and PFA blends, additional peaks that belong to raw PFA at ≈ -106.8 (Q^4) and GGBS at ≈ -76 ppm are assigned to remove the effect of unreacted SCMs [10, 14, 97, 98]. Normally, a small and controversial Q^{0H} peak throughout the hydration will be assigned at the chemical shift quite close to γ-C_2S [14, 87], however, this peak is ignored due to its small amount and the presence of γ-C_2S.

Figure 5-15 gives the distribution of silicate anion units in the C-A-S-H phase in different blends varied from 7 to 270 d. The data of each Q^n(mAl) are normalized to 100%, which indicate more clearly how the silicate species change with age.

It is clear that the early-age (7 d) C-A-S-H is dominated by Q^1 in neat wPC or TiO_2 blends (≈ 65-70%), which is consistent with the previous studies that concluded the dominant silicate group is dimer at early hydration of either C_3S paste [87] or neat wPC [14]. The lower amount of Q^1 tetrahedra is evidence of a higher hydration degree of clinkers in TiO_2 blend. In PFA blend (Figure 5-15c), the fraction of Q^1 drops down to around 60% at the same age but only limited changes on Q^2(1Al), indicating the silicate reactions are accelerated but the PFA did not start to hydrate. Both TiO_2 and PFA blends show the enhanced hydration at 7 d, which is the result of the so-called ‘filler effect’. However, the fraction of Q^1 drops down to around 50% accompanied by an increasing fraction of Q^2(1Al) at 7 d in GGBS blend (i. e. from ≈ 12% in neat wPC to ≈ 20%), which indicates the sign of GGBS reaction.

The Q^1 tetrahedra remarkably decreases with age in neat wPC and TiO_2 blends until 91 d and remains stable till 270 d, accompanied by an increase in Q^2(0Al) but stable Q^2(1Al). This observation is caused by the limited alumina sources that are present in the wPC system. Overall,

the TiO_2 blends possess higher fractions of Q^2 compared with that of neat wPC, which means a higher hydration degree of silicate phases are achieved throughout the testing ages. In contrast, PFA blends show a continuous decreasing trend of Q^1 tetrahedra and an increasing trend of Q^2(1Al) units, which shows evidence for the PFA reaction. However, the fraction of Q^2(0Al) remains quite similar to that in neat wPC or TiO_2 blends. The silicate tetrahedra distribution, especially Q^2(1Al) units, is different in GGBS blends. Specifically, the Q^1 tetrahedra drops dramatically between 7 and 14 d, accompanied by increased Q^2(1Al) but limited change to Q^2(0Al). This result indicates that the reaction of GGBS is fast during the corresponding ages (7-14 d) but slows down thereafter. In comparison with neat wPC or TiO_2 blends, the Q^2(1Al) tetrahedra are increased significantly after 30 and 14 d in PFA and GGBS blends respectively.

An interesting observation of Q^2(0Al) in all samples, is that it is quite similar at 270 d (≈ 35-40 %, i. e. over 1 in 3), which agrees with Richardson's study of water- and KOH activated PFA blends [14]. The main difference between these systems is the fraction of Q^1 and Q^2(1Al) (i. e. the end-chain tetrahedra and the paired tetrahedra adjacent to the Al bridging tetrahedra). These data support that the differences in C-A-S-H between SCM blends and inert filler/neat blends are mainly the incorporation of additional Al tetrahedra at bridging sites only, which further lengthens the MCL of C-A-S-H [14, 78, 89]. The results of MCL and the occupancy factor of the bridging site (SOF_{BT}) will be discussed in the following section. Thus, the increase of Q^2(1Al) tetrahedra is also an indicator for the reaction of SCMs, but not a sign of the start of the reaction. As shown in Figure 5-15, it can be confirmed that PFA reacts continuously and slowly between 30 d (i. e. the Q^2(1Al) fraction over the highest value in $30TiO_2$ blends) to 270 d and GGBS reacts between (but not starting at) 10 d (i. e. the Q^2(1Al) fraction over the highest value in $60TiO_2$ blends) to 270 d.

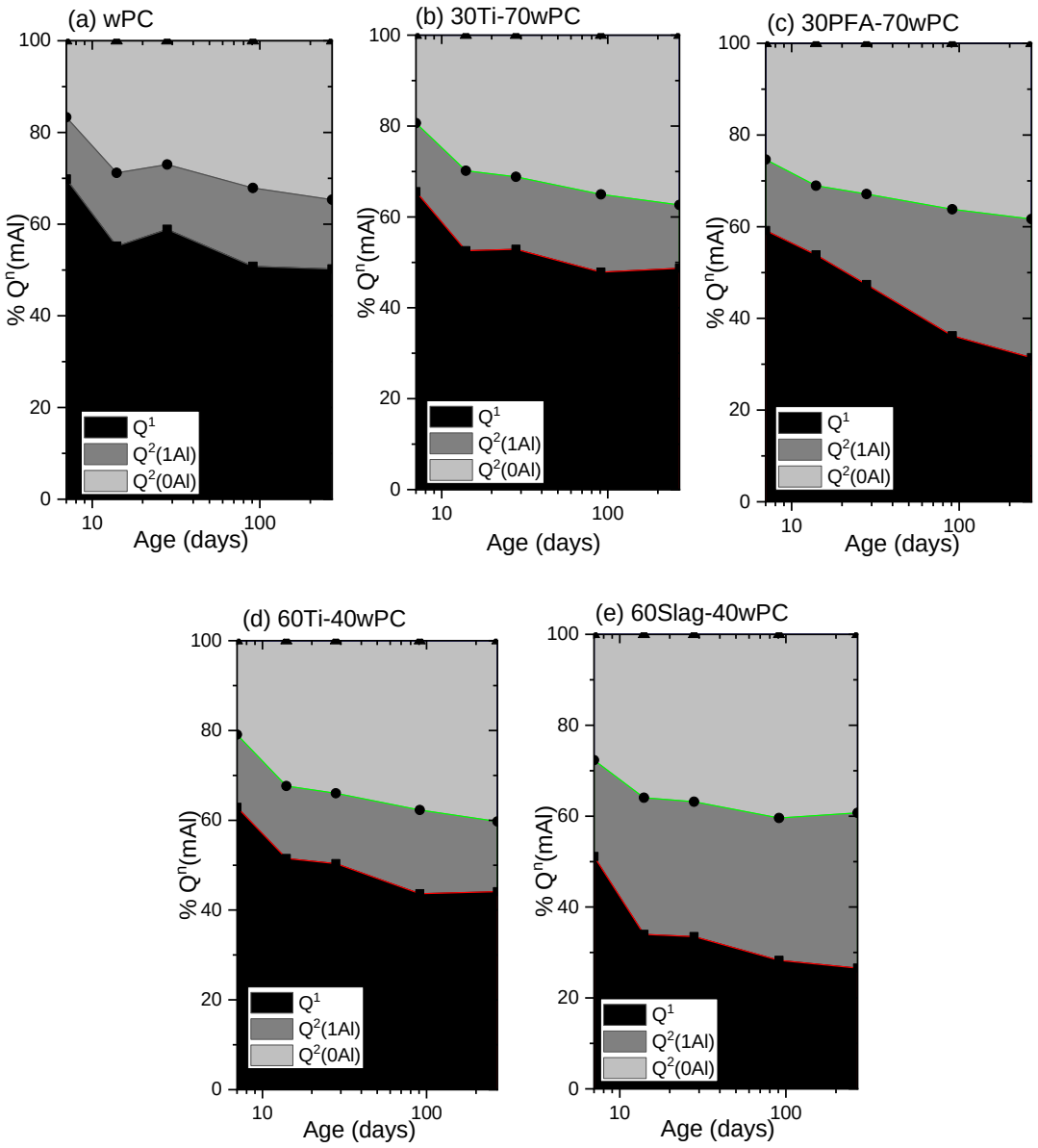

Figure 5-15 Normalized silicate species distribution of blended cements against time: (a) 270d wPC; (b) 270d 30Ti-70wPC; (c) 270d 30PFA-70wPC; (d) 270d 60Ti-40wPC; (e) 270d 60GGBS-40wPC.

Figure 5-16 shows the hydration degree of the silicate phases of clinker that are determined by NMR for different blends, against age. As expected, the inert filler (TiO_2) blends give higher hydration degree all through 7 to 270 d, which is consistent with the results of CH^{act}/CH^{exp} as shown in Figures 5-10 and 5-11. This experimental phenomenon is believed to be brought about by the 'filler effect'. Similarly, a higher hydration degree of (alite + belite) is achieved in PFA blend at 7 d, which can also be attributed to the 'filler effect'. However, slightly lower hydration degrees of PFA blends are found afterwards. The same results are found in GGBS blends throughout 7 to 270 d. The decreased hydration degree of silicate phases in PFA and GGBS

blends is plausibly related to the hydration of the glassy phases, which supplements the additional Si and Al for the formation of C-A-S-H, thus decreasing the requirements of silicate phases in clinker.

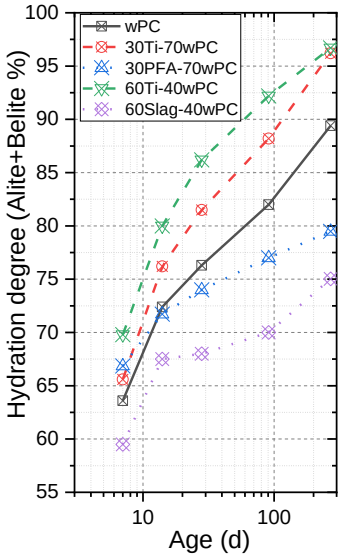

Figure 5-16 Hydration degree of silicate phases (alite + belite) of blended cements calculated through Q-NMR.

5.4.2 Nanostructure development of C-S-H gel in blended wPC

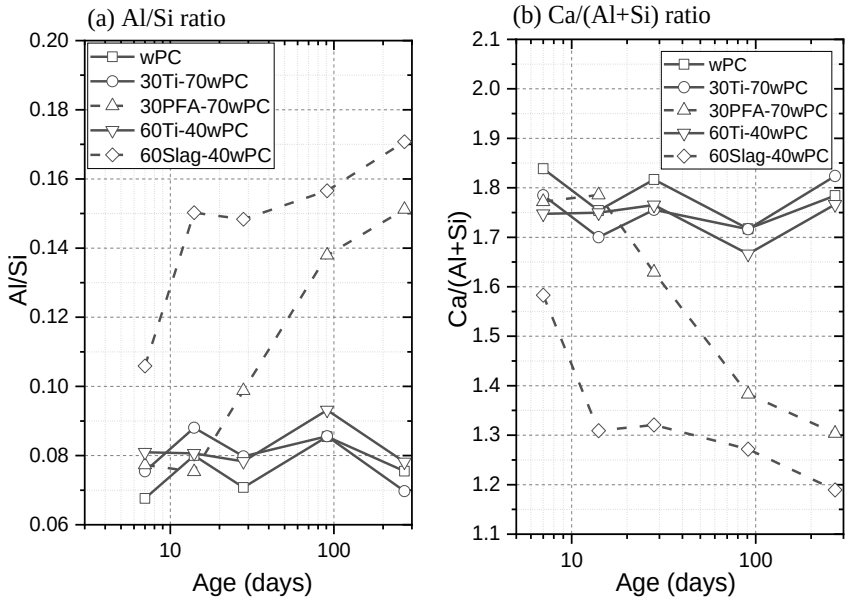

Figure 5-17 (a) Al/Si ratio (determined by NMR results) and (b) Ca/(Al+Si) ratio (calculated from universal relationship) development against time.

The increased polymerization of silicate tetrahedra results in up-field chemical shifts in NMR spectra [73]. Massive studies confirmed the chemical shift of Q^2 tetrahedra moved upfield by 6 ppm when compared to Q^1 group (≈ -79 ppm) in ^{29}Si NMR spectra [73, 85, 116, 196]. The

chemical environments of Si tetrahedra will further be affected by the replacement of Si by Al (only [78]) at bridging sites in an aluminosilicate chain, which generates a down-field chemical shift of ≈ 3-5 ppm [14, 78]. Therefore, the peak at ≈ -82 ppm in ^{29}Si MAS NMR spectra was assigned as Q^2(1Al) throughout all relative studies [3, 5, 6, 78, 90, 131]. In addition, the Al/Si ratio, calculated based on Equation 20 using the deconvolution results as assigned, is in excellent agreement with that measured by TEM (as shown in Fig. 17 in [3] and Fig. 11 in [14]).

The as-calculated Al/Si ratio from quantitative NMR of all blends are shown in Figure 5-17 (a). Unsurprisingly but more clearly, the Al/Si ratios of neat wPC and TiO_2 blends remain stable in range of ≈ 0.07~0.09, which corresponds to the stable Q^2(1Al) in Figure 5-15. The PFA and GGBS blends show a completely different development trend of Al/Si ratio in C-A-S-H. The Al/Si ratio reached > 0.10 at 7 d and rose up to ≈ 0.17, which indicates that GGBS started to react before 7 d and continuously hydrated until 270 d. The PFA blend initially possesses a comparable Al/Si ratio with neat wPC or TiO_2 blends, followed by steeply increasing to ≈ 0.15 at 270 d, which illustrates that PFA reacted mainly at the later-age. These results agree with the CH content evaluation from TG-DSC analysis in Figure 5-11, which exhibits the reaction of SCMs.

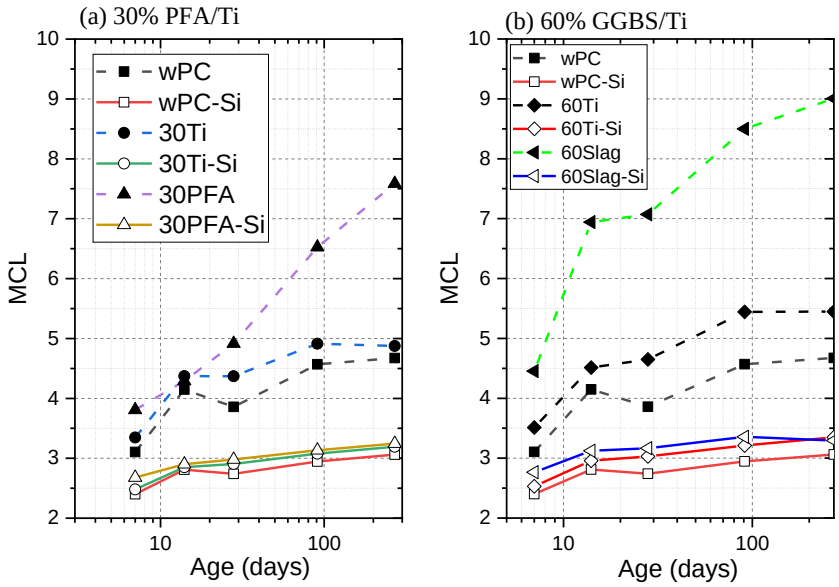

Figure 5-18 MCL and MCL_{si} of blended samples at (a) 30% replacement level and (b) 60% replacement level.

The MCL and MCL_{Si} (i. e. the silicate portions in the linear chains) of aluminosilicate chain in all blends calculated from NMR are given in Figure 5-18. A similar study on 30% PFA blend [14]

showed that the MCL increased from initial ≈ 3 before 28 d up to ≈ 12~14 after several years, whereas the C-A-S-H in the neat wPC possessed a MCL in the range of ≈ 3 before 28 d but up to only ≈ 4~5 in current study. Consistent results are obtained in the current study: (i) neat wPC has an MCL ≈ 3 at 7 d and increases to ≈ 4.5 at 270 d; (ii) TiO_2 blends show a slightly higher MCL than the neat ones, which is attributed to the higher hydration degree. In addition, the increase in MCL with hydration degree in neat wPC was also discussed by Richardson (see Fig.16 in [14]). (iii) 30% PFA blend shows a comparable MCL with neat wPC before 28 d (≈ 3-5) and then gradually increases to ≈ 7.5 at 270 d. (iv) 60% GGBS blend shows significantly higher MCL than neat wPC throughout measured ages, which is ≈ 4.5 at 7 d and then rises to ≈ 9.0 at 270 d. (v) MCL_{Si} of all samples remains close and slightly increases with age.

In general, the MCL increases with age and both Al/Ca and Si/Ca ratios [3, 6, 7, 14, 63]. The observed results also agree the previous findings. The increasing MCL is achieved by the occupation of bridging tetrahedra in the aluminosilicate chain. Therefore, the fact that all samples keep similar MCL_{Si} indicates that the increased MCL is achieved by additional Al[4] tetrahedra sites. It is evident that the bridging tetrahedra position was preferably replaced by Al[4], this is consistent with the conclusion proposed by Richardson: the Al[4] substitutes Si[4] but only in the bridging tetrahedra in the dreierketten chain [78].

Since the formation of C-S-H chains in cement systems follows the sequences of silicate dimer, pentamer, octamer … (3n-1), the insertion of 'bridging tetrahedra' (BT) plays an important role in lengthening the MCL [3, 5, 7, 53, 87, 89]. Removal of some BT in an infinite *'Dreiereinfachketten'* conformation will lead to the presence of dimer, pentamer, octamer … (3n-1) chains that are believed to mix in C-S-H gels [7, 88, 197]. The proportion of BT is shown more clearly in Figure 5-19 that from the variations of BT site occupancy factor (i. e. SOF_{BT}) with age. Apparently, SOF_{BT} of all blends increase with time but significant higher values are achieved for SCMs blends. It is evident that the $SOF_{BT}(Si)$ increases as the hydration goes on in all blends and this value is comparable with that of wPC and TiO_2 blends. The $SOF_{BT}(Si)$ is slightly higher in SCMs blends initially but reached a comparable value (≈ 0.3) to wPC or TiO_2 blends at later age (270 d). Thus, the lengthening of MCL is primarily contributed by $SOF_{BT}(Al)$ (i. e. Al[4] at BT).

This result give a better explanation of Figures 5-17 and 5-18, which suggests again the presence of Al[4] tetrahedron is the reason for longer MCL.

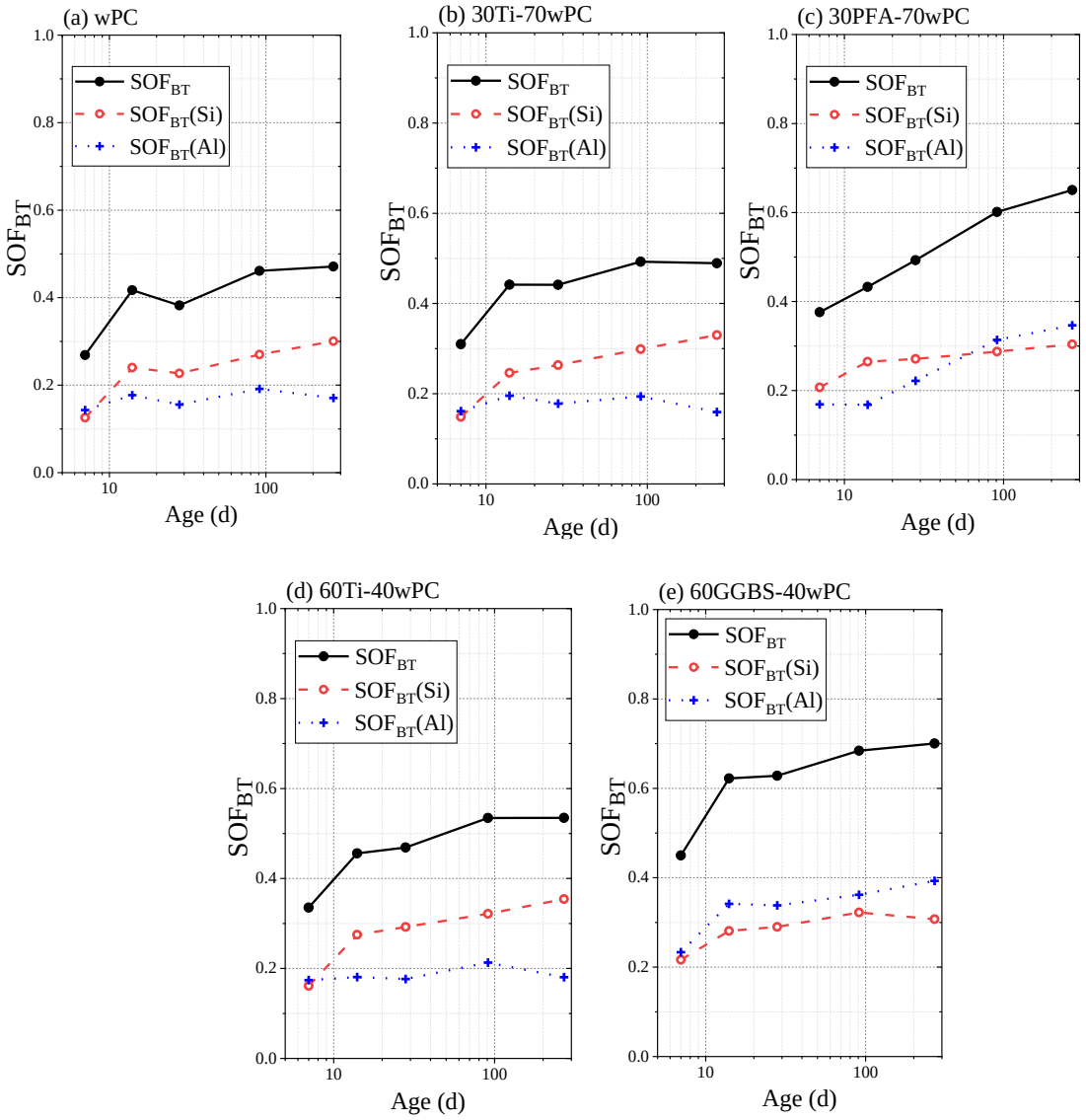

Figure 5-19 Site occupancy factor (total) for bridging sites (SOF_{BT}), site occupancy factor for bridging sites by Si^{4+} ($SOF_{BT}(Si)$) or by Al^{3+} ($SOF_{BT}(Al)$).

Figure 5-20 plots the correlations between Ca/(Si+Al) and the reciprocal MCL for C-A-S-H in all blends. The points 'C-D-E' and 'F-G-H' stand for dimer jennite and tobermorite units with the protonation level varies from maximum (w/n=2) to minimum (w/n=0). Similarly, the points 'U-V-W' and 'X-Y-Z' stand for the same meanings but for infinite chain length. Therefore, the quadrilateral area 'C-E-W-U' represents the mixture of multi-phase jennite nanostructure, whereas 'F-H-Z-X' is for tobermorite-based nanostructure [5, 53]. The main difference between

jennite and tobermorite is the way that Ca-O sublayers are ribbed between *'Dreiereinfachketten'* conformations, which results in the lower Ca/Si ratio in tobermorite units.

The results show that most points fall into the jennite-based area, which suggest a mixture of jennite-based C-A-S-H is suitable for the description of these samples. However, some SCMs blends that have longer MCL fall towards the intermediate zone between jennite- and tobermorite-based C-A-S-H structures. This finding roughly agrees with the results of the relationships in metakaolin-, PFA-, and GGBS-blends that are summarised by Richardson [14], but at earlier ages. The C-A-S-H with longer MCL tends to fall into tobermorite-based nanostructure zone 'F-H-Z-X'. It is believed that the change of morphology of C-A-S-H in water activated SCMs blends starts from the intermediate zone in this figure, which is critical for durability of concrete.

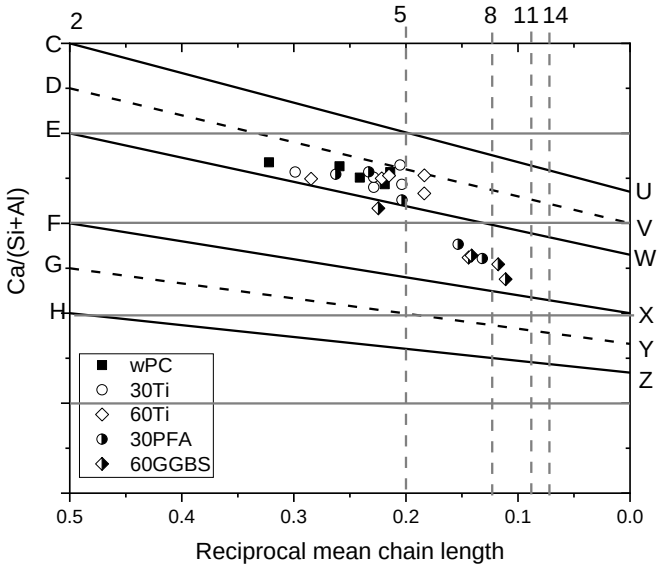

Figure 5-20 Relationships between reciprocal mean chain length and Ca/(Si+Al) ratio of blended wPC samples.

Based on the parameters above, Richardson and Groves' model (see Section 2.3) is used to express the average composition of C-A-S-H gel at different ages based on minimum protonation assumptions. The chemical-structural formula can be found in **Appendix H**.

5.5 Morphology and chemical composition of C-S-H gel in blended wPC samples

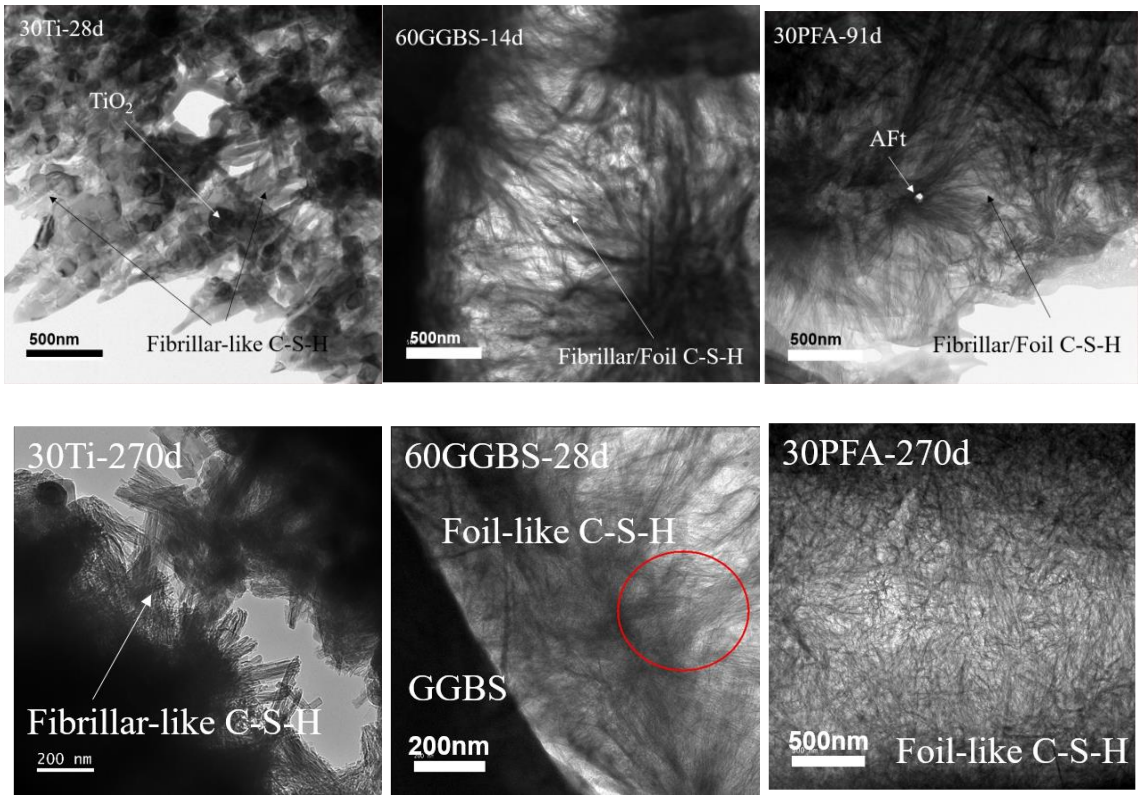

Figure 5-21 Morphology of C-S-H in different samples: 30TiO_2-70wPC at 28 and 270 d; 60GGBS-40wPC at 14 and 28 d; 30PFA-70wPC at 91 and 270 d. The TiO_2-containing samples showed unchanged C-S-H morphology until 270 d, while GGBS/PFA containing samples showed C-S-H morphology change at certain hydration degree.

Morphology of C-A-S-H shows strong correlations to the mechanical and transport properties of hardened cementitious materials [119]. Two distinct areas 'IP C-S-H and OP C-S-H' in cement samples show totally different morphology features. The IP C-S-H normally shows fine-scale and homogenous morphology in either alite or blended cements systems [5]. However, it has been discussed and summarised by Richardson that the morphology of OP C-A-S-H in GGBS-, PFA-, and metakaolin- blended cements changes from fibrillar at low Si/Ca and Al/Ca ratio to foil-like at high ratios [14], which is believed to be the reason for permeability improvement by adding these pozzolanic admixtures. Indeed, the morphology of OP C-A-S-H directly shows the capillary pores that are interlaced by these gel phases. The space constraints, fineness, and aspect ratios of these fibres define the shape, size, and amount of capillary pores [14, 119, 122, 198, 199], thus affecting the durability of structure. Therefore, the morphology change of OP C-A-S-H is the object in this study.

Figure 5-21 is the TEM images of TiO_2-, PFA, and GGBS blends at different ages. The ages selected for these SCMs (PFA-91, 270d/GGBS-14, 28d) are supposed to be the morphology change of C-A-S-H due to the secondary reaction. The bright field TEM images show that the TiO_2 blends always have a coarse fibrillar like OP C-S-H, which is the typical morphology throughout cement or alite hydration [5, 13, 119, 198]. The unchanged morphology indicates that the inert filler will not change the nature of C-S-H. The morphology of OP C-A-S-H shown in PFA and GGBS blends at the age of 91 and 14 d are similar, which is thin fibrillar-like C-S-H. The capillary pores interlaced by these fine fibres can also be identified easily. In addition, AFt relict is also found in the OP C-A-S-H in PFA blend. However, after hydrated to a certain level of each SCM, the OP C-A-S-H morphology changes to much finer/denser fibrillar and some regions change totally to foil-like. Yet not all areas appear foil-like (see GGBS blend at 28d), the fibres tends to be much finer than their early-age morphologies. The morphology at this stage is always described as 'mixed fine-fibrillar/foil-like morphology', based on the summary of multi-SCMs blends TEM images [14]. In addition, the total foil-like morphology can only be achieved by water activated 100% GGBS paste or all 5 *M* KOH (high alkali) activated neat cement or blended cement [5, 14, 90]. A TEM image example (Fig. 19 in [14]) of 30% PFA blends show that the fibrillar morphology can still be found after 1-year hydration.

The TEM morphology change is also needed to be analysed in joint with EDX data. Figures 5-22 to 5-24 summarise the TEM-EDX data of OP C-A-S-H in OPC, PFA blends, and GGBS blends from the previous studies [8, 10, 14, 43, 90, 98, 200]. Two C-S-H atomic models from T/CH or T/J points of views [5] (see Section 2.3.1) are given as the references for the distribution of TEM-EDX point analysis (Al/Ca-Si/Ca).

The experimental data that shown in these figures are outer products (OP) C-A-S-H. The other symbols stand for the compositions of tobermorite (T-) or jennite-based (J) structural units with the chain lengths of 2, 5, 8, 11, 14, 17, and ∞. Three ideal protonation (Si-O-H) levels of the silicate chains are also given: the maximum level (Si/Ca highest; w/n=0), an intermediate level (Si/Ca medium; w/n=1), and the minimum level (Si/Ca lowest; w/n=2). Most of the units (T_n and J_n) are saturated with Al at bridging sites (i. e. all bridging tetrahedra in silicate chain are AlO_4).

The exceptions include T_{11}(1Al) or T_{11}(2Al), where only 1 or 2 Al sites substitute Si tetrahedra at bridging sites (i. e. the silicate chain is not saturated with Al in this case, Al/(Al+Si)=1/11 or 2/11). The Al saturation condition should be Al/(Al+Si) = 3/11, which is labelled as T_{11}. The same meaning can be extended to different saturation levels and the T_{11} with different Al replacement content are connected by dash lines. Figures 5-22 to 5-24 show that the C-A-S-H gels present in pure wPC/OPC, PFA blends, or GGBS blends are in confirmation of T/J model (plots tend towards to J_2 unit), which means that a mixtures of T/J units can better describe the C-A-S-H phases in cement system with water activation. This is different from those in alkali-activated blends, which shows the distribution of Al/Ca-Si/Ca plots tend to lie towards origin [14].

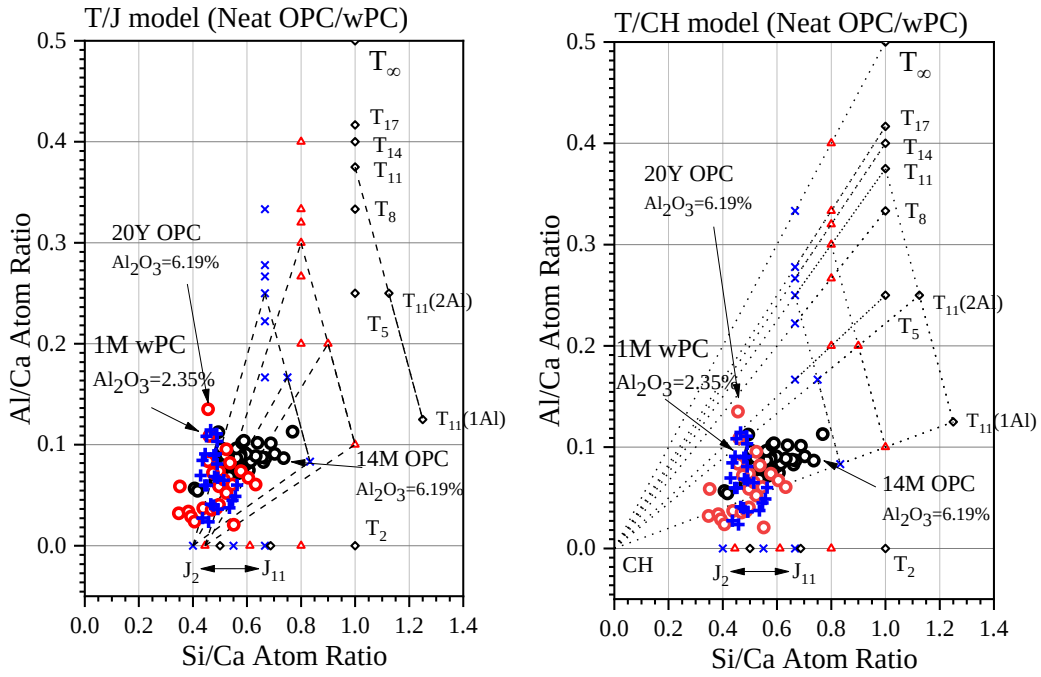

Figure 5-22 Summary of TEM-EDX data for OP C-A-S-H in wPC or OPC hydrated for 1 M (month) to 20 Y (years). The cross (blue) stands for the wPC hydrated for 1 M at 25 C; the empty circles stand for OPC hydrated for 14 M and 20Y. Although the Al_2O_3 content for OPC is 6.19% much higher when compared to that of wPC (2.35%), the Al/Si ratio did not significantly increase. Additional Al should present in Al-bearing phases such like AFt, AFm, and TAH. Data were taken from [8, 10, 200].

Figure 5-22 gives the Al/Ca-Si/Ca plots for pure wPC/OPC (without SCMs) from both T/J and T/CH approaches. These points include pure wPC and OPC hydrated from 1 month to 20 years and the Al_2O_3% content for wPC is 2.35% and for OPC is 6.19%. The circles correspond to OPC and the cross are points for wPC. As expected, the scatter points tend to move towards to J_2 unit, which are consistent with T/J model and may further be associated to fibrillar morphology [5, 14]. In addition, the Al/Ca atomic ratio of all pure cement samples remain under 0.10 regardless of

hydration time or Al content. This can be attributed to enough Ca source in this system, which allows a higher Ca/Si ratio C-S-H gel to form. Accordingly, the MCL of these C-S-H gels will not increase to a higher level and limits the insertion of Al sites. The experimental results show that the MCL of C-S-H gel in β-C_2S, OPC, and C_3S (high Ca system) are ~2.75, ~3.40, and ~3.60 hydrated for ~1 year with an average Ca/Si ratio ranges from ~1.7 to 1.9 [4]. The additional Al should be present in Al-bearing phases such like AFt, AFm, and TAH [14, 35].

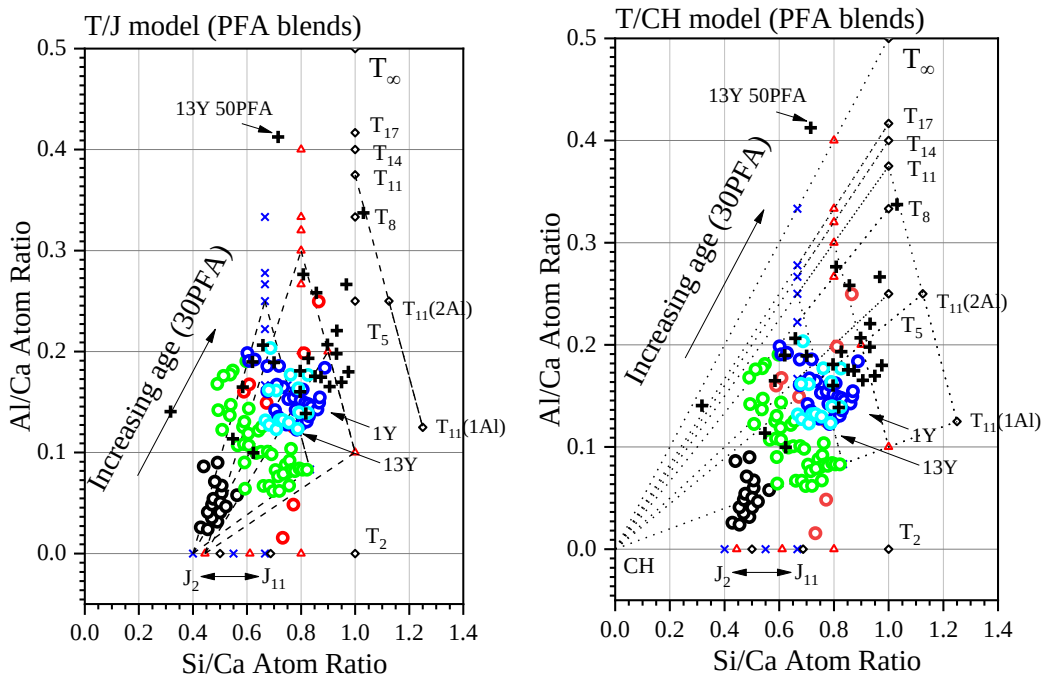

Figure 5-23 Summary of TEM-EDX data for OP C-A-S-H in PFA blends hydrated for 28 d to 13 years. The empty circles stand for 30PFA-70wPC blends hydrated for 28d, 1M, 1Y and 13Y; the black cross stands for 50PFA/50wPC hydrated for 13Y. Data were taken from [8, 12, 14]

Figure 5-23 is the Al/Ca-Si/Ca plots of OP C-A-S-H for PFA blends from T/J and T/CH points of view. These points include 30PFA-70wPC blends (empty circles) hydrated for 28 days, 1 month, 1 year, and 13 years and 50PFA-50wPC blend (black cross) hydrated for 13 years. The empty circles with different colours stand for samples with different ages. A general trend of increasing Al/Ca ratio along with Si/Ca ratio can be observed as hydration time increases in PFA blends. Also, a higher PFA content results in higher Al/Ca and Si/Ca ratios. It is clear that the EDX scatter points fit well with T/J model, especially at early age (black empty circle). However, with the extended hydration time, the points fall into the area that can be explained by both T/J and T/CH models like 30PFA blend hydrated for 1 year and 13 years. In addition, limited Al/Ca

ratio changes between 30PFA hydrated from 1 year to 13 years, which indicates the hydration degree of PFA is mostly achieved before 1 year. Another interesting finding is that the differences between the data for 30PFA blends hydrated for 28 days and 1 month, which should be similar but not. By comparing these two samples, the chemical compositions of PFA are the same, but the curing condition may cause the difference. The sample cured in a fog room at 20 ℃ [14] shows significantly lower Al/Ca ratios than that cured under stirred water bath at 25 ℃ [8], indicating a higher hydration degree of PFA was reached under a higher temperature condition. This finding was also confirmed by exposing these samples to even higher temperatures (55 and 85 ℃) [8, 98, 201, 202].

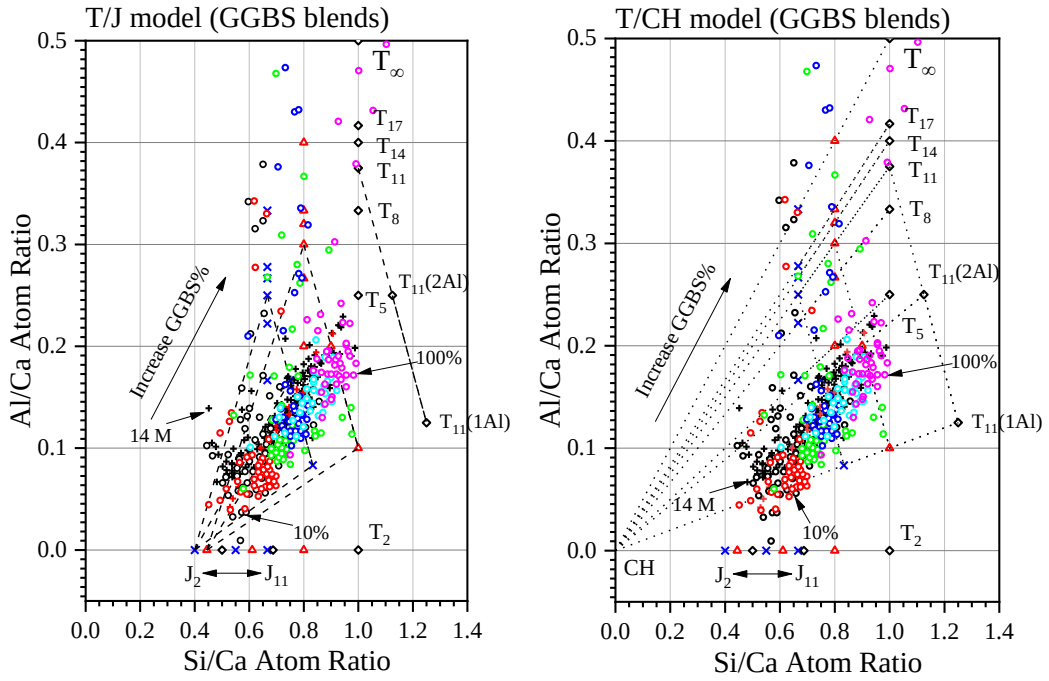

Figure 5-24 Summary of TEM-EDX data for OP C-A-S-H in GGBS blends hydrated for 14 months to 20 years. The black cross stands for the GGBS/OPC blends hydrated for 14 months; the empty circles stands for the same samples but hydrated for 20Y. The GGBS replacement levels range from 10% to 100%. Data were taken from [9, 10, 90, 131].

Summary of TEM-EDX data of GGBS blends hydrated for 14 months (average values, black cross) and 20 years (scatter points, empty circles) with GGBS loading ranging from 10% to 100% are given in Figure 5-24. Again, all data points confirmed T/J model better at lower replacement levels (<10%) and then can be explained by both T/J and T/CH models at higher levels. With the increasing content of GGBS in blends, the Al/Ca and Si/Ca ratio increase simultaneously. By comparing the TEM-EDX data in Figure 5-22 for wPC/OPC, the main reason should attribute to

the lower CaO content by increasing GGBS load which limits the combination of CaO layers in C-S-H structures. The increasing trend is not changed from 14 months to 20 years, and the Al/Ca ratio depends on the replacement levels of GGBS other than hydration time.

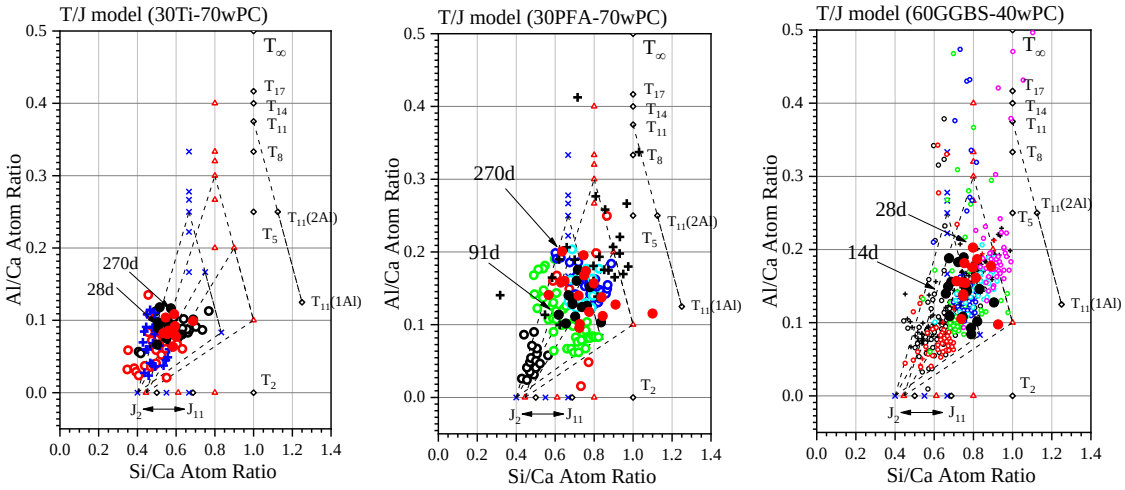

Figure 5-25 TEM-EDX data of 30TiO$_2$, 30PFA, and 60GGBS blends hydrated from 14 to 270 days on the basis of Figures 5-22 to 5-24; the black filled circles stand for short-age samples and the red ones stand for long-age samples in individual blend.

Further to the summary of existing data from previous works, the TEM-EDX experimental data of different samples are plotted in Figure 5-25 for 30Ti-70wPC, 30PFA-70wPC, and 60GGBS-40wPC blends. Meanwhile, the average compositions and standard deviation of these data are summarised in Table 5-1. The scatter data in Figure 5-25 are given based on different systems for a purpose of comparison with Figures 5-22 to 5-24, in which the black solid circles are for younger ages samples and the red solid circles are for the older ones; the smaller empty circles or cross stands for the same meaning as the previous figures. All data are plotted in T/J model due to the better explanation at the areas close to J2 structure, however, the up-field (higher Al/Ca and Si/Ca) areas are also compatible with T/CH model [10].

The TiO$_2$ blends exhibits similar Al/Ca-Si/Ca plots with that of neat wPC. The Al/Ca ratio is always lower than 0.10 and keeps stable against time. The structure of C-S-H gel in TiO$_2$ blends can be explained by the combination of T2/T5 and J2/J5, which is consistent with the MCL (≈ 3.0) as shown in Figure 5-18. For PFA blends, significant higher Al/Ca ratio is observed and this value increases with time (from 0.131 at 91 d to 0.144 at 270 d). Therefore, the structure of C-(A)-S-H falls into the area of T5/T8 and J5/J8 with minimum protonation, which agrees with the MCL (≈

6.0 ~ 8.0) for PFA blends hydrated for 91 ~ 270 days. The Al/Ca ratio for GGBS blends at 14 and 28 d are even higher than that for PFA blends due the higher replacement ratio and reactivity. The Al/Ca ratio value remains at the range of 0.10 ~ 0.20 and increases from 14 d to 28 d. Then the Al/Ca-Si/Ca plot falls into the area of T5/T8 and J5/J8 with minimum or intermediate protonation level.

Table 5-1 Chemical composition of C-A-S-H gel in blended cements from TEM-EDX analysis.

Sample/Age	Al/Si ± S.D.	Ca/(Si+Al) ± S.D.	Number of tests
30Ti-28d	0.090 ± 0.015	1.828 ± 0.121	12
30Ti-270d	0.088 ± 0.012	1.719 ± 0.105	11
30PFA-91d	0.131 ± 0.022	1.410 ± 0.109	12
30PFA-270d	0.144 ± 0.031	1.347 ± 0.201	16
60GGBS-14d	0.138 ± 0.033	1.397 ± 0.153	15
60GGBS-28d	0.156 ± 0.030	1.292 ± 0.097	13

Finally, the relationships of Al/Si or Ca/(Si+Al) ratios obtained from NMR and TEM-EDX are given in Figure 5-26. The correlation between these two ratios are also given along with the standard deviation. The black dash lines in Figure 5-26 stand for diagonal line (y=x), which are used as the guidelines for the relationship. It is clear that all data distributed along the diagonal line, indicating a good relationship between the results TEM-EDX and NMR. Similar relationship of TEM-EDX and NMR data extended to multi-SCMs/PC systems is established by Richardson [14]. Furthermore, a decreasing trend of Al/Si-Ca/(Si+Al) plot is identified in Figure 5-26 regardless of blended systems.

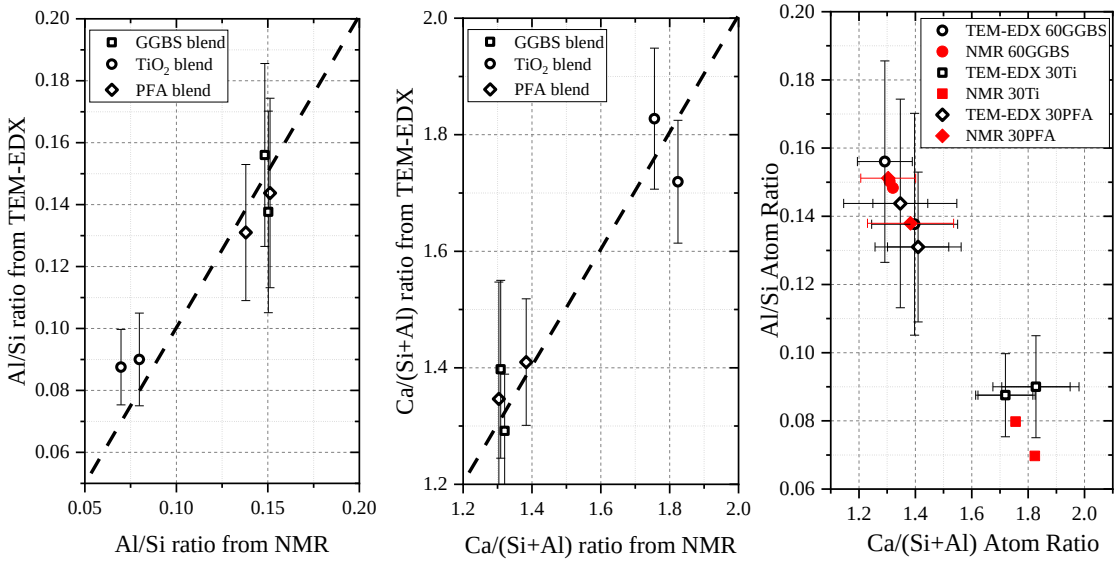

Figure 5-26 Relationships of Al/Si ratio (left), Ca/(Si+Al) ratio (middle), and Al/Si-Ca/(Si+Al) (right) calculated from NMR and TEM. The black dash lines stand for y=x function.

5.6 Pore solution analysis and thermodynamic calculations

Figure 5-27 shows the main element concentrations in pore solutions from selected blended cement pastes together with the reference lines of chemical compositions from CEM I pore solutions [147]. Since the ICP-OES mainly gives the element concentrations, the following chemical symbols are elements instead of ions. The Na and K concentrations are crucial for the maintenance of alkalinity of the pore solution but depend mostly on the original chemical compositions of cement. Figure 5-27(a)-(b) show that the Na and K concentrations in the current study are lower than the reference CEM I sample. The reason should attribute to the lower N_2O% and K_2O% contents (0.249 wt.% and 0.087 wt.%) of starting wPC when compared to those of CEM I (0.20-0.31 wt.% and 0.76-1.03 wt.%) [147]. As expected, the addition of SCMs results a lower Na/K concentration, which should be attributed to some of them being charge-balanced in C-A-S-H structure. Nevertheless, the trend of increasing Na/K concentration against time that results from the increasing hydration degree are undoubtful.

The Ca concentration in pore solution is highly dependent on its counterpart-silicate groups ($H_xSiO_4^{(4-x)}$) and hydroxide ions (OH^-). In most cases, the long-term pore solution remains a low Ca concentration below 10 mmol/L as shown in most previous studies [15, 25, 33, 36, 47-49, 147, 148, 203], however, in the cement pore solution (wPC) with low pH value, this concentration can reach ~ 30 mmol/L and then stabilise at ~ 10 mmol/L [33, 148]. The data of the pore solution in wPC in this study fall between ~ 1 and 10 mmol/L. These values are slightly higher than that of ordinary PC but lower than the wPC in Ref. [33, 148]. The reason should still attribute to the alkali content of starting cements, where the high Ca concentration is achieved by 0.13 wt.% N_2O and 0.02 wt.% K_2O in starting wPC [33, 148]. The general trend of decreasing Ca is identified, which is attributed to the increased alkali concentrations.

The Al concentration is really hard to detect due to the lower content of C_3A present in wPC (2.089 wt.% Al_2O_3) and the high stability of Al/S-bearing phases [17]. Therefore, the Al concentration remains fairly low at ~ 0.1 mmol/L and shows a stable trend against time. The addition of GGBS gives a higher concentration of Al.

The Si concentration is crucial for the stability of C-S-H, which is a counterpart to Ca in the pore solutions. The slight increase in the trend can be confirmed, which is opposite to that of Ca concentration as expected [164, 204]. Moreover, the addition of SCMs will increase the Si concentration.

Finally, the hydroxide ions (OH^-) concentration obtained from the pH values increases as the hydration goes on. This is because the hydration will continuously release the alkali-ions that are boned in the clinker phases. Therefore, the OH- should roughly be charge-balanced with that of the sum of free Na and K concentrations. In addition, the increased alkalinity will react upon Ca concentrations. The relatively lower OH^- concentration when compared to that of CEM I also results from the lower alkali content in starting cement.

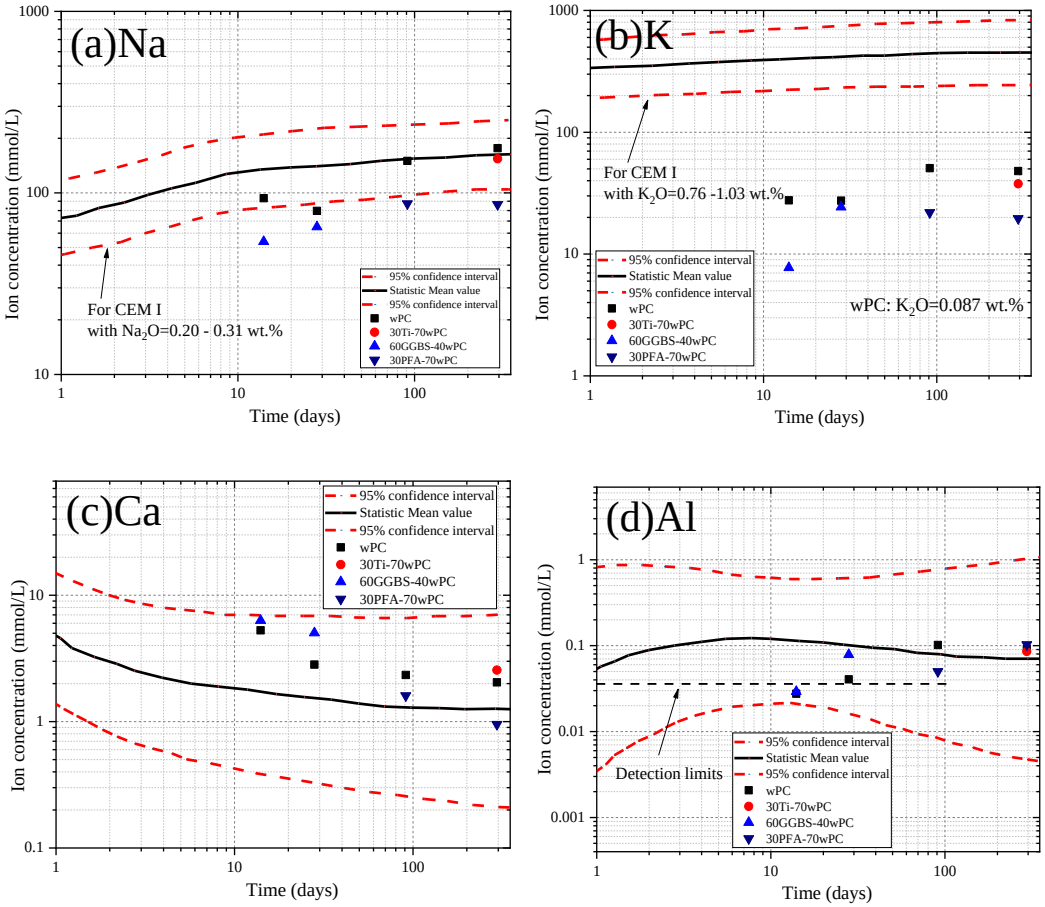

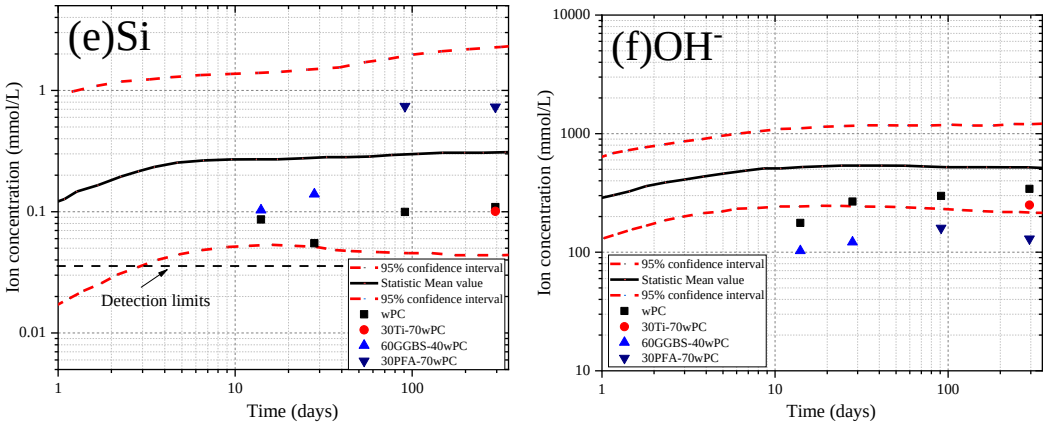

Figure 5-27 Chemical composition of pore solution from blended cement pastes: (a) Na; (b) K; (c) Ca; (d) Al; (e) Si; and (f) hydroxide ion. The concentrations of hydroxide ion refer to the free concentrations based on the measured pH values [25, 47, 49, 205]. The black solid line in each figure stands for the average concentration of individual ion (element) in CEM I system and the red dash lines stand for the 95% confidence interval as summarised by Vollpracht et. al [147], which is used for comparison.

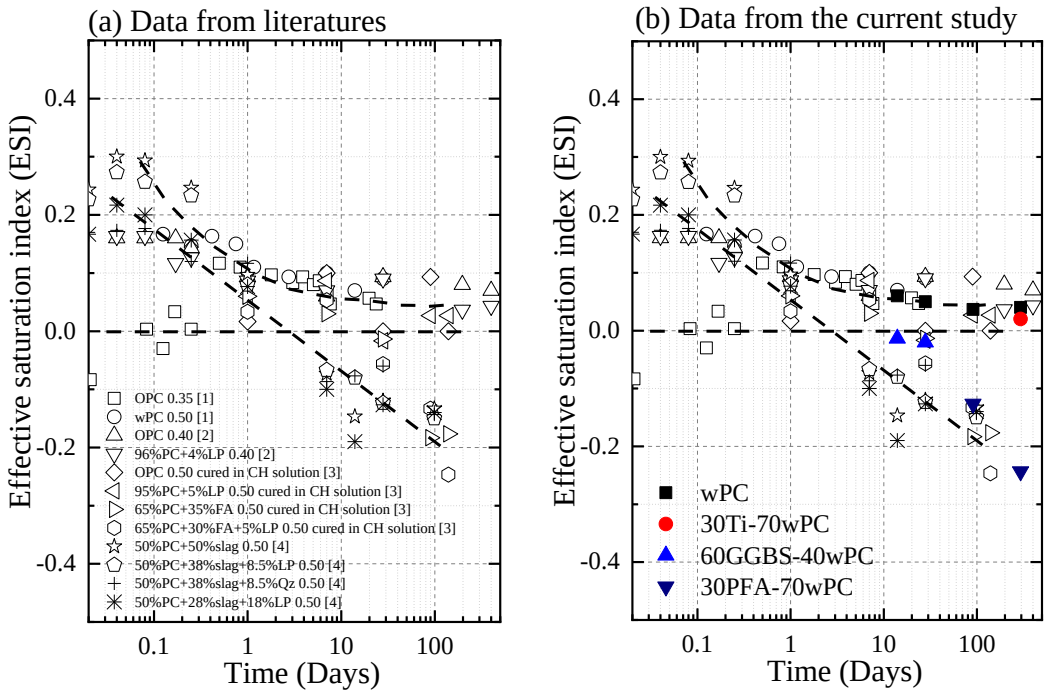

Figure 5-28 Effective saturation index (ESI) of CH in different pure cements or blended cements: (a) data from literatures (empty symbols) and (b) data from the current study (solid symbols). The references [1-4] shown in this figure stands for Refs. [20, 25, 148, 206]. The following discussions are also based on these data.

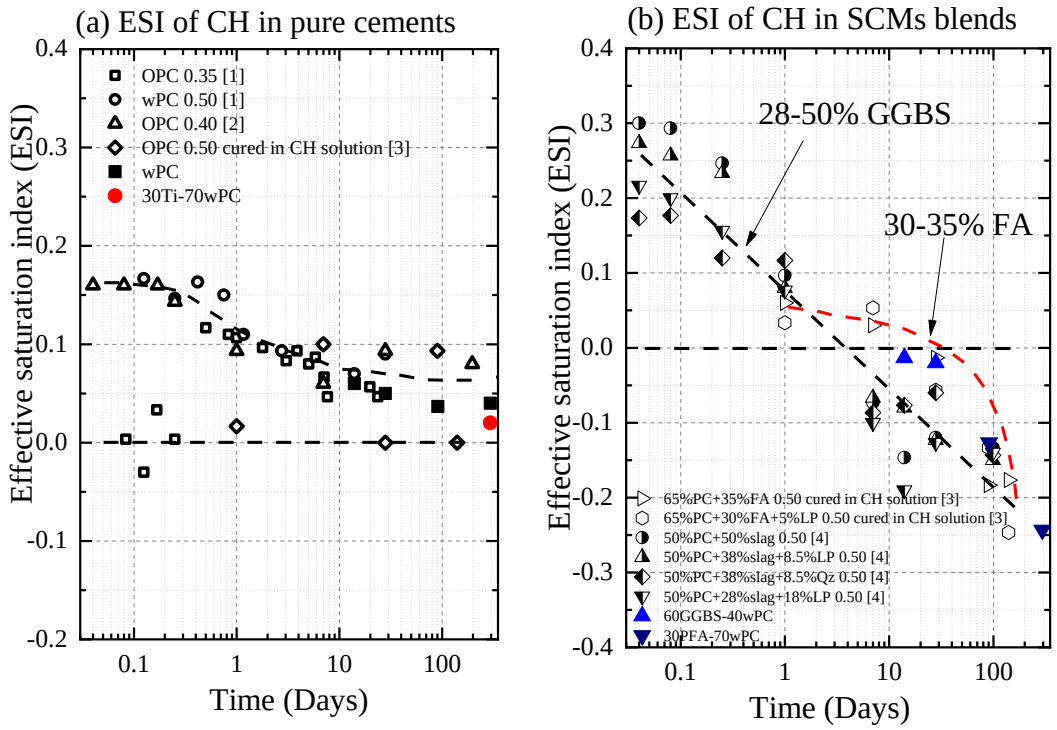

Figure 5-29 ESI of CH for (a) pure cement systems and (b) SCMs blended cements. The data points are the same as Figure 5-27 but separated into two different systems for a clearer view.

Figures 5-28 and 5-29 show the ESI values of CH in both pure cement systems and blended cements. Clearly, all the ESI values trend to two directions as shown in Figure 5-28. These trends become clearer when separating the pure and the blended cement systems as shown in Figure 5-29. The general trend of ESI-CH seen in pure cement system starts at ~ 0.15 and then stabilises at ~ 0.05. The values steeply drop between 0.2 ~ 1 d and then gradually decrease until around 10 d. The experimental values (filled symbols) fall on the stable line after 10 d. On contrast, the SCMs-contained samples have the ESI-CH values that change from positive to negative at long age as shown in Figure 5-29(b). The GGBS-containing samples show a higher ESI-CH value than that of pure cement before 1 d, which should attribute to the initial low pH value of the pore solution that results in a higher Ca concentration. However, as the hydration goes on, this value drops quickly below zero, showing that the continuous consumption of CH happens in such systems. The general tendency gives a linear decrease trend against time. It should be noticed that the ESI-CH values at 14 and 28 d are lower than zero, which is associated with changed morphology (from fibrillar/foil mixture to fine-fibrillar/foil) of C-S-H gels in the system. The black dash-line suggests that the ESI-CH drops down to -0.15 at around 28 d.

Unlike the ESI-CH values in GGBS blends, those in PFA blends stay positive before ~ 40 d as shown by the red dash line in Figure 5-29(b). Similarly, this trend suggests that -0.15 may be the critical value of the morphology change discussed in Section 5.5.

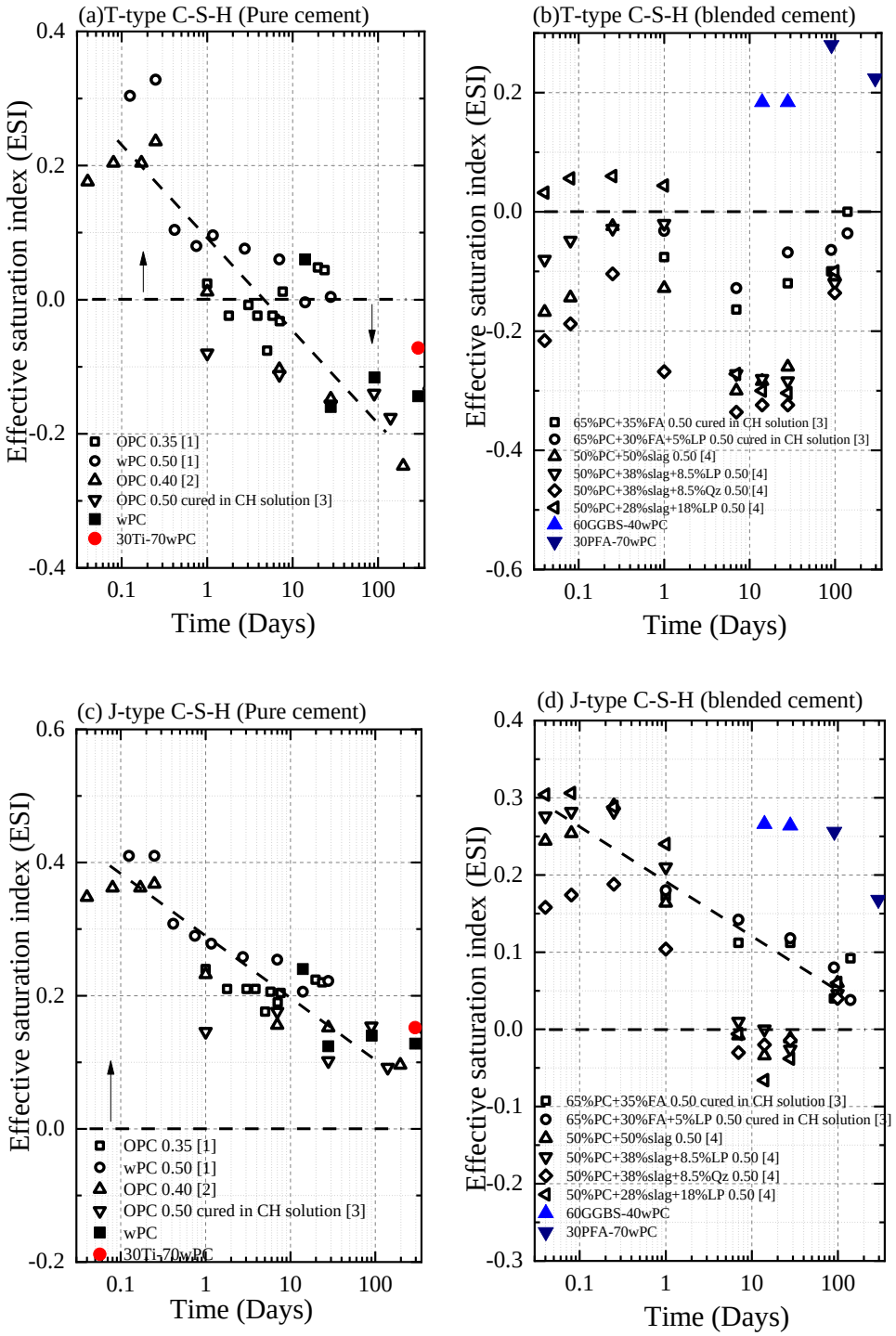

Figure 5-30 ESI of different C-S-H gels in pure or blended cements: (a) T-type C-S-H in pure cement; (b) T-type C-S-H in blended cements; (c) J-type C-S-H in pure cement; (d) J-type C-S-H in blended cements. The T-type stands for tobermorite type C-S-H (Ca/Si ratio = 0.83) and the J-type stands for jennite type C-S-H (Ca/Si ratio=1.67) [15].

Figure 5-30 gives the ESI values of T/J-type C-S-H gels (that described in Refs. [25] in the database named cemdata2007) in both pure and blended cement systems. The equilibrium of C-S-H gel depends on the Ca, Si, and OH^- concentrations in the pore solution. For the T-based C-S-H, the higher Ca and OH- concentrations will result in a lower IAP (ionic activity product) value and thus a lower ESI value. The decreasing trend of ESI-T-C-S-H can be confirmed in pure cement system, which results from the increased pH values of pore solutions. However, for the blended cements, the lower pH values and possible higher Si concentration will maintain a relative higher ESI-T-C-S-H values than that of pure cements. However, no significant trend can be identified from the current values. The experimental data from the current study support that the presence of T-based C-S-H in the blended systems. Figure 5-30 (c)-(d) give the same information but for J-based C-S-H in both systems. Unlike T-based C-S-H, the higher Ca, Si, and OH- concentrations will result a higher IAP and thus a higher ESI value. Therefore, the decreasing trend of ESI-J-C-S-H must result from the decreasing Ca concentration against time in pore solution. Similar deceasing trends can be plotted in both pure and blended systems in range of 0.1 ~ 0.4 and 0 ~ 0.3 respectively. Some of these values even fall below zero. However, the data in this study gives a relatively higher value, which may be due to the lower pH values by using wPC. One possible link between the morphology-change and the ESI of C-S-H gels may be that the fine-fibrillar/foil-like morphology is associated to the ESI-J-C-S-H < 0.1.

5.7 Discussions on relationships the nature of C-S-H and the solution environment in wPC systems

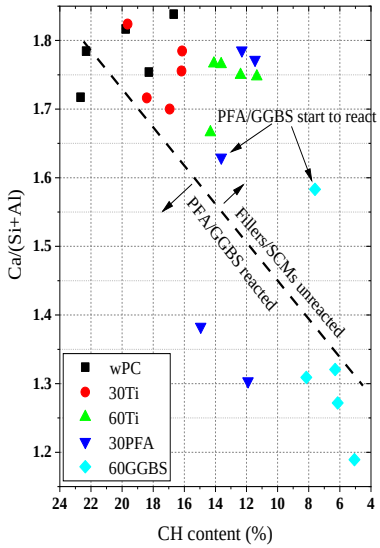

Figure 5-31 Relationship between CH content (%) and the Ca/(Si+Al) of C-S-H gels that calculated from ^{29}Si MAS NMR.

C-S-H morphology vs. solid phase composition-one of the most important solid phases that in wPC systems is CH, which is continuously consumed by the secondary reactions of SCMs. Firstly, the evidence of fibrillar C-S-H morphology in TiO_2-blends shows that the absolute CH content in the system is not the direct factor that affects the morphology-change from fibrillar to foil. On the other hand, the CH^{act}/CH^{exp} can be a reliable factor, which gives the information of the levels of CH that is consumed by SCMs in the system. The critical value of morphology-change should be around 0.85 in both PFA and GGBS blends, which is same to that found in previous research [14].

Figure 5-31 shows the changes of Ca/(Si+Al) ratio of C-S-H against CH content in the system. It is clear that the Ca/(Si+Al) ratio of C-S-H gel remains at 1.7 ~ 1.9 in pure wPC system, however, the CH content consciously increase as the hydration goes on. Similar conclusion can also be identified in TiO_2-blends. In SCMs blends, a decreasing Ca/(Si+Al) ratio against CH content can be observed. The black dash line plots the general trend as a guide for the eye. The points above this line should be the time that fillers/SCMs are limited reacted, whilst those below the dash line should be the consumptions of SCMs by reacting with CH. Therefore, a negative correlation between Ca/(Si+Al) ratio and CH content should only be found in the blended systems (as shown in Fig. 24 in Ref. [14]).

In addition, the DoH of clinker shows no direct influence on the morphology-change of C-S-H gel as shown in Figure 5-16. The DoH of SCMs do affects the morphology-change, however, it depends on the replacement ratio, activity, and chemical compositions of the SCM used. Figure 5-32 (a) gives the DoH of PFA and GGBS in the blends from NMR (but ignoring the sideband), which shows no universal relationships can be linked to the morphological change. In addition, the odd DoH at 91 d was affected by the sideband effect of PFA, which resulted in the experimental error.

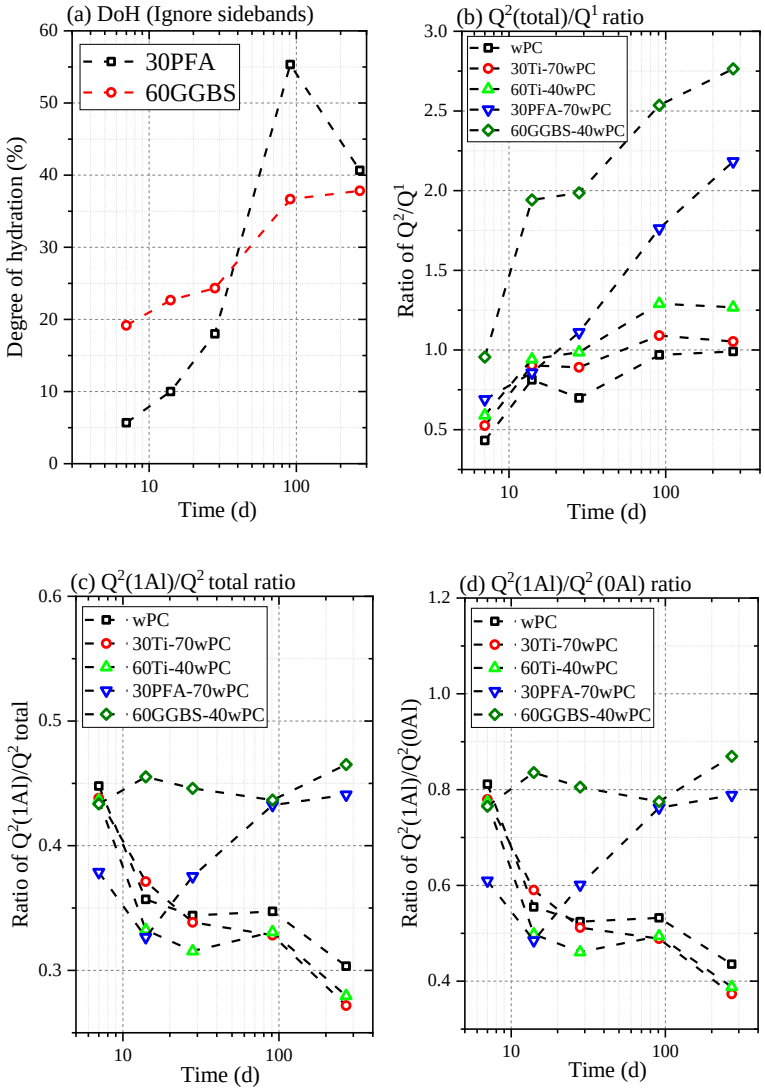

Figure 5-32 Further information calculated from ^{29}Si MAS NMR: (a) hydration degree of SCMs (ignoring the sidebands, which will result a lower value than expected); (b) Q^2(total)/Q^1 ratio; (c) Q^2(1Al)/Q^2(total) ratio (proportion of Q^2(1Al) units in all Q^2 units); and (d) Q^2(1Al)/Q^2(0Al).

C-S-H morphology vs. its nanostructure-as shown by the experimental observations given in Sections 5.4-5.5, the nanostructure of C-S-H shows crucial effects on its morphology. Firstly, the

foil-like morphology is linked with the MCL ≈ 7 ~ 8, with the average Ca/(Si+Al) ratio < 1.30 and the Al/Si > 0.15. It is well known that the morphology of C-S-H depends on the aspect ratio of these fibres [5, 14]. Therefore, it is speculated that the longer MCL will give a higher aspect ratio and thus exhibit a much finer morphology. Meanwhile, the $Q^2(1Al)$ plays an important role in the changing of MCL that associated with the morphology-change. It is found that $Q^2(1Al)$ > 30% is the critical value for changing. Figure 5-32 shows some further comparison of $Q^2(1Al)$ and other Q^2 units, which gives more parameters related to the above value. Specifically, $Q^2(total)/Q^1$ ratio > 2.0, $Q^2(1Al)/ Q^2(total)$ > 0.45, and $Q^2(1Al)/ Q^2(0Al)$ > 0.80 are three related parameters that affect the morphology-change. In addition, the SOF factors can also be used as then indicator for morphology change when SOF_{BT} > 0.60 or $SOF_{BT}(Al)$ > 0.30.

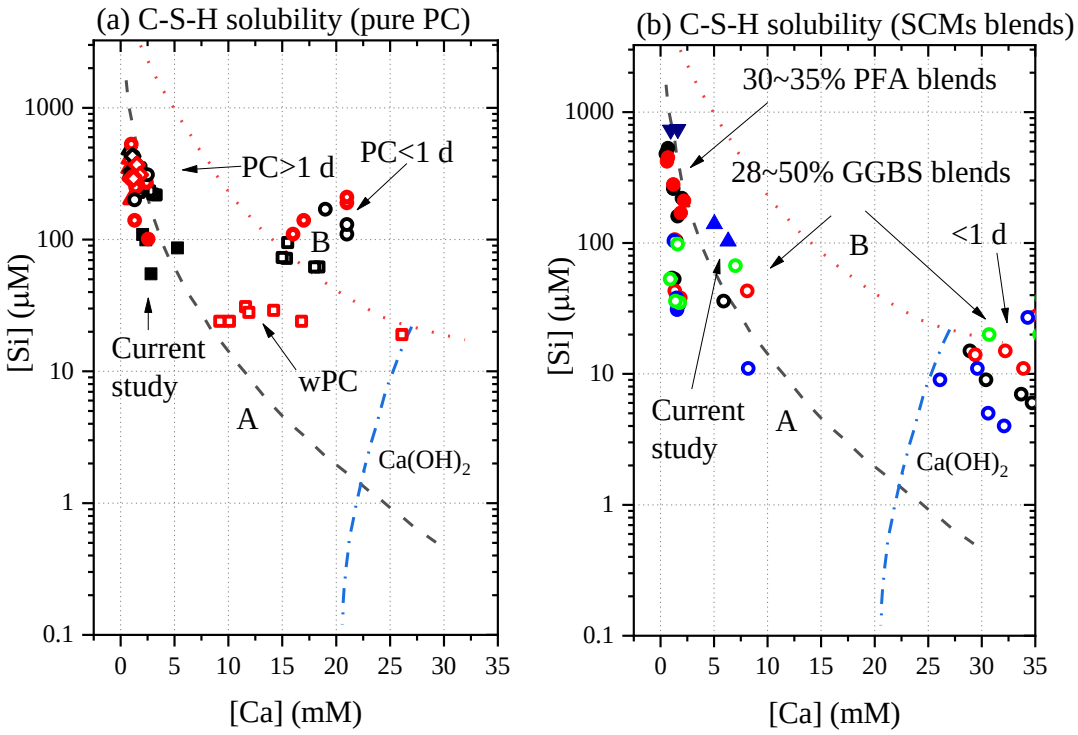

Figure 5-33 C-S-H gel equilibrium in cement systems from literatures (empty circles and the black/red filled circles) and the current study: (a) in pure cement system (the red filled circle is 30Ti-70wPC-270d and the black filled squares are pure wPC); and (b) in blended cements (the blue filled up-triangles are 60GGBS-40wPC and the navy-blue filled down-triangles are 30PFA-70wPC).

C-S-H morphology vs. pore solution composition-Figure 5-33 shows the equilibrium curves of two types of C-S-H gels as summarised by Jennings [164]. Curve A is believed to link with the metastable solubility curve of C-S-H (I), whilst Curve B is associated with a structurally distinct C-S-H that forms from C_3S or exists in an aqueous environment without a diffusion barrier [164].

Figure 5-33(a) shows that all the solution data that hydrated less than 1 d fall on Curve B, whilst those hydrated for longer time fall on Curve A. The exceptions are wPC with extreme low alkali content (0.13 wt.% Na_2O and 0.02 wt.% K_2O [148]), which allows a higher Ca concentration can be achieved. It is plausible that the diffusion barrier (C-S-H) are not enough during the early-age hydration, which results the equilibrium of C-S-H before 1 d fall on Curve B.

For the blended cements as shown in Figure 5-33(b), the long-term data fall on Curve A again but with the possible trend of a higher Ca concentration in GGBS blends and a lower Ca concentration in PFA blends. The data from GGBS blends hydrated less than 1 d fall on Curve B again but tend to the area of higher Ca concentration. The NMR data show that the transformation of nanostructure in C-S-H, however, two cluster data (pure/blend cements) still fall on Curve A. This result suggests that the Curve A may be associated with the stable C-S-H, which is not only the tobermorite-based structure. The Curve B may be linked with the instable C-S-H or in an aqueous solution without enough diffusion barrier (stable C-S-H).

The C-S-H morphology-change cannot be easily distinguished through the C-S-H equilibrium curves. However, two thermodynamic parameters that are associated with CH and C-S-H gel show the possible link with the morphology-change. The data in Section 5.6 suggest that the foil-like morphology may be linked with the ESI-CH < -0.15 and the ESI of J-based C-S-H < 0.1.

5.8 Summary

The morphological change of C-S-H gel in blended cements are investigated. Two SCMs (PFA, GGBS) and one inert filler (TiO_2) are selected to mix with wPC to produce the blended cements. It is found that the morphology C-A-S-H in SCMs blended cements change from thin fibrillar-like to mixed fine-fibrillar/foil-like, whilst those in pure or inert-filler blended cements remain coarse fibrillar throughout hydration. Both solid and liquid phases are characterised by multiple techniques to explain the reasons of morphology changing. The main links between these phenomena are summarised as follows:

(a) The morphology-change happens in 60%GGBS blends within 14 ~ 28 d and in 30%PFA blends within 91 ~ 270 d;

(b) The C-S-H morphology-change is dominated by its chemical composition, nanostructure, and solution environment;

(c) The morphology-change happens when CH^{act}/CH^{exp} < 0.85 in the solid phase of cement systems;

(d) The foil-like morphology appears when the C-S-H gels show the following characteristics: Ca/(Si+Al) ratio < 1.3 and Al/Si ratio > 0.15; the MCL ≈ 7 ~ 8; the SOF_{BT} > 0.6 or SOF_{BT}(Al) > 0.3; the proportion of Q^2(1Al) > 30%; Q^2(total)/Q^1 ratio > 2.0; Q^2(1Al)/ Q^2(total) ratio > 0.45; Q^2(1Al)/ Q^2(0Al) ratio > 0.80;

(e) The foil-like morphology appears when the pore solutions show the following characteristics: ESI of CH < -0.15 and ESI of J-based C-S-H gel < 0.1;

(f) The DoH of clinker and the absolute CH content are not the direct factors that related to foil-like morphology C-S-H; The DoH of SCMs depends on their replacement ratio, activity, and chemical compositions.

Chapter 6

Morphology-structural change of C-S-H gel during early-age hydration of alite

As shown by the results in SCMs modified wPC, the morphology of C-S-H gel changed possibly with its structural conformation, phase assemblage in the matrix, and the solution environment. The major clinker phase presented in cement is alite, which is impure C_3S with additional ions substitute Ca ions in the crystal lattice. The hydration of alite will form C-S-H gel with an average Ca/Si ratio of 1.75 and crystalline CH [14]. The OP C-S-H formed in pure alite paste after 1 d hydration is fibrillar-like [99, 126], 'honeycomb' like [207, 208] or lath radiating shape particles [198]. However, the very early age particles (several hours hydration) always exhibit crinkled foils [198], flakes (type E) [208], or foil-like [120, 208]. All these morphologies can be well-distinguished by two terminologies in TEM observations as 'foil-like' and 'fibrillar-like' by Groves and Richardson [5, 99, 126] or as 'foils' and 'fibres' by Grudemo [119]. Grudemo also pointed out the morphological change from 'foils' to 'fibres' is corresponding to the 'low' to 'high' Ca/Si ratio based on the TEM studies on C-S-H. This conclusion is identified in Chapter 5 or summarised by Richardson in Ref. [14] in blended cements. Additionally, the relationship of the solution environmental change would possibly affect the morphological variations of C-S-H gel during alite hydration.

This Chapter examines the mineralogical evaluations, morphological changes, and nanostructure of C-S-H during alite hydration. Meanwhile, thermodynamic-focused dissolution and precipitation behaviours of alite [149, 154, 157] and C-S-H gel [158] are also discussed based on the changes of solution environment during hydration. For a better understanding of the dissolution associated physicochemical changes and extend the undersaturation period of CH phase, a w/s ratio of 10 was used throughout experiments.

6.1 Phases evaluation through XRD, STA and FTIR

The phase assemblages during alite hydration are examined by (Q)XRD, TG-DSC, and FTIR. Figure 6-1 shows the XRD patterns of alite hydrated from 5 min to 24 h under a constant w/s ratio of 10. The CH peak in this pattern is enlarged on the right side of Figure 6-1. Clearly, CH firstly appears at 6 h and increased content is confirmed as the hydration goes on. The reduction of main silicate peak between 30-35 ° 2θ can also be identified. Meanwhile, two QXRD fitting examples are given in Figure 6-2, which are used for calculation of alite and CH contents in the system and further used for the estimation of hydration speed and degree of alite.

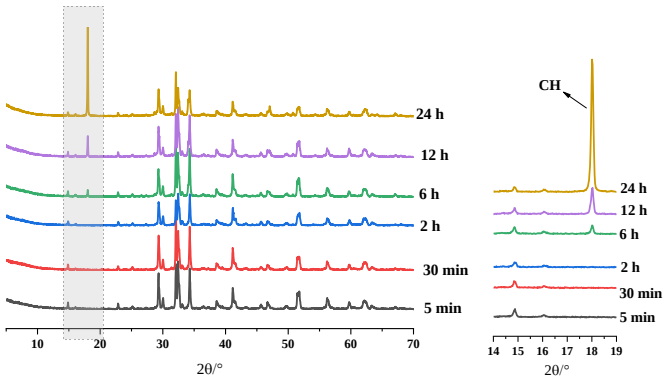

Figure 6-1 XRD patterns (left) and a close look at CH peak (right) of alite during 24 h hydration.

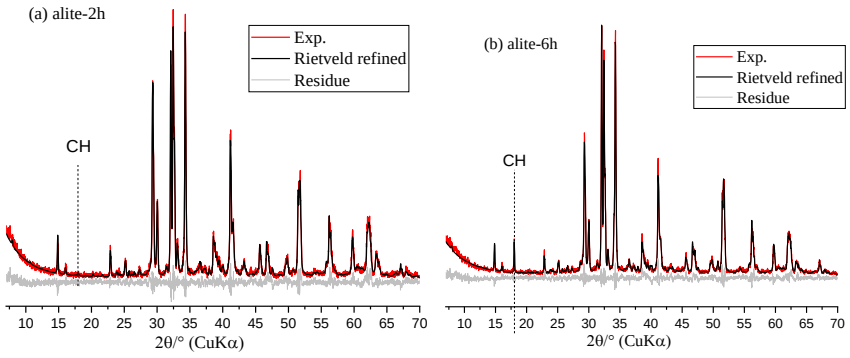

Figure 6-2 Examples of QXRD fitting: (a) alite hydrated for 2h and (b) alite hydrated for 6 h.

Figure 6-3 gives the TG-DSC analysis of hydrated alite samples. The peak at around 400 ~ 450 °C is identified as the dehydration of CH. Again, the CH appears firstly at 6 h, which is consistent with XRD results. The corresponding endothermic peak of CH is also shown in DSC curves. More importantly, the chemically combined water, which is supposed to present in C-S-H phase, increases significantly with hydration. These specific CH and water content are quantified using the same method mentioned in Section 3.1.2 and further used for the calculation of

hydration degree (DoH) of alite. The quantification of DoH using CH content is based on assumption of the average Ca/Si ratio of C-S-H is 1.75 and water molecules in a C-S-H unit is 4.0 (which corresponding to 90% RH), thus the mass percentage of CH in a fully hydrated C_3S paste is 28.7% [14]; that using water content is based on a model proposed by Wang, where concluded that 1 g hydrated C_3S will generate 0.236 g bounded water [134, 209].

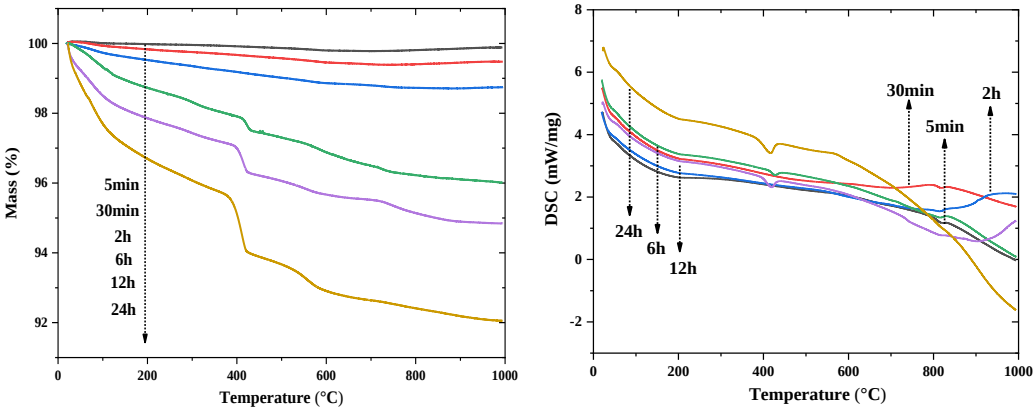

Figure 6-3 TG (left) and DSC (right) results of alite during 24h hydration.

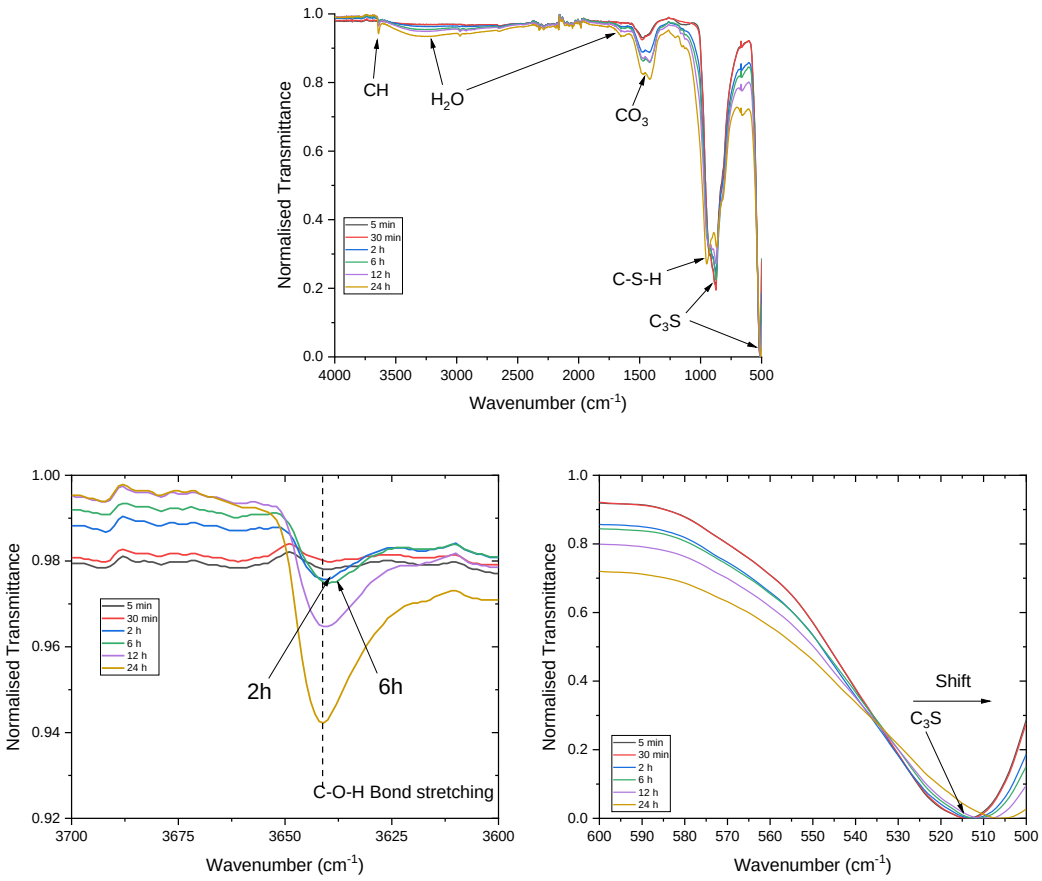

Figure 6-4. FTIR analysis of alite during 24h hydration, the upper figure shows the spectrum in the range of 500-4000 cm^{-1}, the lower ones show the spectra in the range of 3600-3700 cm^{-1} and 500-600 cm^{-1}.

The same alite samples are tested by FTIR and the normalised transmittance results lie between 500 and 4000 cm^{-1} are shown in Figure 6-4. Clearly, the significant peaks at 512 cm^{-1} and other peaks in range of 800 ~ 1000 cm^{-1} are due to the Si-O bonds that presented in alite silicate tetrahedra [210, 211]. The C-S-H characteristic peaks that associated to simultaneously Si-O stretching and Si-OH bending modes are overlapped under 900-1200 cm^{-1} and at 1350 cm^{-1} [210], which become more evident after 24 h hydration. The υ_2 H_2O peak at 1640-1650 cm^{-1} and (υ_1+υ_3) H_2O peak at 3250 ~ 3500 cm^{-1} become more significant as hydration goes on, which indicates more water molecules are combined during hydration and is consistent with TG-DSC results shown in Figure 6-3. Interestingly, some carbonate groups (υ_3 C-O) are also shown in samples and accumulated against time at 1400 ~ 1500 cm^{-1} [210-212]. The FTIR is very sensitive the symmetry stretching like carbonate group, thus other than carbonation, the adsorption of CO_2 from the air will also generate this signal [213]. The other peak that associated to the Ca-OH stretching that related to CH is identified at around 3640 cm^{-1} [210, 211].

Two enlarged parts, focusing on the range of 500 ~ 600 and 3600 ~ 3700 cm^{-1} are also given in Figure 6-4, which provide a closer look at alite and CH peaks. A slight shifting towards to near-field happened to alite peak, indicating the dissolution of alite and precipitation of C-S-H. The Ca-OH peak firstly appears at 2 h then remains quite similar at 6 h. This seems to be controversial when compared with TG or XRD results. However, the Ca-OH stretching signal can appear when only the precursor of CH mineralization process forms, for example, the formation of $CaOH^+$ in the solution [15, 175]. Therefore, the existing of Ca-OH signal during early age hydration of cementitious materials cannot be used as the indicator for CH formation.

Figure 6-5(a) summarises the phase evaluation (i. e. alite residue) determined by QXRD and TG. At the very beginning of hydration (first 2 h), the alite remains almost unchanged from the quantity of CH, but consumes around 10% according to chemically combined water calculation. The reason is possibly due to the superficially hydroxylated surface on alite [63, 87, 105, 175]. Furthermore, the average alite residue is given in Figure 6-5(b) accompanied with the logistic function fitting to describe the whole process, which was further use in the calculation of the DoH and the corresponding reaction rate of alite (as shown in Figure 6-5(c)). The simulated results

illustrate that CH firstly appears in the range of deceleration period, which agrees the results in Ref. [28].

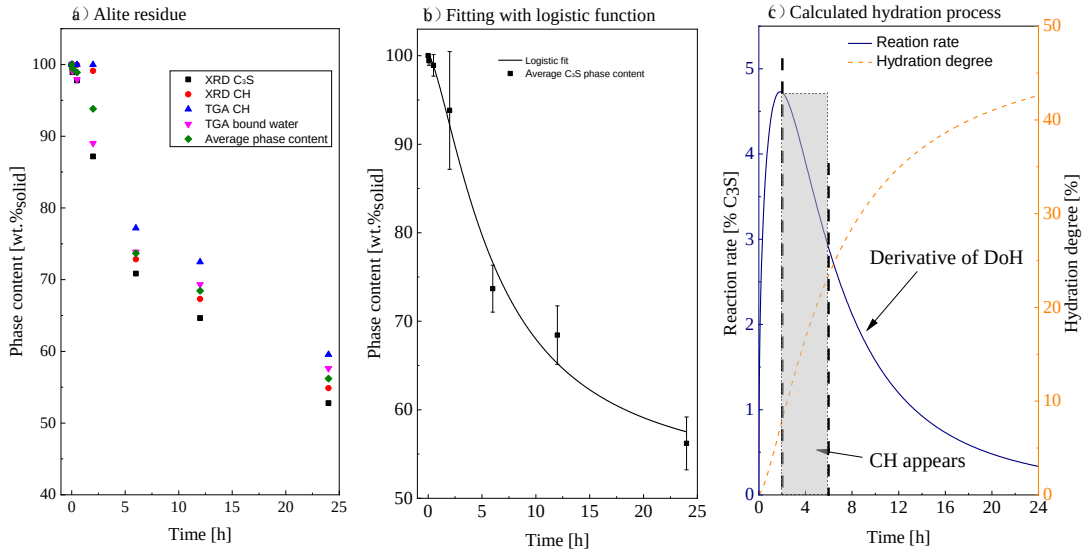

Figure 6-5. The phase assemblage during alite hydration: (a) the alite residue determined by QXRD and TGA, (b) Fitting the average phase residue using logistic function, and (c) the calculated hydration degree and reaction rate.

6.2 ^{29}Si NMR analysis of alite samples

6.2.1 Experimental observations

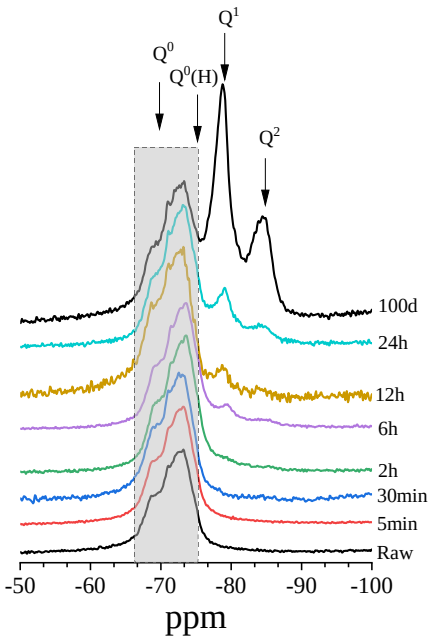

Figure 6-6 ^{29}Si MAS NMR observations of alite, alite hydrated from 5 min to 24 h, and hydrated for 100 d. The alite and 100 d alite spectra were used for the confirmation of deconvolution peaks associated to Si tetrahedra.

Figure 6-6 plots the ^{29}Si MAS NMR experimental observations of alite, alite hydrated for within 24 h, and for 100 d. The long-term hydrated sample helps to confirm the positions of Q^1

and Q^2 units that are not obvious in the very early-age samples. The alite helps to detect whether the suspected Q^0(H) presented during the hydration. The presence of Q^0(H) is still controversial, for example, Brough [87] gave a good explanation of C-S-H gel formation mechanism in C_3S system based on the percentage of Q^0(H), and Rodriguez [13, 197] did not include the Q^0(H) group for the explanation of C_3S hydration.

The deconvolution of alite samples are given Figure 6-7. Deconvolution of NMR spectrum (starting alite) is based on the minimum residue principle (blue curve shows the residue after deconvolution) and four Q^0 peaks are identified in this alite. It should be pointed out that these Q^0 peaks are not the real Q^0 groups existed but are used throughout in the deconvolution of the spectra of the hydrated samples. By keeping the same Q^0 peaks as the starting alite, a small peak at ≈ -77.5 ppm is confirmed in the following samples. The chemical shift of this peak is upper-field shift from Q^0 (-68 ~ -76 ppm) but lower field from Q^1 (-79 ppm), thus, the Q^0(H) group is assigned here for all samples [87]. A better way of the confirmation of Q^0(H) group is comparing the ^{1}H-^{29}Si CPMAS NMR spectrum with the single pulse one for the same sample [86, 87]. As shown from the deconvolution, the order of silicate groups appears is Q^0(H), Q^1, Q^{2p}, and Q^{2b}. The Q^1 sites firstly appear at 2 h and the Q^2 sites firstly appear at 6 h. The intensity of Q^0(H) group remains stable throughout hydration, which is consist with the conclusion drawn by Brough [87]. Apparently, the intensity of Q^1 and Q^2 peaks increased with hydration time.

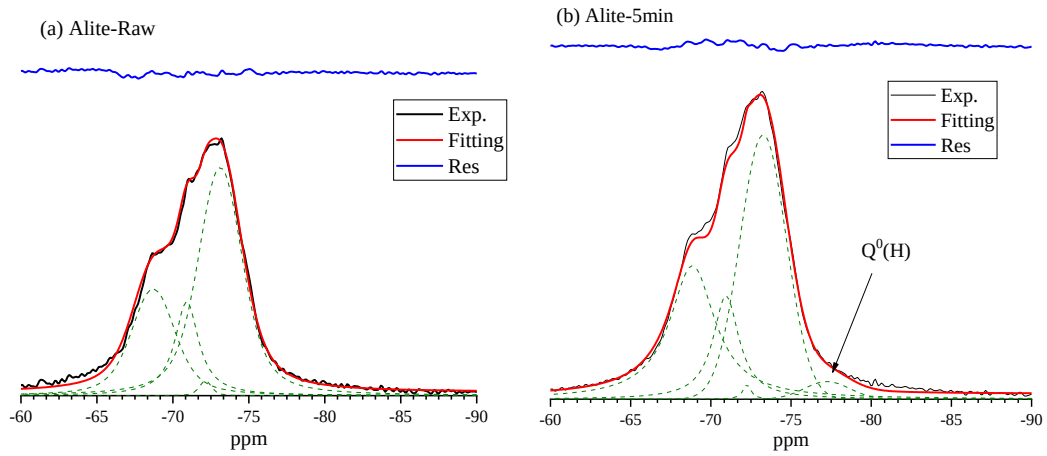

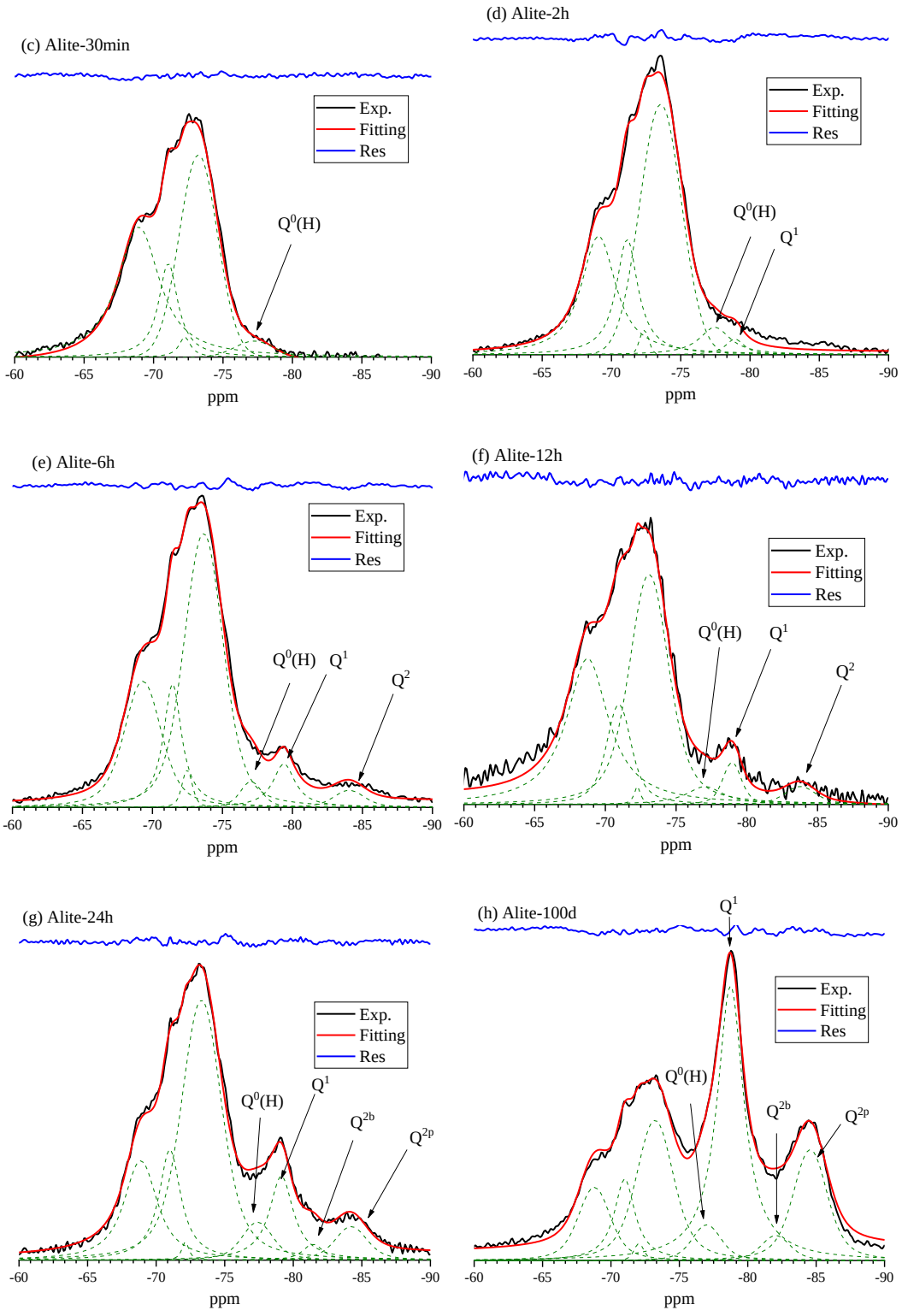

Figure 6-7 Deconvolution of alite NMR spectra: (a) alite; (b) 5 min; (c) 30 min; (d) 2 h; (e) 6 h; (f) 12 h; (g) 24 h; (h) 100 d. The alite spectrum is used for the confirmation of Q^0 groups and the parameters of these fitting peaks are used throughout the deconvolution with only peak intensity reducing. The long-term sample is used for confirmation of the Q^1 and Q^2 peaks for better deconvolution for early-age spectra.

6.2.2 Nanostructure development of C-S-H gel in alite system

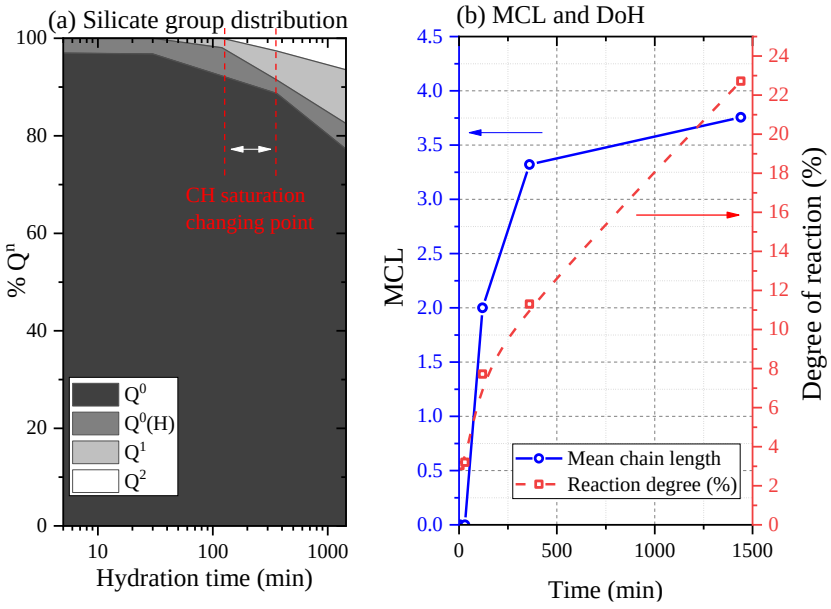

Figure 6-8 (a) Silicate spices distribution (left) and (b) MCL or degree of hydration of alite.

Figure 6-8 summarises the results from alite NMR spectra deconvolution, following by the calculation of MCL of resulted C-S-H gel and DoH of alite. The silicate group distribution of alite hydrated for within 24 h is shown in Figure 6-8 (a), where Q^0 is still the dominated sites, indicating the DoH of alite still remains low after 24 h hydration. The $Q^0(H)$ group keeps stable at around 2.0%, which agrees the conclusion drawn by Brough et al. [87]. Since the XRD, TG-DSC, and FTIR results confirmed that the CH firstly appears at 6 h, which interestingly is accompanied with the appearance of Q^2 sites. Meanwhile, the MCL increases together with DoH and reached ≈ 3.70 and 23% after 24 h hydration.

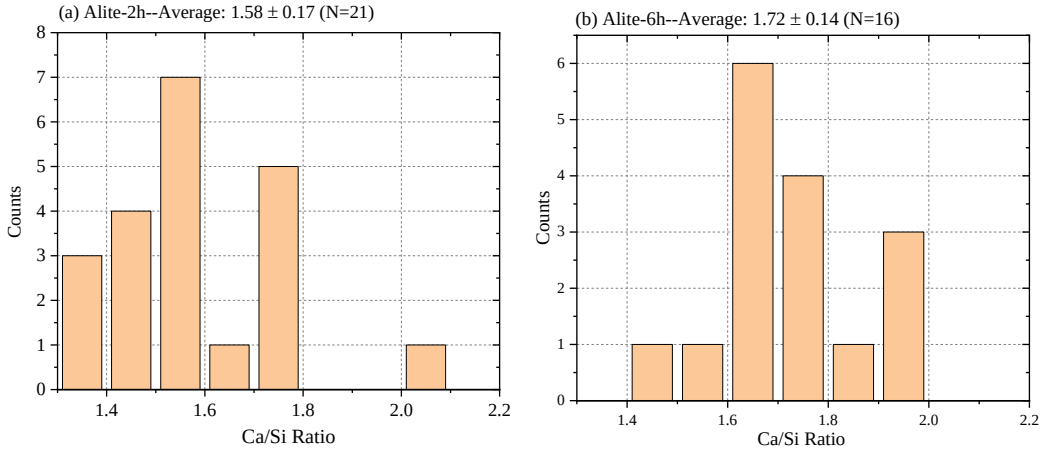

Figure 6-9 Ca/Si ratio of OP C-S-H of alite hydrated for (a) 2 h and (b) 6 h.

Figure 6-9 gives the histogram of Ca/Si ratio along with the average value of OP C-S-H in alite hydrated for 2 and 6 h. It is clear that the initial average Ca/Si ratio at 2 h is 1.58, which is lower than that at 6 h (= 1.72). On one hand, the higher Ca/Si ratio may result from the intermix with fine-crystal CH as shown by XRD, TG, and FTIR, whereas no CH presents in the 2 h alite sample. On the other hand, the saturation of Ca ions in the surrounding solution may provide essential Ca-O layer for the formation of C-S-H gel, which is also observed in Rodriguez's work [13] by using [CaO] solution with constant concentration: the Ca/Si ratio that calculated from either TEM-EDX or equilibrium method shows an increasing trend with the increased [CaO] concentration [13].

6.3 Morphology and structural chemical formulae of C-S-H gel in alite system

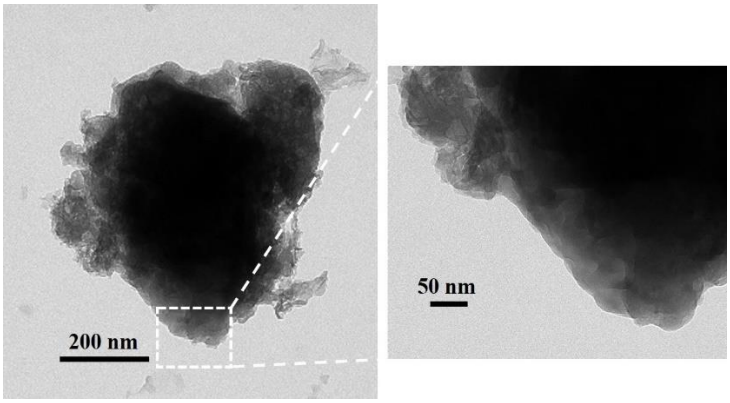

Figure 6-10 TEM images show the foil-like morphology (left) of alite hydrated for 2 h and the right image is a close look at the edge.

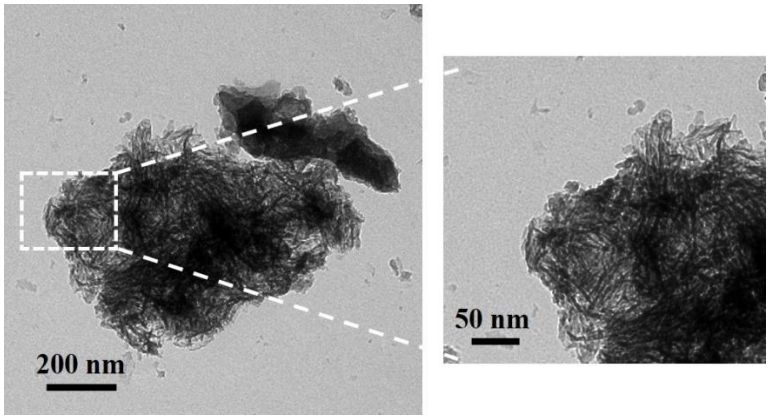

Figure 6-11 TEM images show the fibrillar-like morphology (left) of alite hydrated for 6 h and the right image is a close look at the edge.

Figures 6-10 and 6-11 show the bright-field TEM images of alite particles hydrated for 2 and 6 h with a close look at the edge (OP). At 2 h, the OP C-S-H gel exhibits the foil-like morphology and with large parts remain unhydrated in the centre. For alite that hydrated for longer time, the

fibrillar C-S-H particle appears at the edge of the alite. These long-thin C-S-H units forms the OP C-S-H gel that mostly observed in previous studies [13, 119, 121, 122, 126, 208, 214].

The structural chemical formulae of C-S-H gel in alite-2 h sample can be written from both T/CH and T/J points of view, the following examples are based on minimum protonation assumption:

$$\textbf{\textit{Alite-2h T/CH:}}\ Ca_3Si_2O_7 \cdot 0.16Ca(OH)_2 \cdot mH_2O$$

$$\textbf{\textit{Alite-2h T/J:}}\ Ca_2Si_2O_7 \cdot (OH)_{0.32} \cdot Ca_{1.16} \cdot mH_2O$$

Similarly, the structural chemical formulae of C-S-H in alite-6 h sample can be written as (minimum protonation):

$$\textbf{\textit{Alite-6h T/CH:}}\ Ca_{4.32}Si_{3.32}O_{10.96} \cdot 1.39Ca(OH)_2 \cdot mH_2O$$

$$\textbf{\textit{Alite-6h T/J:}}\ Ca_{2.88}Si_{3.32}O_{10.96} \cdot (OH)_{2.78} \cdot Ca_{2.83} \cdot mH_2O$$

Interestingly, the alite-2 h sample shows a dimer tobermorite-based (T2) structure since no (or limited) Q^2 confirmed from the NMR spectrum. By observing the T/CH model, it can be concluded that the C-S-H gel in alite-2 h sample is consist of only limited CH mixed with T2 structure, whereas for alite-6 h sample, the C-S-H gel in mainly a mixture of T2/T5 structure with more CH. These structural chemical formulae agree perfectly with the results shown by XRD, TG, and FTIR, where significant CH only appears after 6 h hydration. For T/J model point of view, the C-S-H in alite-2 h sample is consist of T2/J2 units, whereas that in alite-6 h sample is consist of T2/T5 and J2/J5 units.

6.4 Solution chemistry of alite hydration and thermodynamic calculations

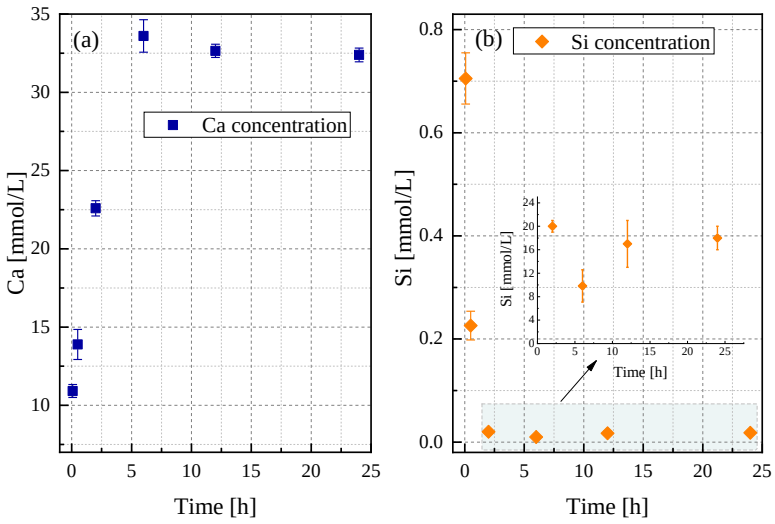

Figure 6-12 Solution composition development of alite hydrated at w/b ratio of 10.

Figure 6-12 shows the Ca and Si element concentrations that present in the solution during alite hydration. Previous study shows that Ca:Si concentration ratio in the infinite dissolution environment (liquid: solid=1:10,000) of C_3S is 3.0, which is consistent with its chemical composition [154]. This situation is based on the free dissolution and without C-S-H precipitation. However, the current experimental condition does not allow alite to freely dissolve and the C-S-H precipitate at the same time. The experimental results indicate that Ca concentration is much higher than that of Si. The Ca concentration in the solution rises up from just above 10 mmol/L at 5 min to around 33 mmol/L at 6 h, and then keeps stable until 24 h. The highest Ca concentration is much higher than that of CH saturation condition (around 20~25 mmol/L), and very close to an experimental result conducted by Bellmann [156], where the highest Ca concentration (~ 30 mmol/L) of C_3S dissolved in w/s=10 is achieved at ~ 7 h. On the other hand, the Si concentration possesses the highest concentration (700 µmol/L) at 5 min and then drops down to around 9 ~ 20 µmol/L after 2 h hydration. The initial Si concentration in this study is much higher than those (~ 40 ~ 160 µmol/L under different w/s ratios and solutions) obtained by Bellmann et al. [156-158, 215], but closer to those (~ 400 µmol/L) [149, 154]. Then the stabilised Si concentration agrees the studies taken by Bellmann et al. [156-158].

Furthermore, the saturation indices (SI) in regard to different solid phases including C_3S, CH, and C-S-H gels are calculated using database given in **Appendix C** and shown in Figures 6-13 and 6-14. Although some guest ions are introduced into C_3S to form alite used in this study, the thermodynamic database that for C_3S is used as the represented values or indicators for a purpose of comparison.

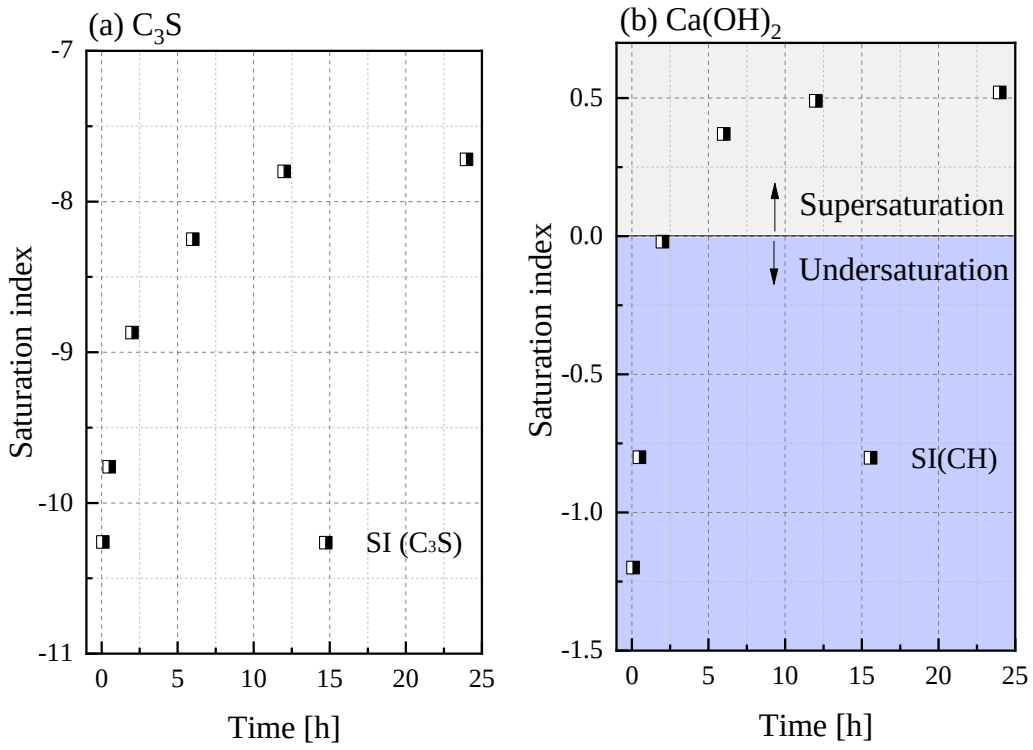

Figure 6-13 Saturation indices of C_3S and CH during hydration.

Figure 6-13 gives the SI of C_3S and CH of alite hydrated for within 24 h. Clearly, the SI of alite phase (mainly Fe, F-doped C_3S) keep negative throughout hydration, indicating the continuous hydration process. The absolute value of alite SI decreases along time and is gradually close to the equilibrium value (≈ -7.6), which means a decreasing undersaturation condition of alite. On the other hand, the initial SI of CH remains negative until 2 h, indicating the undersaturation of CH and no (or limited) solid CH precipitated in the system. The SI turns to positive between 2 and 6 h, indicating that CH appears simultaneously. These results agree the analysis conducted on solid phases that discussed in Section 6.1.

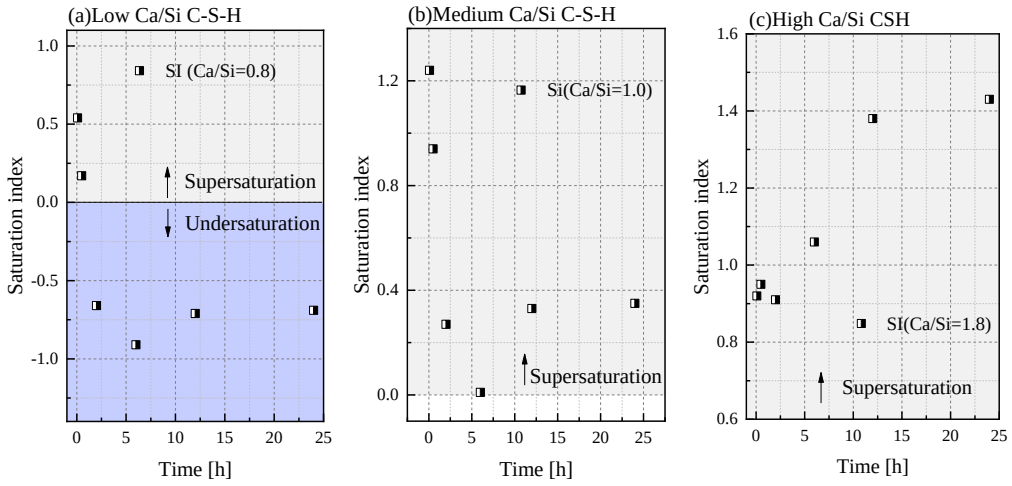

Figure 6-14 Saturation indices of C-S-H gels

Figure 6-14 gives the SI of C-S-H gels that generated during alite hydration. Three kinds of C-S-H gels are used as represented units followed the discussion given by Bullard and Scherer [216]. This ideal model then was implemented by Bellmann and Scherer for the calculation of C-S-H growth rate [158]. The details of these assumptions are summarised as the following balancing Equations 64-67 (where the β is the supersaturation of individual end-members, β_{total} stands for the sum of the supersaturation for C-S-H gels):

$$\beta_1 = (Ca^{2+})^{0.80}(H_3SiO_4^-)(OH^-)^{0.60}/1.26 \cdot 10^{-7} \quad \textit{Equation 64}$$

$$\beta_2 = (Ca^{2+})^{1.00}(H_3SiO_4^-)(OH^-)^{1.00}/1.68 \cdot 10^{-9} \quad \textit{Equation 65}$$

$$\beta_1 = (Ca^{2+})^{1.81}(H_3SiO_4^-)(OH^-)^{2.62}/2.76 \cdot 10^{-14} \quad \textit{Equation 66}$$

$$\beta_{total} = \beta_1 + \beta_2 + \beta_3 \quad \textit{Equation 67}$$

As assumed, three C-S-H gels with low (0.80), medium (1.00), and high (1.81) Ca/Si ratios are used for discussion in this study. The SI of these C-S-H gels during alite hydration are plotted in Figure 6-14. The C-S-H with low Ca/Si ratio initially possesses positive SI value, indicating a thermodynamic equilibrium condition can be achieved. Then this value decreases to negative after 30 min and remains negative afterwards, demonstrating the instability of C-S-H with low Ca/Si ratio. The development of SI of C-S-H with medium Ca/Si ratio shows a similar trend but all values keep positive throughout hydration, indicating the thermodynamic stability of C-S-H with medium Ca/Si ratio. However, the absolute SI value shows a decreasing trend from 5 min to 6 h. Finally, the SI of C-S-H with high Ca/Si ratio keeps positive and increases (and then stabilises) with the hydration time.

The trend of SI of C-S-H gels can be compared to the trend of Ca and Si concentrations (Figure 6-12) during hydration. Interestingly, the C-S-H gels with low or medium Ca/Si ratio are mainly controlled by the Si concentration, which is reflected by the fact that developing trend of the SI of these C-S-H gels are similar to that of Si elements in solution. However, the C-S-H with high Ca/Si ratio is dominated by the counterpart (Ca concentration). In other words, the high Ca concentration is the vital condition for producing C-S-H with high Ca/Si ratio. The experiments that performed by Rodriguez [13] also support this opinion, which proved that the hydration of C_3S in higher [CaO] concentration solution can generate C-S-H with higher Ca/Si ratio regardless of hydration time.

6.5 Dissolution and precipitation models during alite hydration

The dissolution of alite (mainly C_3S) and the precipitation of C-S-H models are mainly based on the previous research taken by Nicoleau et al. [149, 154, 155, 217] and Bellmann et al. [156-158]. Although the alite used in this study is ion doped C_3S, these models' adaptability is believed to cover the current condition as discussed [149, 154, 158]. In this case, C_3S is also used to refer to the alite in the following discussion.

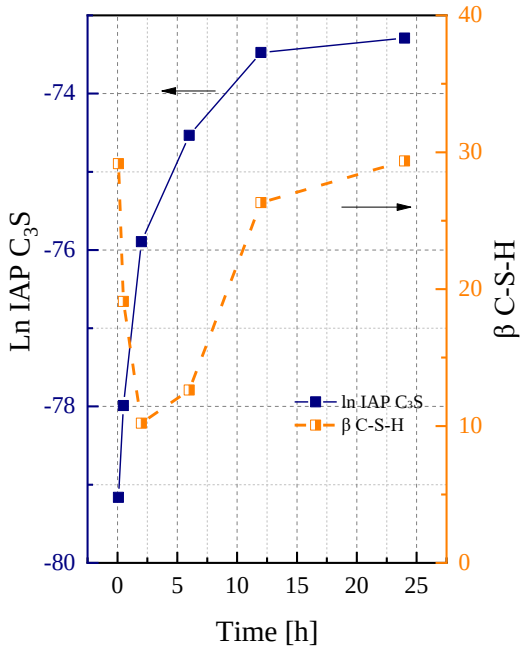

Figure 6-15 Ln IAP C_3S and β C-S-H development within 24 h.

Figure 6-15 summarises the development of ln IAP_{C3S} and $\beta_{C\text{-}S\text{-}H}$, which are crucial parameters for the following calculations. The IAP C_3S is determined by expressing the ideal dissolution process of C_3S as Equation 68:

$$IAP_{C_3S} = (Ca^{2+})^3(H_4SiO_4)(OH^-)^6 \qquad \textit{Equation 68}$$

These values (ln IAP_{C3S}) are normally in the range of -96.1 ~ -81.7 under unlimited dissolution (w/s=10000 ~ 50000) or -46 ~ -40 when C_3S is dissolved in saturated CH solution at w/s=10 [149, 154]. The sum of supersaturation of C-S-H gels is calculated according to Equation 67 by using thermodynamic calculation. The calculated results are also reasonable when compared to that (~5 to 35) in the work taken by Naber et al. [215]. The Ca concentration in this work is lower than the abovementioned work, which results in a lower supersaturation of C-S-H gels.

Based on these parameters, five rates (including dissolution, precipitation, and overall) are given and used for discussion in this work. Table 6-1 summarises the concepts of the mentioned rates, which are clarified and denoted by different symbols.

Table 6-1. The definition of different rates calculated in this work

Types of rate	Symbol	Unit	Definition
Interfacial dissolution rate of C_3S	r_{C_3S}	$\mu mol \cdot s^{-1} \cdot m^{-2}$	Interfacial rates (r) are the rate with respect to the interface between solution and solids.
Interfacial precipitation rate of C-S-H	r_{CSH}	$nmol \cdot s^{-1} \cdot m^{-2}$	
Determined dissolution rate of C_3S	R_{C_3S}	$\mu mol \cdot s^{-1} \cdot g^{-1}$	Determined reaction rates (R) from interfacial rates are the individual kinetic rates such as dissolution rate and precipitation rate.
Determined precipitation rate of C-S-H	R_{CSH}	$nmol \cdot s^{-1} \cdot g^{-1}$	
Hydration rate	R_{hyd}	% C_3S/h	$R_{hyd.}$ is the overall reaction rate of C_3S.

Generally, the interfacial rate (r) (i. e. interfacial C_3S dissolution rate (r_{C_3S}) and interfacial C-S-H precipitation rate (r_{CSH})) represents the reaction rate per unit of solid-liquid interfacial area. The determined rate (R) (i. e. determined C_3S dissolution rate (R_{C_3S}) and determined C-S-H precipitation rate (R_{CSH})) is different from the interfacial rate, which stands for the rate per unit of

mass. In other words, the determined rates are derived from the interfacial rates with the consideration of surface area (A). Those interfacial rates are calculated from pore solution compositions in combination with thermodynamic calculation. However, the hydration rate (R_{hyd}) is determined from experimental results such as XRD and TGA, which is given and discussed in Section 6.1. It shows the overall hydration rate rather than individual steps (i. e. dissolution or precipitation).

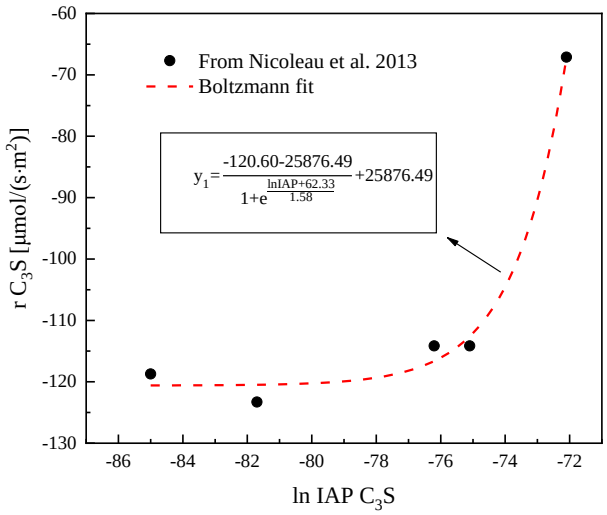

Figure 6-16 Boltzmann fitting of ln IAP C_3S against interfacial dissolution rate of C_3S. Data are taken from Nicoleau's work on the dissolution of C_3S with multiple approaches [154]. This Boltzmann fit established the relationship between ln IAP and rC_3S (y_1), which is used for the confirmation of the rC_3S from known IAP values in this work.

For alite interfacial dissolution rate, Nicoleau et al. [154] used the Boltzmann fitting to establish the relationship between ln IAP_{C3S} and r_{C_3S} over a broad range of concentrations of Ca and Si. The Boltzmann equation parameters used for fitting is based on the ln IAP_{C3S} values that are within the range in this study. Therefore, the r_{C_3S} can be calculated through the obtained Boltzmann model (Equation is given in Figure 6-16). Since the surface area (A) of alite is determined through BET method (0.870 m^2/g in Section 4.2.1, assuming to be constant during hydration), the determined C_3S dissolution rate can be calculated through the following Equation 69:

$$R_{C_3S} = A_{C_3S} \cdot r_{C_3S}(lnIAP) \qquad \textit{Equation 69}$$

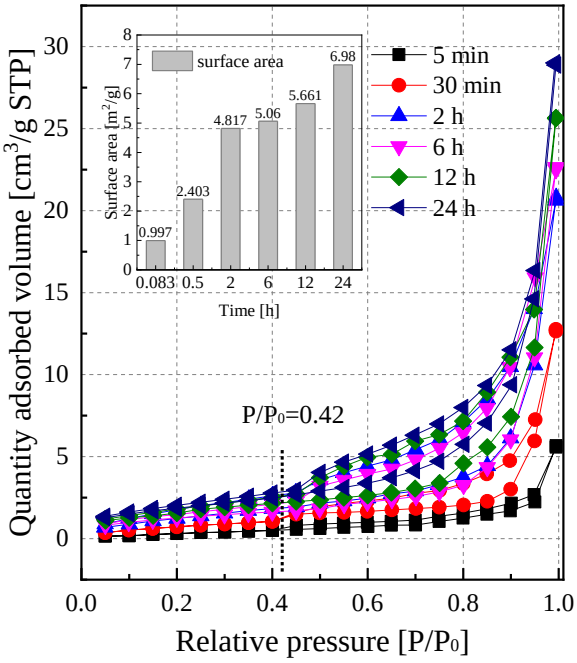

Figure 6-17 Gas adsorption curves and surface area (BET method) of alite at different hydration time. The difference between the values shown in this figure and the same parameter for alite is used as the surface area of C-S-H.

For the interfacial precipitation rate of C-S-H gel, Equation 70 shows the methodology of acquiring the $r_{C\text{-}S\text{-}H}$ in combination with the assumptions given in Equations 64-67. This method is proposed by Bellmann and Scherer [158] and applied or discussed in many works [215, 216, 218].

$$r_{CSH} = 0.013 \cdot \beta^2 - 0.185 \cdot \beta - 2.095 \qquad \textit{Equation 70}$$

According to the definition, the determined C-S-H precipitation rate can be calculated based on the interfacial rate multiply the surface area of C-S-H generated during hydration (Equation 69). As shown in Figure 6-17, the surface area of the solid residues is tested by nitrogen adsorption and the surface area is determined by BET method. Two assumptions are used here for modelling: (1) the C-S-H specific surface area is calculated based on the difference between that of solid residues and alite; (2) the specific surface area of CH is neglected.

$$R_{CSH} = A_{CSH} \cdot r_{CSH}\ （\beta_{CSH}） \qquad \textit{Equation 71}$$

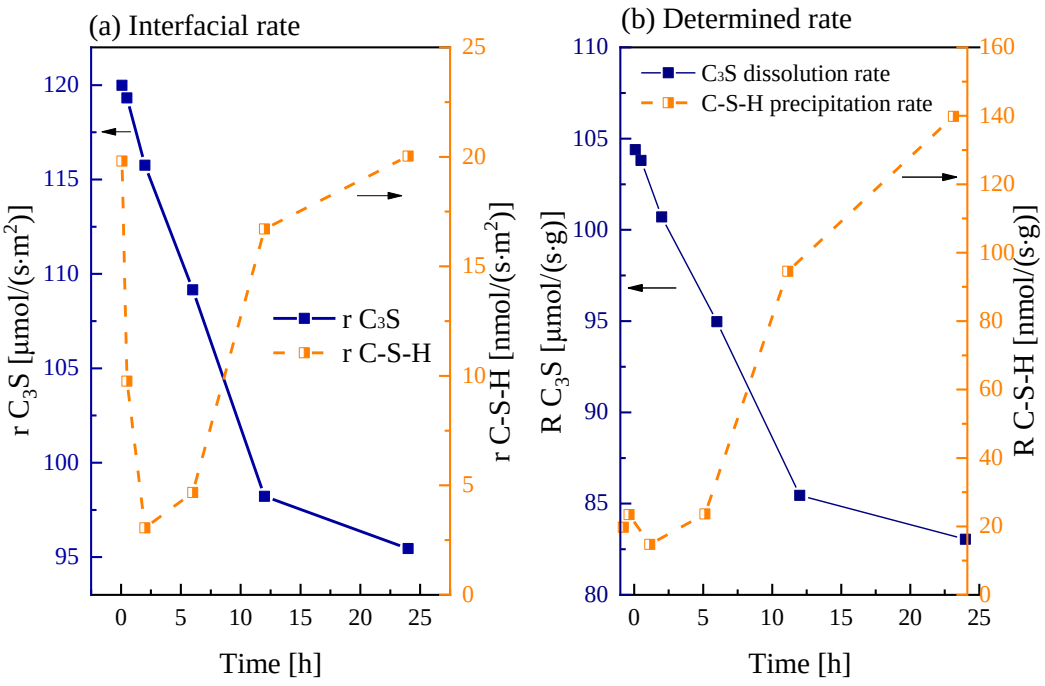

Figure 6-18 Interfacial and determined rates of C_3S (dissolution) and C-S-H (precipitation).

Figure 6-18 shows the interfacial and determined rates of C_3S and C-S-H in this work. The alite dissolution rate (r or R) decreased along with the hydration time. This is reasonable due to the increasing Ca ions in the solution, which affects the thermodynamic equilibrium, thus reducing the dissolution driving force of alite. This decreasing curve can be divided into two phases: fast dissolution from 5 min to 12 h; slower dissolution from 12 h to 24 h. Meanwhile, the C-S-H interfacial precipitation rate ($r_{C\text{-}S\text{-}H}$) shows a U-shape curve and the bottom of this 'U'-curve happens at 2 h. The 'U' shape interfacial precipitation needs to be explained in joint with the SI of C-S-H gels. Initially, the C-S-H with low Ca/Si ratio dominates this system, which reflected a fast precipitation before 2 h. Then the precipitation of C-S-H with medium or high Ca/Si ratio governs together with the instability of the low Ca/Si, which result in an increasing C-S-H interfacial rate. Furthermore, the C-S-H determined precipitation rate ($R_{C\text{-}S\text{-}H}$) exhibits a stable curve until 2 h and then significantly increases afterwards. It is also reasonable since this precipitation rate reflects the overall C-S-H generated in the whole system.

6.6 Discussions on the relationships between the nature of C-S-H gel and the solution environment in alite system

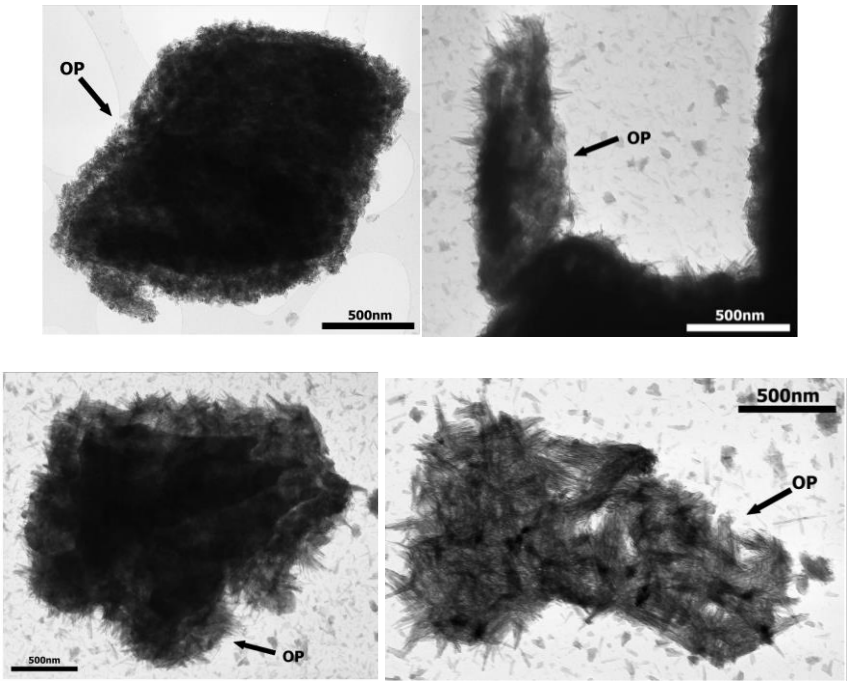

Figure 6-19 TEM morphology of C_3S hydrated at w/b of 0.5 for 2h (upper left), 4h (upper right), 6h (lower left), and 8h (lower right), taken from Q. Li [219].

Morphology analogy- Figure 6-19 shows the TEM images of early age C_3S hydrated within 8 h taken from Q. Li [219]. The morphology-change of C-S-H gel in this system exhibits quite a similar phenomenon to the current study. At 2 h, the OP C-S-H has a foil-like morphology, which is exactly the same as the observation in this study regardless of w/s ratio. As the hydration goes on, the foil-like feature gradually changes to fibrillar-like at 4 h (and afterwards), which agrees again with the images shown in Section 6.3. The Ca/Si ratio of C-S-H in Li's study is 1.57 ± 0.24 (4 h, N=37), 1.49 ± 0.15 (6 h, N=36), and 1.37 ± 0.25 (at 8 h, N=55). This parameter is quite different from the current study at 6 h, which needs more investigations in the later study. However, the morphology change supports the current experiments' observations.

Explanations of C-S-H compositions at 2 h and 6 h- The explanations of C-S-H gel requires insights of the formation mechanism of C-S-H gel. Richardson[2] considers that the Ca-O layer should be the first part and served as the matrix for the formation of monomers, dimers, and ultimately to the kinked silicate chains (i.e. 2, 5, 8, … (3n-1)). The Ca-O layers can form by

[2] The original statement is given in IGR's lecture (CIVE2301) at the University of Leeds.

repeated condensation of Ca-complexes (i.e. for example $[Ca(H_2O)_5(OH)]^+$). This mechanism perfectly agrees with the NMR observations (Section 6.2), where the Q^0(H) group (i.e. monomers) forms initially after 5 min and stays in the system along hydration. The dimers (Q^1) dominate after 2 h of hydration and pentamers (Q^2) form at 6 h, indicating that the monomers combine after longer hydration to form dimers, and the insertion of BT forms the pentamers.

J. Chen [63] divided the mechanism of silicate polymerization into two conditions: at low (~ 1.2) and high (~ 1.7-1.8) Ca/Si ratio. The polymerization of silicate groups at lower Ca/Si ratio is mainly achieved by removing the interlayer Ca or by adding BT. The silanol (Si-OH) group are present at this stage and they can interact through condensation reactions rapidly (i.e., ≡Si-OH + OH-Si≡ → Si-O-Si). This mechanism can explain the formation of monomers (5 min throughout hydration), dimers (> 2 h), and pentamer (> 6 h) during hydration. The mechanism for high Ca/Si ratio is based on a fact that the neat C_3S paste will form the C-S-H gel with almost constant Ca/Si ratio (~ 1.7-1.8) but the MCL will continue to increase up to 5 with age, which indicates a structural-change that maintains the Ca/Si ratio but increases MCL. The mechanism of this phenomenon is argued as the formation of Ca-OH group (i.e., the transformation from tobermorite- into jennite-like structure). More supporting experimental results are also discussed, for example, the IR and ^{1}H NMR showed that no Si-OH are present at high Ca/Si ratio at early age (discussed in Chapter 5 in Ref. [63]). Some evidences of Ca-OH information are also given (in Chapter 4 in Ref. [63]) by inelastic neutron spectroscopy (INS), which shows around 25% Ca is charge-balanced by OH group. These evidences all support that the late-age C-S-H gel in C_3S paste should possess jennite-like structure.

Based on the discussions above, the C-S-H that formed at 2 h and 6 h in this study can be explained and visualised. The C-S-H gel at 2 h has an MCL ≈ 2 and a Ca/Si ratio ≈ 1.58, which indicates the dimers are the main components. The early-age C-S-H gel resembles tobermorite-like structure, which confirms the Ca-O layer characteristic. Further, no CH (XRD, STA) and possibly no Si-OH group (as discussed above) are present in the C-S-H gel, the Ca/Si ratio must be achieved by the C-S-H gel itself. In this case, the major units in C-S-H gel at 2 h are possible as a T2 structure with minimum protonation as shown in Figure 6-20(a). The C-S-H gel at 6 h has

an MCL ≈ 3.2 and a Ca/Si ratio ≈ 1.72, which indicates that a mixture of 56.7% dimers and 43.3% pentamers are present under this condition. Argued by the later change of C-S-H gel (which gradually changes to J5 units), it is considered that J5 is not present at this stage [63]. Therefore, the pentamers are assumed as a T5 unit with minimum protonation ($Ca_6Si_5O_{16}$) as shown in Figure 6-20(b). However, the T2 has a Ca/Si ratio of 1.50 and that for T5 is only 1.20. The final Ca/Si ratio of 1.72 at 6 h can be achieved simply by two ways: I. Mix with CH and II. Mix with J2 units. For condition I: the composites cannot have a reasonable proportion (~32.1% CH is needed for minimum protonation, which is not possible) if dimer: pentamer=56.7%: 43.3% is the precondition. For condition II: assuming that no Si-OH is present in J2 (as shown in Figure 6-20(c)), the composites should be mixed by 43.3% T5, 23.7% T2, and 33.0% J2, which satisfies both MCL and Ca/Si ratio preconditions under the minimum protonation assumption. The formation of CH is proved by XRD and TG at 6 h, which supports the explanations from T/CH point of view. However, the FTIR can show that some Ca-OH group forms, but no strong evidence can confirm whether these Ca-OH groups belong to C-S-H or CH. Therefore, both the explanations are reasonable. However, the T/CH point of view cannot explain the current study (both the minimum/maximum protonation assumptions). Based on these, the fibrillar-like morphology may be associated with the presence of jennite-like structure (Ca-OH group).

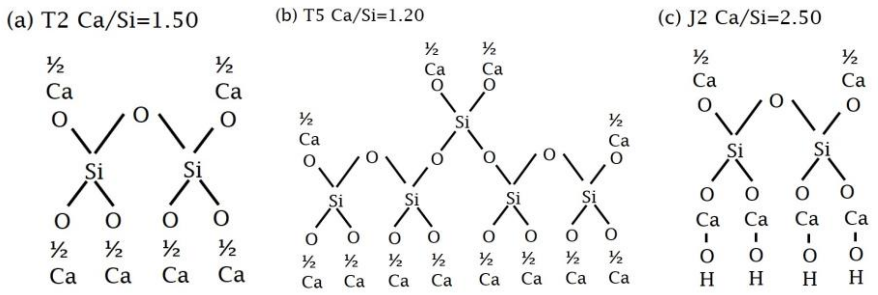

Figure 6-20 Visualisation of C-S-H gel during alite hydration: at 2 h (T2) and at 6 h (mixture of T2, T5 and J2).

Solubility equilibrium of C-S-H and CH- Figures 6-21 plots the solution composition during alite hydration together with some data from various systems for comparison. The reference lines in Figure 6-21(a) are taken from Jennings' classic work on the aqueous solubility relationships for two types of C-S-H [164] and that in Figure 6-21(b) is drawn based on the standard K_{sp} of CH at 25 °C. The solubility curves of C-S-H (ternary system) is based on the Gibbs phase rule that there

is only one degree of freedom for a liquid/solid equilibrium at a fixed temperature and pressure. Therefore, if one component changes, the concentrations of the other must change in a well-defined manner.

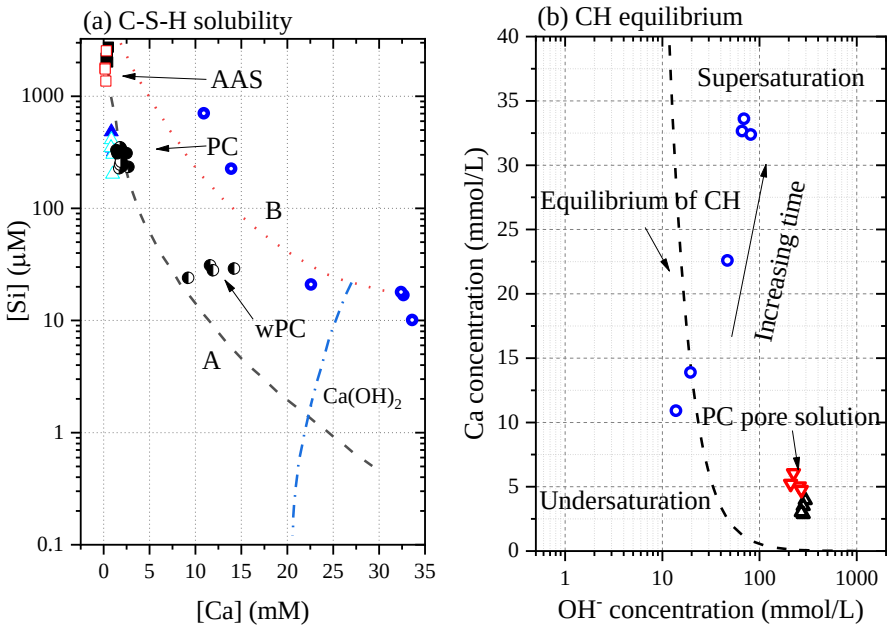

Figure 6-21 Aqueous equilibrium of (a) C-S-H and (b) CH during alite hydration; some other points are pore solutions of sodium silicate solution activated GGBS or Portland cement taken from [175] and wPC taken from [148].

Experimental data from the C-S-H prepared by the reactions between CH (or CaO) and silicic acid, or by mixing solutions of sodium silicate and a soluble calcium salt fall around the Curve A. Thus, Curve A is linked with the metastable solubility curve of C-S-H(I). Whereas the Curve B contains most experimental data starting with C_3S reaction that has a large range of mixing conditions (w/s ratio or reaction time). Therefore, Curve B is regarded as a structurally distinct C-S-H, which may be a mixture of C-S-H(I) and C-S-H(II). The data that are obtained in the current study lay around Curve B, agrees with the discussions given by Jennings [164]. Unreacted alite in the system maintains a higher Si concentration throughout hydration. This condition implies the near-equilibrium between the solid and the solution, which means a continuous hydration happens along Curve B. Whereas data of the pore solution either from sodium silicate-GGBS paste (AAS) or PC/wPC pastes fall around Curve A, which indicates a metastable condition may be achieved. It is noted that extremely low Ca concentration in the paste (although some pastes contain CH as Ca barrier) after long-term hydration is quite different from the early-age hydration of alite. The

morphology change of C-S-H gel cannot be easily distinguished from C-S-H solubility curves, which need to be discussed in joint with the saturation conditions.

Figure 6-21(b) gives the solubility curve of CH without the consideration of Ca complexes that are normally present in alkali aqueous condition. Consequently, this figure is only used as an indicator, the saturation condition of CH is more accurate when using thermodynamic calculations (Figure 6-13). A much higher Ca concentration and lower pH of alite solution are observed when compared to that of PC. A higher pH can be achieved by PC is because of the release of alkali ions (Na^+, K^+) during hydration, which also restricts the concentration of its counterpart (Ca^{2+}). However, the C-S-H gels in both of them are possibly fibrillar-like. In this way, the pH (OH^- concentration) is also another important parameter for the morphological change. Therefore, any elemental concentration in pore solution cannot be a direct indicator for the formation of C-S-H morphology.

Possible related indicators responsible for C-S-H morphology change- As shown by TEM, the morphology of C-S-H change from foil-like to fibrillar-like between 2 h and 6 h. Therefore, the corresponding data are crucial: Firstly, the CH appears at 6 h as shown by XRD or TG together with the SI turns to positive; Secondly, the Q^2 group initially appears between 2 h and 6 h; Thirdly, the SI of C-S-H with high Ca/Si ratio significantly rise up to higher than 1; Fourthly, the interfacial precipitation rate of C-S-H passed the bottom of 'U'-shape curve as shown in Figure 6-18, whilst the determined dissolution rate decreased to under 100 μmol/(s·g).

6.7 Summary

A synthetic alite is hydrated under a constant w/s ratio of 10 for the investigation of morphological change of C-S-H gel. QXRD, STA, FTIR, ^{29}Si MAS NMR, and TEM-EDX are used to analyse the solid phase during hydration, whilst ICP-OES is used for detecting the elemental compositions of aqueous phase in combination with thermodynamic modelling calculations (achieved by PHREEQC). Meanwhile, a thermodynamically based dissolution/precipitation model is also implemented on the data from current study. Some key findings are summarised below:

(a) The morphology of C-S-H changes from foil-like at 2 h to fibrillar-like at 6 h;

(b) The CH initially appears at 6 h as confirmed by XRD and TG. The Ca-OH group is present since 2 h of hydration in FTIR spectrum, which cannot be used as the evidence for the formation of CH;

(c) Q^0(H) group is possibly present throughout hydration and Q^1 tetrahedra first appears at 2 h and Q^2 tetrahedra first appears at 6 h;

(d) The SI of CH changes from negative at 2 h to positive at 6 h; The SI of C-S-H with high Ca/Si ratio is stable before 2 h, but increase dramatically afterwards;

(e) The C-S-H interfacial precipitation rate ($r_{C\text{-}S\text{-}H}$) shows a U-shape curve and the alite dissolution rate shows a decreasing trend as the hydration goes on.

(f) The C-S-H at 2 h can be explained as the tobermorite-like dimer (T2) with minimum protonation; and that at 6 h can be explained as a mixture of minimum protonated 43.3% T5, 23.7% T2, and 33.0% J2 (T/J model). The foil-like C-S-H gel may be related to the tobermorite-like structure.

(g) The change in C-S-H morphology from foil to fibrillar during alite hydration may be associated with: the supersaturation of CH (i. e., the appearance of CH); the appearance of Q^2 tetrahedra; the SI of C-S-H with high Ca/Si ratio significantly rise up to higher than 1; the interfacial precipitation rate of C-S-H passed the bottom of 'U'-shape curve; the determined dissolution rate decreased to under 100 μmol/(s·g).

Chapter 7

Morphology-structural change of synthetic C-S-H

Many efforts have been put to synthesise the single-phase C-S-H in laboratory that is similar to the binding phase formed in hardened cement. Most of these studies successfully made the C-S-H phases that exhibit a close analogy to clinotobermorite, namely C-S-H(I), which can be prepared with a Ca/Si ratio between 2/3 and ≈ 1.4 [7]. This cluster of C-S-H is synthesised by mixing soluble silicate ions and calcium salt in dilute aqueous suspension at temperature below ≈ 333K. From a thermodynamic equilibrium point of view, the C-S-H at this level of Ca/Si ratio theoretically shows a larger Ksp (i. e. an example given in Equation 76-78 in Chapter 6) but is less dependent on the higher Ca concentration solution environments [57, 158]. Therefore, C-S-H(I) is easy to achieve under normal condition, which is further widely studied [7].

One main feature of C-S-H(I) is that it normally shows a foil-like morphology, which is quite different to the fibrillar-like C-S-H(II) formed at later stage in real cement or alite system. C-S-H(II) has a Ca/Si ratio higher than 1.4 and is considered as a close analogy to jennite[3] [63]. TEM images in Chapters 5 and 6 show the fibrillar-like C-S-H(II) that has a Ca/Si ratio ≈ 1.75 dominates the pure cement system, however, foil-like C-S-H will form either by long-term reaction of SCMs in blends (Chapter 5) or at very early-age hydration of alite (Chapter 6). In any case, the solution environment of foil-like C-S-H gives a much lower Ca concentration than that of fibrillar-like one. More clear experimental results are given by Rodriguez [13], who found that the C-S-H prepared via silica-lime reaction with higher [CaO] concentration (> 20 mmol/L) has a Ca/Si ratio higher than 1.50. Further attempts to synthesise C-S-H with extremely high Ca/Si ratio (up to 1.81) were implemented by controlling the concentration of Ca solution via the reaction of lime-tetraethoxysilane (TEOS) solution under lower temperature [16]. Unsurprisingly, the

[3] The C-S-H with a high Ca/Si ratio in real cement system can be explained as mixture of tobermorite/jennite or tobermorite/CH as described by either Richardson and Groves' model or Taylor's model, however, the evidence of the percentage of Ca-OH group bears the resemblance of C-S-H gel to jennite at late times in Chapter 5 of this reference.

morphology of these C-S-H gels that have a Ca/Si ratio higher than 1.58 in [13] or 1.61 in [16] turn from entire foil-like to mixture of fibrillar/foil-like, and ultimately to entire fibrillar-like after the Ca/Si ratio becomes higher than 1.61 in [13] or 1.69 in [16]. These results plausibly indicate that the C-S-H with a significant high Ca/Si ratio can be achieved through maintaining a constant high Ca concentration environment during synthesis. Unfortunately, due to the limitation of CH solubility at normal temperature (≈ 20 mmol/L at 25 °C), a lower temperature is needed to achieve the high lime (Ca) concentration [14, 16].

This Chapter firstly repeats the same method (i. e. autoreactor method used in [16] but modified as described in Section 4.3) to obtain the synthetic C-S-H with the high Ca/Si ratio. Furthermore, the effects of alkali and aluminium on the formation of C-S-H are studied. Two methods, direct addition during synthesis or immersing in solutions using obtained C-S-H, are used to prepare C-(Na, Al)-S-H. The morphology, composition, and solution environments are examined through multi-techniques and discussed in this Chapter.

7.1 Characterisations of synthetic C-S-H using "Autoreactor method"

7.1.1 Morphology, composition, and nanostructure of AR-C-S-H

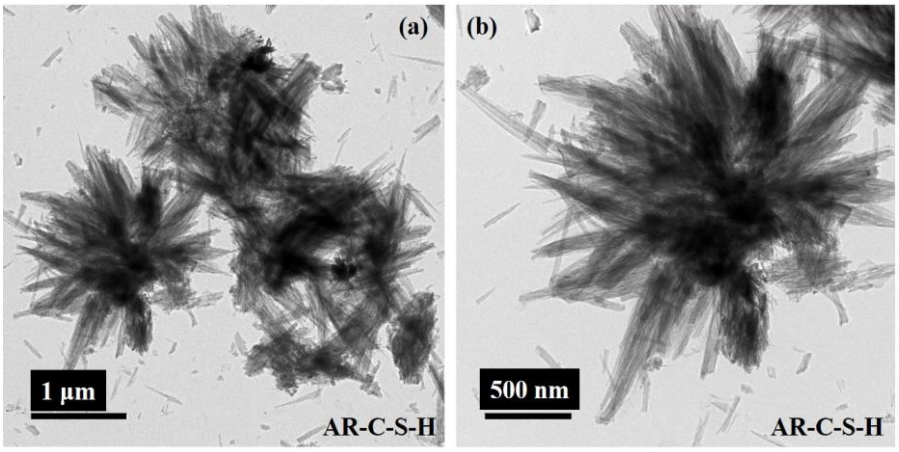

Figure 7-1 TEM image shows the morphology of AR-C-S-H.

Figure 7-1 shows the C-S-H synthesised using autoreactor method at 5 °C. Clearly, the C-S-H possesses the fibrillar-like morphology, which agrees with Vinnakota's results [16]. The morphology is however closer to the C-S-H with a Ca/Si ratio of 1.79~1.81 that is synthesised at 1 °C [16]. This is because the final conductivity of that synthesis at 5 °C is 9.88, whilst the

conductivity continuously rises up to 10.00 in this study, which is closer to the final conductivity of 9.97 under 1 °C in that study [16]. This reaction is between the supersaturated CH solution and small amount of TEOS/ethanol that slowly is added into the system. When 4% TEOS is dispersed into 96% ethanol, the following hydrolysis and condensation reactions happen:

Hydrolysis:

$$Si(OC_2H_5)_4\ (TEOS) + nH_2O\ \rightarrow\ Si(OC_2H_5)_{4-n}(OH)_n + nROH$$

Alcohol condensation:

$$\equiv Si - OC_2H_5 + HO - Si \equiv \rightarrow \equiv Si - O - Si \equiv\ + nROH$$

Water condensation:

$$\equiv Si - OH + HO - Si \equiv \rightarrow \equiv Si - O - Si \equiv\ + H_2O$$

During the alcohol or water condensation process, oligomers ($\equiv Si - O - Si \equiv$) quickly form after the hydrolysis process, however, TEOS prefers to form three-dimensional silicate networks if some basic catalysts media are used [220]. Therefore, the linear silicate oligomer plays key role in formation of linear C-S-H chain in this study.

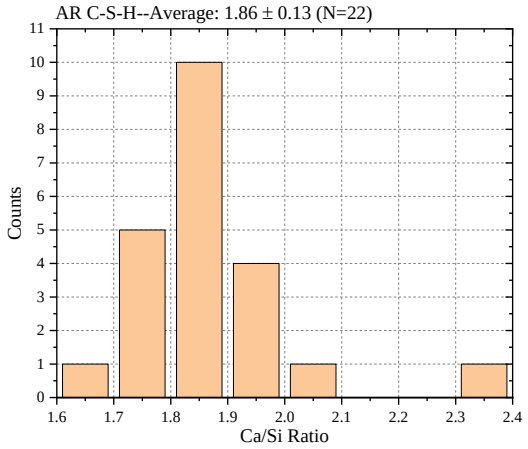

Figure 7-2 Frequency distribution histogram of Ca/Si ratio from TEM-EDX.

Figure 7-2 gives the frequency distribution histogram of Ca/Si ratio calculated from atomic fraction in TEM-EDX. The results show an average Ca/Si ratio of 1.86 ± 0.13 (N=22) is achieved, which again agrees with the results (1.81 ± 0.04, N=60) from similar experiments but under 1 °C [16]. The value of Ca/Si ratio is consistent with the fibrillar-like morphology in Figure 7-1, which is typically shown in C-S-H with a Ca/Si ratio higher than 1.60 [13, 16]. The TEM-EDX results

indicate the C-S-H with an extremely high Ca/Si ratio is successfully synthesised using the proposed method.

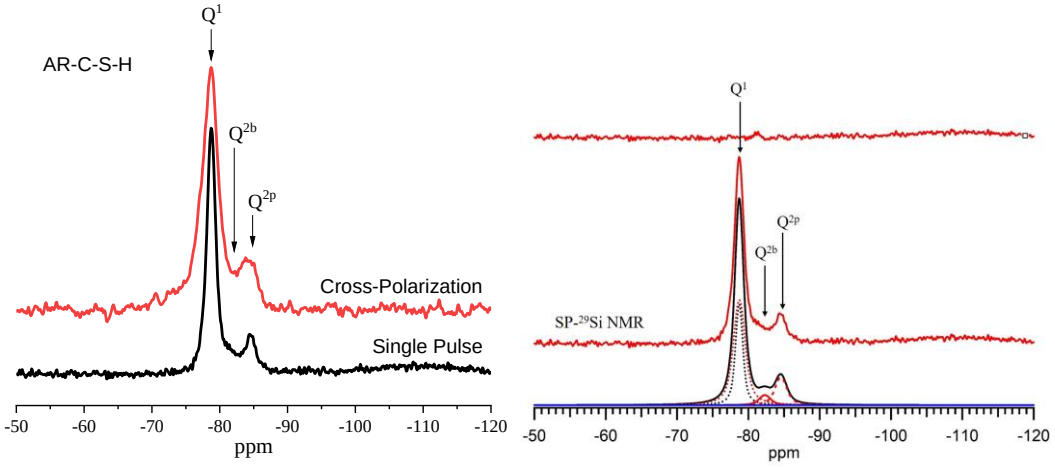

Figure 7-3 ^{1}H-^{29}Si cross polarization (CP)/^{29}Si single pulse (SP) MAS NMR (left) and deconvolution of ^{29}Si SP NMR (right).

Both ^{1}H-^{29}Si CP and single-pulse ^{29}Si MAS NMR of the autoreactor C-S-H is plotted in Figure 7-3 together with the deconvolution of SP-spectrum. The cross polarization happens only when the Hartman-Hahn condition is achieved and the theory of ^{1}H-^{29}Si CP applied in C-S-H system is summarised by X. Cong and R. J. Kirkpatrick [221]. Therefore, the ^{1}H-^{29}Si CP MAS NMR is a powerful tool to study the interaction between silicon and proton (i. e. Si-O-H group). However, the contact time will affect the ratio of resonances which restricts the quantitative study of CP NMR [87, 221]. For example, the ^{1}H-^{29}Si CPMAS NMR spectra of the C-S-H with the contact time varied between 0.2 and 30 mS show that the Q^2/Q^1 ratio increases with increasing contact time [221]. Further conclusion [221] shows that the CP peak intensity of both Q^2 and Q^1 reached its highest at around 2 mS, which is then selected to apply in the current study. Figure 7-3 confirms that only Q^2 and Q^1 are present in AR C-S-H sample, in which, the majority silicate unit is Q^1. The CP NMR indicates most Si-O-X group is protonated although the Q^2/Q^1 ratio slightly increased. The deconvolution results of SP ^{29}Si NMR spectrum are Q^1:81.5%; Q^{2b} 4.90%; Q^{2p} 13.6%, which is corresponding to an MCL of 2.51 and again agrees with the MCL of samples synthesised under 1 °C (MCL= 2.40 ~ 2.46) [16].

Since the evidence from ^{1}H-^{29}Si CP NMR indicates the presence of Si-O-H group, the Richardson and Groves' structural chemical formulae of AR C-S-H is assumed at maximum protonation condition, which can be expressed as below:

$$\textbf{AR C-S-H T/CH: } Ca_{2.51}H_2Si_{2.51}O_{8.54} \cdot 2.16Ca(OH)_2 \cdot mH_2O$$

$$\textbf{AR C-S-H T/J: } Ca_{2.34}H_2Si_{2.51}O_{8.54} \cdot (OH)_{4.32} \cdot Ca_{2.33} \cdot mH_2O$$

Due to the presence of silanol groups, the Ca/Si ratio of AR C-S-H can only be achieved by forming Ca-OH (jennite-based) group or finely intermixed with CH. Additional thermal analysis is needed to explain the fitting model and confirm the amount of water molecule content.

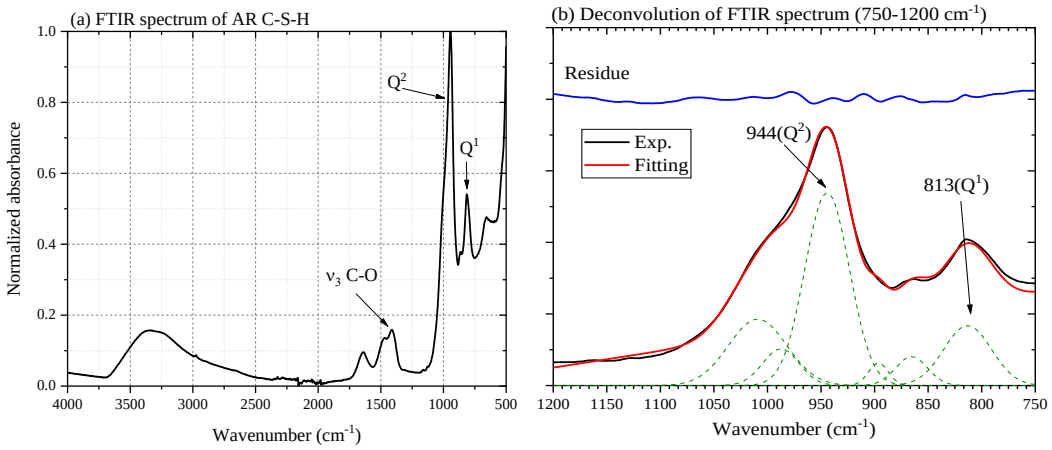

Figure 7-4 ATR-FTIR of autoreactor C-S-H and the deconvolution of Si groups (750-1200 cm^{-1}).

Figure 7-4 gives the ATR-FTIR spectrum of AR C-S-H, with attempts to the deconvolution of silicate group according the existing studies [212, 222]. The peaks shown in FTIR indicate the existing of C-O stretching vibration at ~ 1400-1500 cm^{-1}, typical Si-O asymmetric stretching vibrations of Q^2 at ~ 944 cm^{-1}, and a Si-O signal for Q^1 at ~ 813 cm^{-1}[212]. A broad peak at around 3400 and 1630 cm^{-1} confirms the presence of water molecule, however, no obvious Ca-OH peak can be identified at ~ 3635 cm^{-1} for confirming CH phase [211, 212]. Two interesting things need to be pointed out here: i. The quantitative silicate species obtained by ATR-FTIR are different from that by NMR; ii. The signal of Ca-OH group is present in early-age (2 h) alite sample but absents in AR C-S-H. These findings suggest that more studies need to be done with FTIR technique before strong conclusions can be drawn.

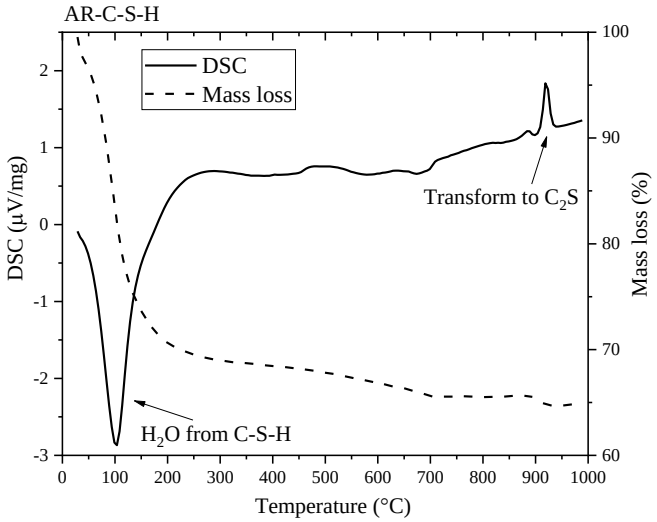

Figure 7-5 TG-DSC curve of autoreactor C-S-H.

The TG-DSC curves of AR C-S-H is given in Figure 7-5 to confirm the CH and water content. The mass loss of water molecules from C-S-H is the main peak in TG curve before around 250 °C [223], which is confirmed from the main endothermic peak in DSC curve. The sample contains almost no CH or CC (calcium carbonate) as no obvious peaks occurred in the temperature interval from 450 to 550 °C or 700 to 900 °C [168, 223]. The key to keep the sample free of CH is to keep the low temperature condition throughout the synthetic process, including the final filtration that is carried out in an ice-bath condition. An exothermal peak at around 920 °C is identified from DSC curve, which is confirmed as the phase transformation to C_2S [16] instead of wollastonite in normal synthetic C-S-H [88]. This conclusion is supported by the ^{29}Si NMR spectrum (Figure 7-27 in Ref.[16]) of the heated AR C-S-H, which only shows Q^0 unit.

Since the evidence shows that no CH is present in the AR C-S-H, T/J model with maximum protonation condition is suitable for the current case. The mass loss of water molecules in C-S-H is 30.10% (before 250 °C), which corresponds to a H_2O/Si = 4.72 (m=11.87). This value is much higher than that of C-S-H(I) or C-S-H(II) prepared from fully reacted bottle-hydrated C_3S [7], indicating a larger interlayer of C-S-H may be achieved or a gentle drying condition is applied when compared to those samples. Therefore, the structural chemical formulae can be written as:

$$\textbf{\textit{AR C-S-H T/J:}}\ Ca_{2.34}H_2Si_{2.51}O_{8.54}\cdot(OH)_{4.32}\cdot Ca_{2.33}\cdot 11.87H_2O$$

The AR C-S-H possesses an MCL of 2.51 and a Ca/Si ratio of 1.86, indicating a mixture of 83% dimer and 17% pentamer jennite-based units[4]. A theoretical Ca/Si ratio of 1.93 can be calculated if perfect J2/J5 units with maximum protonation are present in the system, indicating very small proportion of maximum protonated T2 (Ca/Si ratio=1.0) or T5 (Ca/Si ratio=0.8) are also present to achieve the average Ca/Si ratio. The visualized J2 and J5 units are given in Figure 7-6.

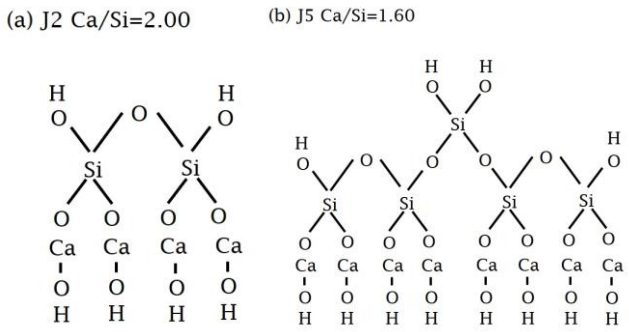

Figure 7-6 Visualization of AR C-S-H compositions: (a) J2 unit with maximum protonation and (b) J5 unit with maximum protonation degree. The AR C-S-H is composed of 83% dimers and 17% pentamers, most of these are J2 and J5 units shown above. Some T2 and T5 units (replace the Ca-OH group in (a) and (b) with 1/2 Ca) are also possibly present to minimise the Ca/Si ratio.

7.1.2 Analysis of filtrates of AR-C-S-H

Table 7-1 summarises the chemical composition of the final filtrate of the AR C-S-H together with the thermodynamic calculation results shown in Table 7-2. The Ca concentration in the solution is 28.13 mmol/L, which is much higher than the theoretical (empirical) solubility (23.37 mmol/L according to Equation 9 in Ref.[14]). The high Ca concentration limits the Si concentration in the solution to a value below the equipment testing limit (0.002 ppm or 0.00071 mmol/L). The current solution composition is favourable to form C-S-H with a high Ca/Si ratio. The species distribution in the solution is given in Table 7-2, indicating both $CaOH^+$ and Ca^{2+} species are present. These species help to form the Ca-O layers for both jennite- and tobermorite-based structure. The SI of CH remains -0.38 according to the thermodynamic calculation, which probably is due to the lower pH value and temperature.

[4] The assumption of this calculation is based on no silicate chains are longer than 5. In reality, the octamers (or longer) may be present but remain very low content as suggested by TMS-GPC in OPC (3. Richardson, I.G., *The nature of C-S-H in hardened cements.* Cement and Concrete Research, 1999. **29**: p. 1131-1147.). The latter discussion on the proportions of dimers and pentamers is based on the same assumptions.

Table 7-1 Chemical composition of the final filtrates from AR C-S-H.

Ca (mmol/L)	Si (mmol/L)	pH	Conductivity (mS/cm)
28.13	<0.00071	12.70	9.35 (24.62 mmol)

Table 7-2 Species distribution from thermodynamic calculation (5 °C and 0.00071 mmol is used for Si, (mmol/L)).

Ca^{2+}	$CaOH^{+}$	$H_3SiO_4^{-}$	$H_2SiO_4^{2-}$	H_4SiO_4	ESI(CH)
18.89	9.247	0.000625	0.000083	0.000015	-0.38

7.2 Effect of sodium and aluminium on AR-C-S-H

7.2.1 Effect of sodium on AR-C-S-H: composition and filtrates analysis

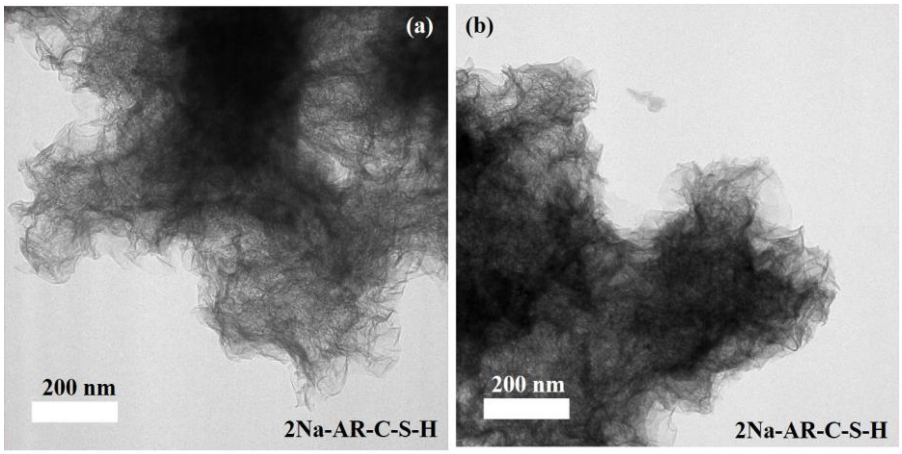

Figure 7-7 TEM images of 2Na-AR C-S-H.

Figure 7-7 shows the morphology of AR C-(Na)-S-H that is synthesised with initial Na/Si bulk ratio of 2.0 (**Appendix F**). Clearly, the morphology changed from fibrillar-like (AR C-S-H in Figure 7-1) to foil-like. The TEM-EDX frequency distribution histograms are plotted in Figure 7-8 for Ca/Si, Na/Si, and Na/Ca atomic ratios. The Ca/Si ratio reduces from 1.86 ± 0.13 for AR C-S-H to 1.447 ± 0.095 (N=17), indicating the potential replacement of Ca^{2+} by Na^{+} or the inhibition of the formation of Ca-OH groups in C-S-H. The Na/Si ratio is only 0.012 ± 0.009 (N=17), which is much lower than the starting bulk ratio of 2, showing that limited sodium ions are incorporated into the C-S-H and most ions are present in the aqueous phase. The Na/Ca ratio is 0.008 ± 0.007 (N=17), indicating most Si-O-X groups are balanced by Ca-containing unit. However, the limited combined sodium together with the altered solution environment changes the morphology and chemical composition hugely.

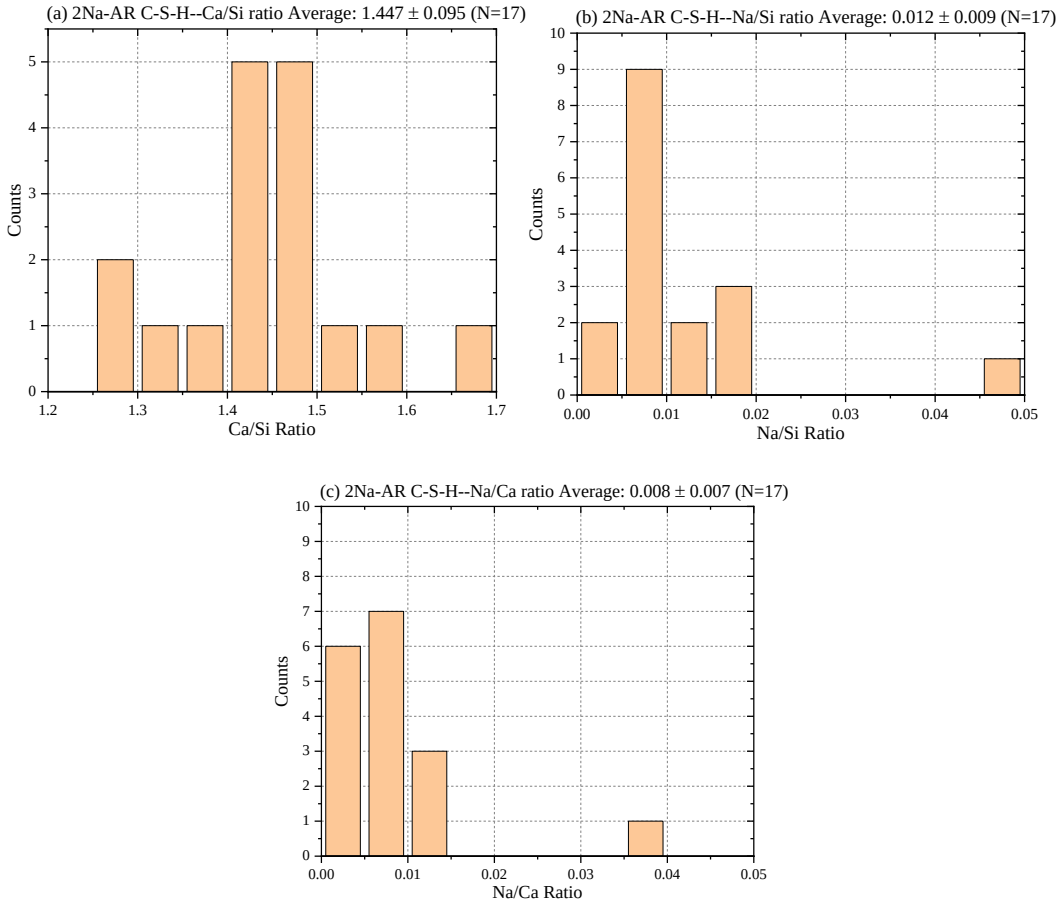

Figure 7-8 Frequency distribution histograms of TEM-EDX of 2Na-AR C-S-H: (a) Ca/Si ratio; (b) Na/Si ratio; (c) Na/Ca ratio.

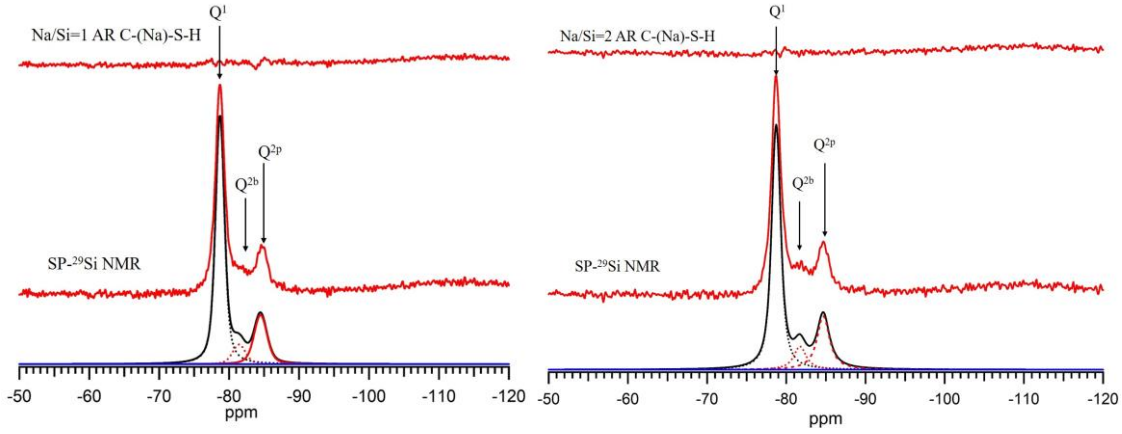

Figure 7-9 Deconvolution of single pulse ^{29}Si MAS NMR spectra of (left) Na-AR C-S-H and (right) 2Na-AR C-S-H.

Figure 7-9 shows the deconvolution results of single pulse ^{29}Si NMR spectra of AR C-(Na)-S-H: a) Na/Si=1: Q^1: 72.5% Q^{2b}: 7.9% Q^{2p}: 19.6% MCL=2.87; b) Na/Si=2: Q^1:68%; Q^{2b} 9.7%; Q^{2p} 22.3%, MCL=3.08. These results indicate that the addition of NaOH reduces the proportion of Q^1 unit and the higher Na content is corresponding to a lower Q^1 content. Therefore, a higher MCL is obtained in the C-S-H with more alkali added.

By combining the results from TEM-EDX and NMR, the structural chemical formulae of 2Na-AR C-S-H can be written based on the assumption of maximum protonation degree from both T/CH and T/J points of view:

2Na-AR C-S-H T/CH: $Ca_{3.08}H_{1.96}Na_{0.04}Si_{3.08}O_{10.25} \cdot 1.39Ca(OH)_2 \cdot mH_2O$

2Na-AR C-S-H T/J: $Ca_{2.72}H_{1.96}Na_{0.04}Si_{3.08}O_{10.25} \cdot (OH)_{2.78} \cdot Ca_{1.75} \cdot mH_2O$

Again, the adaptable model and amount of water molecule need to be confirmed through TG-DSC analysis. Due to the Na/Si ratio from TEM-EDX is ≈ 0.012, 2% (0.04/2) of total Si-O-X group is charge-balanced by Na ions under maximum protonation assumptions.

The existing form of Na in C-Na-S-H is probed by ^{23}Na MAS NMR as plotted in Figure 7-10. Two obvious peaks shown in the samples: i) in the range of -2.19 ~ -1.66 ppm; ii) at 7.30 ppm. In Na-AR C-S-H, only one broad peak centred at -1.66 ppm appears, which further downfield shifts to -2.19 ppm in 2Na-AR C-S-H. This peak should be associated to the charge-balanced Na ions at silicate tetrahedra (i. e. Si-O-Na) [224-227]. This speculation is based on the study of structure of sodium aluminosilicate gels, in which, the aluminium-centred tetrahedra (i. e. Al-O-Na) exhibits a broad resonance centred at ≈ -0.2 ~ -4.2 ppm [226], which is also shifted to higher chemical shift at later age [227]. Additional sharp resonance centred at 7.30 ppm, which is more likely to be associated with a fine crystal. Some possible Na-bearing crystals exhibits the similar resonances peaks, for example, NaCl and NaF at ≈ 7.00 ~ 7.4 ppm [228, 229]; Na1 in Na_2CO_3 at ≈ 7.50 ppm[5] [228]. However, the resonances of NaOH exhibits significant quadrupolar effect, which gives a dual peak shape with the main peak centred at 25.5 ppm [228]. Therefore, the resonance in 2Na-AR C-S-H is not solid NaOH, but possibly assigned to Na_2CO_3 due to the possible carbonation of NaOH.

[5] Na_2CO_3 has two resonances in ^{23}Na NMR spectrum: one sharp peak at ~7.50 ppm and one broad peak with low intensity at -5 ~ -20 ppm, which may be covered by the broad peak centred at -2.19 ppm.

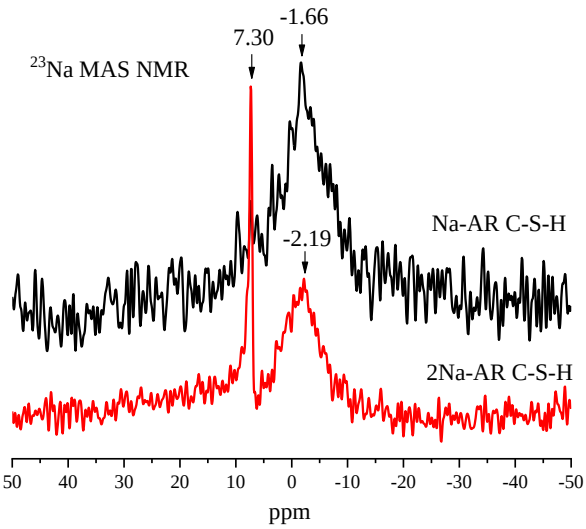

Figure 7-10 Comparison of ^{23}Na MAS NMR of Na-AR C-S-H and 2Na-AR C-S-H.

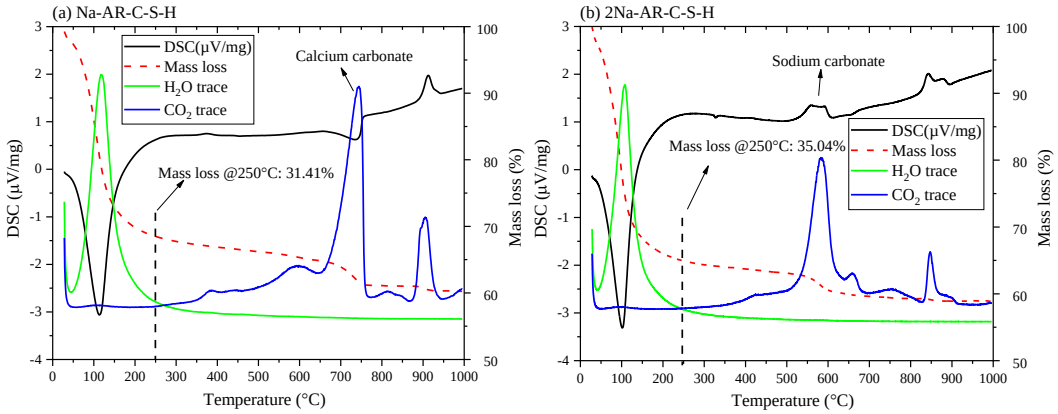

Figure 7-11 TG-DSC curves along with H_2O and CO_2 traces from mass spectroscopy: (a) Na-AR C-S-H; (b) 2Na-AR C-S-H.

Figure 7-11 provides the TG-DSC curves for both (a) Na-AR C-S-H and (b) 2Na-AR C-S-H together with the H_2O and CO_2 traces. The main mass loss before ~ 250 °C again is contributed from the water molecules lost from C-S-H. The H_2O trace clearly shows that no other water is removed from samples, indicating that the sample is free of CH. Two peaks are identified in CO_2 trace curves in both samples. The second peak is again accounted for the transformation to C_2S as discussed in Section 7.1. However, the first peak in Na-AR C-S-H is seen in the range of 650 ~ 750 °C, whilst that in 2Na-AR C-S-H occurs at 500 ~ 650 °C. The first peak should be interpreted as the decomposition of $CaCO_3$ [183, 223], however, the latter in 2Na-AR C-S-H should be linked with the existence of Na_2CO_3 [230], which also agrees with the ^{23}Na MAS NMR results. The formation of Na_2CO_3 is probably due to the Na ions that are adsorbed on the surface of C-S-H, which is further carbonated.

Since no CH is present in 2Na-AR C-S-H, T/J model is more suitable to express the structural chemical formula. The mass loss of water is 35.04%, which corresponds to a H_2O/Si ratio of 4.66 (m=14.35). This value is close to that in AR C-S-H (H_2O/Si=4.72).

2Na-AR C-S-H T/J: $Ca_{2.72}H_{1.96}Na_{0.04}Si_{3.08}O_{10.25} \cdot (OH)_{2.78} \cdot Ca_{1.75} \cdot 14.35H_2O$

The MCL of 2Na AR C-S-H is 3.08, which corresponds to a mixture of 64% dimers and 36% pentamers. Assuming all centred silicate tetrahedra are charged-balanced by Na (this assumption is based on the discussion on ^{23}Na MAS NMR from Refs. [224-227], which is used as a comparison), a Na/Si ratio of 0.23 can be theoretically calculated, which is much larger than the real Na/Si ratio (≈ 0.012) from TEM-EDX. This difference indicates that the Si-O-X group is favourable for protonation instead of combining Na ions (≈ 5.23% Si-O-Na). Since the Ca/Si ratio is only 1.45, more T2 and T5 units compared to AR C-S-H should be present in this sample. Therefore, the foil-like morphology may be linked with the increased proportion of tobermorite-based unit.

Table 7-3 Chemical composition of the final filtrates from (2)Na-AR C-S-H.

	Ca (mmol/L)	Na (mmol/L)	Si (mmol/L)	pH	Conductivity (mS/cm)
Na/Si=1	23.57	2.81	<0.00071	12.85	9.50
Na/Si=2	23.10	4.35	<0.00071	12.90	9.64

Note: the conductivity cannot be linked directly with Ca concentration due to the presence of other ions;

Table 7-4 Species distribution from thermodynamic calculation (5 °C and 0.00071 mmol is used for Si, (mmol/L)).

	Ca^{2+}	$CaOH^+$	Na^+	$H_3SiO_4^-$	$H_2SiO_4^{2-}$	H_4SiO_4	ESI(CH)
Na/Si=1	13.79	9.78	2.81	0.000599	0.000110	0.00001	-0.32
Na/Si=2	12.87	10.23	4.35	0.000588	0.000121	0.00001	-0.30

Table 7-3 summarises the chemical compositions of filtrates from Na-doped AR C-S-H. Compared to filtrate from AR C-S-H, less Ca ions are present in the solution. Meanwhile, a higher Na concentration leads to a lower Ca concentration due to the common ion effect. The Na concentrations in solution indicate that limited Na is charge-balanced in the structure of C-S-H, which agrees with the low Na/Si ratio from TEM-EDX. The pH values of filtrates slightly increase due to the presence of some sodium ions. The distribution of species in the solution shows that the Ca^{2+} ions is lower but $CaOH^+$ unit slightly increases due to the higher pH value

when compared to that in AR C-S-H. The effective SI of CH remains negative, indicating an undersaturation of CH in the solution.

7.2.2 Effect of aluminium on AR-C-S-H: synthetic process and filtrates analysis

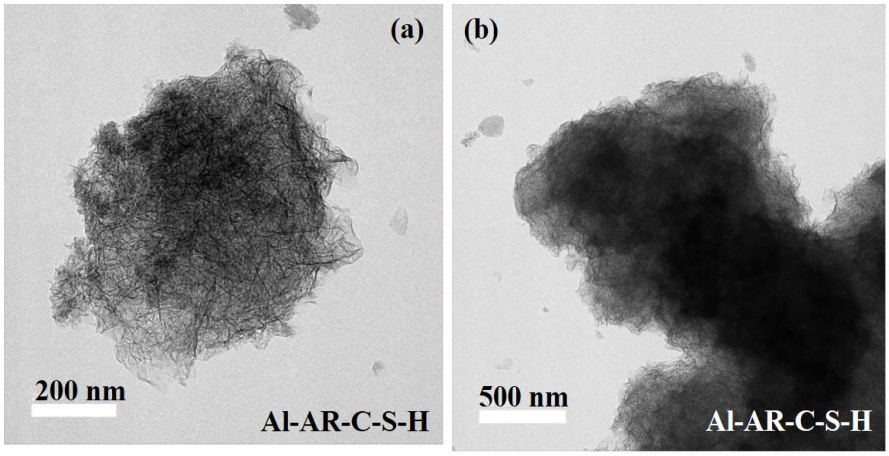

Figure 7-12 TEM images of Al-AR C-S-H.

Figure 7-12 shows the morphology of Al-doped AR C-(A)-S-H with initial bulk Al/Si ratio of 1 (**Appendix F**). It shows an entire foil-like morphology and differs from the fibrillar-like AR C-S-H. The frequency distribution histograms of Ca/Si, Al/Si, and Al/Ca ratios are given in Figure 7-13, which show an average value of 1.495 ± 0.114 (N=19), 0.037 ± 0.010 (N=19), and 0.025 ± 0.007 (N=19). The Ca/Si ratio again is much lower than that of AR C-S-H, indicating the changing of Ca-O layer or the MCL in obtained C-A-S-H. Meanwhile, the Al/Si ratio is much lower than the starting condition, showing that limited Al is incorporated into the C-A-S-H structure.

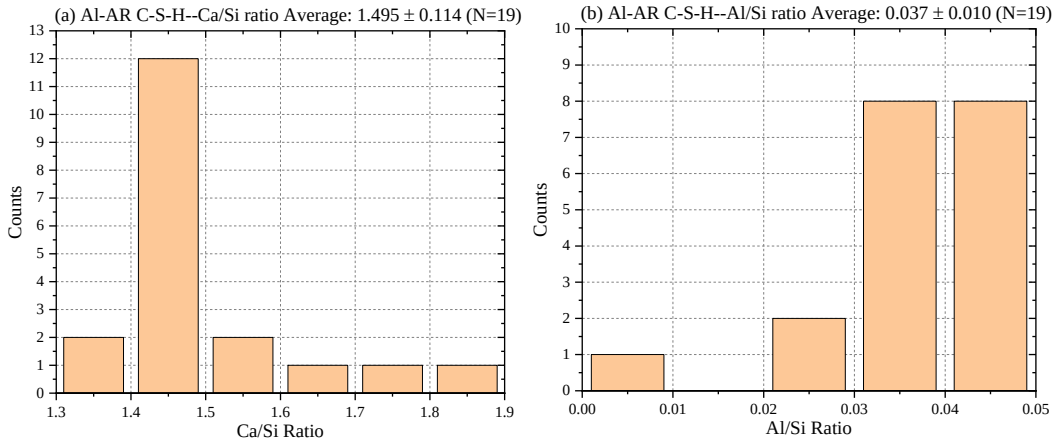

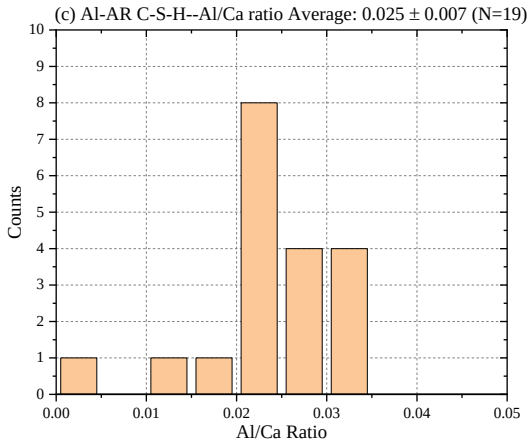

Figure 7-13 Frequency distribution histograms of TEM-EDX of Al-AR C-S-H: (a) Ca/Si ratio; (b) Al/Si ratio; (c) Al/Ca ratio.

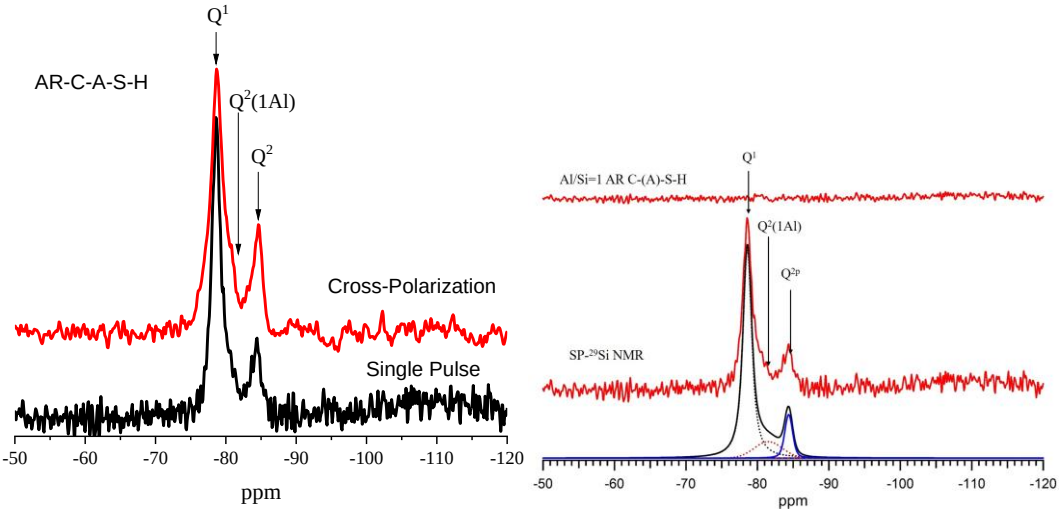

Figure 7-14 ^{1}H-^{29}Si CP/^{29}Si single pulse (SP) MAS NMR (left) and deconvolution of ^{29}Si SP NMR (right).

The structural Si unit is further investigated by both ^{1}H-^{29}Si CP and quantitative ^{29}Si SP MAS NMR as plotted in Figure 7-14. The same CP contact time (2 mS) is applied here and similarly a slightly higher Q^2 tetrahedra peak is identified in CP NMR spectrum along with only slightly lower Q^1/Q^2 ratio when compared to those of SP spectrum. Meanwhile, the Q^2(1Al) peak is more obvious in CP spectrum, indicating that Q^1 may reduce by contrast. The relatively low Q^1 unit seen in CP spectrum indicates that some end-members in the aluminosilicate chains are charge-balanced by Ca^{2+} rather than H^+. The deconvolution results of ^{29}Si SP NMR spectrum are Q^1: 75.1% Q^2(1Al): 13.4% Q^2: 11.5%. The Q^2(1Al) peak is broader than that in NMR spectra of AR C-S-H or AR C-Na-S-H, indicating the incorporation of Al changes the structural units of C-S-H. It should be noticed that the broad Q^2(1Al) resonance also includes the Q^{2b} peak, which cannot be

easily resolved in NMR spectrum [10]. In this case, the Al/Si ratio is calculated as 0.065 from NMR deconvolution, which is larger than the real value.

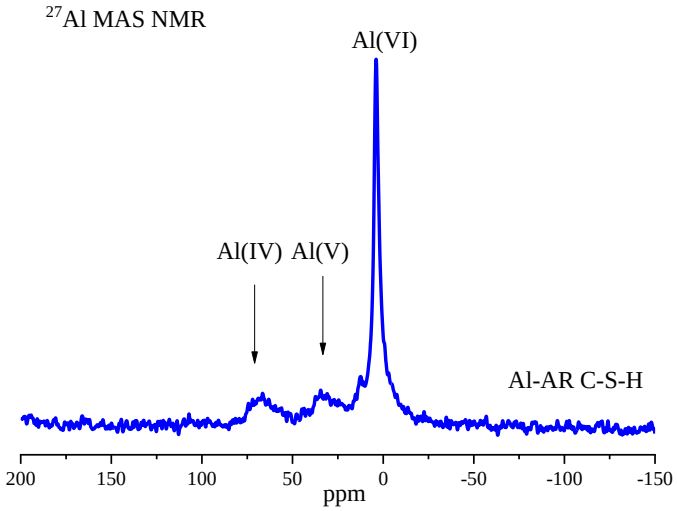

Figure 7-15 ^{27}Al MAS NMR spectrum of Al-AR C-S-H.

^{27}Al MAS NMR spectrum (Figure 7-15) of Al-AR C-S-H shows the coordination of Al in the solid phase. Three resonances can be clearly marked with four to six-coordinated Al-bearing phases. The Al-tetrahedra (four-coordinated) suggests that Al^{3+} substitutes for Si^{4+} in the bridging sites within the *'Dreierketten'* conformation [35, 78, 97, 227, 231]. The five-coordinated aluminium species presented in the interlayer of C-S-H substituting for Ca ions are also identified in Al-AR C-S-H [35, 231]. Finally, the TAH (aluminium calcium hydrates) phases result in the six-coordinated Al resonance [35, 231, 232]. For example, the ^{27}Al NMR spectrum of pure CAH_{10} (Figure 7 in Ref. [232]) gives the same sharp resonance at the similar chemical shift, however, the TAH formed in this study still needs to be confirmed by combining other techniques.

By combining all the results from TEM-EDX and NMR, the structural chemical formulae based on maximum protonation assumption (including the charge-balanced H^+ for Al[IV]) can be written as:

Al-AR C-S-H T/CH: $[Ca_{2.84}H_{2.11}(Si_{0.963}Al^{[4]}_{0037})_{2.84}O_{9.52}] \cdot 1.39Ca(OH)_2 \cdot mH_2O$

Al-AR C-S-H T/J: $[Ca_{2.56}H_{2.11}(Si_{0.963}Al^{[4]}_{0037})_{2.84}O_{9.52}] \cdot (OH)_{2.78} \cdot Ca_{1.67} \cdot mH_2O$

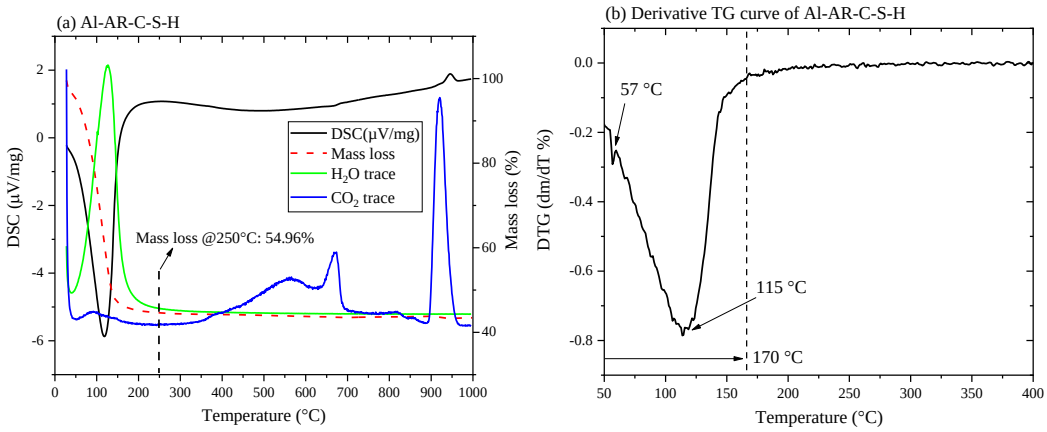

Figure 7-16 TGA of Al-AR C-S-H: (a) TG-DSC curves along with H_2O and CO_2 traces from mass spectroscopy and (b) DTG curve shows the detailed mass loss ranges from 50 to 400 °C.

The TG-DSC results together with H_2O and CO_2 traces are plotted in Figure 7-16 (a) and Figure 7-16 (b) shows the derivative TG (DTG) curve. Undoubtedly, the main mass loss is attributed to the water loss from both C-A-S-H and the TAH phase (as confirmed from NMR). The water trace from mass spectroscopy shows only one main peak and without any water loss in the range of 400 ~ 600 °C, suggesting the absence of CH in this sample. Multiple CO_2 peaks located between 400 ~ 700 °C should be attributed to the slight carbonation or the adsorption of CO_2 [233]. The last CO_2 peak at around 900 °C is linked to the phase transformation of C-S-H, which is similar to all other AR C-S-H above. The DTG shows the main water loss is before 170 °C centred at around 115 °C. This main peak is not only undeniably attributed for C-A-S-H, but also for water in TAH since no additional peaks before 400 °C can be found [234, 235]. Within all TAH phases, only CAH_{10} shows the dehydration temperature mainly between 110 ~ 175 °C, others like C_2AH_8 (170 ~ 280 °C), C_3AH_6 (200 ~ 400 °C) have a higher decomposition temperature [234, 235]. Therefore, mixed TAH in this samples should be CAH_{10}.

From the TG results, no CH is present in the sample, therefore, the T/J model should be selected to describe the structural chemical formulae of this C-A-S-H. The amount of water can be approximately identified through the mass loss (54.96%) from C-A-S-H [6].

Al-AR C-S-H T/J: $[Ca_{2.56}H_{2.11}\left(Si_{0.963}Al^{[4]}_{0.037}\right)_{2.84}O_{9.52}]\cdot(OH)_{2.78}\cdot Ca_{1.67}\cdot 30.37H_2O$

[6] The mass loss here is not only for C-A-S-H, but also include CAH_{10}. In addition, although the charge-balanced ions for Al[IV] is proton as maximum protonation assumption is used, the possible charge-balance ions can also be H_3O^+. Therefore, the water molecules calculated here is not accurate.

Since the MCL of this C-A-S-H is 2.84, which consists of around 72% dimers and 28% pentamers. The difference of Al/Si from NMR (0.065) and TEM-EDX (0.037) indicates that around 56.9% [7] bridging tetrahedra are substituted by Al^{3+} in the C-A-S-H. This value (Al/Si=0.037 from TEM-EDX) is far less than the initial bulk Al/Si ratio, indicating most of other Al may be present in TAH phases or in the solution. Since the maximum protonated J2 and J5(1Al) have the Ca/Si ratio of 2.0, abundant T2 and T5(1Al) (Ca/Si ratio=1.0) are present in the mixture. The ratio of jennite- to tobermorite-based structural units (under the abovementioned assumptions) is around 1.0 (50% to 50%). Surprisingly, the presence of Al promotes the proportion of tobermorite-based structural units, which, in other words, inhibits the formation of Ca-OH group.

The chemical composition of the filtrate from Al-AR C-S-H is given in Table 7-5 together with the thermodynamic calculation results as summarised in Table 7-6. The Al concentration is extremely low in the filtrate because the high Ca concentration and pH value will form the TAH like CAH_{10} as discussed above. Therefore, the Al concentration is below 0.001 mmol/L (detection limitation), which is further used in the thermodynamic calculation [17, 56]. Similar results are also obtained in the study of solution chemistry during C_3A hydration, where 0.003 mmol/L (detection limitation of that equipment) is used when the Al concentration is below the detection limit [17]. The species distribution in the solution is given in Table 7-6, which shows around 10.06 mmol $CaOH^+$ complex in the solution. The effective SI of CH in this filtrate is -0.33.

Table 7-5 Chemical composition of the final filtrates from Al-AR C-S-H.

Ca (mmol/L)	Al (mmol/L)	Si (mmol/L)	pH	Conductivity (mS/cm)
26.13	<0.001	<0.00071	12.80	9.56

Note: the conductivity cannot be linked directly with Ca concentration due to the presence of other ions;

Table 7-6 Species distribution from thermodynamic calculation at 5 °C (0.001 and 0.00071 mmol is used for Al and Si, (mmol/L)).

Ca^{2+}	$CaOH^+$	$Al(OH)_4^-$	$H_3SiO_4^-$	$H_2SiO_4^{2-}$	H_4SiO_4	ESI(CH)
16.07	10.06	0.001	0.000609	0.000100	0.00001	-0.33

[7] The Al/Si ratio from NMR includes the silicate bridging tetrahedra and that from TEM-EDX is believed to be the real Al/Si ratio in C-A-S-H phase.

7.2.3 Comparison of Al/Na- AR C-S-H

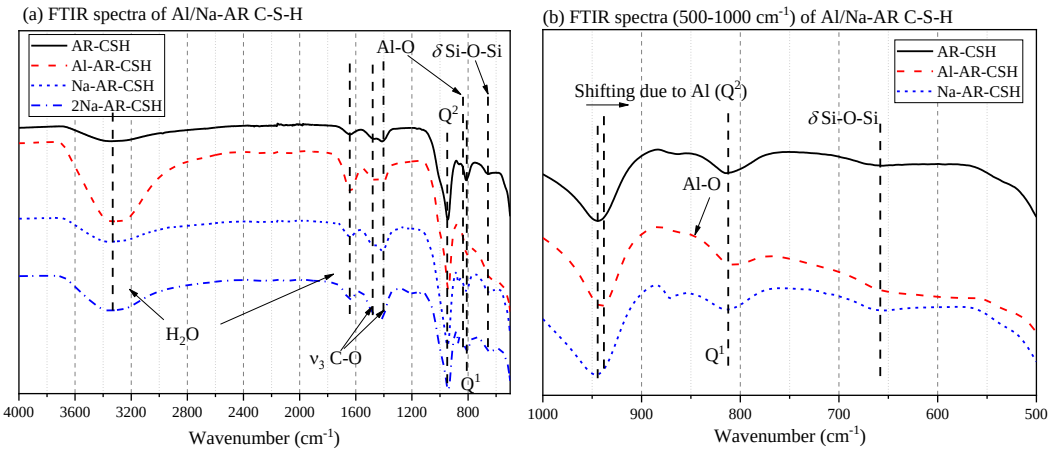

Figure 7-17 FTIR comparison of synthetic C-S-H (a) and the enlarged part of (a) to show the shifting of Q^2 peak due to the presence of Al.

Figure 7-17 shows the comparison of the FTIR spectra of synthetic AR C-S-H. The water peak (~3400 and ~ 1640 cm^{-1}) can be identified from the FTIR spectra as given in Figure 7-17(a), whilst no CH peak can be identified at around 3640 cm^{-1} [211]. Also, the vibration of C-O group can be found in all samples due to the surface adsorption or carbonation. Enlarged FTIR spectra of synthetic AR C-S-H from 500 ~ 1000 cm^{-1} are given in Figure 7-17(b) to show the silicate tetrahedra signals. Similar to NMR, the position of Q^1 does not change, whilst the centred position of Q^2 is shifted to a lower wavenumber due to the incorporation of Al-tetrahedra at bridging sites. Again, the Q^1/Q^2 ratio in FTIR is not consistent with that from NMR.

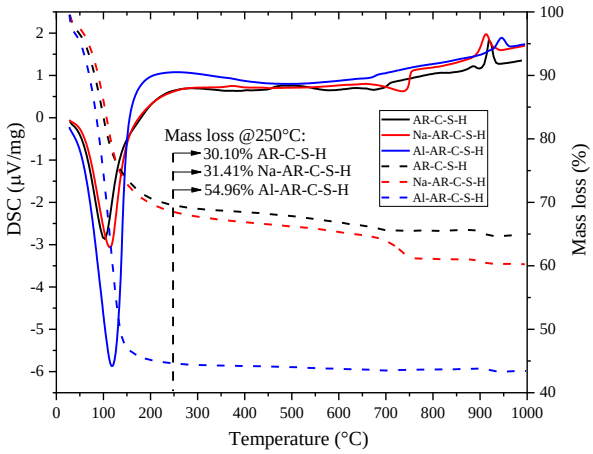

Figure 7-18 Comparison of TG-DSC curves of synthetic C-S-H.

The TG-DSC curves of synthetic AR C-S-H is plotted in Figure 7-18 for comparison. The mass loss of water from C-S-H increased by incorporating either Na or Al. The significant high amount

of water content in Al-AR C-S-H is due to the intermixture with CAH_{10} in the solid phase. The pure C-A-S-H phase that is free of other Al-bearing phases is difficult to synthesise using common methods as summarised by Richardson [7]. Furthermore, the transformation temperature of C-A-S-H is higher than that of other C-S-H because of the substitution of Si by Al.

The addition of NaOH and $Al(NO_3)_3$ will increase the MCL but decrease the Ca/Si ratio of the synthetic C-S-H. The possible mechanism is due to the inhibition of Ca-OH group formation, which changes the jennite-like unit into tobermorite-like structural unit. The increased MCL and decreased Ca/Si ratio result in a decreased proportion of dimers but increased pentamers in Na/Al-AR C-S-H.

7.3 Leaching behaviours of AR-C-S-H in deionized water (DIW)

7.3.1 Characterisations of residues: TG and FTIR

The leaching behaviour of the similar AR C-S-H (synthesised under 1 °C, noted as AR-8) in DIW is also investigated in the previous study [16]. The Ca/Si ratio (TEM-EDX) of that AR C-S-H changes from 1.81 ± 0.04 (N=60) before leaching to 1.20 ± 0.02 (N=28) after leaching. The ^{29}Si NMR deconvolution results show that the proportion of Q^1 units decreases from 83.0% to 43.1%, whilst that of Q^2 units increase from 17.0% to 56.9%, resulting in an increase in MCL from 2.40 to 4.64. Also, the morphology changes from fibrillar-like to entirely foil-like. Since the properties of the AR-8 is very close to the one synthesised in the current study, the TEM-EDX and NMR are not repeated. However, these results [16] are used for discussion in this thesis.

The visualised structural composition of AR C-S-H is given in Section 7.1.1 (Figure 7-6), showing that the AR C-S-H is plausibly made of J2 and J5 units with maximum protonation. The MCL suggests that it is composed of 83% dimers and 17% pentamers, whilst the MCL after leaching indicates that ARL C-S-H-DIW is made of 12% dimers and 88% pentamers. The leaching mechanism can be explained by removing the Ca-O from sublayers of C-S-H, thus reducing the Ca/Si ratio. Based on the compositions of AR C-S-H, the leaching will result in the removal of Ca-OH groups in jennite-like structure. Once all the Ca-OH group is removed from the J2 units, the hydrolysis process of oligomers ($\equiv Si - O - Si \equiv$) may happen or otherwise the

oligomers will remain in the solution [236, 237]. In addition, the J2 or J5 with the omittance of some Ca-OH group are formed in the leached AR C-S-H (ARL C-S-H-DIW) and the percentage of the omitted Ca-OH group is calculated as ~ 26% of all Ca-OH positions in the residues[8]. The represented process of leaching mechanism using J2 unit is illustrated in Figure 7-19(a)-(c) and (d)-(e) shows the possible structural units that are present in ARL C-S-H-DIW.

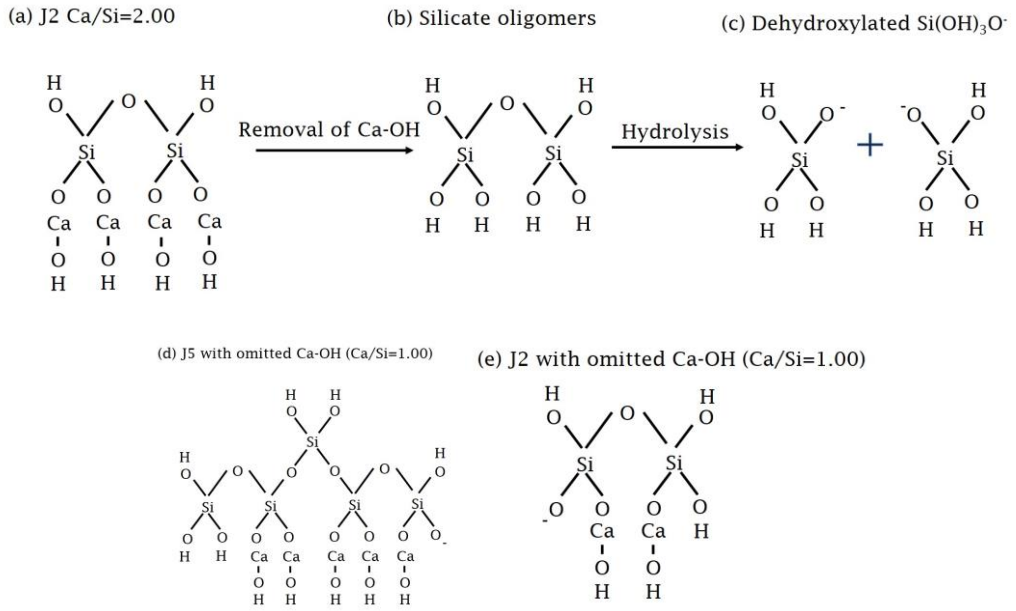

Figure 7-19 Visualization of the leaching mechanism of AR C-S-H, showing the 'removal of Ca-OH' and 'hydrolysis' process using J2 unit as an example. The resulted units are (b) the silicate oligomer and (c) dehydroxylated silicate units that are present in the solution. The residues are composed of some J2 (e) or J5 (d) units that with the omittance of Ca-OH groups, some of the Si-O-X is balanced by H. (d) and (e) are just examples of incomplete jennite units and other formats such like incomplete tobermorite units (T2 and T5) may also present as discussed in Section 7.1.1.

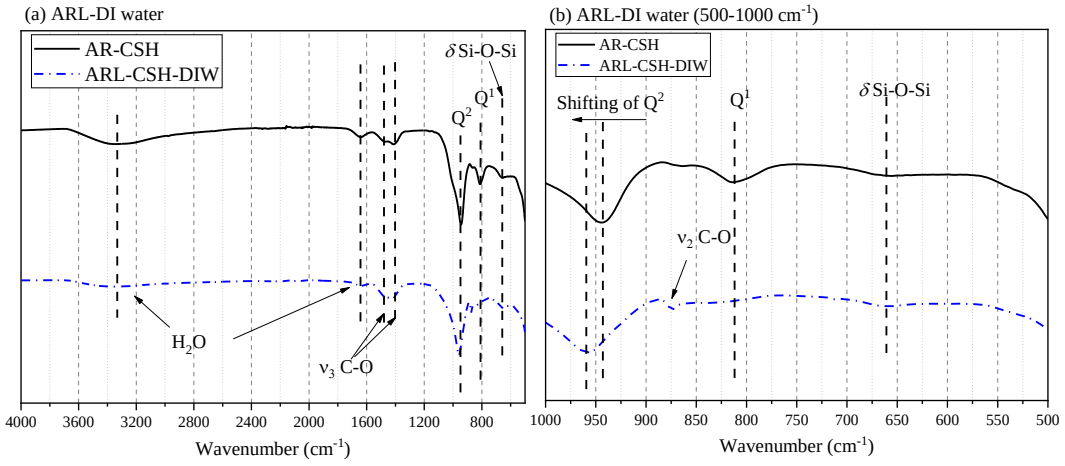

Figure 7-20 Comparison of ATR-FTIR spectra of AR C-S-H before and after leaching. The silicate group area of 500-1000 cm^{-1} is enlarged in (b).

[8] This value is based on the assumption that the J2/J5 in the initial AR C-S-H is saturated with Ca-OH group as discussed in Section 7.1.1. The value then calculated based on the changes of Ca/Si ratio before and after leaching. The 26% is the percentage of all possible interlayer Ca-OH positions in the residue C-S-H.

Figure 7-20 shows the ATR-FTIR spectra of AR C-S-H before and after leaching. Clearly, the H_2O and C-O vibration peaks can be found in both samples. In the enlarged spectrum of silicate groups area, the Q^1 units reduce dramatically after leaching, which is consistent with the NMR results. The peak of Q^2 units also reduce and shows a shifting of centred-position to larger wavenumbers, which indicates the change of charge-balanced groups results in a change of chemical environment of Si-O-Si bonds in Q^2 units. In addition, the Q^2 unit peak is broader, indicating the Q^2-tetrahedra have become more complex (multiple types of Q^2).

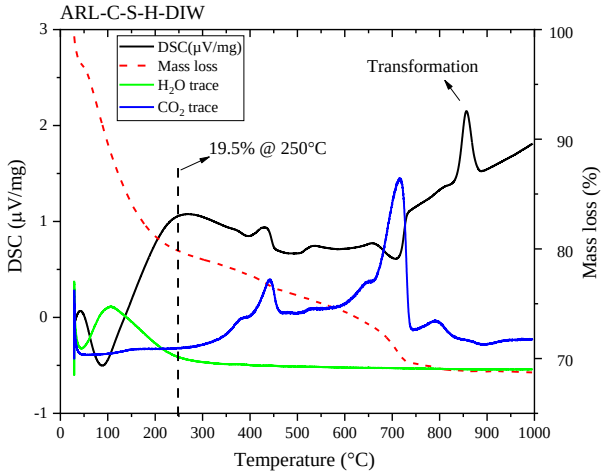

Figure 7-21 TG-DSC curves of ARL C-S-H-DIW together with the H_2O and CO_2 traces.

Figure 7-21 gives the TG-DSC curves of the ARL C-S-H-DIW along with the mass spectroscopy traces during the temperature change. Only one peak is seen in the H_2O trace, which is from the mass loss of water molecules in leached C-S-H. Several peaks appear in the CO_2 trace, indicating the sample is carbonated. The CO_2 peak at ~ 425 °C is associated with an endothermic DSC peak at the similar position (the difference is due to the thermal lag [234]), indicating a phase-transformation occurs. The second CO_2 peak at 600 ~ 750 °C is due to the decomposition of calcium carbonates. The last CO_2 peak at ~ 800 °C is plausibly linked with the transformation, which also happens in all synthetic AR C-S-H. The thermal lag is more obvious in the leached sample when compared to the other C-S-H.

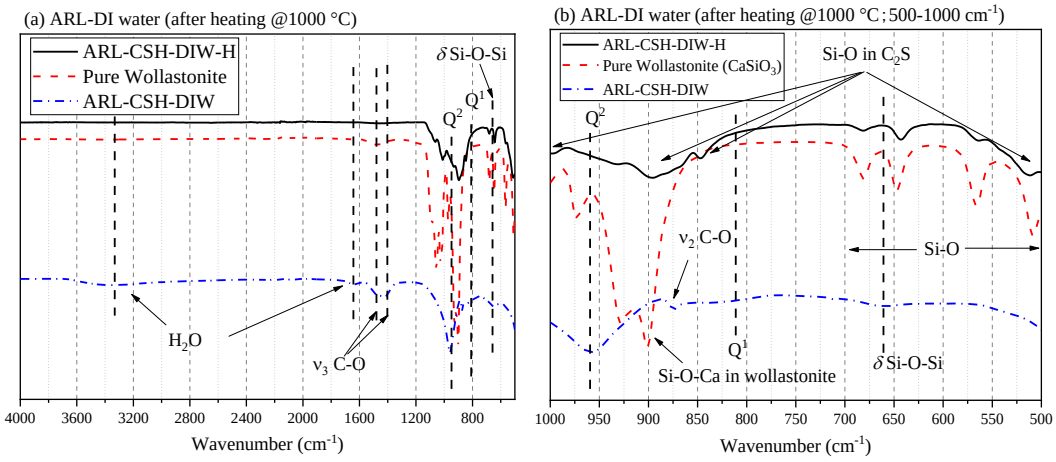

Figure 7-22 FTIR spectrum of ARL C-S-H-DIW after heating, showing the mineralogy change of transformation peak in Figure 7-21.

In order to identify the phases after transformation at ~ 850 °C, the ATR-FTIR test is carried out on the residue of TG analysis. The pure wollastonite spectrum tested under the same condition is also given for a purpose of comparison. The H_2O and C-O vibrations disappear after heating together with more Si-O stretching peaks are shown in the spectrum. Also, the typical Q^1 and Q^2 units disappear, which agrees with the NMR results of heated AR C-S-H (only Q^0 peak appears in the ^{29}Si NMR spectrum) [16]. The wollastonite spectrum shows the typical Si-O-Ca peak [238] which does not appear in heated ARL C-S-H-DIW sample, indicating the leached C-S-H also does not transform to wollastonite. However, the four typical peaks of Si-O in C_2S are all identified in the sample [239], showing that the transformed phase of leached AR-C-S-H after heating remains unchanged.

7.3.2 Solution chemistry of leachate and thermodynamic calculations

The chemical composition of the leachate is analysed through ICP-OES and the results are summarised in Table 7-7. The initial pH value increases from 7.00 to 11.66 due to the leaching of Ca-OH groups as expected. Meanwhile, the Ca concentration is far higher than the Si, which is consistent with the low Ca/Si ratio of leached AR C-S-H, indicating more Ca-OH is dissolved into the DIW compared to Si-O-X groups. This phenomenon also agrees with the proposed leaching mechanism above, indicating some incomplete jennite-like C-S-H units remain in the residue (as shown in Figure 7-19).

Furthermore, the ion species distribution in the leachate from AR C-S-H is given through thermodynamic calculation. Clearly, most Ca ions are present as Ca^{2+} and the distribution of Si ions does not include silicate oligomers formats. In addition, the leachate is much undersaturated to CH with an ESI value of -0.77.

Table 7-7 Chemical composition of leachate from AR C-S-H in DIW (20 °C; w/s=150).

Ca (mmol/L)	Si (mmol/L)	pH	Initial pH
6.24	0.144	11.66	7.00

Table 7-8 Species distribution of ions in leachate from AR C-S-H in DIW.

Ca^{2+}	$CaOH^{+}$	$H_3SiO_4^{-}$	$H_2SiO_4^{2-}$	H_4SiO_4	ESI(CH)
5.919	0.321	0.137	0.0043	0.0022	-0.77

7.4 Leaching behaviours of AR-C-S-H in NaOH solutions

7.4.1 Characterisations of residues: TEM, NMR, TG, and FTIR

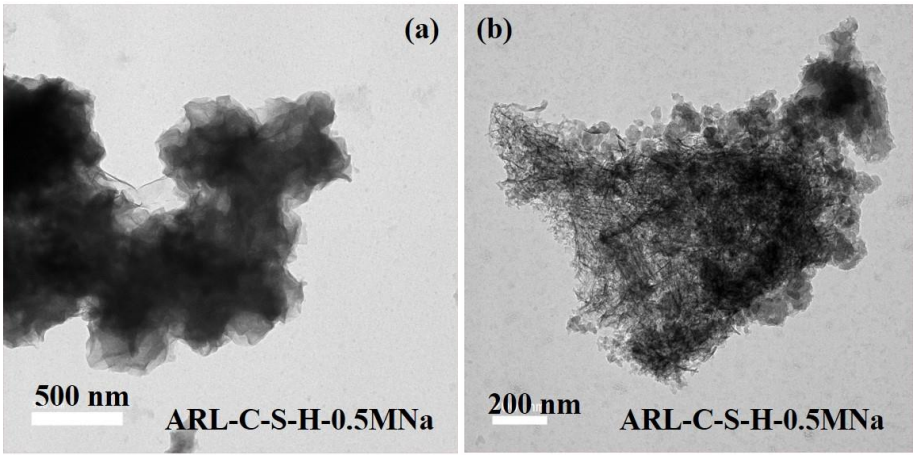

Figure 7-23 Morphology of leached AR C-S-H in 0.5 M NaOH solution (ARL-C-S-H-0.5MNa).

Figure 7-23 shows the foil-like morphology of ARL C-S-H-0.5MNa and the chemical compositions determined by TEM-EDX is given in Figure 7-24. The Ca/Si ratio of ARL C-S-H-0.5MNa reduces from 1.86 ± 0.13 before leaching to 1.474 ± 0.220 (N=18) after leaching, which is because of the removal of Ca-OH groups by leaching or the replacement of Ca by Na ions in some positions. The Na/Si ratio is 0.616 ± 0.219 (N=18), which is much higher than that of 2Na-AR C-S-H, indicating a higher replacement ratio of Na^{+} in C-S-H structure (i. e. Si-O-X or

adsorption) occurs during leaching. Meanwhile, the Na/Ca ratio is 0.427 ± 0.161 (N=18), showing that abundant Na^+ ions are incorporated into the C-S-H structure.

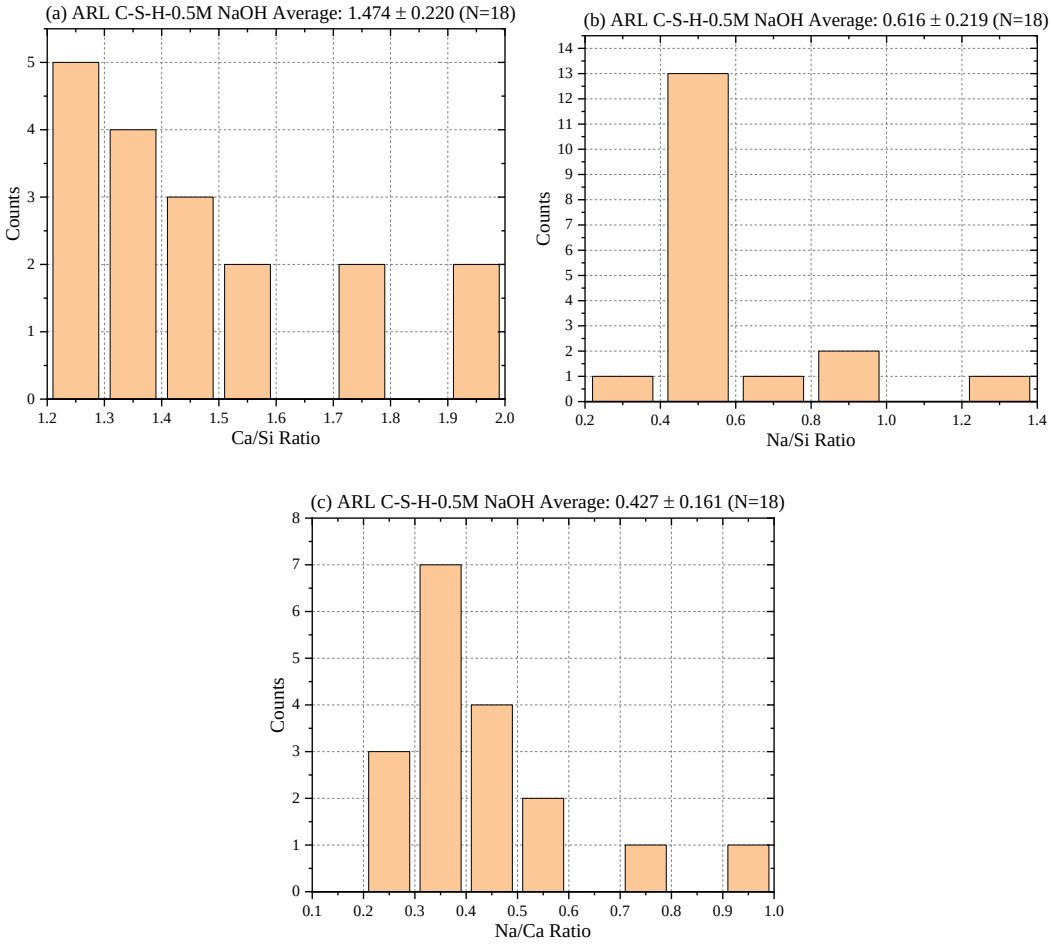

Figure 7-24 Frequency distribution histograms of TEM-EDX of ARL-C-S-H-0.5MNa: (a) Ca/Si ratio; (b) Na/Si ratio; (c) Na/Ca ratio.

In order to study the charge-balanced ions of Si-O-X group, ^{1}H-^{29}Si CP NMR MAS NMR for ARL-C-S-H in NaOH solutions is conducted as plotted in Figure 7-25. The CP NMR spectrum of AR-C-S-H is used as the reference.

As expected, the Q^1 peaks in all samples reduce dramatically with the increased NaOH concentration, indicating a reducing proportion of Si-O-H units in ARL C-S-H. However, the Q^2 peak is affected less than Q^1 in 0.01M NaOH solution, resulting a higher Q^2/Q^1 ratio than that of AR C-S-H. This phenomenon shows that the Na^+ ions prefer to replace the H^+ in the end-member or dimer silicate tetrahedra in C-S-H in NaOH solution with very low concentration (0.01M). In the medium concentration (0.1M), the Si-O-H in Q^2 silicate tetrahedra can be more easily replaced by Na^+ than that in 0.01M NaOH solution, since the Q^2/Q^1 ratio is lower than that of

ARL-C-S-H-0.01MNa. However, the Q^1 tetrahedra is still easier to be replaced as evidenced by a lower Q^1/Q^2 ratio when compared to AR C-S-H. The total-deprotonation happens in AR C-S-H leached in 0.5M NaOH solution as shown in CP NMR spectrum, meaning that all the available Si-O-X groups are charge-balanced by Na^+ instead of proton.

The Na-replace mechanisms can be summarised as follows: i) in low NaOH concentration (0.01M), the 'H' in Si-O-H groups in end-member or dimer (Q^1) tetrahedra are preferred to be replaced by Na^+; ii) in medium NaOH solution (0.1M), the Si-O-'H' groups in either Q^1 or Q^2 tetrahedra are able to be replaced by Na^+, however, those in Q^1 tetrahedra are still easier to be replaced when compare to those in Q^2 units; iii) in high NaOH solution (0.5M), all available Si-O-X position will be balanced by Na^+; iv) leaching will also remove the Ca-OH in the interlayer, the only thing that can be confirmed is that all the available Si-O-H in the interlayer should be charge-balanced by Na^+ in high concentration NaOH solution.

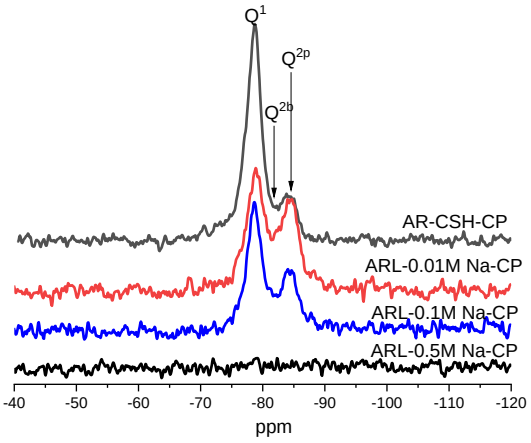

Figure 7-25 ^1H-^{29}Si cross polarization (CP) NMR comparison of AR-C-S-H and its leached residues in 0.01M, 0.1M, and 0.5M NaOH solutions (i. e. ARL-C-S-H-0.01M/0.1M/0.5MNa).

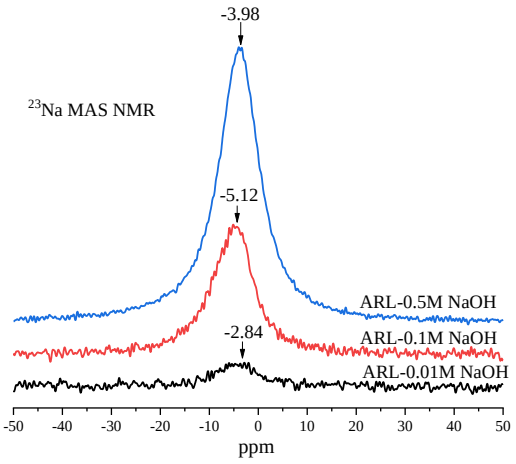

Figure 7-26 ^{23}Na MAS NMR of leached residues in 0.01M, 0.1M, and 0.5M NaOH solutions (i. e. ARL-C-S-H-0.01M/0.1M/0.5MNa).

In order to reveal the structural information of Na^+ in leached samples, ^{23}Na MAS NMR is performed on each sample as shown in Figure 7-26. Only one broad peak in range of -2.84 ~ -5.12 is identified and the peak intensity increases with increasing Na^+ concentration. As discussed in Section 7.2.1, this peak should be associated to the charge-balanced Na ions with silicate tetrahedra (i. e. Si-O-Na) as speculated by Walkley [224-227], indicating the Na^+ is only charge-balanced with Si-O-X group and no other intermixed Na-bearing phase is present in leached C-S-H.

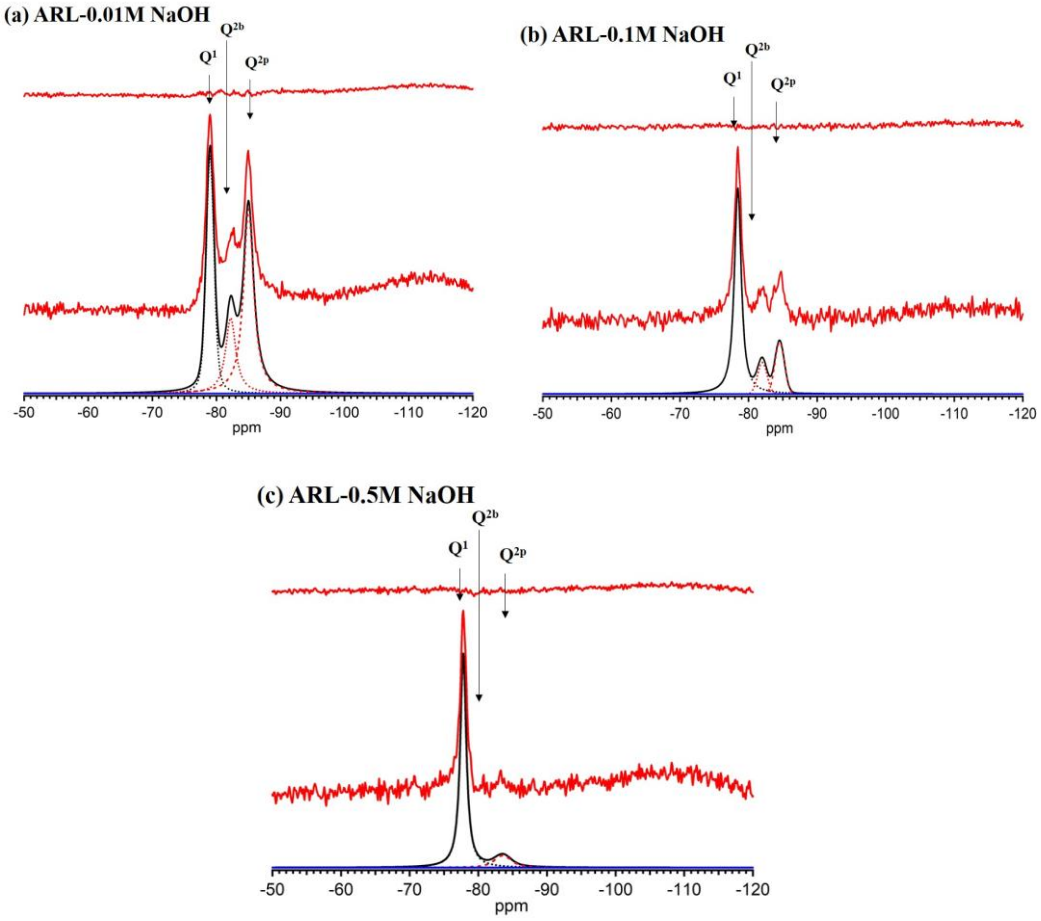

Figure 7-27 Deconvolution of single pulse ^{29}Si MAS NMR of leached residues in 0.01M, 0.1M, and 0.5M NaOH solutions (i. e. ARL-C-S-H-0.01M/0.1M/0.5MNa).

The main silicate structure in ARL-C-S-H-0.01M/0.1M/0.5MNa is explored by ^{29}Si MAS NMR and the deconvoluted spectra are given in Figure 7-27. The deconvolution results of these spectra are summarised in Table 7-9. The NMR results of AR C-S-H and ARL-C-S-H-DIW are also given as the reference. Similar to the leaching behaviour in DIW, the ^{29}Si NMR resonances

of 0.01M NaOH-leached C-S-H show a reduction in Q^1 but an increase in Q^2. The MCL thus increases from 2.51 to 6.07, indicating the leaching behaviour of AR C-S-H in low NaOH concentration is similar to that in DIW. With the increase of NaOH concentration (0.1M), the proportion of total Q^2 is reduced when compared to that in DIW or 0.01M NaOH solution leached sample. The MCL changes from 2.51 to 2.91, indicating smaller amount of Ca is leached from AR C-S-H and more Q^1 groups remain in the residue. In high NaOH concentration (0.5M), the total Q^2 units proportion further reduces and is close to that in AR C-S-H. Meanwhile, the MCL is also shorter than that of original C-S-H, indicating some pentamers may break up.

In summary, the leaching mechanisms in NaOH solutions can be summarised as: i) in low NaOH concentration (0.01M), the leaching behaviour is similar to that in DIW (as discussed in Section 7.3), which mainly behaves as the leaching of Ca-OH groups; ii) in medium (0.1M) and high (0.5M) NaOH concentrations, less Ca-OH groups are removed or the entire C-S-H structure are broken. The main observed behaviour is the replacement of available Si-O-X positions by Na^+; iii) in high NaOH concentration, some pentamers break up and most of Q^1 left in the solid.

Table 7-9 Deconvolution results of single pulse ^{29}Si MAS NMR of leached residues in 0.01M, 0.1M, and 0.5M NaOH solutions.

	Q^1	**Q^{2b}**	**Q^{2p}**	**Q^2 total**	**MCL**	**Ca/Si ratio**
AR C-S-H	81.5	4.9	13.6	18.5	2.51	1.86 ± 0.13
ARL-DIW	43.1*	--	--	56.9*	4.64*	1.20 ± 0.02*
0.01M NaOH	36.0	18.6	45.4	64	6.07	--
0.1M NaOH	72.3	10.5	17.2	27.1	2.91	--
0.5M NaOH	87.4	0.2	12.4	12.6	2.29	1.47 ± 0.22

Note: Data with '*' are taken from Ref.[16], the original AR C-S-H is synthesised with the same method and has 83% Q^1 and 17% Q^2, the leaching condition is same as the current study.

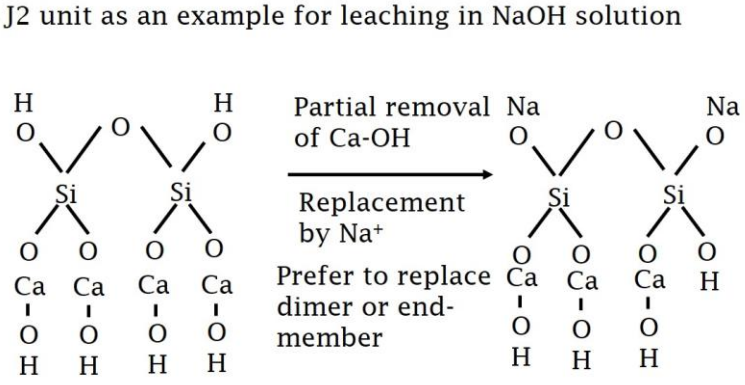

Figure 7-28 Leaching process of a J2 unit in the NaOH solution: partial removal of Ca-OH resulting a reduction in Ca/Si ratio; The replacement of H^+ in Si-O-H by Na^+ gives a high Na/Si ratio and this replacement prefers to start from Q^1; the sub-layer Si-O-X also can be replaced by Na^+.

By combining the results of the TEM and NMR, the leaching behaviours of AR C-S-H in both low and high NaOH concentration solutions are visualised in Figure 7-28. In 0.5M NaOH solution, it is clearly seen that all available positions are charge-balanced by Na^+ (Figures 7-25 and 7-26) and the TEM-EDX results show that the Na/Si ≈ 0.616, given a (Ca+1/2Na)/Si ≈ 1.78. However, this value cannot be compared to the Ca/Si ratio of AR C-S-H since the evidence shows that the AR C-S-H is full protonated and the Ca comes only from the inter Ca-OH layer, whilst the Na^+ can replace both positions of proton and Ca-OH. The MCL of ARL-C-S-H-0.5MNa is only 2.29, suggesting that it is made of 90.3% jennite-based dimers and 9.7% pentamers. The H/Si ratio of J2 and J5 at maximum protonation is 1.0 and 0.8 respectively, suggesting a maximum Na/Si ratio that can be achieved is 0.98 if all the external Si-O-X is balanced by Na, which is far higher than the current Na/Si ratio. The calculation implies that not all the Si-O-'H' is replaced by Na, however, the proportion of Si-O-H cannot give a significant signal in ^1H-^{29}Si CP NMR. Since the Ca/Si ratio reduces from 1.86 to 1.47, suggesting around 21% of Ca-OH groups are removed by NaOH solution. Therefore, the structural chemical formulae can be written in T/J point of view as (the assumptions are maximum protonation and no Na-replaced Ca-OH):

ARL C-S-H-0.5MNa T/J: $[Ca_{2.19}H_{0.59}Na_{1.41}Si_{2.29}O_{7.87}] \cdot (OH)_{2.17} \cdot Ca_{1.18} \cdot mH_2O$

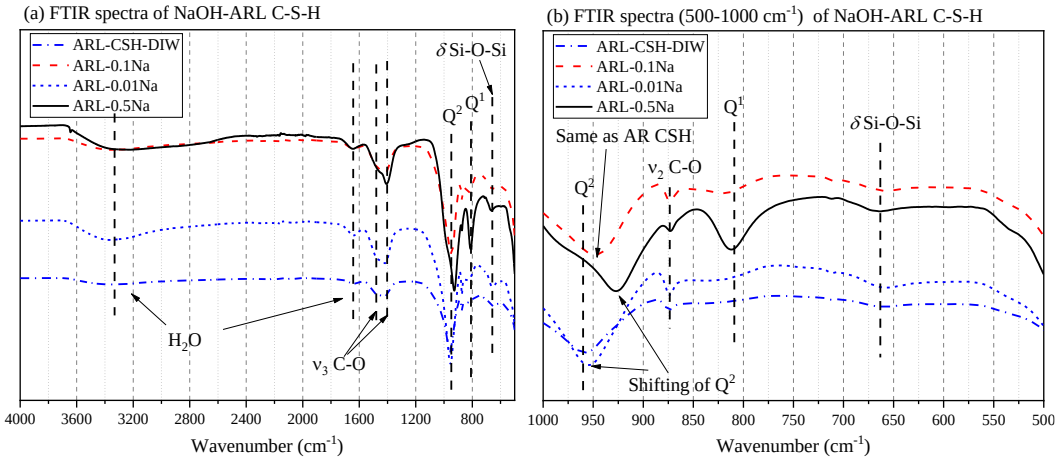

Figure 7-29 ATR-FTIR spectra of (a) comparison of ARL C-S-H-DIW and AR C-S-H leaching in 0.01M, 0.1M, and 0.5M NaOH solutions; (b) enlarged parts of silicate signal wavenumbers.

The ATR-FTIR spectra of ARL C-S-H-0.01/0.1/0.5MNa and the ARL C-S-H-DIW is used as the reference. The common peaks in Figure 7-29(a) in range of 1200 ~ 4000 cm^{-1} are attributed to H-O and C-O vibrations. The Si-species shown in Figure 7-29(b) gives some information that agrees with the ^{29}Si NMR: i) the Q^1 unit of ARL C-S-H-0.01/0.1MNa reduces dramatically; ii) the Q^2 unit of the abovementioned samples increases; iii) The Q^1 unit of ARL C-S-H-0.5MNa remains high. The shifting of Q^2 tetrahedra in the solution is obvious when compared to that of ARL C-S-H-DIW. Specifically, the AR C-S-H leached in 0.01M NaOH solution has a similar Q^2 tetrahedra compared to that leached in DIW, indicating limited Na-replaced Si-O-X groups are present in the leached sample. However, the centred-position of Q^2 tetrahedra shifted to smaller wavenumbers with the increase of NaOH concentration, which is plausibly due to the presence of Si-O-Na structures [240, 241].

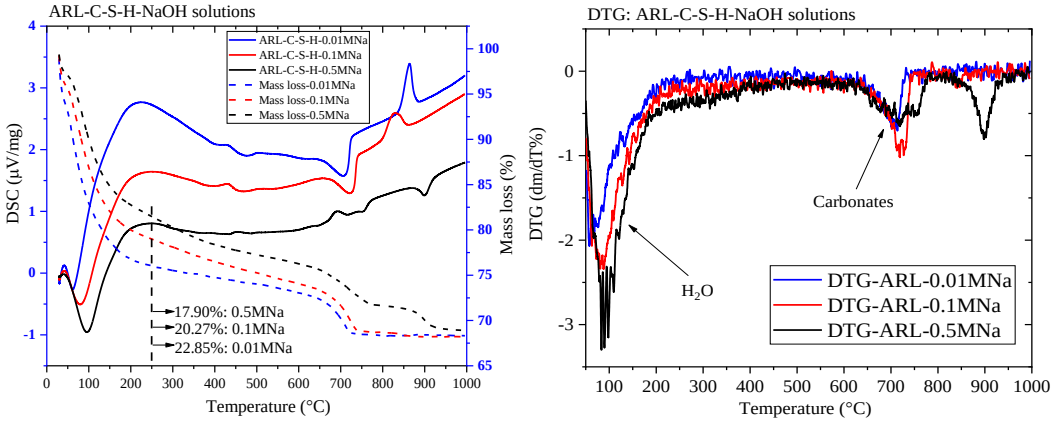

Figure 7-30 TG-DSC-DTG curves of leached residues in 0.01M, 0.1M, and 0.5M NaOH solutions.

The TG-DSC-DTG curves of the AR C-S-H leached in 0.01M, 0.1M, and 0.5M NaOH solutions are drawn in Figure 7-30. The major peak before 200 °C should be identified as the water mass loss from the C-S-H. The water loss gradually reduces from 22.85% for ARL C-S-H-0.01MNa to 17.90% for ARL C-S-H-0.5MNa as the NaOH concentration increases. The second major peak between 600 ~ 750 °C is due to the presence of calcium carbonates, indicating the carbonation occurs during the storage or test. Interestingly, the similar exothermal peaks at ~ 800 °C are found in ARL C-S-H-0.01M/0.1MNa samples, which is attributed to the phase transformation. However, in ARL C-S-H-0.5MNa, no exothermal peaks can be identified and an endothermic peak is confirmed at ~ 920 °C instead. More investigations need to be carried out to

confirm the decomposition phase at this temperature. Based on the mass loss of ARL C-S-H-0.5MNa, the structural chemical formulae can be further calculated as (H_2O/Si=2.09):

ARL C-S-H-0.5MNa T/J: $[Ca_{2.19}H_{0.59}Na_{1.41}Si_{2.29}O_{7.87}] \cdot (OH)_{2.17} \cdot Ca_{1.18} \cdot 4.78H_2O$

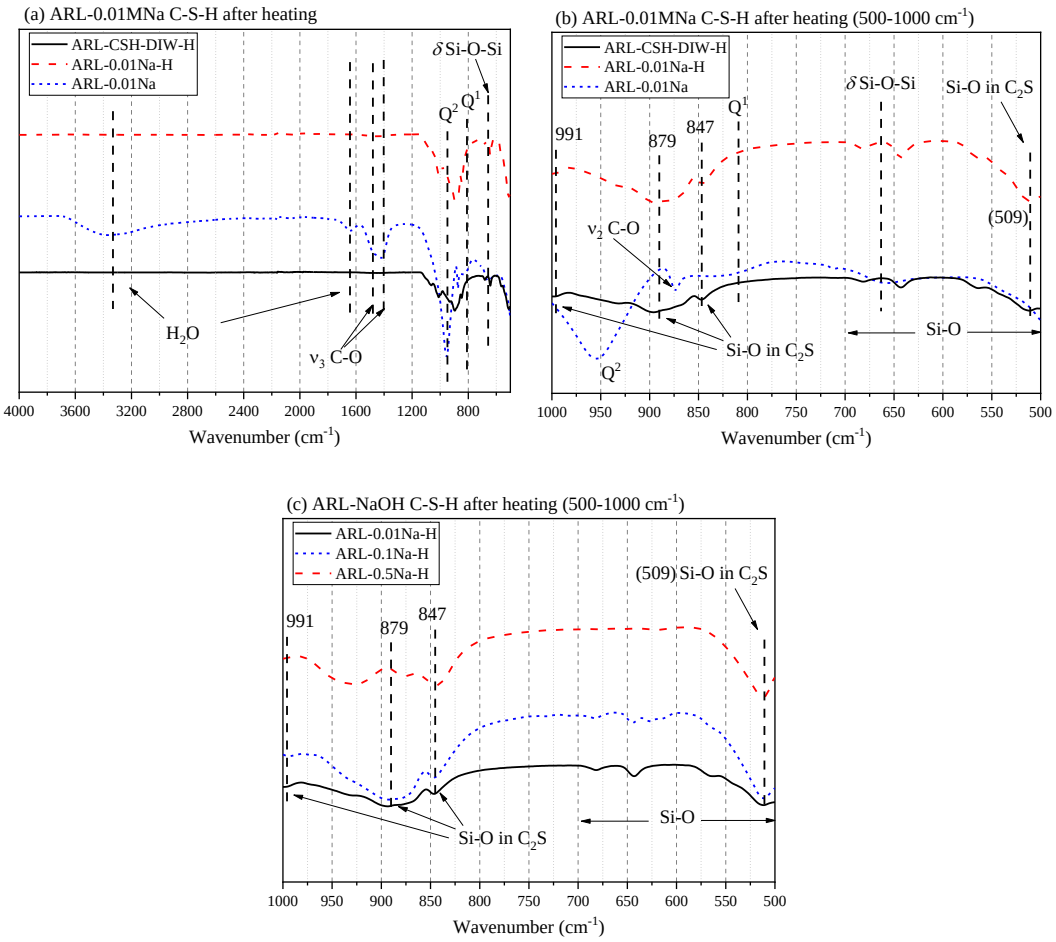

Figure 7-31 ATR-FTIR of ARL-C-S-H-NaOH solutions after heating: (a) comparison with ARL-C-S-H leached in DIW after heating; (b) enlarged silicate signals area of (a); and (c) comparison between ARL-C-S-H in different NaOH solutions.

In order to confirm the phase-transformation related to the exothermal peak in TG curves, ATR-FTIR (Figure 7-31) is carried out for the ARL samples after heating at 1000 °C. The ARL C-S-H-DIW and original ARL C-S-H-0.01MNa are used as the reference in Figure 7-31(a) and (b). Clearly, no water and carbonates are present in the heated samples as shown in Figure 7-31(a) when compared to original ARL C-S-H-0.01MNa. Similarly, the transformed phase is still C_2S as four related Si-O bonds peaks are identified [242]. In the heated ARL C-S-H-0.5MNa, only two peaks (~ 509 and ~ 847 cm^{-1}) related to C_2S can be found, indicating that the phase after heating at 1000 °C is not C_2S and these two related peaks may only link with normal Si-O bonds. The

peak at ~ 930 cm^{-1} is plausibly related to Na-O-Si bond as discussed above, which did not change, indicating a totally different phase formed after heating when compared to other AR(L) C-S-H.

7.4.2 Solution chemistry of leachate and thermodynamic calculations

Table 7-10 Chemical composition of leachates from AR C-S-H in NaOH solutions (20 °C; w/s=150).

	Ca (mmol/L)	Na (mmol/L)	Si (mmol/L)	Ca/Si (sol.)	Final pH	Initial pH
0.01M NaOH	3.33	8.34	0.144	23.13	11.86	11.95
0.1M NaOH	1.64	90.86	0.212	7.74	12.59	12.88
0.5M NaOH	2.30	387.10	0.412	5.58	12.96	13.49

Table 7-11 Species distribution of ions in leachate from AR C-S-H in NaOH solutions.

	Ca^{2+}	$CaOH^{+}$	Na^{+}	$H_3SiO_4^{-}$	$H_2SiO_4^{2-}$	H_4SiO_4	ESI(CH)
0.01M NaOH	3.065	0.265	8.34	0.136	0.067	0.014	-0.73
0.1M NaOH	1.211	0.429	90.86	0.158	0.054	0.0003	-0.43
0.5M NaOH	1.416	0.884	387.10	0.213	0.199	0.0001	-0.21

The chemical composition of the leachates from AR-C-S-H leached in NaOH solutions are explored by ICP-OES and summarised in Table 7-10. Clearly, the Si concentration increases with increased NaOH concentration, indicating more $(SiO_4)Na_x^{(4-x)}$ groups formed in the solution, which come from the entire-decomposition of C-S-H in NaOH solutions. The Ca/Si ratio in the solution decrease from ~ 23.13 in 0.01M NaOH solution to ~ 5.58 in 0.5M NaOH solution, indicating the removal of Ca-OH is the main behaviour of AR C-S-H in 0.01M NaOH, which is similar to the mechanism of C-S-H leaching in water and agrees to NMR results. However, the Ca concentration does not consistently decrease as the NaOH increase. Although the Ca/Si ratio of leachate of ARL C-S-H-0.5MNa is extremely low when compared to others, the Ca concentration is higher than that in 0.1M NaOH leachate. The reason should be attributed to the entire-decomposition of C-S-H, which release more Ca ions. Unlike the entire-decomposition, some incomplete C-(Na)-S-H should be the main composition in the residues. By combining the NMR data, the decomposition in 0.5M NaOH solution will break the pentamers as discussed above.

The ionic species distributions of the ions groups in the leachates are summarised in Table 7-11 and the $(SiO_4)Na_x^{(4-x)}$ groups should be the main ionic group after a jennite-like dimer or pentamer is fully balanced by Na (all Ca-OH are replaced). These sodium silicate solutions will show gel-like characteristics [243]. If there are still Ca-OH left in the dimer or pentamer C-S-H, the phase (Ca-Na-S-H) should keep as the solid and left in the residue.

7.5 Leaching behaviours of AR-C-S-H in $Al(NO_3)_3$ solutions

7.5.1 Characterisations of residues: TEM, NMR, TG, and FTIR

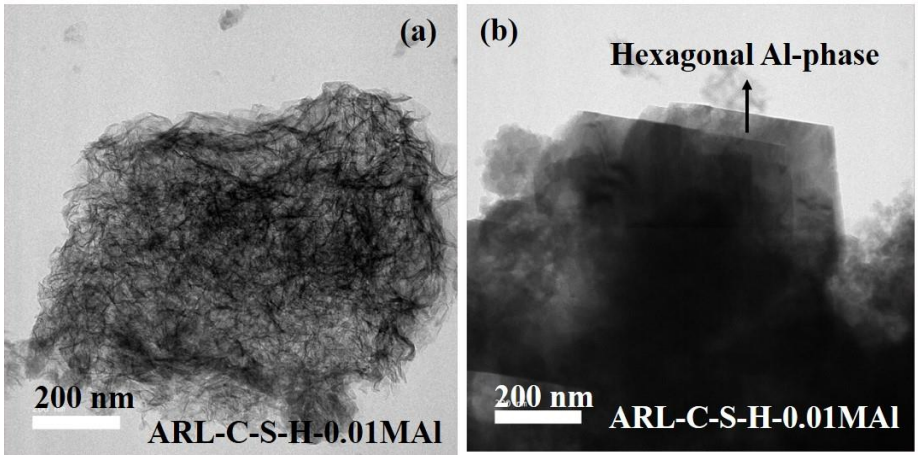

Figure 7-32 Morphology of leached AR C-S-H in 0.01 M $Al(NO_3)_3$ solution (ARL-C-S-H-0.01MAl): (a) typical entire-foil like morphology and (b) a mixture with hexagonal Al-phase, which is plausible CAH_{10}.

Figure 7-32 shows the morphology of AR C-S-H leached in 0.01M $Al(NO_3)_3$ solution: (a) the typical foil-like morphology and (b) a mixture of foil-like C-A-S-H and hexagonal Al-phase. The TEM-EDX frequency distribution histograms are given in Figure 7-33. The chemical compositions of foil-like C-A-S-H phase (Figure 7-32(a)) are summarised in Figure 7-34 (a)-(c) and the Ca/Al ratio of the hexagonal Al-crystal is given in Figure 7-34(d). The Ca/Si ratio of the obtained C-A-S-H reduces to 1.023 ± 0.197 (N=14) and the Al/Si ratio is 0.254 ± 0.074 (N=14), which results a Ca/(Si+Al) ≈ 0.816. This value is therefore much lower than that of ARL C-S-H-DIW (Ca/Si ≈ 1.20), indicating both leaching and Al-Si substitution occur in the current solution environment. The average Al/Ca ratio then comes to 0.258 ± 0.092 (N=14), which is higher than that of the ordinary synthetic C-A-S-H(I) as summarised by Richardson [7]. The Ca/Al ratio of the hexagonal Al-crystal is 0.560 ± 0.088 (N=7), which is quite close to that of CAH_{10}

($CaAl_2(OH)_8(H_2O)_6$). As discussed in Section 7.2, the CAH_{10} may form during the synthetic process, which probably can still form by using AR C-S-H leached in 0.01M $Al(NO_3)_3$ solution.

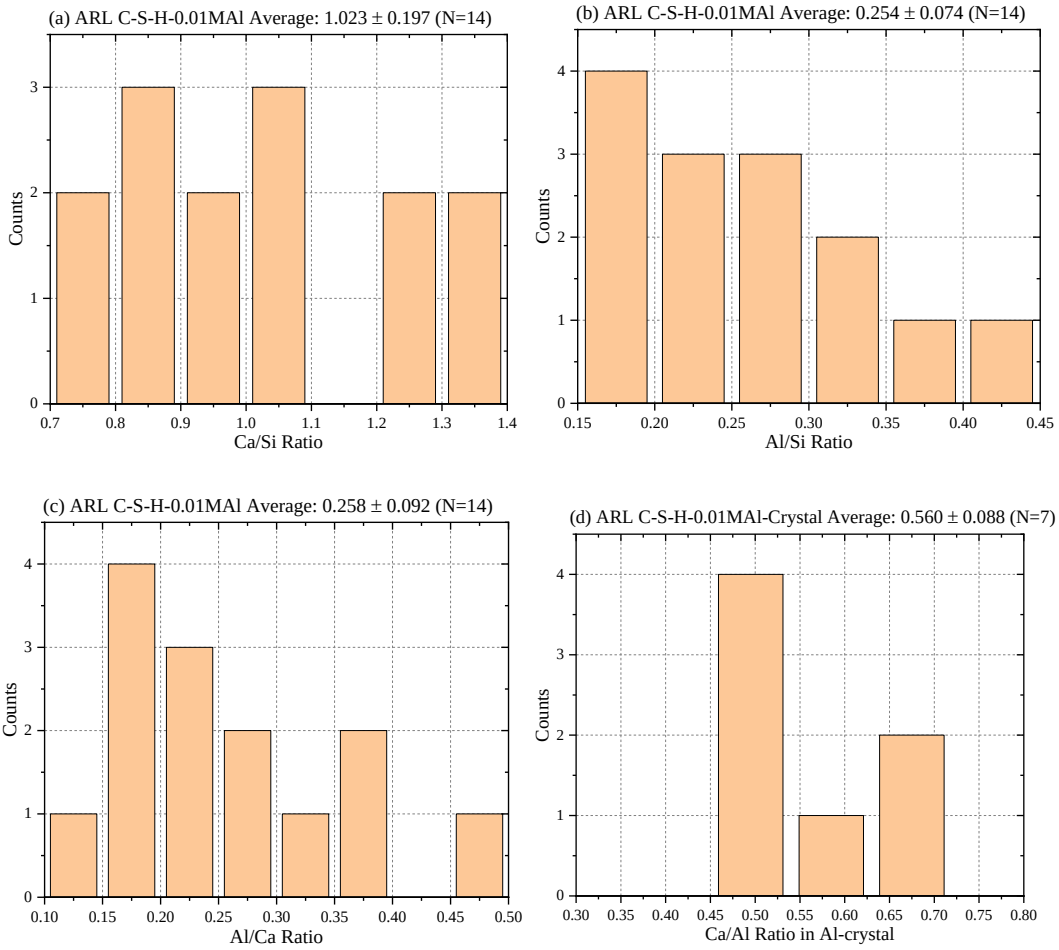

Figure 7-33 Frequency distribution histograms of TEM-EDX of ARL C-S-H-0.01MAl: (a) Ca/Si ratio in foil-like C-A-S-H; (b) Al/Si ratio in foil-like C-A-S-H; (c) Al/Ca ratio in foil-like C-A-S-H; (b) Ca/Al ratio in Al-bearing crystal.

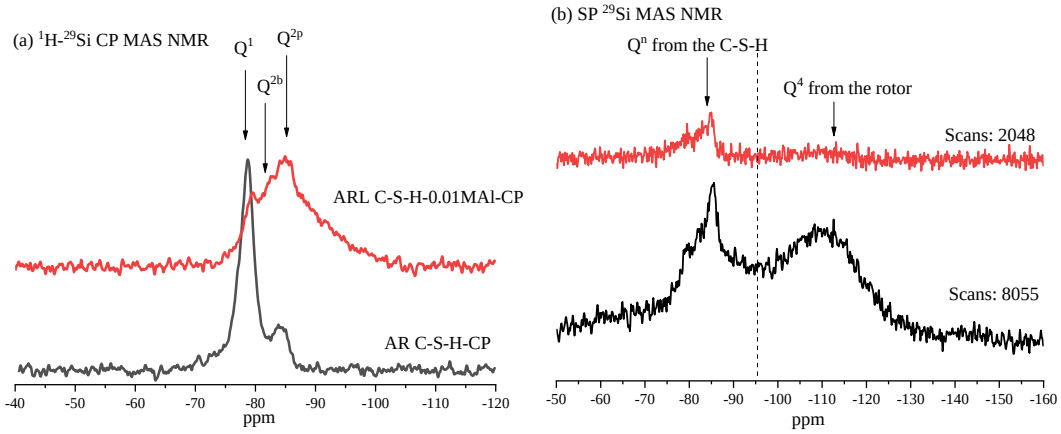

Figure 7-34 (a): A comparison of ^1H-^{29}Si CP MAS NMR of AR-C-S-H and ARL-C-S-H-0.01Mal; (b): Single pulse ^{29}Si MAS NMR spectra of ARL C-S-H-0.01MAl with different scans, the Q^4 is the signal from the rotor. Since the signal of Q^n from the C-S-H is weak at 2048 scans, the 8055 scans are carried out to enhance the signal. Therefore, the Q^4 signal from the rotor is also enhanced, which generated an oblique-line background from -70 to -95 ppm. This background is removed before deconvolution.

Both ^{1}H-^{29}Si CP and ^{29}Si SP MAS NMR (Figure 7-34) are used for revealing the silicate structure in the obtained C-A-S-H. By comparing with the CP NMR spectrum of AR C-S-H (before leaching), the leaching destroys most jennite-like dimer, however, most of Q^2 units remains in the sample. For SP ^{29}Si NMR, only weak signal can be obtained for C-A-S-H after 2048 scans, therefore, a higher number of scans (8055) is used for a better resolution of silicate tetrahedra in C-A-S-H phase. However, a background from rotor (Q^4 at ≈ -112 ppm) results a hump between Q^2 and Q^4. In this case, an oblique-line background is removed before deconvolution (as shown in Figure 7-36). The shape of SP ^{29}Si NMR spectrum is similar to the CP spectrum, indicating only small amount of Q^1 units remain. Combining the CP and SP NMR results, it is speculated that all jennite-based dimers are gone in ARL C-S-H-0.01MAl. The reason should be attributed to the $Al(NO_3)_3$ solution, which generates abundant H^+ during the hydrolysis of $[Al(H_2O)_6]^{3+}$ groups, followed by a replacement of Ca-OH units by proton in all dimers. If all the Ca-OH groups are replaced by proton in dimer, then the hydrolysis of the oligomer silicates will keep these units in the solution. The process of decomposition of jennite-based dimer in $Al(NO_3)_3$ solution is visualised in Figure 7-35.

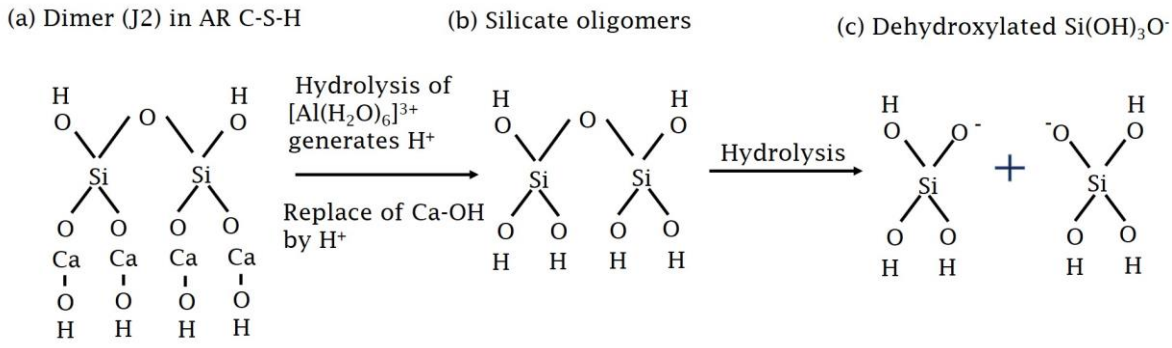

Figure 7-35 Decomposition of J2 in AR C-S-H by leaching in $Al(NO_3)_3$ solution. It is suspected all dimers are removed from the AR C-S-H after leaching. In addition, both (b) silicate oligomers and (c) dehydroxylated $Si(OH)_3O^-$ are present in the leachate.

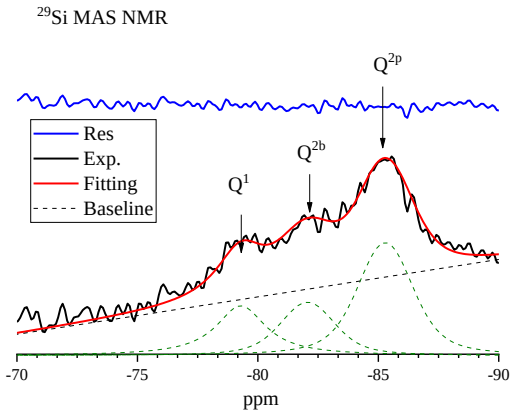

Figure 7-36 Deconvolution of Single pulse ^{29}Si MAS NMR of ARL C-S-H-0.01MAl.

The deconvolution of SP ^{29}Si MAS NMR of ARL C-S-H-0.01MAl after removing the background is given in Figure 7-36, resulting 24.87% Q^1, 29.97% Q^{2b} (or Q^2(1Al)), and 51.15 Q^{2p}. The deconvolution result gives an MCL of ≈ 9.0 and an Al/Si ratio of ≈ 0.12. The Al/Si ratio from NMR is much lower than that from TEM-EDX, indicating the intermixture of micro Al-crystals with C-A-S-H.

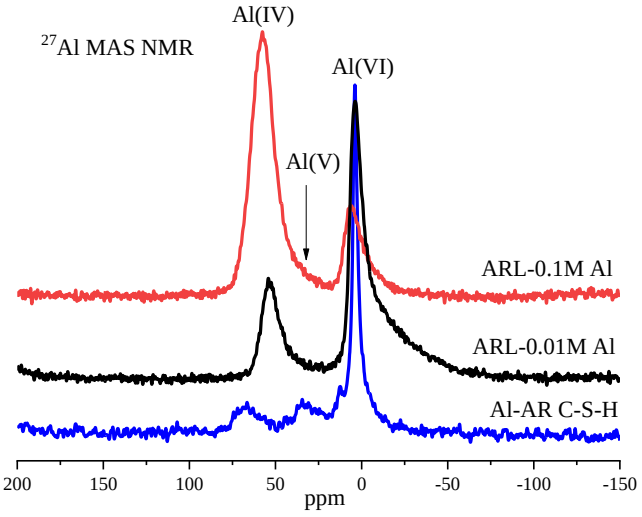

Figure 7-37 ^{27}Al MAS NMR of ARL C-S-H-0.01/0.1MAl and that of Al-AR-C-S-H is given as the reference. The sample ARL C-S-H-0.1MAl is only enough, therefore, only the ^{27}Al MAS NMR is carried out for the solid residue.

^{27}Al MAS NMR spectra (Figure 7-37) of ARL C-S-H-0.1/0.01MAl shows the coordination of Al in the solid phase and that of Al-AR C-S-H is used as the reference. The similar TAH resonance is shown in all samples, and the resonance of Al[IV] becomes more significant when leaching in Al solutions. This TAH peak is therefore linked to CAH_{10} as evidenced by the TEM-EDX (Figure 7-33(d)) and TG curve (Figures 7-16, 7-39). Meanwhile, the peak of Al[V] is not

shown (covered by Al[IV] peak), indicating limited five-coordinated Al is found in ARL C-S-H-Al samples.

By combining the Ca/Si ratio from TEM-EDX and the deconvolution results from NMR, the structural chemical formulae of this C-A-S-H from T/J point of view based on maximum protonation assumption is (the charge-balance ions for Al[4] is assumed to be proton):

$$\textbf{\textit{ARL-0.01MAl T/J:}}\ [Ca_{6.67}H_{2.99}\left(Si_{0.89}Al^{[4]}_{0.11}\right)_{9.00}O_{28.01}]\cdot(OH)_{4.99}\cdot Ca_{4.83}\cdot mH_2O$$

The results suggest that ARL C-S-H-0.01MAl is a mixture of incomplete J5, J8, and J11.

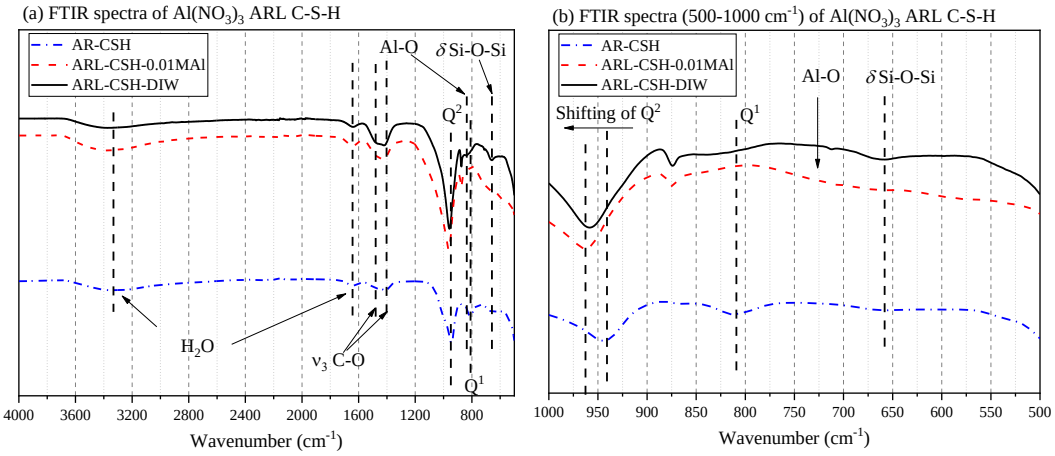

Figure 7-38 ATR-FTIR of ARL C-S-H-0.01MAl and AR C-S-H and ARL C-S-H-DIW are used as the reference.

The ATR-FTIR of ARL C-S-H-0.01MAl is given in Figure 7-38 together with those of AR C-S-H and ARL C-S-H-DIW as the reference. The spectrum shows that most of Q^1 is removed during the leaching, and the peak of Al-O appears at ~ 725 cm^{-1} [244]. The Q^2 peak shifts to a higher wavenumber, which is even further than that in ARL C-S-H-DIW.

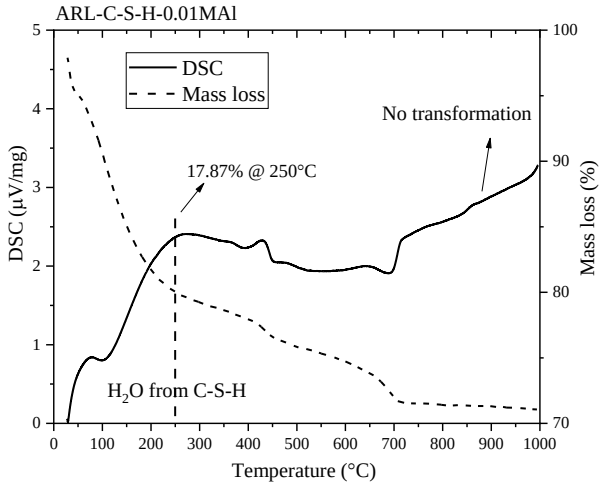

Figure 7-39 TG-DSC curves of ARL C-S-H-0.01MAl.

The TG-DSC curves of ARL C-S-H-0.01MAl is given in Figure 7-39. The first main peak of mass loss is associated with the water loss from C-A-S-H, which is 17.87%. Followed by a phase transformation between 400 ~ 500 °C, which is not CH because the corresponding DSC peak is exothermic. The third peak between 600 ~ 700 °C is the decomposition of carbonates. However, no phase transformation is found at around 800 ~ 900 °C.

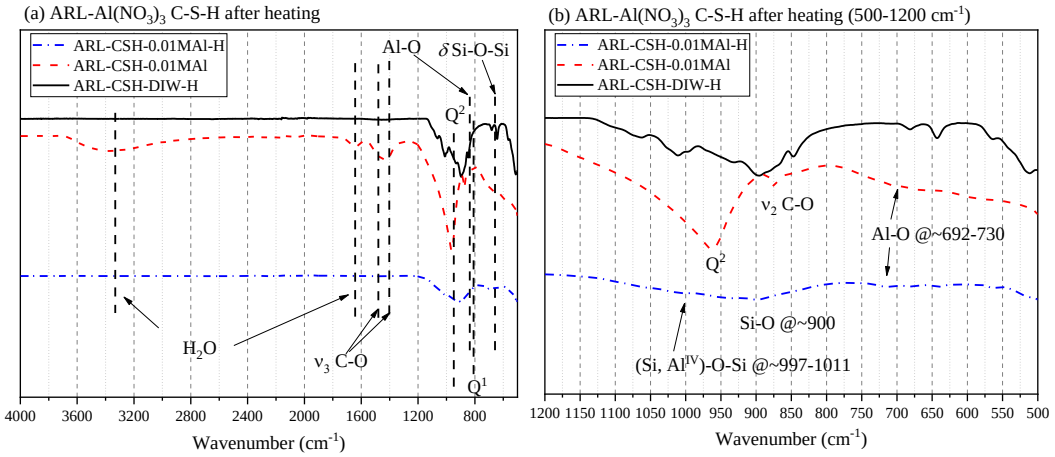

Figure 7-40 ATR-FTIR of ARL C-S-H-0.01MAl after heating and ARL C-S-H-0.01MAl/ARL C-S-H-DIW-H are used as the reference.

The ATR-FTIR spectrum of ARL C-S-H-0.01MAl after heating at 1000 °C is shown in Figure 7-40. Unlike the peak-change in heated ARL C-S-H-DIW sample, all C_2S related peaks are not identified in heated ARL C-S-H-0.01MAl. A broad (Si, Al[4])-O-Si peak at ~ 997~1011 cm^{-1} is shown in the heated sample, indicating the Al-/Si-tetrahedra structure are still present in the sample after heating.

7.5.2 Solution chemistry of leachate and thermodynamic calculations

Table 7-12 Chemical composition of leachates from AR C-S-H in $Al(NO_3)_3$ solutions (20 °C; w/s=150).

	Ca (mmol/L)	Al (mmol/L)	Si (mmol/L)	Final pH	Initial pH
0.01M $Al(NO_3)_3$	17.62	<0.001	0.246	10.15	3.69
0.1M $Al(NO_3)_3$	37.88	24.45	3.924	3.09	3.27

Table 7-13 Species distribution of ions in leachate from AR C-S-H in $Al(NO_3)_3$ solutions.

	Ca^{2+}	$CaOH^+$	Al^{3+}	$Al(OH)_4^-$	$H_3SiO_4^-$	$H_2SiO_4^{2-}$	H_4SiO_4	ESI(CH)
0.01M $Al(NO_3)_3$	17.59	0.025	--	0.001	0.166	0.080	0.0002	-1.65
0.1M $Al(NO_3)_3$	37.88	--	24.36	--	0.392	--	--	-6.31

The chemical composition of the leachates of ARL C-S-H-0.1/0.01MAl is given in Table 7-12. As expected, some C-S-H phases are decomposed in the acid solutions, results a very high Ca and Si concentration when compared to other samples. With the increase of $Al(NO_3)_3$ concentration, the higher Ca and Si concentrations are achieved, showing that more C-S-H are decomposed in the solution. However, even with the high Ca concentration existing in the leachates, most of Ca elements stay in the format of Ca^{2+}. In addition, the ESI of CH remains at a very low level.

7.6 Discussions on the relationships between the nature of C-S-H and the solution environment in synthetic C-S-H systems

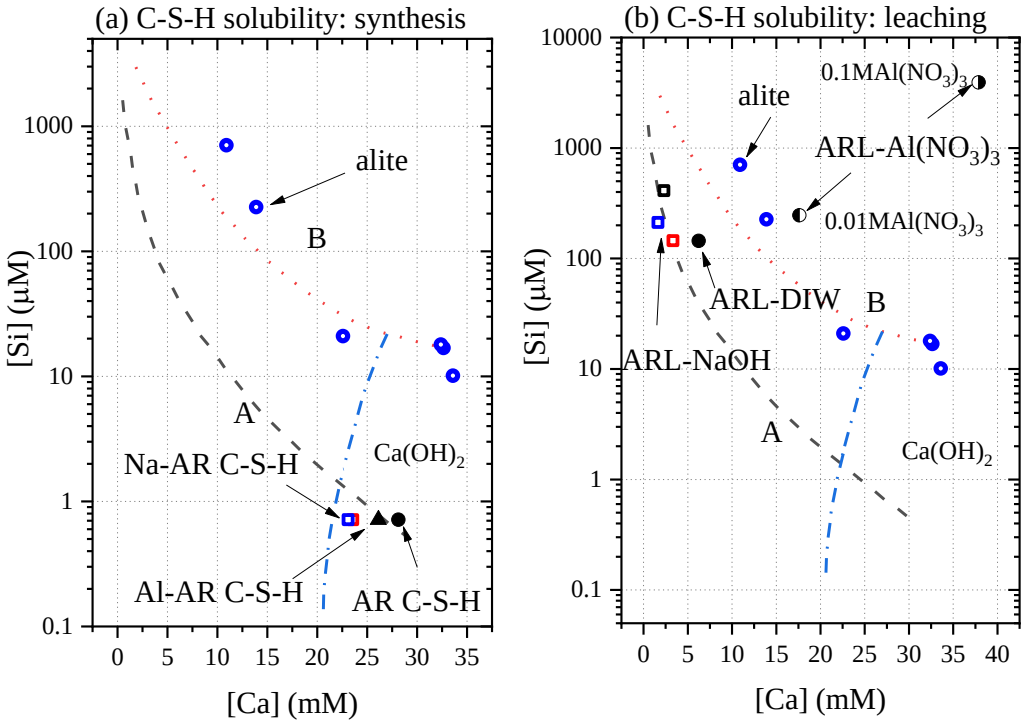

Figure 7-41 Relationship between [Ca] and [Si] concentration: (a) the filtrates from synthesis process; (b) the equilibrium during leaching. The blue circles are the points related to alite in Chapter 6, which is used as the represented points for Curve B. The reference curves are taken from [164].

Figure 7-41 shows the aqueous solubility relationships for two kinds of C-S-H. The points of the filtrates from the synthetic C-(Na, Al)-S-H are plotted together with the points from alite hydration in Chapter 6 for comparison. Clearly, all points from the filtrates (Figure 7-41(a)) fall on the Curve A, which is supposed to be the tobermorite-like C-S-H(I) [164]. Also, the filtrates compositions fall in the area of supersaturation to CH (without the consideration of the decreasing temperature). However, the low synthetic temperature will maintain the filtrates that are

undersaturated to CH as calculated above. Again, the leachates of the AR C-S-H leached in NaOH solutions or DIW still fall on the Curve A. However, that from ARL 0.01MAl falls on Curve B and that from ARL 0.1MAl falls even far from Curve B. The Curve B is argued as forming from C_3S and the C-S-H gel that is structurally (thermodynamically) distinct from Curve A [164]. Therefore, the chemical compositions of leachates from $Al(NO_3)_3$ solutions indicate that the residual C-S-H in such solutions is unstable, which agrees that the C-S-H is decomposed under the circumstance (Section 7.5).

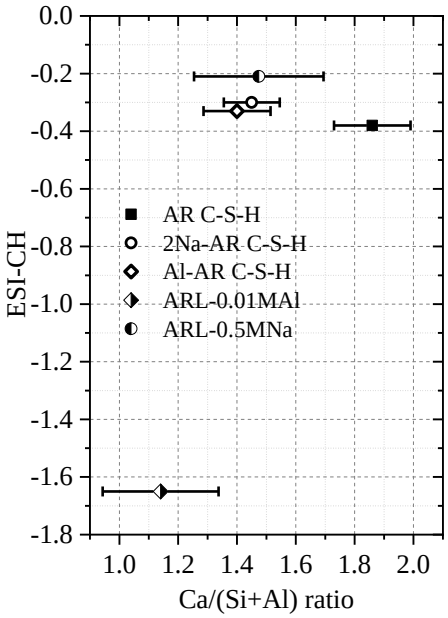

Figure 7-42 Relationship between Ca/(Si+Al) ratio and the ESI-CH of the leachates (ARL) and filtrates (AR).

Figure 7-42 shows the relationship between Ca/(Si+Al) ratio and the ESI to CH of solutions. All groups except ARL-0.01MAl possess the ESI-CH that is lower than but close to 0, indicating that these solutions are undersaturated to CH. The reason for the undersaturation during synthesis should attribute to the low temperature, but that for the NaOH leachates is because of the low Ca concentration. These calculations agree that no CH precipitated in the samples as observed by TG-DSC analysis. The presence of NaOH maintains a higher pH value, which generates the ESI-CH values that are closer to 0. However, the results show that a higher NaOH concentration will not increase the Ca/Si ratio of the synthetic C-S-H, which is opposite to the results as observed by Kumar [245]. The Na will replace the ‘H’ in Si-O-H and some ‘Ca’ in CaO layer as observed in the current study, which will further reduce the Ca/Si ratio of C-S-H. Nevertheless, the foil-like

morphology of synthetic C-S-H by adding NaOH [222, 245] or in NaOH solutions [246] follow the same phenomenon.

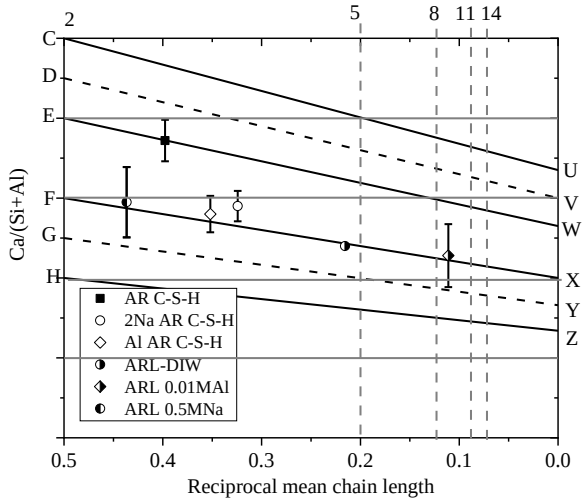

Figure 7-43 Relationship between reciprocal MCL and Ca/(Si+Al) ratio of synthetic C-S-H and the ARL C-S-H.

Figure 7-43 shows the relationship between the reciprocal MCL and the Ca/(Si+Al) ratio of the synthetic and ARL C-S-H. The quadrilateral C-U-W-E and F-X-Z-H represent jennite- and tobermorite-based models with different protonation levels [5]. Interestingly, the AR C-S-H falls on the line of maximum protonated jennite-based structure (line E-W), which exactly agrees with the maximum protonated J2/J5 mixture as speculated in Section 7.1.1. The other two synthetic C-S-H (2Na AR C-S-H and Al AR C-S-H) fall into the area of E-W-X-F, which are supposed to be a mixture of jennite- and tobermorite-based C-S-H. This also agrees with the speculations in Section 7.2. For the AR C-S-H immersed into different solutions, the ARL C-S-H all fall on the line of minimum protonated tobermorite-based structure (line F-X). However, the leaching mechanism suggests that these samples should be incomplete jennite-based structure. Within all samples, only the completed jennite-based structure AR C-S-H shows fibrillar-like morphology, whilst the others (i. e. mixture of T/J or incomplete J-structure) all show the foil-like morphology.

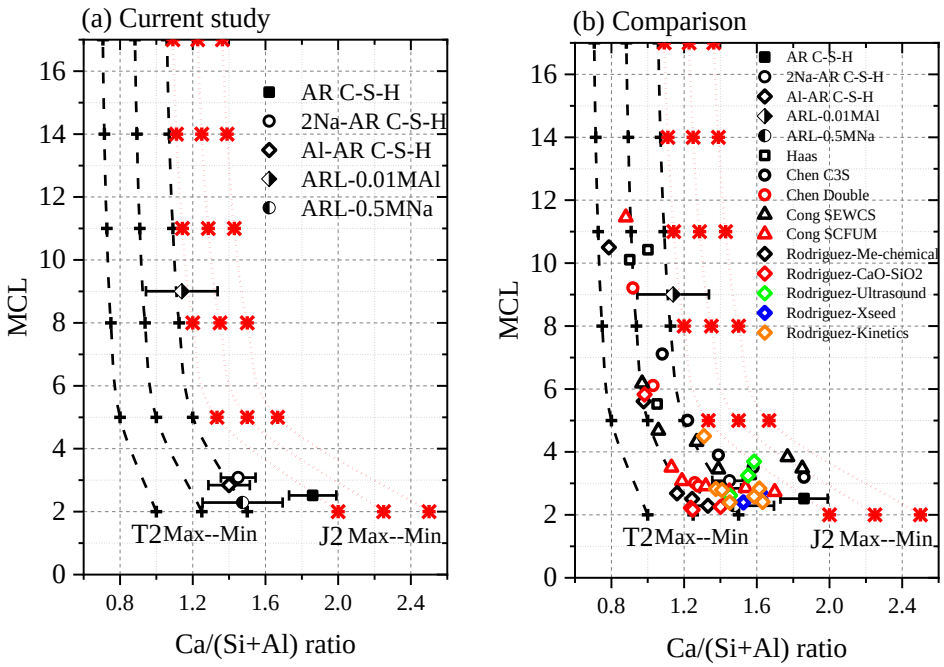

Figure 7-44 Comparison of MCL vs. Ca/(Si+Al) ratio: (a) points in current study and (b) a comparison with data collected form literatures [13, 63, 116, 221, 247, 248]. The black dash lines stand for the tobermorite structure and the red dot lines stand for the jennite structure. Both of two cluster of curves includes the conditions from maximum to minimum protonation.

The MCL-Ca/(Si+Al) ratio plot (Figure 7-44) shows similar information to Figure 7-43 but includes more data from literature for comparison. Again, the AR C-S-H falls on the maximum protonated jennite-based structural line. When compared to the data from literatures as plotted in Figure 7-44(b), the only points that fall into the area of jennite-based structure are prepared from C_3S (i.e. Chen) [63] and β-C_2S (i.e. Cong SEWCS series) [116, 221]. Clearly, the structural transformation from tobermorite (or impure jennite) to jennite-based analogies happens in the abovementioned systems. The high Ca/Si ratio C-S-H gel prepared from C_3S and β-C_2S show fibrillar morphology [5] as that of AR C-S-H. The C-S-H synthesised by Rodriguez [13] mostly falls into the area of tobermorite-based structure and gradually transforms to the area of mixed T/J-based structure (for example, X-seeds series). Interestingly, the morphology of C-S-H also transforms from foil to mixed foil-fibrillar morphology [13].

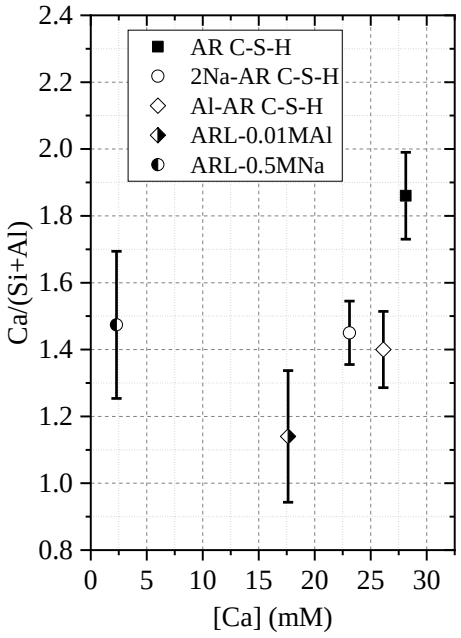

Figure 7-45 Relationship between [Ca] concentration in solution and the Ca/(Si+Al) ratio of the solid.

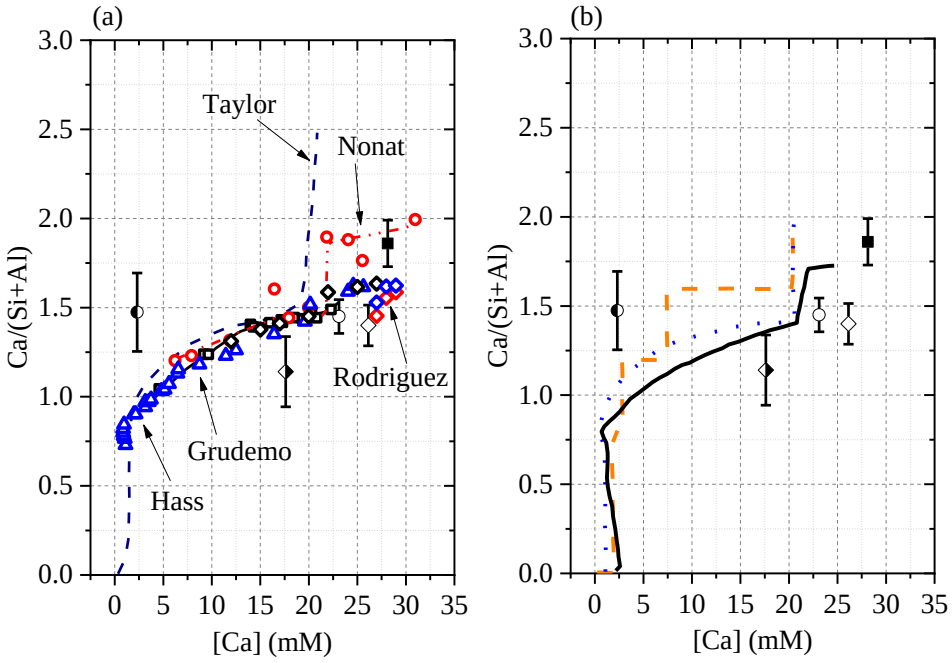

Figure 7-46 Relationship between [Ca] concentration to Ca/(Si+Al) ratio: a. compare with data from Taylor (dark blue line)[249], Grudemo (black line and black squares)[16], Nonat (red line and red circles)[250], Hass (blue triangles)[248], and Rodriguez (black diamond: Kinetic series; red diamond: Ultrasound series; blue diamond: Xseed series)[13]; (b) compare with Barbara's summary [204].

Figures 7-45 and 7-46 show the relationship between Ca concentration in solution and the Ca/(Si+Al) ratio in the solid. Several models (see the Captions of Figure 7-46) are used for comparison. The general trend shows the positive relationship between Ca concentration and Ca/(Si+Al) ratio, however, the Na-bearing C-S-H deviate from model curves, which show a lower

Ca concentration than expected. The reason should be attributed to the common ions effect (Na^+ and Ca^{2+}) that results in a lower Ca concentration in the solution. The AR C-S-H falls on the line of Nonat's model [250], which results from the hydration of C_3S.

7.7 Summary

The C-S-H with high Ca/Si ratio is successfully synthesised through 'autoreactor' (AR) method. Additional ions effects on the morphology, composition, and nanostructure of AR C-S-H are explored by two methods, i.e. directly adding and immersion in solutions (NaOH and $Al(NO_3)_3$). The changing mechanisms by adding different ions are investigated by multi-techniques (i.e. XRD, TG-DSC, CP/SP MAS NMR, ATR-FTIR, TEM-EDX, and ICP-OES) and some key findings are summarised as follows:

(a) The AR C-S-H shows a fibrillar-like morphology and has a Ca/Si ratio of ~1.86 and an MCL of ~ 2.51. It is mixed of ~ 83% dimer and ~ 17% pentamer jennite-based units (J2/J5) with maximum protonation levels. The mixture may contain some T2/T5 units or some impure J2/J5 with vacancies of Ca ions to reduce the Ca/Si ratio. The Ca concentration in the filtrate is 28.13 mmol/L;

(b) The synthetic AR C-(Na)-S-H (2Na-AR C-S-H) with starting condition of Na/Si bulk ratio of 2 shows a foil-like morphology. The Ca/Si ratio reduces to ~ 1.45 and the Na/Si ratio is ~ 0.012. The MCL slightly increases to ~ 3.08, which is mixed of ~64% dimers and 36% pentamers. These silicate units include more tobermorite-based structure to reduce the Ca/Si ratio. A broad resonance centred at ~ -2.19~-1.66 ppm in ^{23}Na MAS NMR corresponding to sodium induced silicate tetrahedra (i. e. Si-O-Na) is confirmed, however, these silicate tetrahedra prefer to be charge-balanced by proton instead of Na under the synthetic conditions. The Ca concentration in the filtrate reduces to 23.10 mmol/L;

(c) The synthetic AR C-A-S-H (Al-AR C-S-H) with starting condition of Al/Si bulk ratio of 1 shows a foil-like morphology and has the Ca/Si and Al/Si of ~ 1.495 and ~ 0.037. The MCL of this C-A-S-H is 2.84, corresponding to a mixture of ~ 72% dimers and ~ 28% pentamers. Around 50% tobermorite-based structural units are mixed in the samples. The

difference of Al/Si ratio from NMR and TEM-EDX shows ~ 56.9% bridging sites in the pentamers are substituted by Al[IV]-tetrahedra. The ^{27}Al MAS NMR spectra show that Al[IV], Al[V], and Al[VI] are all present in the samples, corresponding to Al-replaced Si, Ca in C-S-H and TAH phase (CAH_{10}). The Ca concentration in the filtrate reduces to 26.13 mmol/L;

(d) The leaching mechanism includes the removal of 'Ca-OH' units and the 'hydrolysis' process. The dimers prefer to be removed firstly, showing that ARL C-S-H-DIW is composed of ~ 12% dimers and ~ 88% pentamers. Leaching in DIW results in omitting of ~ 26% Ca-OH in the residual C-S-H (ARL C-S-H-DIW). The ARL C-S-H-DIW shows a foil-like morphology and the Ca concentration in the leachate is 6.24 mmol/L;

(e) The morphology of AR C-S-H that leaches in 0.5M NaOH solution shows a foil-like morphology. The Na-replacement preferably starts from the end-member or dimer tetrahedra. The changing mechanisms of AR C-S-H immersed into NaOH solutions can be summarised as: i) in low NaOH concentration (0.01M), the leaching behaviour is similar to that in DIW, which mainly behaves as the leaching of Ca-OH groups; ii) in medium (0.1M) and high (0.5M) NaOH concentrations, less Ca-OH groups are removed or the entire C-S-H is broken. The main observed behaviour is the replacement of available Si-O-X positions by Na^+; iii) in high NaOH concentration, some pentamers break up and most of Q^1 is left in the solid. The Ca/Si ratio in solution decrease significantly in the leachates with the increase of Na concentration;

(f) Most of the dimers are gone in $Al(NO_3)_3$ solution and the leaching mechanism should be attributed to the proton ions generated by the hydrolysis of Al-bearing complex. Again, the TAH phase (CAH_{10}) is generated in the residues. This immersion will also increase the MCL of ARL C-S-H-0.01MAl by inserting Al-tetrahedra. The residue shows a foil-like morphology and is mixed of incomplete J5, J8, and J11 units. The Ca and Si concentration increase with the increase of $Al(NO_3)_3$ solution, indicating the breaking of C-S-H units;

(g) All the C-S-H except those leached in $Al(NO_3)_3$ solutions (the C-S-H structure is destroyed) equilibrate at Curve A. Only the AR C-S-H mixed of integrated J2/J5 units

shows fibrillar-like morphology, others that are either made of T/J units or incomplete jennite-based units show foil-like morphology. Although the Ca concentration during the synthesis of Na/Al doped C-S-H remains higher than 23 mmol/L, the morphology of these C-S-H remain foil-like, indicating that the morphology of C-S-H should depend more on its own nanostructure.

Chapter 8

Conclusions and future work

8.1 Main conclusions

The morphology, nanostructure, and chemical composition of C-S-H (gels) prepared from the hydrated blended cements, hydrated alite, and reactions between TEOS and CH solution are investigated through multiple techniques in this thesis, aiming to find the factors that affect the morphological changes of C-S-H. It is found that the C-S-H morphology-change is dominated by its chemical composition, nanostructure, and solution environment. The main findings in individual systems are summarised as follows:

In blended cement systems:

The morphology of (OP) C-A-S-H gel in SCMs-blends change from thin fibrillar-like to mixed fine-fibrillar/foil-like, whilst that in inert-filler blended cements remain coarse fibrillar throughout hydration. The morphological change happens in 60%GGBS blends within 14 ~ 28 d and in 30%PFA blends within 91 ~ 270 d.

The foil-like morphology appears when: a) CH^{act}/CH^{exp} < 0.85 in the solid phase of cement systems; b) the C-A-S-H shows the characteristics of Ca/(Si+Al) ratio < 1.3 and Al/Si ratio > 0.15; the MCL ≈ 7 ~ 8; the SOF_{BT} > 0.6 or SOF_{BT}(Al) > 0.3; the proportion of Q^2(1Al) > 30%; Q^2(total)/Q^1 ratio > 2.0; Q^2(1Al)/ Q^2(total) ratio > 0.45; Q^2(1Al)/ Q^2(0Al) ratio > 0.80; c) the pore solutions show the characteristics of ESI of CH < -0.15 and ESI of J-based C-S-H gel < 0.1.

The DoH of clinker and the absolute CH content are not the direct factors related to foil-like morphology C-S-H; The DoH of SCMs depends on their replacement ratio, activity, and chemical compositions.

In alite system:

The C-S-H morphological changes from foil-like at 2 h to fibrillar-like at 6 h when CH initially appears. The C-S-H at 2 h can be explained as the tobermorite-like dimer (T2) with minimum protonation; and that at 6 h can be explained as a mixture of minimum protonated 43.3% T5, 23.7%

T2, and 33.0% J2 (T/J model). The foil-like C-S-H gel may be related to the tobermorite-like structure.

The C-S-H interfacial precipitation rate ($r_{C\text{-}S\text{-}H}$) shows a U-shape curve and the alite dissolution rate shows a decreasing trend as the hydration goes on.

The appearance of fibrillar-like C-S-H is associated with: the supersaturation of CH (i. e., the appearance of CH); the appearance of Q^2 tetrahedra; the SI of C-S-H with high Ca/Si ratio significantly rise up to higher than 1; the interfacial precipitation rate of C-S-H passed the bottom of 'U'-shape curve; the determined dissolution rate decreased to under 100 μmol/(s·g).

In synthetic C-S-H systems:

The C-S-H with a high Ca/Si ratio (~ 1.86) shows fibrillar-like morphology, which is mixed of ~ 83% dimer and ~ 17% pentamer jennite-based units (J2/J5) with maximum protonation levels. The mixture may contain some T2/T5 units or some impure J2/J5 with vacancies of Ca ions to reduce the Ca/Si ratio. The Ca concentration in the final filtrate can reach 28.13 mmol/L; Leaching in the DIW will change the fibrillar-like C-S-H to foil-like C-S-H that is composed of ~ 12% dimers and ~ 88% pentamers. Leaching in DIW results the omitting of ~ 26% Ca-OH in the residual C-S-H; the foil-like C-S-H is in equilibrium at a Ca concentration of 6.24 mmol/L;

The addition of NaOH by either adding during synthesis or immersing in solutions will change the fibrillar-like C-S-H to foil-like C-(Na)-S-H. A broad resonance centred at ~ -2.19~-1.66 ppm in ^{23}Na MAS NMR corresponding to sodium induced silicate tetrahedra (i. e. Si-O-Na) is confirmed under both conditions. The Na-replacement preferably starts from the end-member or dimer tetrahedra. Adding NaOH solution during synthesis will promote the proportion of tobermorite-based units and immersion into NaOH solutions will replace the Ca-OH and protons that attach to Si-O-X by Na. Both methods will reduce the Ca/Si ratio of obtained C-Na-S-H, followed by changing of morphology from fibrillar to foil-like. Meanwhile, the addition of NaOH will reduce the Ca concentration in solution, however, this will not reduce the ESI of CH simultaneously.

The addition of $Al(NO_3)_3$ solution by either adding during synthesis or immersing in solutions will change the fibrillar-like C-S-H to foil-like C-(A)-S-H. The ^{27}Al MAS NMR spectrum shows

that Al[IV], Al[V], and Al[VI] are all present in the samples, corresponding to Al-replaced Si, Ca in C-S-H and TAH phase (CAH_{10}). Around 50% tobermorite-based structural units are mixed in the synthetic C-A-S-H when starting with the bulk Al/Si = 1, where ~ 56.9% bridging sites in the pentamers are substituted by Al[IV]-tetrahedra. The C-S-H breaks when immersing in $Al(NO_3)_3$ solutions. Both methods will reduce the Ca/Si ratio of obtained C-A-S-H, followed by changing of morphology from fibrillar to foil-like. Meanwhile, the addition of $Al(NO_3)_3$ solution will reduce the ESI of CH significantly.

All the C-S-H except those leached in $Al(NO_3)_3$ solutions (the C-S-H structure is destroyed) equilibrate on Curve A (Jennings, 1986). Only the AR C-S-H that is mixed of integrated J2/J5 units show fibrillar-like morphology, others that are made of either T/J units or incomplete jennite-based units show foil-like morphology. Although the Ca concentration during the synthesis of Na/Al doped C-S-H remains higher than 23 mmol/L, the morphology of these C-S-H remains foil, indicating that the morphology of C-S-H should depend more on its own nanostructure.

In summary, the metastable C-S-H gels that are present in blended wPC or synthetic C-S-H systems are observed on the equilibrium Curve A, whilst those equilibrated on Curve B are unstable C-S-H gels that are present in PC < 1 d or alite hydrated in high w/s ratio (continuously dissolution and precipitation happens). The main difference between the two Curves may link with the insufficient diffusion barrier (stable C-S-H).

8.2 Recommendations for future work

Thermodynamic properties of C-S-H with the high Ca/Si ratio

The thermodynamic properties of pure C-S-H with the high Ca/Si ratio need better understandings and investigations. The existing solid solution models lack supporting data from the real (pure) synthetic C-S-H with the high Ca/Si ratio. For example, the C-S-H-II model use CH as the secondary phase to achieve the Ca/Si ratio up to 1.7 [179] and the CSHQ model try to simulate both T/J and T/CH mixtures with theoretical calculation [57]. This thesis provides the synthetic C-S-H with the Ca/Si ratio of ~ 1.86 and gives the first-time reveal of its nanostructure.

Further thermodynamic properties that need to dissolve this C-S-H under wide-range temperature are of interest. These experimental solubility data are expected to provide fundamental evidences for current thermodynamic models [179].

Better understanding of Al-coordinated C-S-H phase using high-field NMR spectroscopy

Since the spin quantum number of Al is 5/2, which will result four additional satellite transitions during MAS NMR experiments. The odd spectrum will reduce its accuracy under normal solid-state NMR spectroscopy (for example, 9.4T). For example, normally only one sharp peak is shown for AFt phase in normal ^{27}Al NMR spectra [251]. Recently a high resolution ^{27}Al MAS NMR spectrum shows the two-sites of Al-octahedra in ettringite [251]. Therefore, the high-field (MQ)MAS NMR spectroscopy will help to better understand the Al sites in C-A-S-H phase.

Determination of Ca-OH bonding in C-S-H

The Ca-OH bonding is the key factor for understanding the accurate structure of C-S-H. Chen [63] tried to use the Inelastic Neutron Scattering (INS) for the determination of Ca-OH bonding. However, the accuracy of the spectra (Figure 4.1 in [63]) need to be improved with proper manner. The FTIR spectrum can show the Ca-OH groups, which normally are regarded to be from CH. However, the position of Ca-OH in FTIR spectrum needs more investigations.

Appendix A. Fitting parameters and QXRD fitting patterns

A1. Fitting parameters

Table A-1 Structures used for Rietveld refinements.

Phase	ICSD code	Reference
Alite M3	94742	De la Torre et al. 2002
Alite R	22501	Il'inets et al. 1985
Alite T	4331	Golovastikov et al. 1975
Belite β	81096	Mumme et al. 1995
Belite γ	81095	Mumme et al. 1995
Aluminate cubic	1841	Mondal and Jeffery 1976
Aluminate mono	100221	Takeuchi et al. 1980
Gypsum	409581	Boeyens and Ichharam. 2002
Portlandite	202220	Chaix-Pluchéry et al. 1987
Ettringite	155395	Goetz-Neunhoeffer et al. 2006
Monosulfoaluminate	100138	Allman 1977
Hydrotalcite	81963	Bellotto et al. 1996

Table A-2 MAC values for calculation (Cukα).

Oxide	CaO	SiO_2	Al_2O_3	Fe_2O_3	MgO	Na_2O	K_2O	SO_3	TiO_2	H_2O
μ_i	124.78	35.90	31.66	214.68	28.69	25.00	122.33	44.26	124.51	10.26

Table A-3 MAC values of powder samples and hydration stopped samples.

Sample	Age (d)	Water content (%)	MAC (cm^2/g)
100wPC	0.2	2.46	93.680
	1	12.81	84.809
	3	18.21	80.181
	7	18.50	79.926
	14	21.06	77.735
	28	20.95	77.831
	91	24.10	75.129
	270	30.28	69.831
30PFA-70wPC	0.2	1.94	80.573
	1	8.86	75.602
	3	12.48	72.998
	7	12.79	72.778
	14	14.72	71.387
	28	15.02	71.172
	91	17.10	69.676
	270	23.3	65.218
60GGBS-40wPC	0.2	1.54	80.092
	1	6.14	76.825
	3	9.86	74.178
	7	10.90	73.440
	14	13.30	71.734
	28	13.96	71.259

	91	14.24	71.063
	270	21.77	65.707

A2. QXRD fitting patterns

a) Raw materials fitting profiles

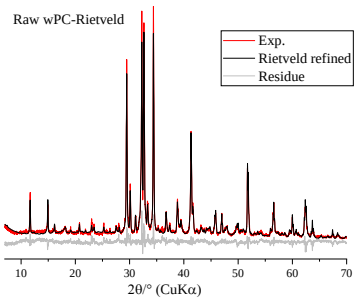

a1) Raw wPC

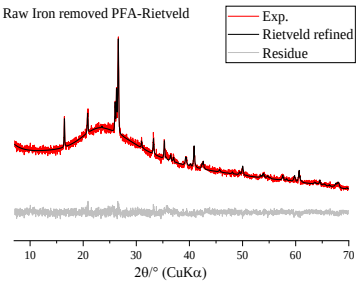

a2) Raw PFA

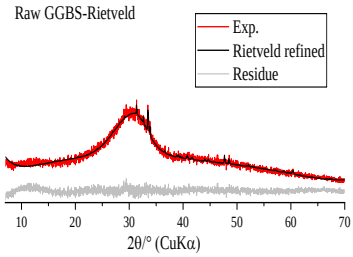

a3) Raw GGBS

b) White Portland cement (wPC) samples

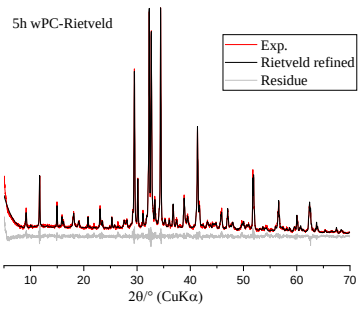

b1) 5h wPC

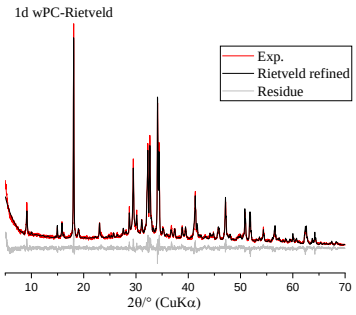

b2) 1d wPC

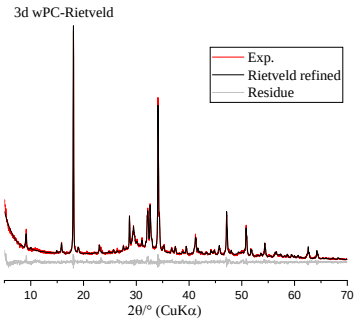

b3) 3d wPC

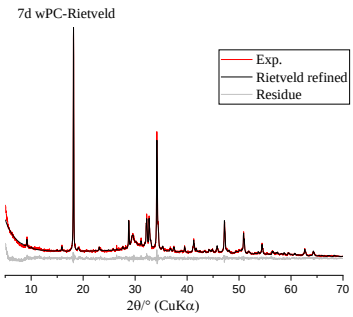

b4) 7d wPC

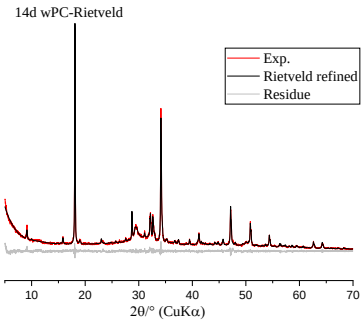

b5) 14d wPC

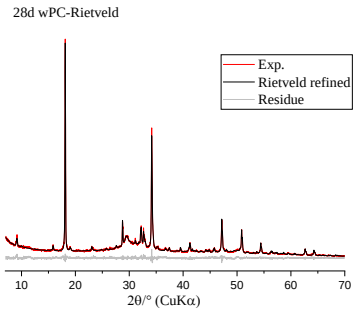

b6) 28d wPC

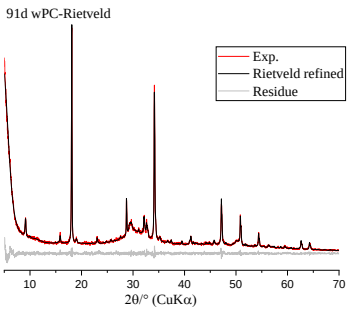

b7) 91d wPC

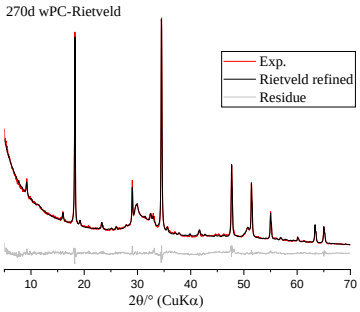

b8) 270d wPC

c) 30PFA-70wPC samples

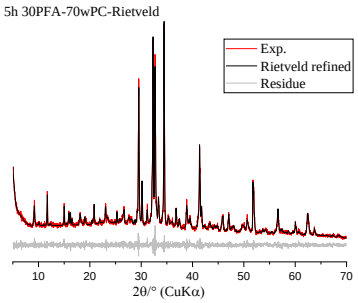

c1) 5h 30PFA-70wPC

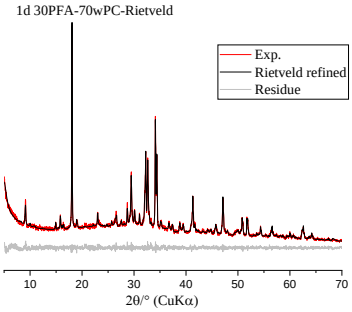

c2) 1d 30PFA-70wPC

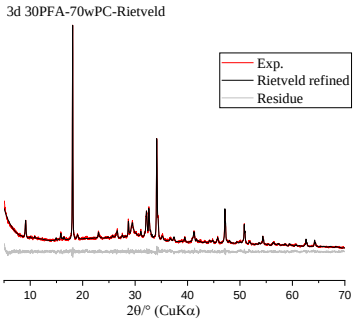

c3) 3d 30PFA-70wPC

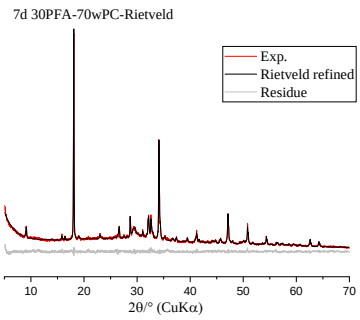

c4) 7d 30PFA-70wPC

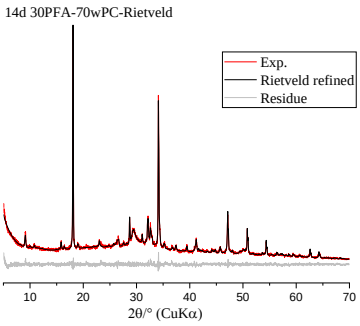

c5) 14d 30PFA-70wPC

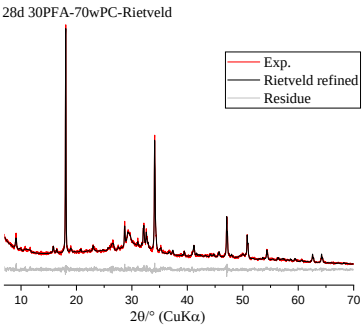

c6) 28d 30PFA-70wPC

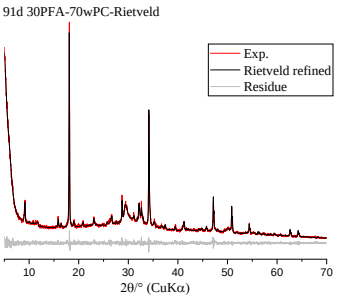

c7) 91d 30PFA-70wPC

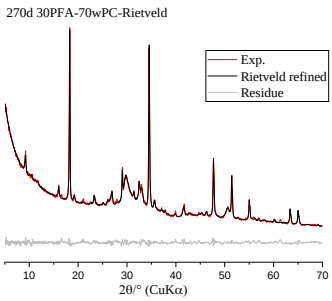

c8) 270d 30PFA-70wPC

d) 30TiO_2-70wPC samples

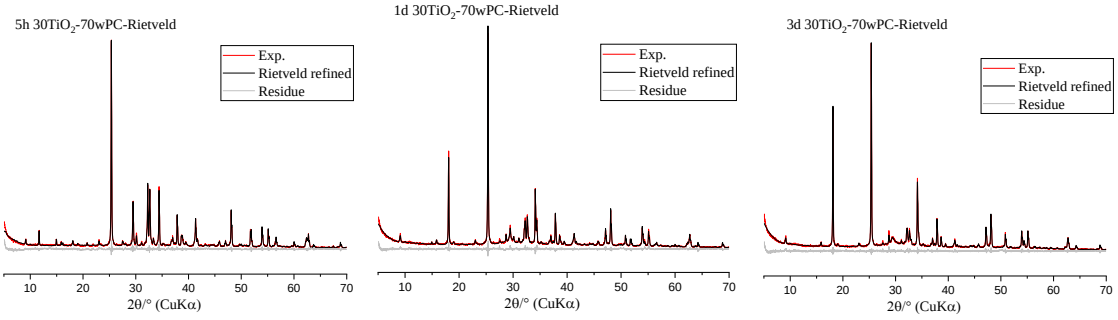

d1) 5h 30TiO_2-70wPC d2) 1d 30TiO_2-70wPC d3) 3d 30TiO_2-70wPC

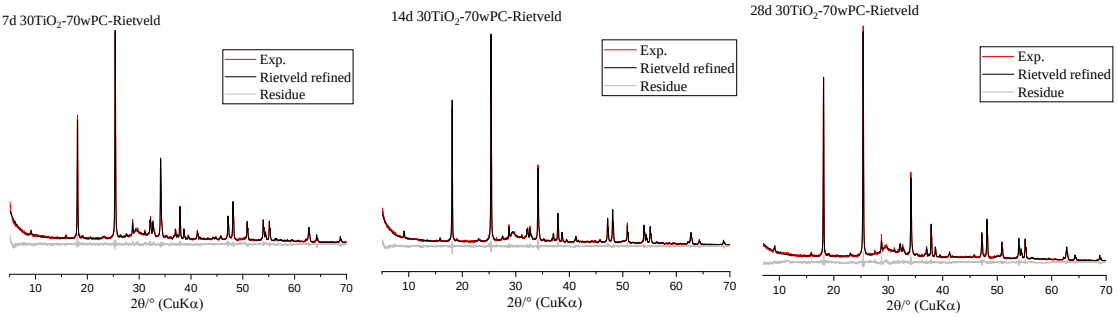

d4) 7d 30TiO_2-70wPC d5) 14d 30TiO_2-70wPC d6) 28d 30TiO_2-70wPC

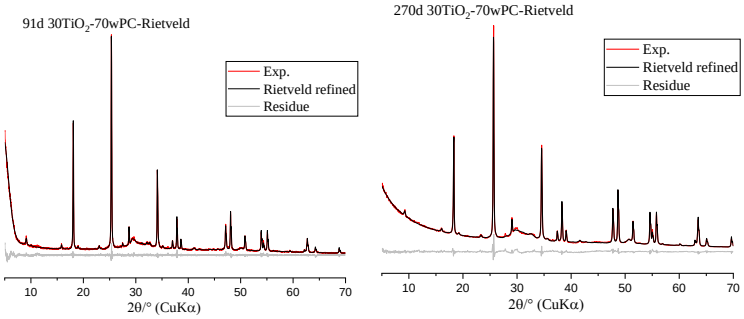

d7) 91d 30TiO_2-70wPC d8) 270d 30TiO_2-70wPC

e) 60GGBS-40wPC samples

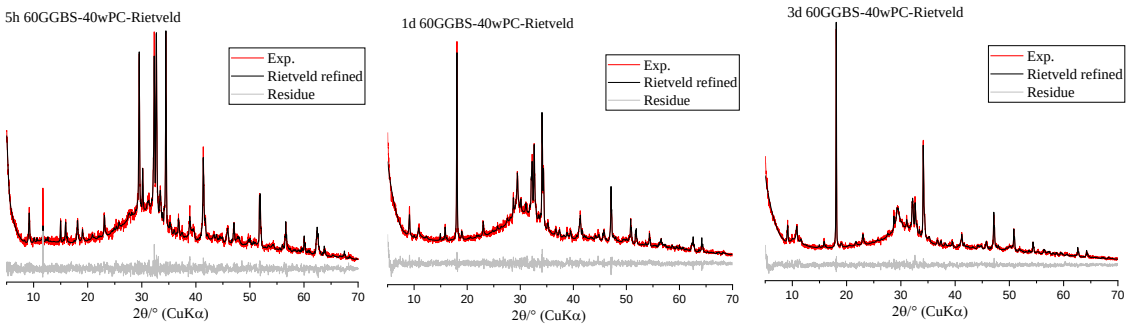

e1) 5h 60GGBS-40wPC e2) 1d 60GGBS-40wPC e3) 3d 60GGBS-40wPC

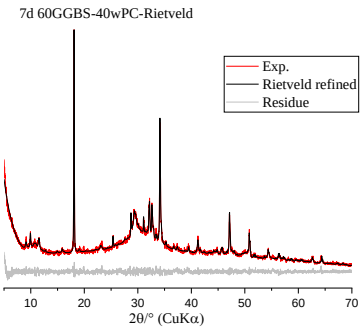

e4) 7d 60GGBS-40wPC

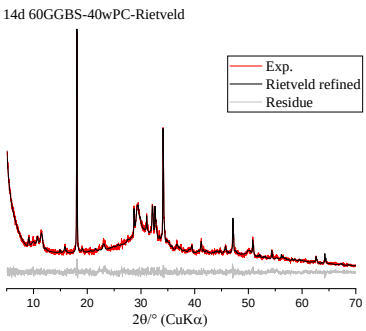

e5) 14d 60GGBS-40wPC

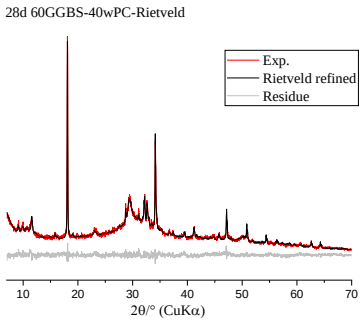

e6) 28d 60GGBS-40wPC

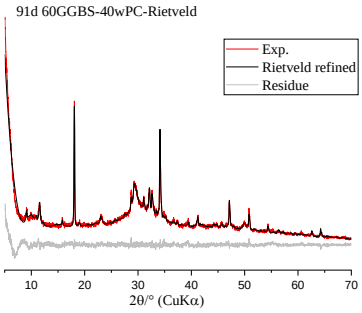

e7) 91d 60GGBS-40wPC

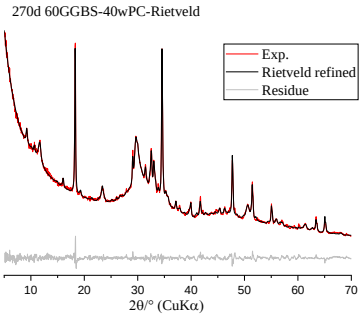

e8) 270d 60GGBS-40wPC

f) 60TiO_2-40wPC samples

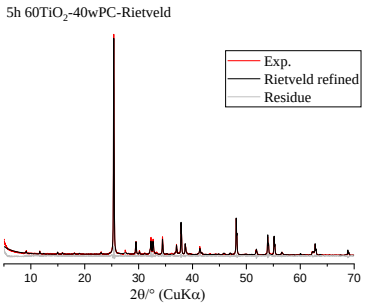

f1) 5h 60TiO_2-40wPC

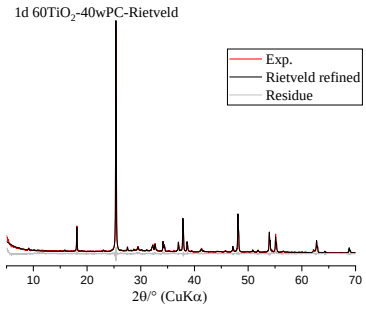

f2) 1d 60TiO_2-40wPC

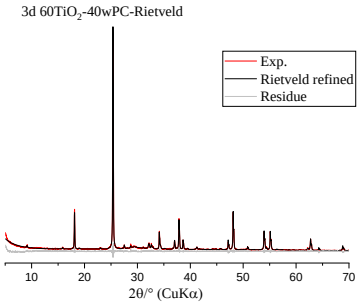

f3) 3d 60TiO_2-40wPC

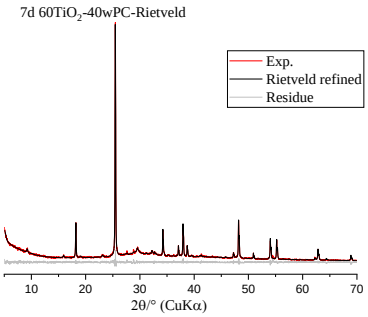

f4) 7d 60TiO_2-40wPC

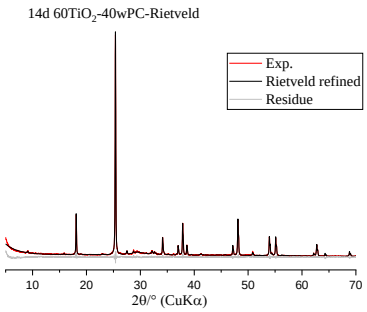

f5) 14d 60TiO_2-40wPC

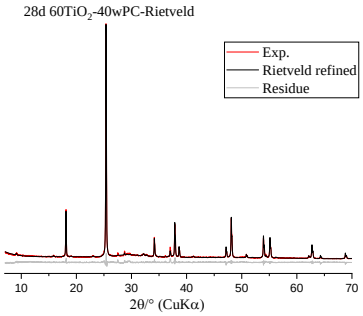

f6) 28d 60TiO_2-40wPC

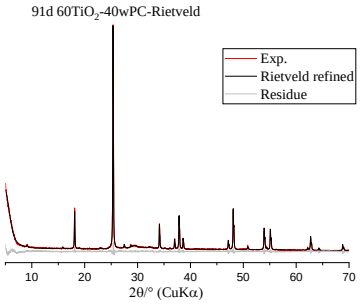

f7) 91d 60TiO_2-40wPC

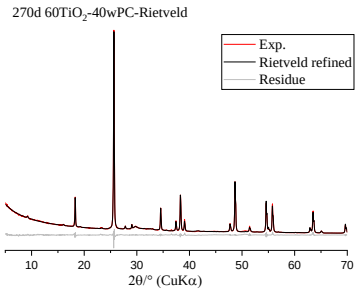

f8) 270d 60TiO_2-40wPC

Figure A2-1 QXRD fitting patterns of a) raw materials profiles; b) wPC samples; c) 30PFA-70wPC samples; d) 30TiO_2-70wPC; e) 60GGBS-40wPC; f) 60TiO_2-40wPC.

Appendix B. Modelling and Validation

B1. Modified Bogue method

MATLAB code for modified Bogue method:

A=[0.713 0.635 0.566 0.475;0.252 0.315 0.037 0.036;0.010 0.021 0.313 0.219;0.007 0.009 0.051 0.214];
B=[CaO wt.%;SiO_2 wt.%;Al_2O_3 wt.%;Fe_2O_3 wt.%];
R_A=rank(A);
X=A\B

The parameters in Matrix A are taken from Taylor [181] and the oxide content is from XRF test.

B2. Verification of thermodynamic modelling in Phreeqc V3.4.0

To confirm the reliability of the software, the simulation process was conducted based on the data in Ref. [148], in which the simulation temperature condition was 22℃ for the pore solution of OPC paste at 12 h. Hence, a comparison was taken under a condition of 22℃ firstly and the results are summarised as follows (the database can be found in **Appendix C**):

The ionic strength in Ref. [148] is 0.40 and simulated ionic strength is 0.41, these values are comparable. Further, the ions distribution of 12 h group is demonstrated in Table B2-1. It can be seen that most ions present in the solution are close, which indicate that the simulation software has a high reliability.

Table B2-1 Comparison of ions distribution between Ref.[148] and test under 22 ℃ [ln(ions activity)].

	Ca^{2+}	$CaSO_4^0$	$CaOH^+$	K^+	KSO_4^-	KOH^0	Na^+	$NaSO_4^-$	$NaOH^0$	$Al(OH)_4^-$	SO_4^{2-}	$H_2SiO_4^{2-}$	$H_3SiO_4^-$	$H_4SiO_4^0$
Ref.[3]	-3.42	-3.59	-2.97	-0.70	-2.15	-1.82	-1.19	-2.77	-2.06	-4.35	-2.27	-4.31	-4.47	-8.00
Test	-3.49	-3.53	-2.87	-0.72	-2.17	--	-1.14	-2.73		-4.38	-2.28	-4.37	-4.53	-8.06

Table B2-2 Comparison of calculated Saturation indices (SI).

	Portlandite	Gypsum	Ettringite	Monosulphate
Ref. [148]	0.36	-1.12	6.44	1.98
Test	0.27	-1.20	5.91	1.70

Note: For Portlandite, Gypsum, Ettringite and Monosulphate, ESI=SI/3, SI/2, SI/15, and SI/11.

However, it is found that the results are quite different for CH saturation index (Table B2-2, the definition is in Section 4.2.1). Hence, the simulation temperature is changed to 23 ℃. Because their temperature condition is written like (~22℃), it is suspected that the simulation condition is taken under a condition around 22 ℃, but not accurately given. Under this condition, the simulated ionic strength is 0.42 and the ions distribution (Table B2-3) still remains close.

Table B2-3 Comparison of ions distribution between Ref.[148] and test under 23 ℃ [ln(ions activity)].

	Ca^{2+}	$CaSO_4^0$	$CaOH^+$	K^+	KSO_4^{2-}	KOH^0	Na^+	$NaSO_4^-$	$NaOH^0$	$Al(OH)_4^-$	SO_4^{2-}	$H_2SiO_4^{2-}$	$H_3SiO_4^-$	$H_4SiO_4^0$
Ref[3]	-3.42	-3.59	-2.97	-0.70	-2.15	-1.82	-1.19	-2.77	-2.06	-4.35	-2.27	-4.31	-4.47	-8.00
Test	-3.49	-3.53	-2.87	-0.72	-2.17	--	-1.14	-2.73		-4.38	-2.28	-4.36	-4.55	-8.10

Table B2-4 Comparison of Saturation index of phases (23 ℃).

	Portlandite	**Gypsum**	**Ettringite**	**Monosulphate**
Ref.[148]	0.36	-1.12	6.44	1.98
Test	0.35	-1.21	5.89	1.80

Most importantly, the SI for each phase is really close (especially for Portlandite). Further, SI of all ages are calculated using Phreeqc V3.3.12 and the results are shown in Figure B2-1. This result indicates that the SI calculation with Phreeqc is reliable and repeatable.

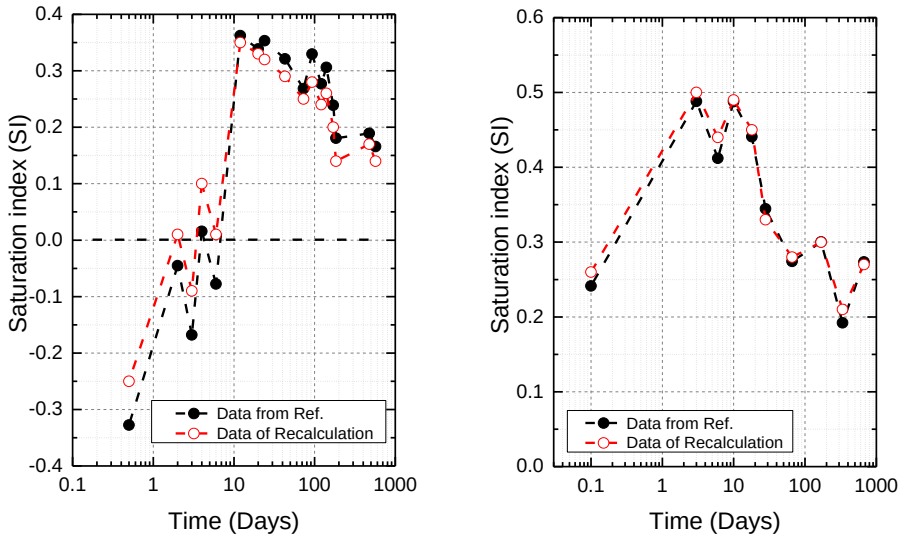

Figure B2-1 Comparison of CH Saturation index (SI) results in Ref. [148]. These results indicate that the method using phreeqc is right and there are little differences in SI of CH. Further, for the effective SI (ESI), the gaps should be less (For CH, ESI=SI/3). The open circles represent recalculated results. Left is OPC with w/c of 0.35 and the right is wPC with w/c of 0.50.

Appendix C. Thermodynamic model database

Thermodynamic database that used in this thesis is given in Tables C-1 and C-2.

Table C-1 Thermodynamic fitting parameters for activity coefficient calculation.

Ion species	Deby-Hückel å	Deby-Hückel bγ
Ca^{2+}	5	0.165
H^{+}	9	0
K^{+}	4	0.075
Na^{+}	4	0.075
SO_4^{2-}	5	-0.04

Table C-2 Thermodynamic data for the solubility calculations (25 °C).

Phases or species	Formation or reaction	log Ksp	ΔH_r(kJ/mol)
OH-	$H_2O - H^+$	-14.00	55.81
CaOH+	$Ca^{2+} + OH^-$	1.18	21.66
CaSO4	$Ca^{2+} + SO_4^{2-}$	2.11	5.44
$NaSO_4^-$	$Na^+ + SO_4^{2-}$	0.70	4.69
KSO_4^-	$K^+ + SO_4^{2-}$	0.85	9.42
$H_3SiO_4^-$	$H_4SiO_4^0 - H^+$	-9.83	25.61
$H_2SiO_4^{2-}$	$H_4SiO_4^0 - 2H^+$	-23.00	73.64
Ca_3SiO_5	$3Ca^{2+} + H_4SiO_4^0 + 6OH^- - 5H_2O$	-24.11	-444.107
Portlandite	$Ca^{2+} + 2\ OH^-$	-5.18	-17.89
Gypsum	$Ca^{2+} + SO_4^{2-} + 2\ H_2O$	-4.58	-0.46
Ettringite (AFt)	$6Ca^{2+} + 3SO_4^{2-} + 2\ Al(OH)_4^- + 4OH^- + 26\ H_2O$	-45.00	204.5
Monosulphoaluminate (AFm)	$4Ca2+ + SO_4^{2-} + 2\ Al(OH)_4^- + 4OH^- + 6\ H_2O$	-29.43	45.57
Strätlingite (C_2ASH_8)	$2\ Ca^{2+} + 2\ Al(OH)_4^- + H_3SiO_4^- + OH^- + 2\ H_2O$	-19.70	-1439.67*
Hydrotalcite-OH (MAH_{10})	$4\ Mg^{2+} + 2\ Al(OH)_4^- + 6OH^- + 3\ H_2O$	-56.02	-103.98*
Hydrotalcite-CO_3 ($MAcH_9$)	$4\ Mg^{2+} + 2\ Al(OH)_4^- + CO_3^{2-} + 4OH^- + 2\ H_2O$	-51.14	-351.28*
Tobermorite-type CSH	$0.8333Ca^{2+} + H_3SiO_4^- + 0.6666OH^- - 0.5\ H_2O$	-8.0	-1427.56*
Jennite-type CSH	$1.6667Ca^{2+} + H_3SiO_4^- + 2.3334OH^- - 0.5667H_2O$	-13.17	-1417.88*
$Ca_{0.8}SiO_2(OH)_{1.6}(H_2O)$	$0.8Ca^{2+} + H_3SiO_4^- + 0.6OH^-$	-6.84	-#
$CaSiO_2(OH)_2(H_2O)$	$Ca^{2+} + H_3SiO_4^- + OH^-$	-8.80	-#
$Ca_{1.81}SiO_2(OH)_{3.62}(H_2O)$	$1.81Ca^{2+} + H_3SiO_4^- + 2.62OH^-$	-13.61	-#

Note: * stands for the data was calculated by basic formation enthalpy of each phase according to the reactions showed in the table. # stands for the C-S-H gel model used for dissolution and precipitation model calculation in Chapter 6.

Appendix D. TG-DSC experimental patterns

a) Raw materials

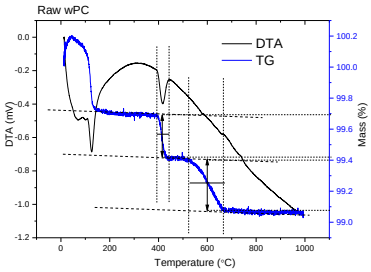

a1) Raw wPC

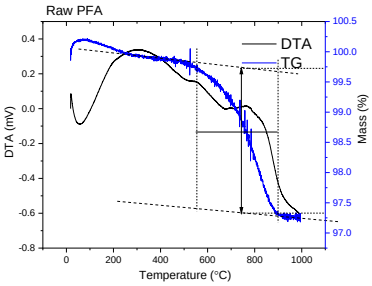

a2) Raw PFA

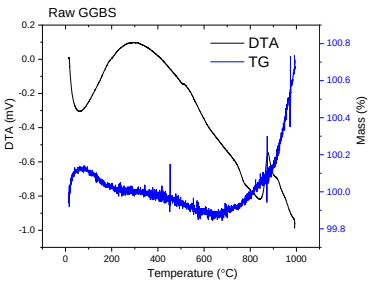

a3) Raw GGBS

b) White Portland cement (wPC) samples

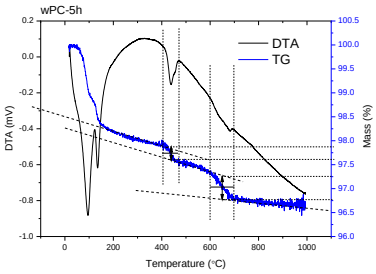

b1) 5h wPC

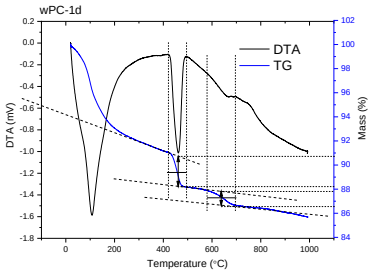

b2) 1d wPC

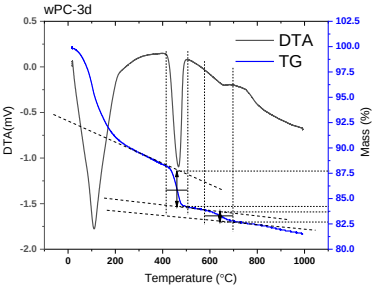

b3) 3d wPC

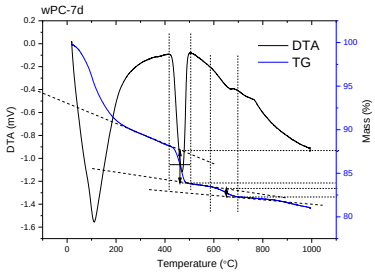

b4) 7d wPC

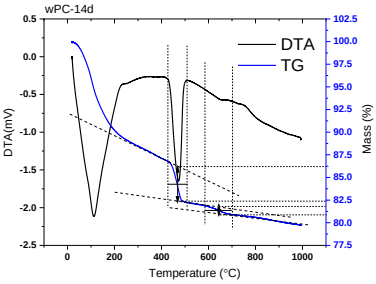

b5) 14d wPC

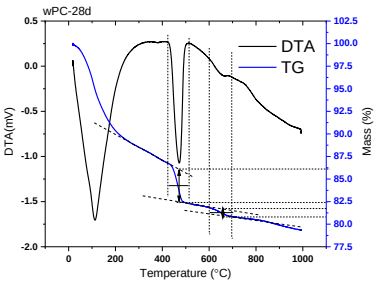

b6) 28d wPC

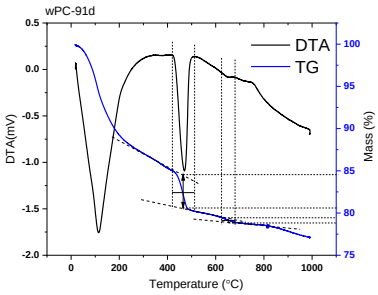

b7) 91d wPC

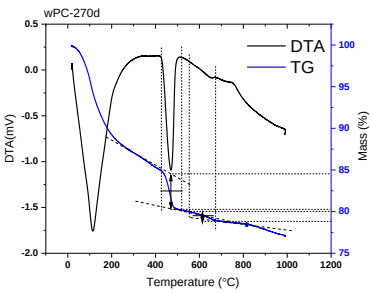

b8) 270d wPC

c) 30PFA-70wPC samples

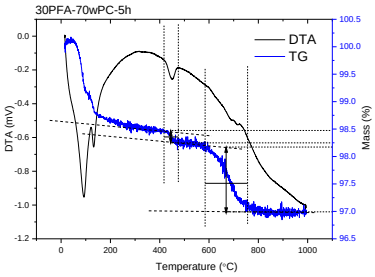

c1) 5h 30PFA-70wPC

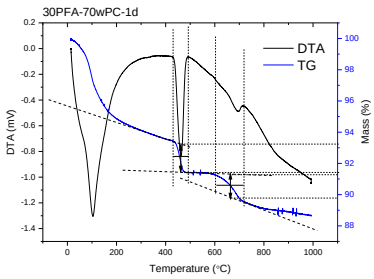

c2) 1d 30PFA-70wPC

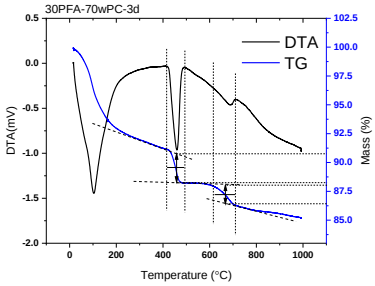

c3) 3d 30PFA-70wPC

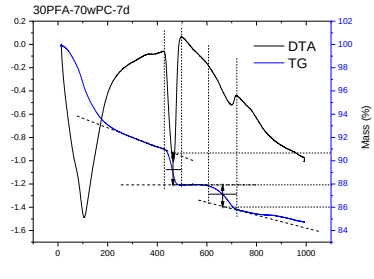

c4) 7d 30PFA-70wPC

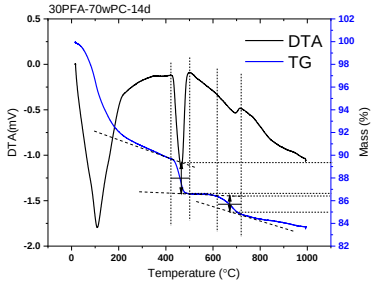

c5) 14d 30PFA-70wPC

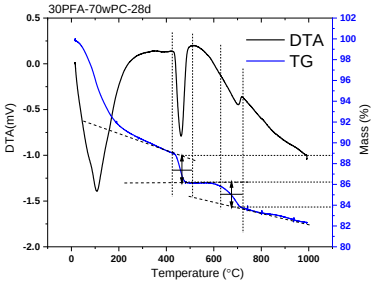

c6) 28d 30PFA-70wPC

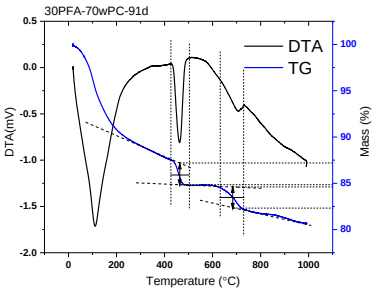

c7) 91d 30PFA-70wPC

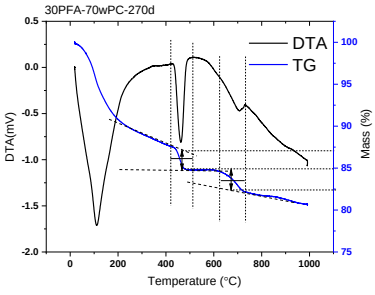

c8) 270d 30PFA-70wPC

d) 30TiO_2-70wPC samples

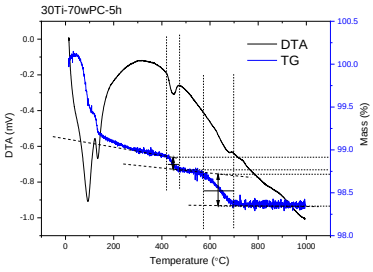

d1) 5h 30TiO_2-70wPC

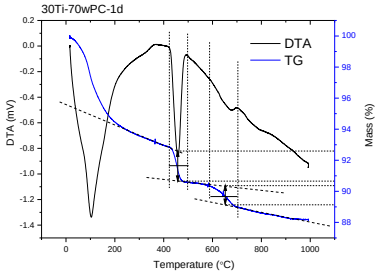

d2) 1d 30TiO_2-70wPC

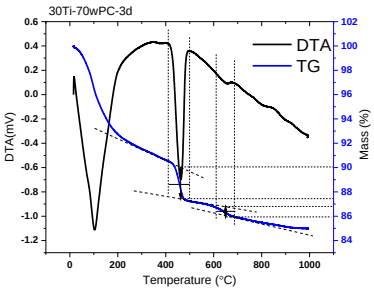

d3) 3d 30TiO_2-70wPC

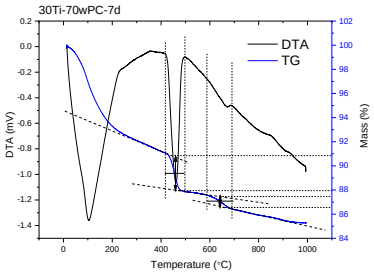

d4) 7d 30TiO_2-70wPC

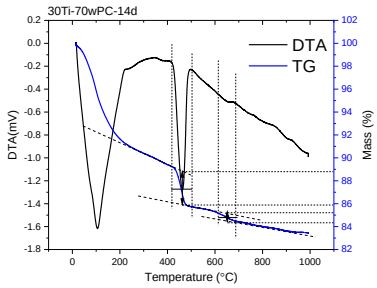

d5) 14d 30TiO_2-70wPC

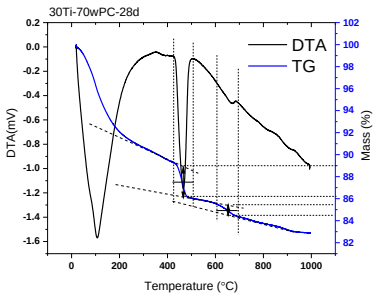

d6) 28d 30TiO_2-70wPC

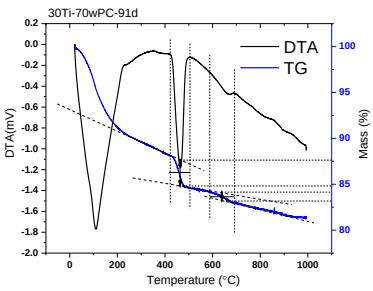

d7) 91d 30TiO_2-70wPC

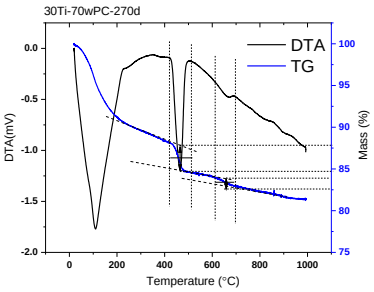

d8) 270d 30TiO_2-70wPC

e) 60GGBS-40wPC samples

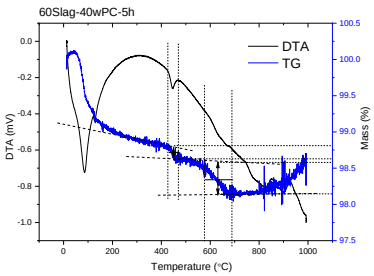

e1) 5h 60GGBS-40wPC

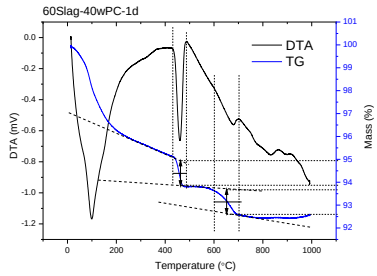

e2) 1d 60GGBS-40wPC

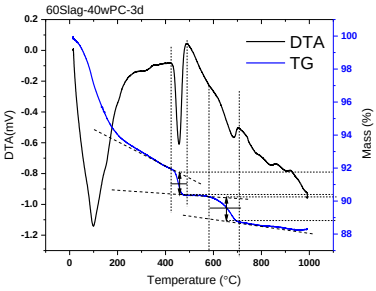

e3) 3d 60GGBS-40wPC

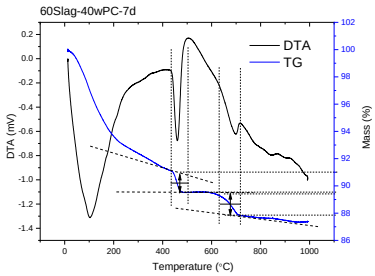

e4) 7d 60GGBS-40wPC

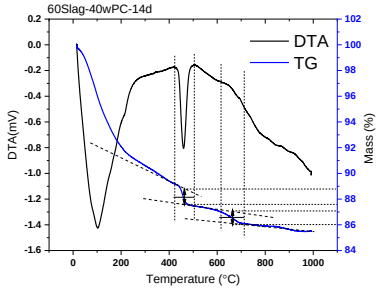

e5) 14d 60GGBS-40wPC

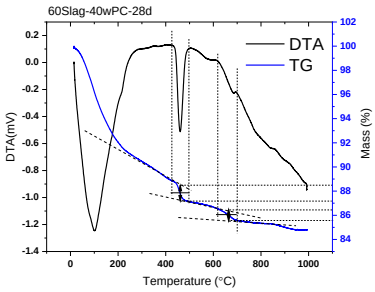

e6) 28d 60GGBS-40wPC

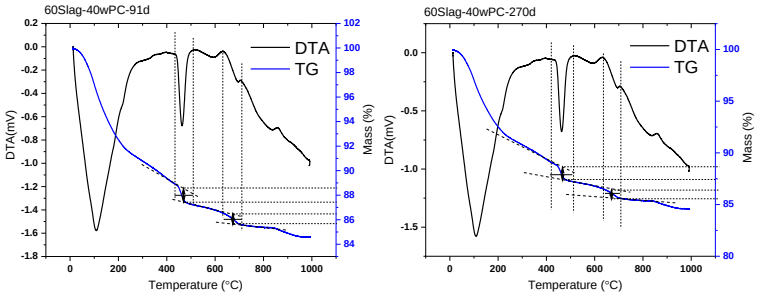

e7) 91d 60GGBS-40wPC e8) 270d 60GGBS-40wPC

f) 60TiO$_2$-40wPC samples

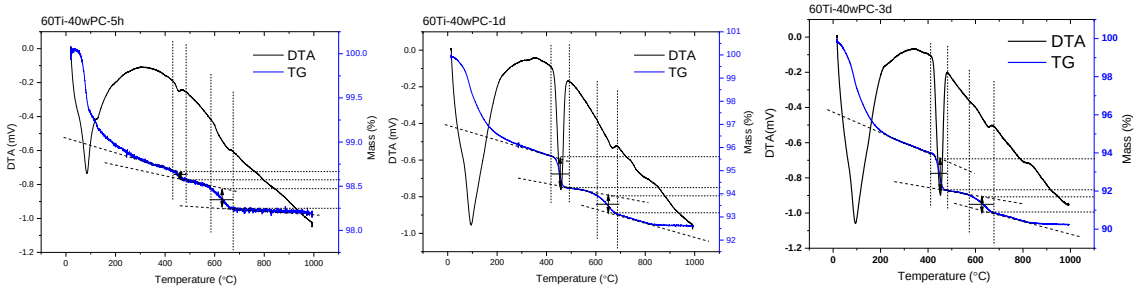

f1) 5h 60TiO$_2$-40wPC f2) 1d 60TiO$_2$-40wPC f3) 3d 60TiO$_2$-40wPC

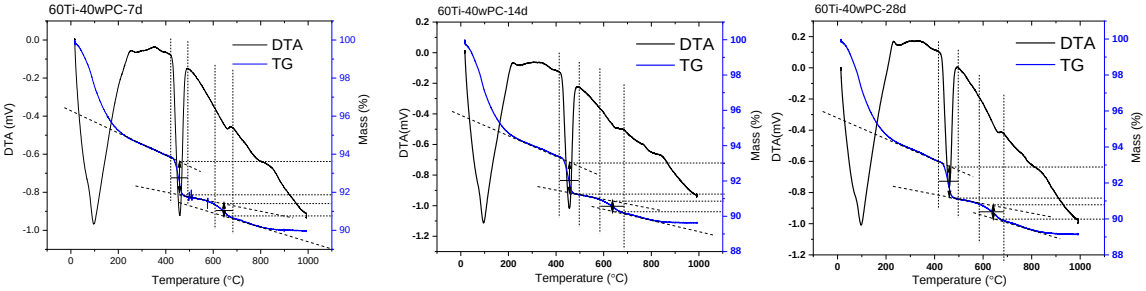

f4) 7d 60TiO$_2$-40wPC f5) 14d 60TiO$_2$-40wPC f6) 28d 60TiO$_2$-40wPC

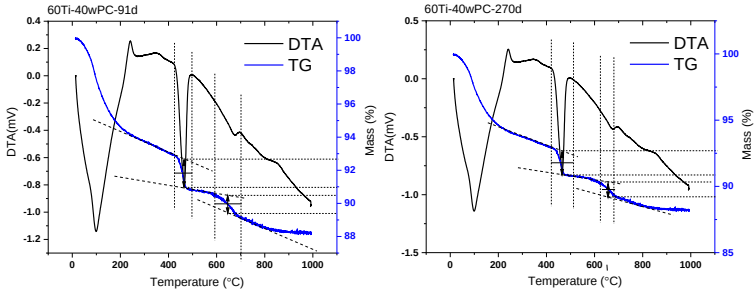

f7) 91d 60TiO$_2$-40wPC f8) 270d 60TiO$_2$-40wPC

Figure D-1. TG-DSC patterns of a) raw materials profiles; b) wPC samples; c) 30PFA-70wPC samples; d) 30TiO$_2$-70wPC; e) 60GGBS-40wPC; f) 60TiO$_2$-40wPC.

Appendix E. Additional FTIR results

Raw materials characterisation

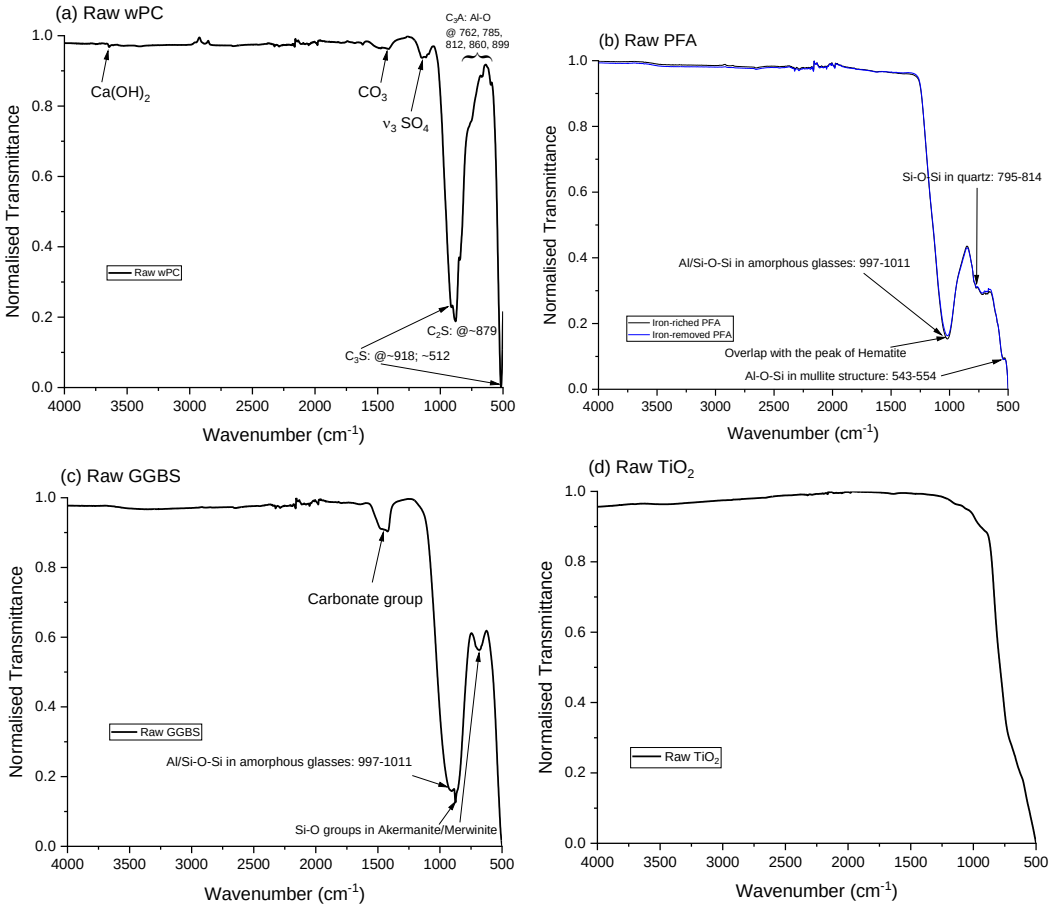

Figure E-1. FTIR characterisation of raw materials: (a) wPC; (b) PFA; (c) GGBS; (d) TiO_2.

Figure E-1 shows the FTIR patterns of starting materials. In wPC sample, the main transmittance peaks are associated to Si-O bonds in Si-bearing phases (i.e. C_3S and C_2S). The signals of Al-O bonds in C_3A are in the range of 762-899 cm^{-1}, which are not obvious in the spectrum. The vibration of sulphate group (S-O bond) indicates the presence of gypsum. In addition, a small peak at around 3500 cm^{-1} shows the signal of Ca-OH, which may confirm the presence of CH and is consistent with TG-DSC data (Figure 4-8). Signal of carbonate group is also found, which was given by TG-DSC-MS as well. For raw PFA, no signal related to carbonate group confirms that the CO_2 released from TG analysis is from unreacted carbon. The removal of hematite was also proven in FTIR peak change. Some Si-O/Al-O bonds present in crystalline are found in both PFA and GGBS. Meanwhile, the main glassy structure in both PFA and GGBS is also identified. TiO_2 (anatase) is transmittable to IR light in ranges of 1000-4000 cm^{-1}, but has

strong shield effect in 500-750 cm^{-1}. These results may indicate that the anatase/cement blends are not suitable for FTIR analysis.

In-situ hydration characterisation of wPC and PFA blended samples

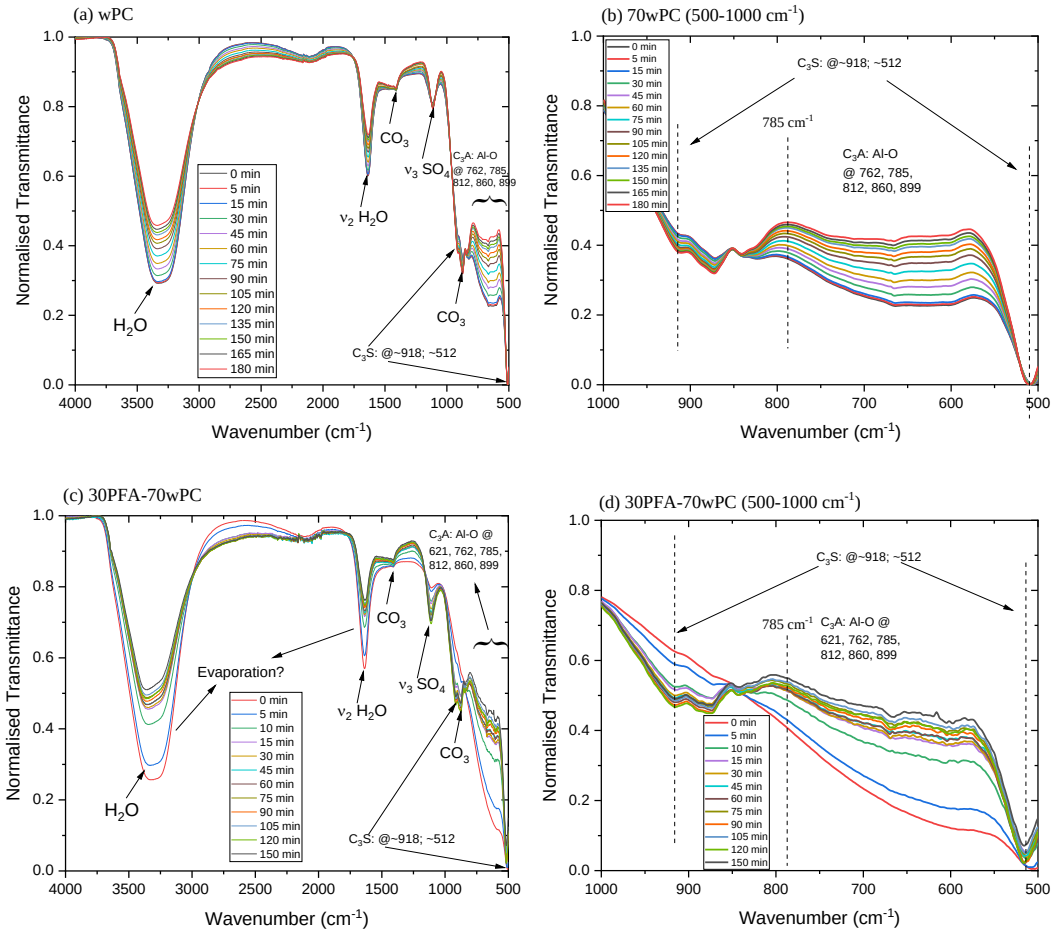

Figure E-2. In-situ FTIR characterisation of wPC and 30% PFA blend.

Appendix F. Identification of Al and Na concentrations used for synthetic C-S-H

Dosage of Al

4% TEOS ($SiC_8H_{20}O_4$ Tetraethyl orthosilicate, M=208.33 g/mol; 0.933g/ml)

Calculation of TEOS content in solution

0.04*10 ml=0.4 ml (TEOS)

0.4 ml*0.933 g/ml=0.3732 g

0.3732 g/ 208.33 = 0.0018 mol=Msi

Assume the Al/Si=0.33

$Al(NO_3)_3 \cdot 9H_2O$ (Aluminum nitrate nonahydrate, M= 375.13 g/mol;)

M_{AL}=Msi*0.33

mAl= M_{Al}*M=0.022176g

Using 0.01 M $Al(NO_3)_3 \cdot 9H_2O$ solution (3.75g/L)

0.022176/3.75*1000=6 ml

Dosage of Na

Assume the Na/Si=1.0

NaOH (sodium hydroxide, M= 40 g/mol;)

M_{Na}=Msi*1.0

mAl= M_{Na}*M=0.0018*40=0.072g

Using 0.1 M NaOH solution (4g/L)

0.072/4*1000=18ml

Appendix G. Deconvolution of ^{29}Si MAS NMR patterns of wPC blends

a) White Portland cement (wPC) samples

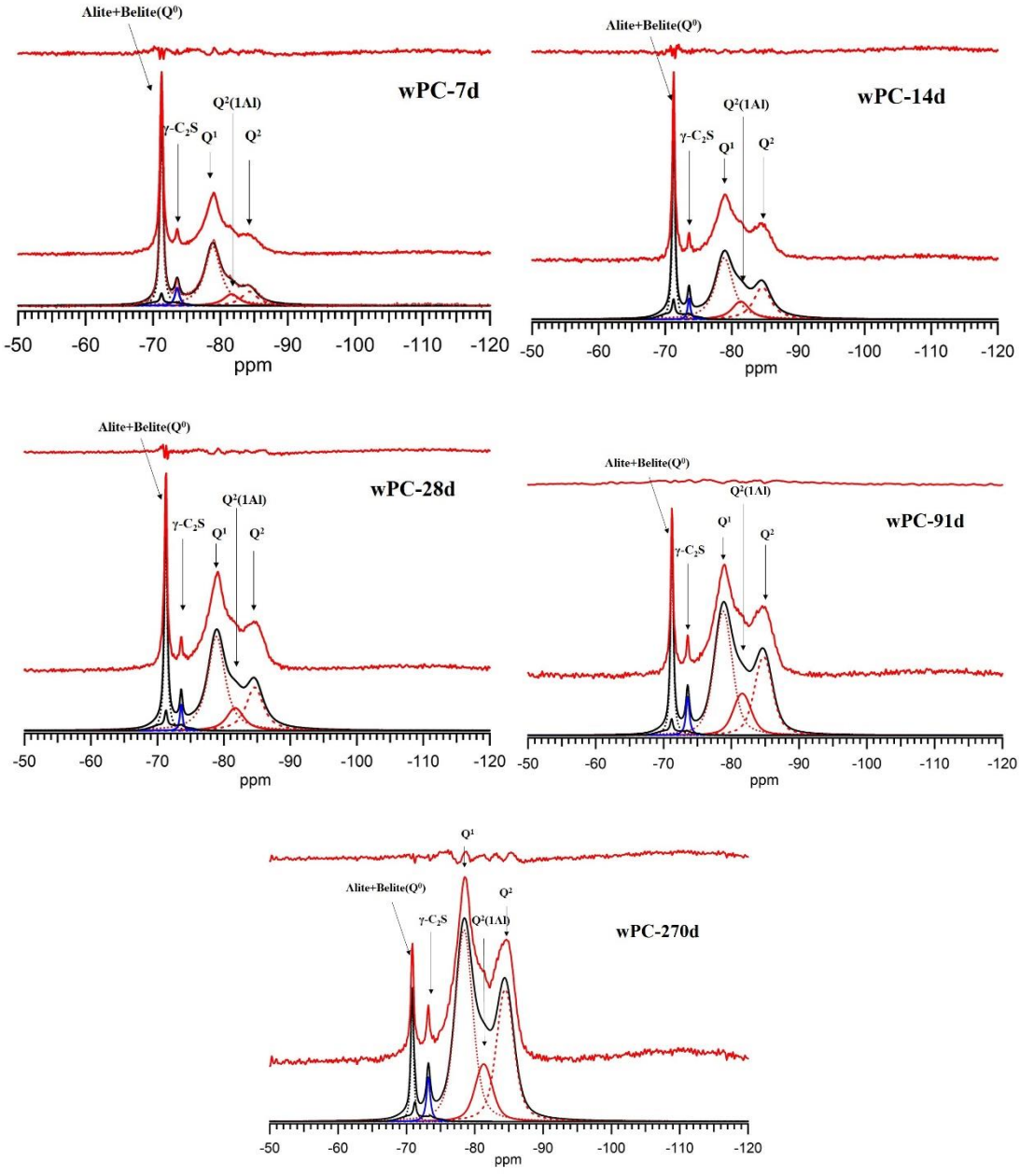

b) 30PFA-70wPC samples

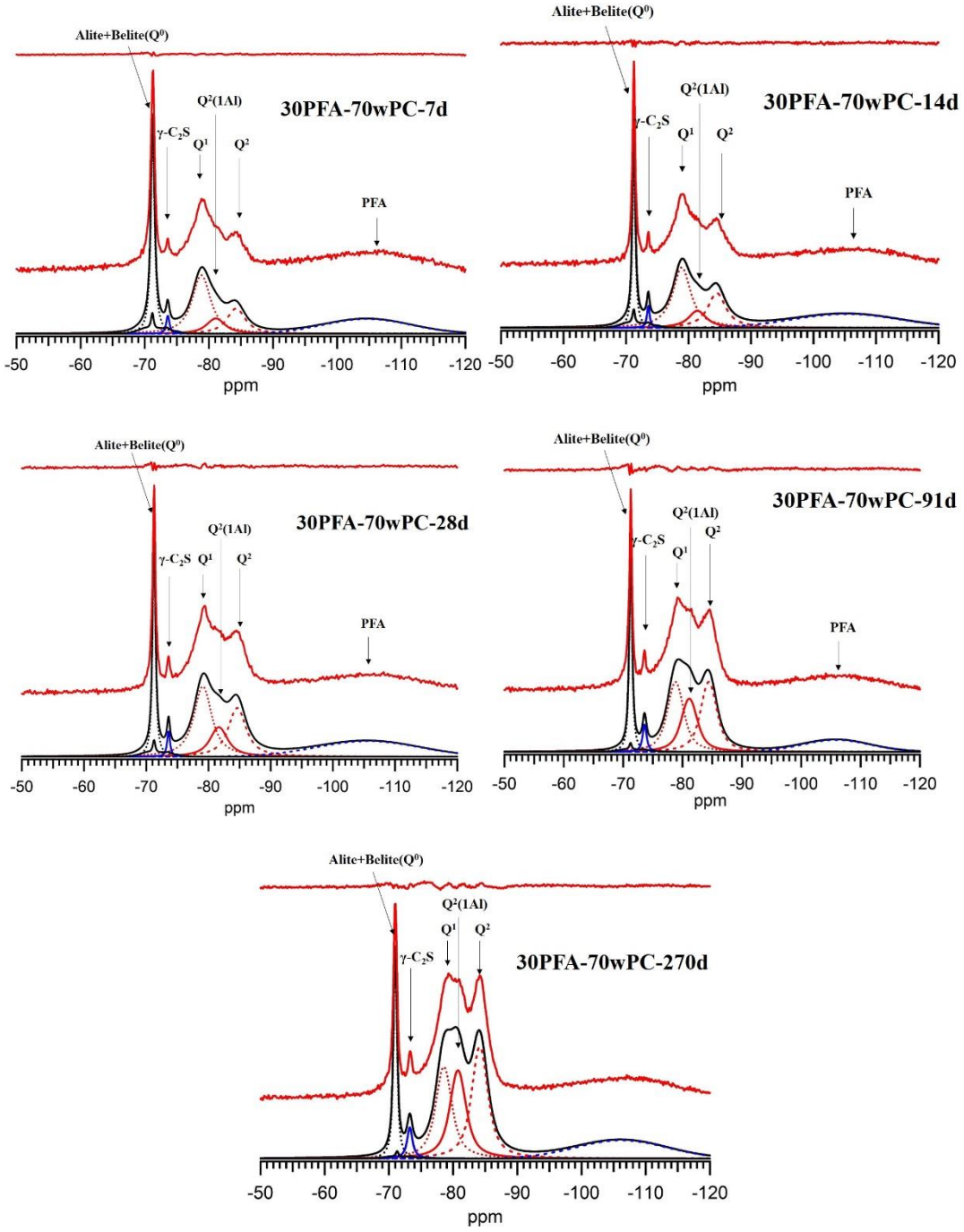

c) 30TiO$_2$-70wPC samples

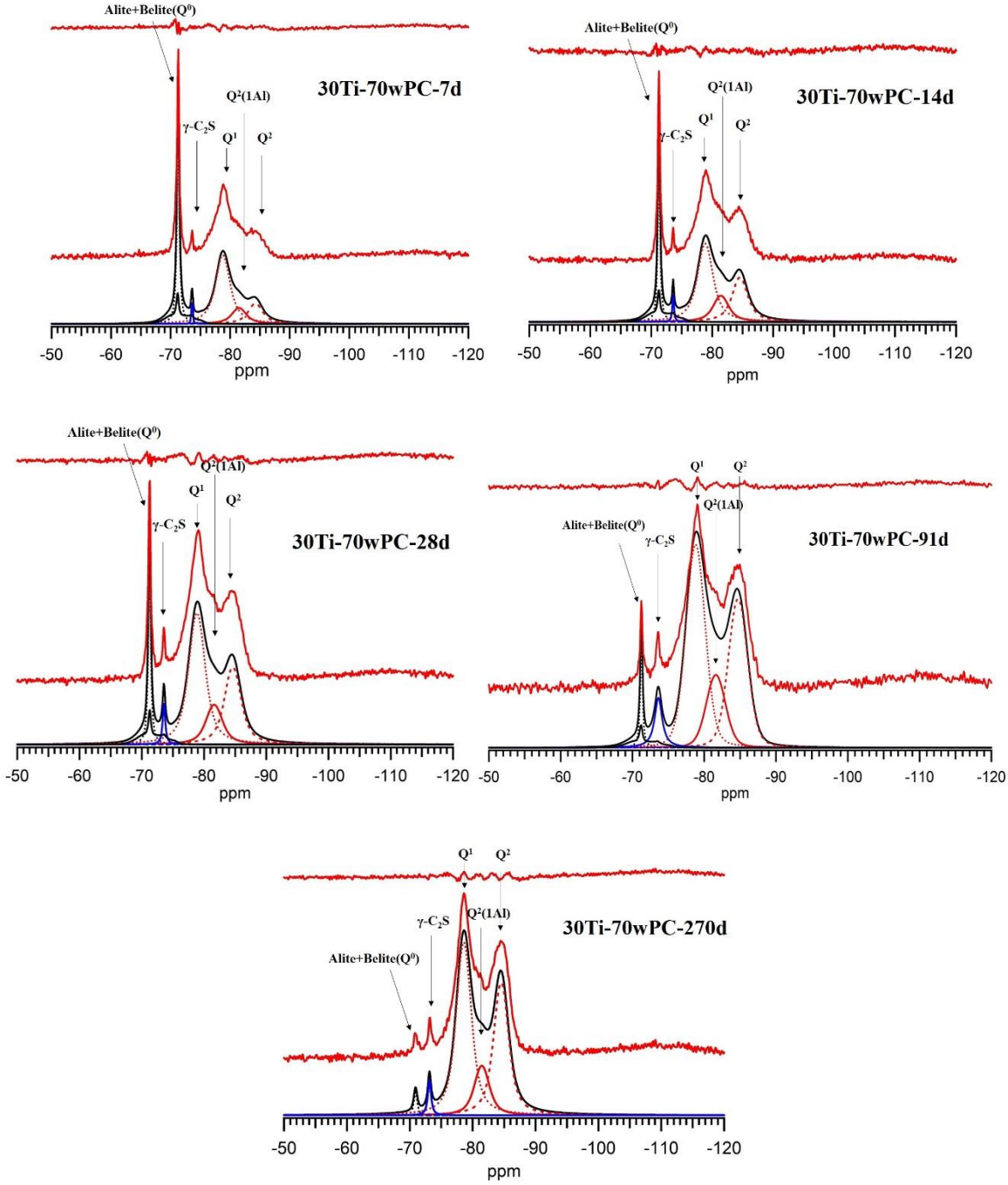

d) 60GGBS-40wPC samples

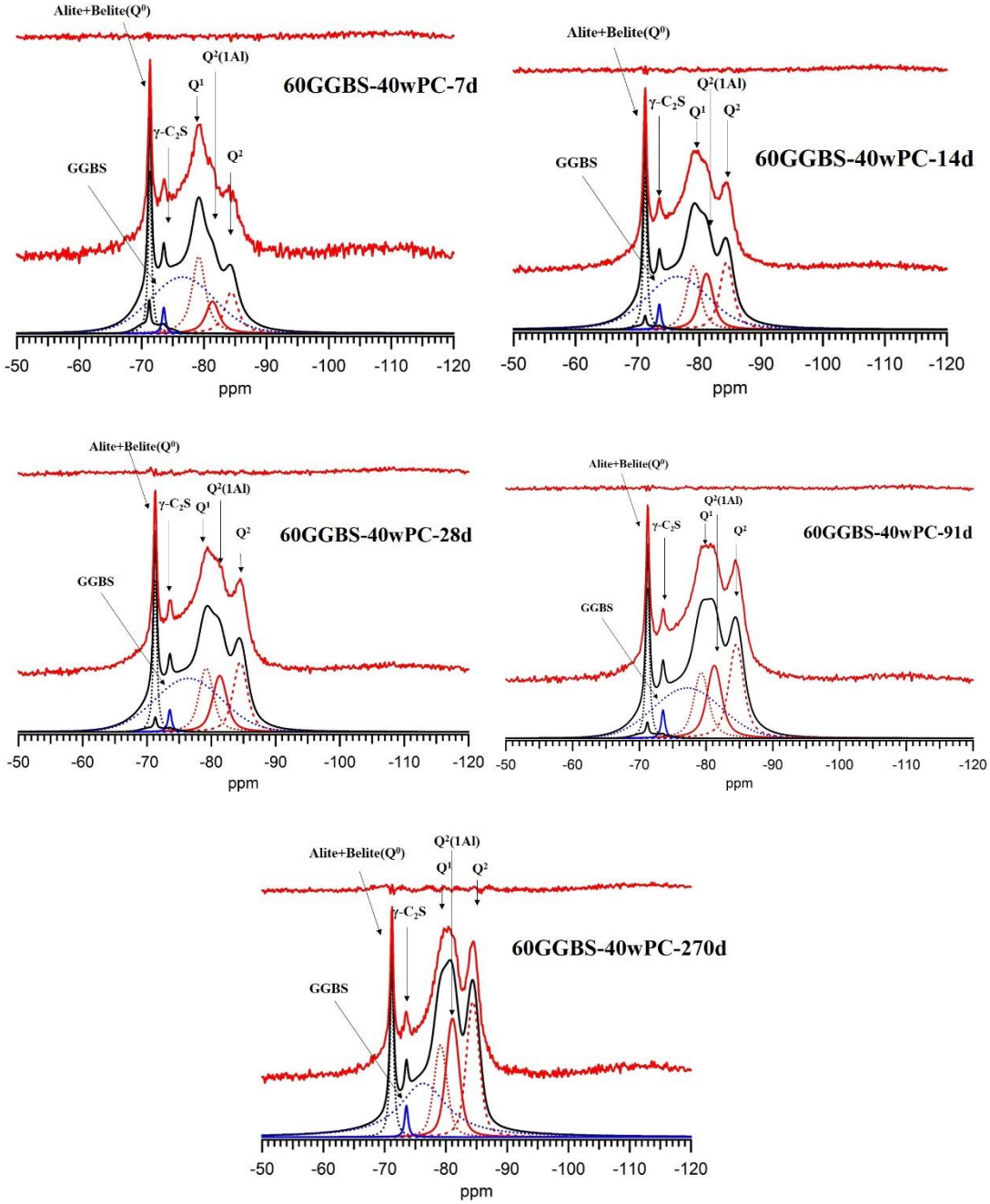

e) 60 TiO_2-40wPC samples

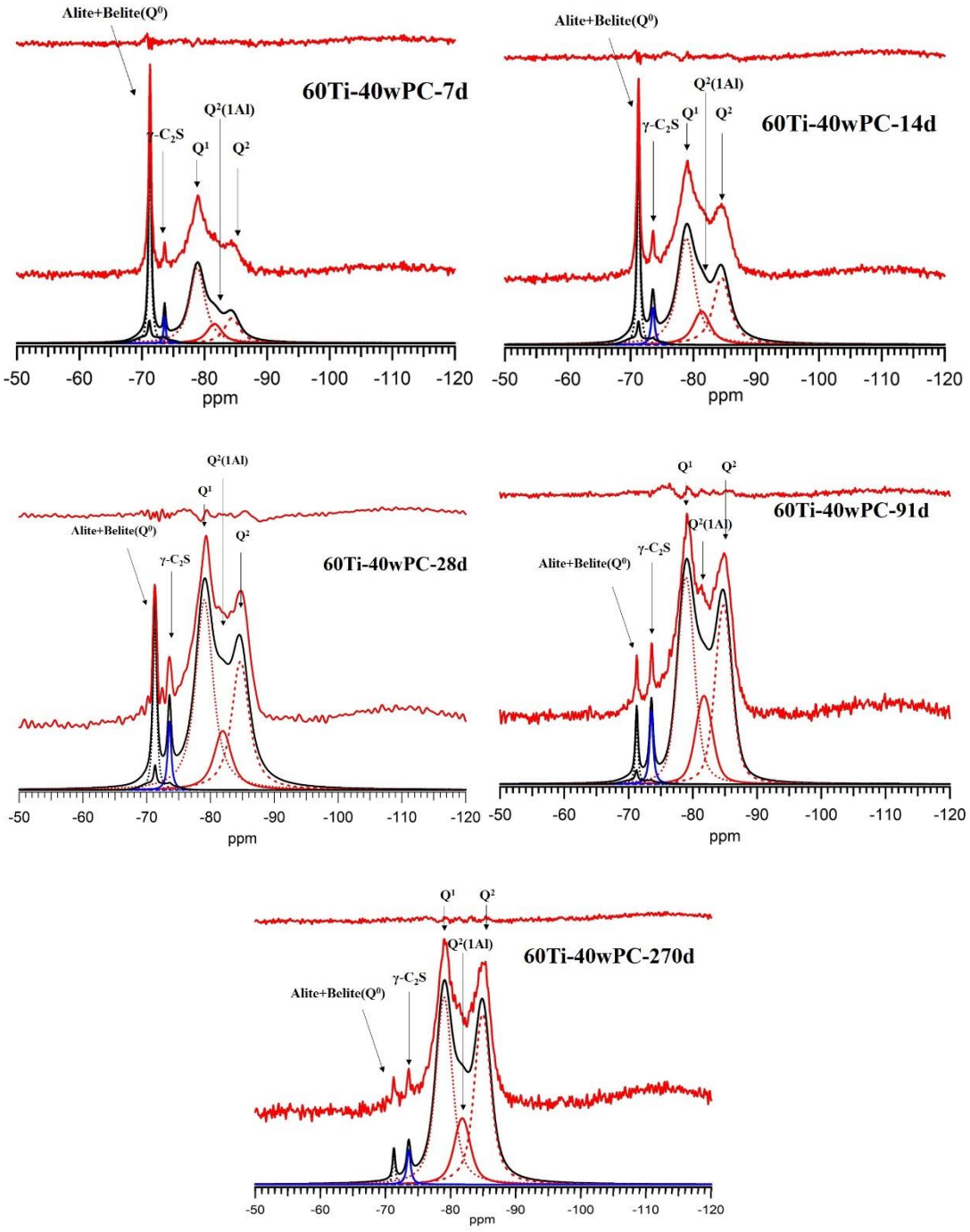

Figure G-1 Deconvolution of single-pulse ^{29}Si MAS NMR patterns of a) raw materials profiles; b) wPC samples; c) 30PFA-70wPC samples; d) 30TiO_2-70wPC; e) 60GGBS-40wPC; f) 60TiO_2-40wPC.

Appendix H. Structural-chemical formulae of C-S-H of wPC blends based on minimum protonation assumption (i. e. w/n=0 in Richardson and Groves' model)

General expressions: (Details can be found in Section 2.3.1)

T/CH: $[Ca_X H_{(6n-2X)}(Si_{1-a}R_a^{[4]})_{(3n-1)}O_{(9n-2)}]I_{\frac{a}{c}(3n-1)}^{c+} \cdot zCa(OH)_2 \cdot mH_2O$

T/J: $[Ca_{2n}H_w(Si_{1-a}R_a^{[4]})_{(3n-1)}O_{(9n-2)}]I_{\frac{a}{c}(3n-1)}^{c+} \cdot (OH)_{w+n(y-2)} \cdot Ca_{\frac{n\cdot y}{2}} \cdot mH_2O$

The ***I*** in the formulae stands for charge-balancing ions such like K^+, Na^+, Ca^{2+}, which was not specified in the following equations. The content of water molecules is not included, which depends on the environmental conditions and drying regime.

In neat wPC samples:

7 d:

T/CH: $[Ca_{4.104}(Si_{0.927}Al_{0.073}^{[4]})_{3.104}O_{10.311}]I_{\frac{a}{c}(3n-1)}^{c+} \cdot 1.988Ca(OH)_2 \cdot mH_2O$

T/J: $[Ca_{2.736}(Si_{0.927}Al_{0.073}^{[4]})_{3.104}O_{10.311}]I_{\frac{a}{c}(3n-1)}^{c+} \cdot (OH)_{3.976} \cdot Ca_{3.356} \cdot mH_2O$

14 d:

T/CH: $[Ca_{5.148}\left(Si_{0.913}Al_{0.086}^{[4]}\right)_{4.147}O_{13.443}]I_{\frac{a}{c}(3n-1)}^{c+} \cdot 2.709Ca(OH)_2 \cdot mH_2O$

T/J: $[Ca_{3.432}(Si_{0.913}Al_{0.086}^{[4]})_{4.147}O_{13.443}]I_{\frac{a}{c}(3n-1)}^{c+} \cdot (OH)_{5.417} \cdot Ca_{4.424} \cdot mH_2O$

28 d:

T/CH: $[Ca_{4.857}(Si_{0.924}Al_{0.076}^{[4]})_{3.857}O_{12.572}]I_{\frac{a}{c}(3n-1)}^{c+} \cdot 2.646Ca(OH)_2 \cdot mH_2O$

T/J: $[Ca_{3.238}(Si_{0.924}Al_{0.076}^{[4]})_{3.857}O_{12.572}]I_{\frac{a}{c}(3n-1)}^{c+} \cdot (OH)_{5.292} \cdot Ca_{4.265} \cdot mH_2O$

91 d:

T/CH: $[Ca_{5.570}(Si_{0.907}Al_{0.093}^{[4]})_{4.570}O_{14.709}]I_{\frac{a}{c}(3n-1)}^{c+} \cdot 2.948Ca(OH)_2 \cdot mH_2O$

T/J: $[Ca_{3.713}(Si_{0.907}Al_{0.093}^{[4]})_{4.570}O_{14.709}]I_{\frac{a}{c}(3n-1)}^{c+} \cdot (OH)_{5.896} \cdot Ca_{4.805} \cdot mH_2O$

270 d:

T/CH: $[Ca_{5.673}\left(Si_{0.918}Al_{0.082}^{[4]}\right)_{4.673}O_{15.018}]I_{\frac{a}{c}(3n-1)}^{c+} \cdot 3.294Ca(OH)_2 \cdot mH_2O$

T/J: $[Ca_{3.782}(Si_{0.918}Al_{0.082}^{[4]})_{4.673}O_{15.018}]I_{\frac{a}{c}(3n-1)}^{c+} \cdot (OH)_{6.589} \cdot Ca_{5.185} \cdot mH_2O$

In 30Ti-70wPC samples:

7 d:

T/CH: $[Ca_{4.347}\left(Si_{0.918}Al_{0.082}^{[4]}\right)_{3.347}O_{11.040}]I_{\frac{a}{c}(3n-1)}^{c+} \cdot 2.077Ca(OH)_2 \cdot mH_2O$

T/J: $[Ca_{2.898}(Si_{0.918}Al_{0.082}^{[4]})_{3.347}O_{11.040}]I_{\frac{a}{c}(3n-1)}^{c+} \cdot (OH)_{4.153} \cdot Ca_{3.525} \cdot mH_2O$

14 d:

T/CH: $[Ca_{5.373}(Si_{0.903}Al^{[4]}_{0.097})_{4.373}O_{14.118}]I^{c+}_{\frac{a}{c}(3n-1)} \cdot 2.716Ca(OH)_2 \cdot mH_2O$

T/J: $[Ca_{3.582}(Si_{0.903}Al^{[4]}_{0.097})_{4.373}O_{14.118}]I^{c+}_{\frac{a}{c}(3n-1)} \cdot (OH)_{5.431} \cdot Ca_{4.506} \cdot mH_2O$

28 d:

T/CH: $[Ca_{5.371}(Si_{0.913}Al^{[4]}_{0.087})_{4.371}O_{14.114}]I^{c+}_{\frac{a}{c}(3n-1)} \cdot 2.915Ca(OH)_2 \cdot mH_2O$

T/J: $[Ca_{3.581}(Si_{0.913}Al^{[4]}_{0.087})_{4.371}O_{14.114}]I^{c+}_{\frac{a}{c}(3n-1)} \cdot (OH)_{5.829} \cdot Ca_{4.705} \cdot mH_2O$

91 d:

T/CH: $[Ca_{5.912}\left(Si_{0.906}Al^{[4]}_{0.094}\right)_{4.912}O_{15.737}]I^{c+}_{\frac{a}{c}(3n-1)} \cdot 3.241Ca(OH)_2 \cdot mH_2O$

T/J: $[Ca_{3.942}(Si_{0.906}Al^{[4]}_{0.094})_{4.912}O_{15.737}]I^{c+}_{\frac{a}{c}(3n-1)} \cdot (OH)_{6.481} \cdot Ca_{5.211} \cdot mH_2O$

270 d:

T/CH: $[Ca_{5.874}(Si_{0.925}Al^{[4]}_{0.075})_{4.874}O_{15.622}]I^{c+}_{\frac{a}{c}(3n-1)} \cdot 3.635Ca(OH)_2 \cdot mH_2O$

T/J: $[Ca_{3.916}(Si_{0.925}Al^{[4]}_{0.075})_{4.874}O_{15.622}]I^{c+}_{\frac{a}{c}(3n-1)} \cdot (OH)_{7.271} \cdot Ca_{5.593} \cdot mH_2O$

In 60TiO_2-40wPC samples:

7 d:

T/CH: $[Ca_{4.513}\left(Si_{0.912}Al^{[4]}_{0.088}\right)_{3.513}O_{11.538}]I^{c+}_{\frac{a}{c}(3n-1)} \cdot 2.123Ca(OH)_2 \cdot mH_2O$

T/J: $[Ca_{3.008}(Si_{0.912}Al^{[4]}_{0.088})_{3.513}O_{11.538}]I^{c+}_{\frac{a}{c}(3n-1)} \cdot (OH)_{4.245} \cdot Ca_{3.628} \cdot mH_2O$

14 d:

T/CH: $[Ca_{5.512}\left(Si_{0.912}Al^{[4]}_{0.088}\right)_{4.512}O_{14.536}]I^{c+}_{\frac{a}{c}(3n-1)} \cdot 3.019Ca(OH)_2 \cdot mH_2O$

T/J: $[Ca_{3.675}(Si_{0.912}Al^{[4]}_{0.088})_{4.512}O_{14.536}]I^{c+}_{\frac{a}{c}(3n-1)} \cdot (OH)_{6.038} \cdot Ca_{4.857} \cdot mH_2O$

28 d:

T/CH: $[Ca_{5.647}(Si_{0.915}Al^{[4]}_{0.085})_{4.647}O_{14.942}]I^{c+}_{\frac{a}{c}(3n-1)} \cdot 3.199Ca(OH)_2 \cdot mH_2O$

T/J: $[Ca_{3.765}(Si_{0.915}Al^{[4]}_{0.085})_{4.647}O_{14.942}]I^{c+}_{\frac{a}{c}(3n-1)} \cdot (OH)_{6.399} \cdot Ca_{5.082} \cdot mH_2O$

91 d:

T/CH: $[Ca_{6.444}(Si_{0.897}Al^{[4]}_{0.103})_{5.444}O_{17.333}]I^{c+}_{\frac{a}{c}(3n-1)} \cdot 3.472Ca(OH)_2 \cdot mH_2O$

T/J: $[Ca_{4.296}(Si_{0.897}Al^{[4]}_{0.103})_{5.444}O_{17.333}]I^{c+}_{\frac{a}{c}(3n-1)} \cdot (OH)_{6.943} \cdot Ca_{5.620} \cdot mH_2O$

270 d:

T/CH: $[Ca_{6.448}(Si_{0.915}Al^{[4]}_{0.085})_{5.448}O_{17.345}]I^{c+}_{\frac{a}{c}(3n-1)} \cdot 3.927Ca(OH)_2 \cdot mH_2O$

T/J: $[Ca_{4.299}(Si_{0.915}Al^{[4]}_{0.085})_{5.448}O_{17.345}]I^{c+}_{\frac{a}{c}(3n-1)} \cdot (OH)_{7.855} \cdot Ca_{6.077} \cdot mH_2O$

<u>In 30PFA-70wPC samples:</u>

7 d:

T/CH: $[Ca_{4.808}\left(Si_{0.916}Al^{[4]}_{0.084}\right)_{3.808}O_{12.425}]I^{c+}_{\frac{a}{c}(3n-1)} \cdot 2.462Ca(OH)_2 \cdot mH_2O$

T/J: $[Ca_{3.206}(Si_{0.916}Al^{[4]}_{0.084})_{3.808}O_{12.425}]I^{c+}_{\frac{a}{c}(3n-1)} \cdot (OH)_{4.924} \cdot Ca_{4.065} \cdot mH_2O$

14 d:

T/CH: $[Ca_{5.290}\left(Si_{0.919}Al^{[4]}_{0.081}\right)_{4.290}O_{13.871}]I^{c+}_{\frac{a}{c}(3n-1)} \cdot 2.947Ca(OH)_2 \cdot mH_2O$

T/J: $[Ca_{3.527}(Si_{0.919}Al^{[4]}_{0.081})_{4.290}O_{13.871}]I^{c+}_{\frac{a}{c}(3n-1)} \cdot (OH)_{5.894} \cdot Ca_{4.710} \cdot mH_2O$

28 d:

T/CH: $[Ca_{5.915}\left(Si_{0.890}Al^{[4]}_{0.110}\right)_{4.915}O_{15.745}]I^{c+}_{\frac{a}{c}(3n-1)} \cdot 2.885Ca(OH)_2 \cdot mH_2O$

T/J: $[Ca_{3.943}(Si_{0.890}Al^{[4]}_{0.110})_{4.915}O_{15.745}]I^{c+}_{\frac{a}{c}(3n-1)} \cdot (OH)_{5.770} \cdot Ca_{4.857} \cdot mH_2O$

91 d:

T/CH: $[Ca_{7.524}\left(Si_{0.840}Al^{[4]}_{0.160}\right)_{6.524}O_{20.573}]I^{c+}_{\frac{a}{c}(3n-1)} \cdot 2.744Ca(OH)_2 \cdot mH_2O$

T/J: $[Ca_{5.016}(Si_{0.840}Al^{[4]}_{0.160})_{6.524}O_{20.573}]I^{c+}_{\frac{a}{c}(3n-1)} \cdot (OH)_{5.487} \cdot Ca_{5.252} \cdot mH_2O$

270 d:

T/CH: $[Ca_{8.587}(Si_{0.822}Al^{[4]}_{0.178})_{7.587}O_{23.761}]I^{c+}_{\frac{a}{c}(3n-1)} \cdot 2.799Ca(OH)_2 \cdot mH_2O$

T/J: $[Ca_{5.725}(Si_{0.822}Al^{[4]}_{0.178})_{7.587}O_{23.761}]I^{c+}_{\frac{a}{c}(3n-1)} \cdot (OH)_{5.598} \cdot Ca_{5.661} \cdot mH_2O$

<u>In 60GGBS-40wPC samples:</u>

7 d:

T/CH: $[Ca_{5.453}(Si_{0.822}Al^{[4]}_{0.178})_{4.453}O_{14.359}]I^{c+}_{\frac{a}{c}(3n-1)} \cdot 2.344Ca(OH)_2 \cdot mH_2O$

T/J: $[Ca_{3.635}(Si_{0.822}Al^{[4]}_{0.178})_{4.453}O_{14.359}]I^{c+}_{\frac{a}{c}(3n-1)} \cdot (OH)_{4.687} \cdot Ca_{4.161} \cdot mH_2O$

14 d:

T/CH: $[Ca_{7.942}(Si_{0.822}Al^{[4]}_{0.178})_{6.942}O_{21.826}]I^{c+}_{\frac{a}{c}(3n-1)} \cdot 2.512Ca(OH)_2 \cdot mH_2O$

T/J: $[Ca_{5.295}(Si_{0.822}Al^{[4]}_{0.178})_{6.942}O_{21.826}]I^{c+}_{\frac{a}{c}(3n-1)} \cdot (OH)_{5.234} \cdot Ca_{5.159} \cdot mH_2O$

28 d:

T/CH: $[Ca_{8.071}\left(Si_{0.822}Al_{0.178}^{[4]}\right)_{7.071}O_{22.214}]I_{\frac{a}{c}(3n-1)}^{c+}\cdot 2.652Ca(OH)_2\cdot mH_2O$

T/J: $[Ca_{5.381}(Si_{0.822}Al_{0.178}^{[4]})_{7.071}O_{22.214}]I_{\frac{a}{c}(3n-1)}^{c+}\cdot (OH)_{5.305}\cdot Ca_{5.343}\cdot mH_2O$

91 d:

T/CH: $[Ca_{9.500}\left(Si_{0.814}Al_{0.186}^{[4]}\right)_{8.500}O_{26.500}]I_{\frac{a}{c}(3n-1)}^{c+}\cdot 3.003Ca(OH)_2\cdot mH_2O$

T/J: $[Ca_{6.333}(Si_{0.814}Al_{0.186}^{[4]})_{8.500}O_{26.500}]I_{\frac{a}{c}(3n-1)}^{c+}\cdot (OH)_{6.006}\cdot Ca_{6.170}\cdot mH_2O$

270 d:

T/CH: $[Ca_{10.007}\left(Si_{0.794}Al_{0.206}^{[4]}\right)_{9.007}O_{28.021}]I_{\frac{a}{c}(3n-1)}^{c+}\cdot 2.534Ca(OH)_2\cdot mH_2O$

T/J: $[Ca_{6.671}(Si_{0.794}Al_{0.206}^{[4]})_{9.007}O_{28.021}]I_{\frac{a}{c}(3n-1)}^{c+}\cdot (OH)_{5.068}\cdot Ca_{5.870}\cdot mH_2O$

Appendix I. Dissolution and precipitation rates of alite

Table I-1Development of Ca and Si element concentrations (ICP-OES) and thermodynamic calculation results (Phreeqc Interactive) during alite hydration at w/s=10 starting in water.

Time	Si/ mmol/L	Ca/ mmol/L	Ln IAP	β C-S-H
5 min	0.705	10.916	-79.16	29.16
30 min	0.226	13.888	-77.99	19.10
2 h	0.021	22.588	-75.89	10.21
6 h	0.010	33.600	-74.53	12.63
12 h	0.017	32.650	-73.48	26.32
24 h	0.018	32.388	-73.29	29.36

Table I-2 Interfacial alite (mainly C_3S) dissolution rate and C-S-H precipitation rate coupled with determined total C_3S dissolution rate and C-S-H precipitation rate.

Time	Interfacial C_3S dissolution rate [µmol/(s*m^2)]	Interfacial C-S-H precipitation rate [nmol/(s*m^2)]	Determined C_3S dissolution rate [µmol/(s*m^2)]	Determined C-S-H precipitation rate [nmol/(s*m^2)]
5 min	-119.99	19.81	21.28	104.39
30 min	-119.32	9.75	25.39	103.81
2 h	-115.76	3.06	15.04	100.71
6 h	-109.15	4.68	24.13	94.96
12 h	-98.22	16.70	99.57	85.45
24 h	-95.45	20.03	141.58	83.04

References

1. Taylor, H.F.W., *Cement chemistry 2nd edition*. 1997, London, UK: Thomas Telford
2. Taylor, H.F.W., *Proposed Structure for Calcium Silicate Hydrate Gel.* Journal of American Ceramic Society, 1986. **69**(6): p. 464-467.
3. Richardson, I.G., *The nature of C-S-H in hardened cements.* Cement and Concrete Research, 1999. **29**: p. 1131-1147.
4. Richardson, I.G., *The nature of the hydration products in hardened cements.* Cement and Concrete Composites, 2000. **22**: p. 97-113.
5. Richardson, I.G., *Tobermorite/jennite- and tobermorite/calcium hydroxide-based models for the structure of C-S-H: applicability to hardened pastes of tricalcium silicate, β-dicalcium silicate, Portland cement, and blends of Portland cement with blast-furnace slag, metakaolin, or silica fume.* Cement and Concrete Research, 2004. **34**(9): p. 1733-1777.
6. Richardson, I.G., *The calcium silicate hydrates.* Cement and Concrete Research, 2008. **38**(2): p. 137-158.
7. Richardson, I.G., *Model structures for C-(A)-S-H(I).* Acta Crystallogr B Struct Sci Cryst Eng Mater, 2014. **70**(Pt 6): p. 903-23.
8. Girao, A.V., *The nanostrructure and degradation of csh in portland and blended cements*, in *School of Civil Engineering*. 2007, University of Leeds: UK.
9. Taylor, R., I.G. Richardson, and R.M.D. Brydson, *Nature of C–S–H in 20 year old neat ordinary Portland cement and 10% Portland cement–90% ground granulated blast furnace slag pastes.* Advances in Applied Ceramics, 2013. **106**(6): p. 294-301.
10. Taylor, R., I.G. Richardson, and R.M.D. Brydson, *Composition and microstructure of 20-year-old ordinary Portland cement–ground granulated blast-furnace slag blends containing 0 to 100% slag.* Cement and Concrete Research, 2010. **40**(7): p. 971-983.
11. W., G.G., et al., *Prograssive changes in the structure of hardened C3S cement pastes due to carbonation.* Journal of the American Ceramic Society, 1991. **74**(11): p. 2891-96.
12. Jia, S., *Micro/Nano-structural Evolution in Blended Cement Paste Due to Prograssive Deionised Water Leaching*, in *School of Civil Engineering*. 2014, University of Leeds: UK.
13. Rodriguez, E.T., *Relation between composition, structure and morphology in C-S-H*, in *School of Civil Engineering*. 2015, University of Leeds: UK.
14. Richardson, I.G., et al., *Hydration of water- and alkali-activated white Portland cement pastes and blends with low-calcium pulverized fuel ash.* Cement and Concrete Research, 2016. **83**: p. 1-18.
15. Lothenbach, B., *Thermodynamic equilibrium calculations in cementitious systems.* Materials and Structures, 2010. **43**(10): p. 1413-1433.
16. Vinnakota, S., *Understanding the long-term evolution of C-S-H phases present in cement backfills*, in *School of Civil Engineering*. 2019, University of Leeds: UK.
17. Myers, R.J., et al., *Solution chemistry of cubic and orthorhombic tricalcium aluminate hydration.* Cement and Concrete Research, 2017. **100**: p. 176-185.
18. Oey, T., et al., *The Filler Effect: The Influence of Filler Content and Surface Area on Cementitious Reaction Rates.* Journal of the American Ceramic Society, 2013. **96**(6): p. 1978-1990.
19. Berodier, E., K. Scrivener, and G. Scherer, *Understanding the Filler Effect on the Nucleation and Growth of C-S-H.* Journal of the American Ceramic Society, 2014. **97**(12): p. 3764-3773.
20. Adu-Amankwah, S., et al., *Influence of limestone on the hydration of ternary slag cements.* Cement and Concrete Research, 2017. **100**: p. 96-109.
21. Scrivener, K.L. and A. Nonat, *Hydration of cementitious materials, present and future.* Cement and Concrete Research, 2011. **41**(7): p. 651-665.
22. Nicoleau, L. and A. Nonat, *A new view on the kinetics of tricalcium silicate hydration.* Cement and Concrete Research, 2016. **86**: p. 1-11.

23. Juilland, P., et al., *Dissolution theory applied to the induction period in alite hydration.* Cement and Concrete Research, 2010. **40**(6): p. 831-844.
24. S. Garrault-Gauffin and A. Nonat, *Experimental investigation of calcium silicate hydrate (C-S-H) nucleation.* Journal of Crystal Growth, 1999. **200**: p. 565-574.
25. Lothenbach, B., et al., *Influence of limestone on the hydration of Portland cements.* Cement and Concrete Research, 2008. **38**(6): p. 848-860.
26. Bullard, J.W., et al., *Mechanisms of cement hydration.* Cement and Concrete Research, 2011. **41**(12): p. 1208-1223.
27. Juenger, M.C.G. and R. Siddique, *Recent advances in understanding the role of supplementary cementitious materials in concrete.* Cement and Concrete Research, 2015. **78**: p. 71-80.
28. Scrivener, K.L., P. Juilland, and P.J.M. Monteiro, *Advances in understanding hydration of Portland cement.* Cement and Concrete Research, 2015. **78**: p. 38-56.
29. Krstulović, R. and P. Dabić, *A conceptual model of the cement hydration process.* Cement and Concrete Research, 2000. **30**: p. 693-698.
30. Thomas, J.J., et al., *Modeling and simulation of cement hydration kinetics and microstructure development.* Cement and Concrete Research, 2011. **41**(12): p. 1257-1278.
31. Kocaba, V., E. Gallucci, and K.L. Scrivener, *Methods for determination of degree of reaction of slag in blended cement pastes.* Cement and Concrete Research, 2012. **42**(3): p. 511-525.
32. Flatt, R.J., G.W. Scherer, and J.W. Bullard, *Why alite stops hydrating below 80% relative humidity.* Cement and Concrete Research, 2011. **41**(9): p. 987-992.
33. Thomas, J.J., et al., *Effect of hydration temperature on the solubility behavior of Ca-, S-, Al-, and Si-bearing solid phases in Portland cement pastes.* Cement and Concrete Research, 2003. **33**(12): p. 2037-2047.
34. Myers, R.J., et al., *Effect of temperature and aluminium on calcium (alumino)silicate hydrate chemistry under equilibrium conditions.* Cement and Concrete Research, 2015. **68**: p. 83-93.
35. Jia, S. and I.G. Richardson, *Micro- and nano-structural evolutions in white Portland cement/pulverized fuel ash cement pastes due to deionized-water leaching.* Cement and Concrete Research, 2017.
36. Lothenbach, B., K. Scrivener, and R.D. Hooton, *Supplementary cementitious materials.* Cement and Concrete Research, 2011. **41**(12): p. 1244-1256.
37. Richardson, I.G., *The importance of proper crystal-chemical and geometrical reasoning demonstrated using layered single and double hydroxides.* Acta Crystallogr B Struct Sci Cryst Eng Mater, 2013. **69**(Pt 2): p. 150-62.
38. Richardson, I.G., *Zn- and Co-based layered double hydroxides: prediction of the a parameter from the fraction of trivalent cations and vice versa.* Acta Crystallogr B Struct Sci Cryst Eng Mater, 2013. **69**(Pt 4): p. 414-7.
39. Guo, B., K. Sasaki, and T. Hirajima, *Selenite and selenate uptaken in ettringite: Immobilization mechanisms, coordination chemistry, and insights from structure.* Cement and Concrete Research, 2017. **100**: p. 166-175.
40. Zhang, M., et al., *Immobilization of Cr(VI) by hydrated Portland cement pastes with and without calcium sulfate.* J Hazard Mater, 2017. **342**: p. 242-251.
41. Midgley, H.G. and P.B. Rao, *Formation of strätlingite, $2CaO.SiO_2.Al_2O_3.8H_2O$, in relation to the hydration of high alumina cement.* Cement and Concrete Research, 1978. **8**: p. 169-172.
42. Scrivener, K.L., et al., *TC 238-SCM: hydration and microstructure of concrete with SCMs State of the art on methods to determine degree of reaction of SCMs.* Materials and Structures, 2015. **48**(4): p. 835-862.
43. Richardson, I.G. and G.W. Groves, *Microstructure and microanalysis of hardened cement pastes involving ground granulated blast-furnace slag.* Journal of Materials Science, 1992. **27**: p. 6204-6212.
44. Luke, K. and E. Lachowski, *Internal Composition of 20-Year-Old Fly Ash and Slag-Blended Ordinary Portland Cement Pastes.* Journal of the American Ceramic Society, 2008. **91**(12): p. 4084-4092.
45. Kaufman, M., *Principles of thermodynamics*. 2001, New York: Marcel Dekker, Inc.

46. M. Atkins, et al., *A thermodynamic model for blended cement.* Cement and Concrete Research, 1992. **22**: p. 497-502.
47. Lothenbach, B., et al., *Thermodynamic modelling of the effect of temperature on the hydration and porosity of Portland cement.* Cement and Concrete Research, 2008. **38**(1): p. 1-18.
48. Damidot, D., et al., *Thermodynamics and cement science.* Cement and Concrete Research, 2011. **41**(7): p. 679-695.
49. Lothenbach, B. and F. Winnefeld, *Thermodynamic modelling of the hydration of Portland cement.* Cement and Concrete Research, 2006. **36**(2): p. 209-226.
50. Kulik, D.A., et al., *GEM-Selektor geochemical modeling package: revised algorithm and GEMS3K numerical kernel for coupled simulation codes.* Computational Geosciences, 2012.
51. Marcus, Y., *The properties_of solvents*. Wiley Series in Solution Chemistry, ed. P.G.T. Fogg. 1998, England: John Wiley & Sons.
52. Barret, J., *Inorganic chemistry in aqueous solution*. 2003, UK: The royal society of chemistry.
53. Richardson, I.G. and G.W. Groves, *Models for the composition and structure of calcium silicate hydrate (C-S-H) gel in hardened tricalcium silicate pastes.* Cement and Concrete Research, 1992. **22**: p. 1101-1110.
54. Richardson, I.G., et al., *The characterization of hardened alkali activated slag paste and the nature of the calcium silicate hydrate phase.* cement and Concrete Research, 1994. **24**(5): p. 813-829.
55. Myers, R.J., S.A. Bernal, and J.L. Provis, *A thermodynamic model for C-(N-)A-S-H gel: CNASH_ss. Derivation and validation.* Cement and Concrete Research, 2014. **66**: p. 27-47.
56. Myers, R.J., *Thermodynamic Modelling of CaO-Al_2O_3-SiO_2-H_2O-Based Cements*, in *Department of Materials Science & Engineering*. 2015, University of Sheffield: UK.
57. Kulik, D.A., *Improving the structural consistency of C-S-H solid solution thermodynamic models.* Cement and Concrete Research, 2011. **41**(5): p. 477-495.
58. Lothenbach, B., L. Pelletier-Chaignat, and F. Winnefeld, *Stability in the system CaO–Al_2O_3–H_2O.* Cement and Concrete Research, 2012. **42**(12): p. 1621-1634.
59. Matschei, T., B. Lothenbach, and F.P. Glasser, *Thermodynamic properties of Portland cement hydrates in the system CaO–Al_2O_3–SiO_2–$CaSO_4$–$CaCO_3$–H_2O.* Cement and Concrete Research, 2007. **37**(10): p. 1379-1410.
60. Bennett, D.G., et al., *A thermodynamic model for blend cements. II: Cement hydrate phases; thermodynamic values and modelling studies.* Journal of Nuclear Materials, 1992. **190**: p. 315-325.
61. Juel, I., et al., *A thermodynamic model for predicting the stability of thaumasite.* Cement and Concrete Composites, 2003. **25**(8): p. 867-872.
62. Balonis, M., et al., *Impact of chloride on the mineralogy of hydrated Portland cement systems.* Cement and Concrete Research, 2010. **40**(7): p. 1009-1022.
63. Chen, J.J., *The nanostructure of calcium silicate hydrate*, in *Feild of materials science and engineering*. 2003, Northwestern University USA.
64. Parrott, L.J. and M.G. Taylor, *A development of the molybdate complexing method for the analysis of silicate mixtures.* Cement and Concrete Research, 1979. **9**: p. 483-488.
65. Parrott, L.J., *An examination of silicate structure of tricalcium silicate hydrated at elevated temperature.* Cement and Concrete Research, 1981. **11**: p. 415-420.
66. Hirljac, J., et al., *Silicate polymerization during the hydration of alite.* Cement and Concrete Research, 1983. **13**: p. 877-886.
67. Parrott, L.J. and J.F. Young, *Effect of prolonged drying upon the silicate structure of hydrated alite pastes.* Cement and Concrete Research, 1981. **11**: p. 11-17.
68. Grangeon, S., et al., *X-ray diffraction: a powerful tool to probe and understand the structure of nanocrystalline calcium silicate hydrates.* Acta Crystallogr B Struct Sci Cryst Eng Mater, 2013. **69**(Pt 5): p. 465-73.
69. Battocchio, F., P.J.M. Monteiro, and H.-R. Wenk, *Rietveld refinement of the structures of 1.0 C-S-H and 1.5 C-S-H.* Cement and Concrete Research, 2012. **42**(11): p. 1534-1548.
70. Cuesta, A., et al., *Synchrotron Radiation Pair Distribution Function Analysis of Gels in Cements.* Crystals, 2017. **7**(10): p. 317.

71. Grangeon, S., et al., *Quantitative X-ray pair distribution function analysis of nanocrystalline calcium silicate hydrates: a contribution to the understanding of cement chemistry.* Journal of Applied Crystallography, 2017. **50**: p. 14-21.
72. Grangeon, S., et al., *Structure of nanocrystalline calcium silicate hydrates: insights from X-ray diffraction, synchrotron X-ray absorption and nuclear magnetic resonance.* J Appl Crystallogr, 2016. **49**(Pt 3): p. 771-783.
73. Lippmma, E., et al., *Structural studies of silicates by solid-state high-resolution silicon-29 NMR.* Journal of American Ceramic Society, 1980. **102**: p. 4889-4893.
74. Trapote-Barreira, A., et al., *Structural changes in C–S–H gel during dissolution: Small-angle neutron scattering and Si-NMR characterization.* Cement and Concrete Research, 2015. **72**: p. 76-89.
75. J.Bensted and P.Barnes, *Structure and performance of cement*. 2 Edition ed. 2002, London Spon Press.
76. Lambert, B.J. and P.E. Mazzola, *Nuclear magnetic resonance spectroscopy, an introduction to principles, applications, and experimental method*. 2004, New Jersey: Pearson Education Press.
77. Nanny, A.M., A.R. Minear, and A.J. Leenheer, *Nuclear Magnetic Resonance Spectroscopy in Environmental Chemistry*. A Series of Advanced Textbooks and Monographs, ed. J.W. Birks. 1997, UK: Oxford University Press.
78. Richardson, I.G., et al., *Location of Aluminum in substituted calcium silicate hydrate (C-S-H) gels as determined by ^{29}Si and ^{27}Al NMR and EELS* Journal of the American Ceramic Society, 1993. **76**(9): p. 2285-88.
79. Brydson, R., I.G. Richardson, and G.W. Groves, *Determining the local coordination of aluminium in cement using electron energy loss near-edge structure.* Mikrochimica Acta, 1994. **114/115**: p. 221-229.
80. Brough, A.R., et al., *Alkali activation of reactive silicas in cements in situ ^{29}Si.* Journal of Materials Science, 1996. **31**: p. 3365-3373.
81. Dyson, H.M., I.G. Richardson, and A.R. Brough, *A Combined ^{29}Si MAS NMR and Selective Dissolution Technique for the Quantitative Evaluation of Hydrated Blast Furnace Slag Cement Blends.* Journal of the American Ceramic Society, 2007. **90**(2): p. 598-602.
82. Brough, A.R., et al., *A study of the pozzolanic reaction by solid-state ^{29}Si nuclear magnetic resonance using selective isotopic enrichment.* Journal of Materials Science, 1995. **30**: p. 1671-1678.
83. Sevelsted, T.F. and J. Skibsted, *Carbonation of C–S–H and C–A–S–H samples studied by ^{13}C, ^{27}Al and ^{29}Si MAS NMR spectroscopy.* Cement and Concrete Research, 2015. **71**: p. 56-65.
84. Richardson, I.G., et al., *Characterisation of cement hydrate phases by TEM, NMR and Raman spectroscopy.* Advances in Cement Research, 2010. **22**(4): p. 233-248.
85. Lippmma, E., et al., *A high resolution ^{29}Si NMR study of the hydration of tricalciumsilicate.* Cement and Concrete Research, 1982. **12**: p. 597-602.
86. Rodger, S.A., et al., *Hydration of tricalcium silicate followed by ^{29}Si NMR with cross polarization* Journal of American Ceramic Society, 1988. **71**: p. 91-96.
87. Brough, A.R., et al., *In situ solid-state NMR studies of Ca_3SiO_5: hydration at room temperature and at elevated temperatures using ^{29}Si enrichment.* Journal of Materials Science, 1994. **29**: p. 3926-3940.
88. Tajuelo Rodriguez, E., et al., *Thermal stability of C-S-H phases and applicability of Richardson and Groves' and Richardson C-(A)-S-H(I) models to synthetic C-S-H.* Cement and Concrete Research, 2017. **93**: p. 45-56.
89. Richardson, I.G. and G.W. Groves, *The incorporation of minor and trace elements into calcium silicate hydrate gel in hardened cement pastes.* Cement and Concrete Research, 1993. **23**: p. 131-138.
90. Richardson, I.G. and G.W. Groves, *The structure of the calcium silicate hydrate phases present in hardened pastes of white portland cement GGBFS.* Journal of Materials Science, 1997. **32**: p. 4793-4802.

91. State, H. and D. Muller, *On the coordination of Al in ill-crystallized C-S-H phases formed by hydratio of tricalcium silicate and by precipitation reactions at ambient temperature.* Cement and Concrete Research, 1987. **17**: p. 553-561.
92. Cong, X. and R.J. Kirkpatrick, *^{17}O and ^{29}Si MAS NMR study of beta-C_2S hydration and the structure of calcium-silicate hydrates.* Cement and Concrete Research, 1993. **23**: p. 1065-1077.
93. Rassem, R., Z.H. Theveneau, and D. Heidemann, *Proton high resolution solid state NMR study of C_3S hydration.* cement and Concrete Research, 1993. **23**: p. 169-176.
94. Egerton, R.F., *Physical principles of electron microscopy. An introduction to TEM, SEM, and AEM*. 2005, US: Springer.
95. Goodhew, P.J., J. Humphrey, and R. Beanland, *Electron microscopy and analysis*. Third ed. 2001, New York: Taylor & Francis.
96. Williams, D.B. and C.B. Carter, *Handbook of transmission electron microscopy*. 1996, New York: Plenum Press.
97. Richardson, I.G. and S. Li, *Composition and structure of an 18-year-old 5M KOH-activated ground granulated blast-furnace slag paste.* Construction and Building Materials, 2018. **168**: p. 404-411.
98. Girão, A.V., et al., *Composition, morphology and nanostructure of C–S–H in 70% white Portland cement–30% fly ash blends hydrated at 55°C.* Cement and Concrete Research, 2010. **40**(9): p. 1350-1359.
99. Groves, G.W., P.J. Le Sueure, and W. Sinclair, *Transmission Electron Microscopy and Microanalytical Studies of Ion-Beam-Thinned Sections of Tricalcium Silicate Paste.* Journal of the American Ceramic Society, 1986. **69**(4): p. 353-56.
100. Richard_A._Nyquist, *Interpreting Infrared, Raman, and Nuclear Magnetic Resornace Spectra*. Vol. Vol. 1 Variables in data interpretation of Infrared and Raman spectra. 2001, USA: Acadamic Press.
101. Mollah, M.A., T.R. Hess, and Y.N. Tsai, *An FTIR and XPS investigations of the effects of carbonation on the solidification/stabilization of cement based systems-Portland type V with zinc.* Cement and Concrete Research, 1993. **23**: p. 773-784.
102. Renaudin, G., et al., *Structural characterization of C–S–H and C–A–S–H samples—Part II: Local environment investigated by spectroscopic analyses.* Journal of Solid State Chemistry, 2009. **182**(12): p. 3320-3329.
103. Yu, P., et al., *Structure of calcium silicate hydrate (C-S-H): Near-, Mid-, and Far-Infrared spectroscopy.* Journal of American Ceramic Society, 1999. **82**: p. 742-748.
104. Kirkpatrick, R.J., et al., *Raman spectroscopy of C-S-H, Tobermorite, and Jennite.* Advanced Cement Based Materials, 1997. **5**: p. 93-99.
105. Chen, J.J., et al., *Solubility and structure of calcium silicate hydrate.* Cement and Concrete Research, 2004. **34**(9): p. 1499-1519.
106. Thomas, J.J., et al., *Effects of decalcification on the microstructure and surface area of cement and tricalcium silicate pastes.* Cement and Concrete Research, 2004. **34**(12): p. 2297-2307.
107. Jennings, H.M., *Refinements to colloid model of C-S-H in cement: CM-II.* Cement and Concrete Research, 2008. **38**(3): p. 275-289.
108. Thomas, J.J., A.J. Allen, and H.M. Jennings, *Density and water content of nanoscale solid C–S–H formed in alkali-activated slag (AAS) paste and implications for chemical shrinkage.* Cement and Concrete Research, 2012. **42**(2): p. 377-383.
109. Eitel, W., *Silicate science, silicate structures and dispersoid systems*. Vol. VI. 1975, New York: Acadamic Press.
110. Liebau, F., *Structure chemistry of silicates: Structure, Bonding, and Classification*. 1985, Berlin: Springer-Verlag.
111. Bonaccorsi, E., S. Merlino, and A.R. Kampf, *The Crystal Structure of Tobermorite 14 A (Plombierite), a C-S-H Phase.* Journal of the American Ceramic Society, 2005. **88**(3): p. 505-512.
112. Hara, N. and N. Inoue, *Formation of jennite from fumed silica.* Cement and Concrete Research, 1980. **10**(677-682).

113. Bonaccorsi, E., S. Merlino, and H.F.W. Taylor, *The crystal structure of jennite, $Ca_9Si_6O_{18}(OH)_6{\cdot}8H_2O$.* Cement and Concrete Research, 2004. **34**(9): p. 1481-1488.
114. Garbev, K., *Structure, properties and quantitative Rietveld analysis of calcium silicate hydrates (C-S-H-phases) crystallised under hydrothermal conditions*. 2004, Institut für Technische Chemie.
115. Bernard, E., *Magnesium silicate hydrate (M-S-H) characterization: temperature, calcium, aluminum and alkali*. 2018, Université Bourgogne Franche-Comté: France.
116. Cong, X. and R.J. Kirkpatrick, *^{29}Si MAS NMR study of the structure of calcium silicate hydrate.* Advanced Cement Based Materials, 1996. **3**: p. 144-156.
117. Garbev, K., et al., *Cell Dimensions and Composition of Nanocrystalline Calcium Silicate Hydrate Solid Solutions. Part 1: Synchrotron-Based X-Ray Diffraction.* Journal of the American Ceramic Society, 2008. **91**(9): p. 3005-3014.
118. Pardal, X., I. Pochard, and A. Nonat, *Experimental study of Si–Al substitution in calcium-silicate-hydrate (C-S-H) prepared under equilibrium conditions.* Cement and Concrete Research, 2009. **39**(8): p. 637-643.
119. Zhang, Z., G.W. Scherer, and A. Bauer, *Morphology of cementitious material during early hydration.* Cement and Concrete Research, 2018. **107**: p. 85-100.
120. Schönlein, M. and J. Plank, *A TEM study on the very early crystallization of C-S-H in the presence of polycarboxylate superplasticizers: Transformation from initial C-S-H globules to nanofoils.* Cement and Concrete Research, 2018. **106**: p. 33-39.
121. Ciath, T.D. and E.G. Swenson, *Morphology and microstructure of hydrating portland cement and its constituents II. Changes in hydration of calcium silicates alone and in the presence of triethanolamine and calcium lignosulphonate, both with and without gypsum.* Cement and Concrete Research, 1971. **1**: p. 159-176.
122. Ciath, T.D. and E.G. Swenson, *Morphology and microstructure of hydrating portland cement and its constituents I. Changes in hydration of tricalcium aluminate alone and in the presence of triethanolamine or calcium lignosulphonate.* Cement and Concrete Research, 1971. **1**: p. 143-158.
123. Berger, R.L. and J.D. McGregor, *Influence of admixtures on the morphology of calcium hydroxide formed during tricalcium silicate hydration.* Cement and Concrete Research, 1972. **2**: p. 43-55.
124. Zhang, Z. and G.W. Scherer, *Supercritical drying of cementitious materials.* Cement and Concrete Research, 2017. **99**: p. 137-154.
125. Zhang, Z., M. Thiery, and V. Baroghel-Bouny, *An equation of drying kinetics for cementitious materials.* Drying Technology, 2017: p. 1-14.
126. Groves, G.W., *TEM studies of cement hydration.* Mater. Res. Soc. Symp.(M) Proc. – Microstructural Development During Hydration of Cement, 1986. **85**.
127. Viallis-Terrisse, H., A. Nonat, and J.-C. Petit, *Zeta-Potential Study of Calcium Silicate Hydrates Interacting with Alkaline Cations.* Journal of Colloid and Interface Science, 2001. **244**(1): p. 58-65.
128. He, Y., et al., *Effect of C/S ratio on morphology and structure of hydrothermally synthesized calcium silicate hydrate.* Journal of Wuhan University of Technology-Mater. Sci. Ed., 2011. **26**(4): p. 770-773.
129. Hou, D., H. Ma, and Z. Li, *Morphology of calcium silicate hydrate (C-S-H) gel: a molecular dynamic study.* Advances in Cement Research, 2015. **27**(3): p. 135-146.
130. Li, S., *Microstructure and composition characterisation of three 20-year-old GGBS-OPC blended pastes.* Construction and Building Materials, 2016. **123**: p. 226-234.
131. Richardson, I.G. and J.G. Cabrera, *The nature of C-S-H in model slag-cements.* Cement and Concrete Composites, 2000. **22**: p. 259-266.
132. Chen, W. and H.J.H. Brouwers, *The hydration of slag, part 1: reaction models for alkali-activated slag.* Journal of Materials Science, 2006. **42**(2): p. 428-443.
133. Chen, W. and H.J.H. Brouwers, *The hydration of slag, part 2: reaction models for blended cement.* Journal of Materials Science, 2006. **42**(2): p. 444-464.
134. Wang, X.-Y. and H.-S. Lee, *Modeling the hydration of concrete incorporating fly ash or slag.* Cement and Concrete Research, 2010. **40**(7): p. 984-996.

135. H.F.W. Taylor and J.W. Howison, *Relationships between calcium silicates and clay minerals.* Clay Miner. Bull., 1956. **3**: p. 98-111.
136. Pellenq, R.J.M., et al., *A realistic molecular model of cement hydrates.* Proceedings of the National Academy of Sciences of the United States of America, 2009. **106**(38): p. 16102-16107.
137. Zhang, L., et al., *Hydration for the Alite mineral: Morphology evolution, reaction mechanism and the compositional influences.* Construction and Building Materials, 2017. **155**: p. 413-426.
138. Hou, D., et al., *Reactive molecular dynamics and experimental study of graphene-cement composites: Structure, dynamics and reinforcement mechanisms.* Carbon, 2017. **115**: p. 188-208.
139. Zhou, Y., et al., *Interfacial Connection Mechanisms in Calcium-Silicate-Hydrates/Polymer Nanocomposites: A Molecular Dynamics Study.* ACS Appl Mater Interfaces, 2017. **9**(46): p. 41014-41025.
140. Ye, H., *Creep Mechanisms of Calcium–Silicate–Hydrate: An Overview of Recent Advances and Challenges.* International Journal of Concrete Structures and Materials, 2015. **9**(4): p. 453-462.
141. Taylor, H.F.W. *Chemistry of cement*. in *Proceedings of the fourth international symposium*. 1960. Washigton: National Bureau of Standards Washington, D.C.
142. Feldman, R.F. and P.J. Sereda, *A New model for hydrated Portland cement and its practical implications.* Engineering Journal of Canada, 1970. **53**(8/9): p. 53-59.
143. Rickerby, J.A., *Characterisation of hardened cements incorporating simulated intermediate level waste*, in *School of civil engineering*. 2015, University of Leeds: UK.
144. Jennings, H.M., *A model for the microstructrure of calcium silicate hydrate in cement paste.* Cement and Concrete Research, 2000. **30**: p. 101-116.
145. Ye, H. and A. Radlińska, *Shrinkage mitigation strategies in alkali-activated slag.* Cement and Concrete Research, 2017. **101**: p. 131-143.
146. R. S. Barneyback, J. and S. Diamond, *Expression and analysis of pore fluids from hardened cement pastes and mortars.* Cement and Concrete Research, 1981. **11**: p. 279-285.
147. Vollpracht, A., et al., *The pore solution of blended cements: a review.* Materials and Structures, 2015. **49**(8): p. 3341-3367.
148. Rothestein, D., et al., *Solubility behavior of Ca-, S-, Al-, and Si-bearing solid phases in Portland cement pore solutions as a function of hydration time.* Cement and Concrete Research, 2002. **32**: p. 1663-1671.
149. Nicoleau, L., E. Schreiner, and A. Nonat, *Ion-specific effects influencing the dissolution of tricalcium silicate.* Cement and Concrete Research, 2014. **59**: p. 118-138.
150. Bernard, E., et al., *Formation of magnesium silicate hydrates (M-S-H).* Physics and Chemistry of the Earth, Parts A/B/C, 2017. **99**: p. 142-157.
151. Schöler, A., et al., *Early hydration of SCM-blended Portland cements: A pore solution and isothermal calorimetry study.* Cement and Concrete Research, 2017. **93**: p. 71-82.
152. Gallucci, E., et al., *Advances in dissolution understanding and their implications for cement hydration.* RILEM Technical Letters, 2017. **2**: p. 90.
153. Lasaga, A.C. and A. Luttge, *Variation of crystal dissolution rate based on a dissolution stepwave model.* Science, 2001. **291**(5512): p. 2400-2404.
154. Nicoleau, L., A. Nonat, and D. Perrey, *The di- and tricalcium silicate dissolutions.* Cement and Concrete Research, 2013. **47**: p. 14-30.
155. Nicoleau, L. and A. Nonat, *The solubility of C3S and its related factors*, in *ICCC 2015*. 2015: Beijing, China.
156. Bellmann, F. and H.-M. Ludwig, *Analysis of aluminum concentrations in the pore solution during hydration of tricalcium silicate.* Cement and Concrete Research, 2017. **95**: p. 84-94.
157. Bellmann, F., et al., *Dissolution rates during the early hydration of tricalcium silicate.* Cement and Concrete Research, 2015. **72**: p. 108-116.
158. Bellmann, F. and G.W. Scherer, *Analysis of C-S-H growth rates in supersaturated conditions.* Cement and Concrete Research, 2017.

159. Suraneni, P. and R.J. Flatt, *Use of micro-reactors to obtain new insights into the factors influencing tricalcium silicate dissolution.* Cement and Concrete Research, 2015. **78**: p. 208-215.
160. Nalet, C. and A. Nonat, *Effects of hexitols on the hydration of tricalcium silicate.* Cement and Concrete Research, 2017. **91**: p. 87-96.
161. Nalet, C. and A. Nonat, *Effects of functionality and stereochemistry of small organic molecules on the hydration of tricalcium silicate.* Cement and Concrete Research, 2016. **87**: p. 97-104.
162. Caruso, F., et al., *ICP-OES method for the characterization of cement pore solutions and their modification by polycarboxylate-based superplasticizers.* Cement and Concrete Research, 2017. **91**: p. 52-60.
163. Nalet, C. and A. Nonat, *Impacts of hexitols on the hydration of a tricalcium aluminate-calcium sulfate mixture.* Cement and Concrete Research, 2016. **89**: p. 177-186.
164. Jennings, H.M., *Aqueous Solubility Relationships for two Types of Calcium Silicate Hydrate.* Journal of the American Ceramic Society, 1986. **69**(8): p. 614-618.
165. Song, S. and H.M. Jennings, *Pore solution chemistry of alkali-activated ground granulated blast-furnace slag.* Cement and Concrete Research, 1999. **29**: p. 159-170.
166. Chen, J.J., J.J. Thomas, and H.M. Jennings, *Decalcification shrinkage of cement paste.* Cement and Concrete Research, 2006. **36**(5): p. 801-809.
167. Begarin, F., et al., *Hydration of alite containing aluminium.* Advances in Applied Ceramics, 2013. **110**(3): p. 127-130.
168. Scrivener, K., R. Snellings, and B. Lothenbach, *A practical guide to microstructural analysis of cementitious materials*, ed. K. Scrivener, R. Snellings, and B. Lothenbach. 2016, Boca Raton: CRC Press.
169. Herterich, J.A., *Microstructure and phase assemblage of low-clinker cements during early stages of carbonation*, in *School of civil engineering* 2017, University of Leeds: UK.
170. Duer, M.J., *Solid-State NMR Spectroscopy Principles and Applications*, ed. M.J. Duer. 2002, Osney Mead, Oxford Blackwell Science Ltd.
171. Hill, S.J., *Inductively Coupled Plasma Spectrometry and its Applications*. Analytical Chemistry, ed. A.J. Handley and J.M. Chalmers. 2007, UK: Blackwell Publishing Ltd.
172. Dean, J.R., *Practical Inductively Coupled Plasma Spectrocopy* Analytical Techniques in the Sciences (AnTS), ed. D.J. Ando. 2005, England: John Wiley & Sons Ltd, .
173. Scarlett, N.V.Y. and I.C. Madsen, *Quantification of phases with partial or no known crystal structures.* Powder Diffraction, 2006. **21**(4): p. 278-284.
174. Snellings, R., A. Salze, and K.L. Scrivener, *Use of X-ray diffraction to quantify amorphous supplementary cementitious materials in anhydrous and hydrated blended cements.* Cement and Concrete Research, 2014. **64**: p. 89-98.
175. Zhu, X., et al., *Understanding the aqueous phase of alkali-activated slag paste under bath-curing.* Advances in Cement Research, 2019: p. 1-33.
176. Kang, X., et al., *Hydration of C_3A/gypsum composites in the presence of graphene oxide.* Materials Today Communications, 2020. **23**.
177. Zhu, X. and X. Kang, *Effect of graphene oxide (GO) on the hydration and dissolution of alite in a synthetic cement system.* Journal of Materials Science, 2019. **55**(8): p. 3419-3433.
178. Tres Thoenen, et al., *The Nagra-PSI Chemical Thermodynamic DataBase 12-07*. 2014, Paul Scherrer Institute: Switzerland.
179. Lothenbach, B., et al., *Cemdata18: A chemical thermodynamic database for hydrated Portland cements and alkali-activated materials.* Cement and Concrete Research, 2018. **115**(1): p. 472-506.
180. Whittaker, M.J., *The impact of slag composition on the microstructure of composite slag cements exposed to sulfate attack*, in *School of civil engineering*. 2014, University of Leeds: UK.
181. Taylor, H.F.W., *Modification of the Bogue calculation.* Advanced in cement research, 1989. **2**(6): p. 73-77.

182. Borrachero, M.V., et al., *The use of thermogravimetric analysis technique for the characterization of construction materials-the gypsum case.* Journal of Thermal Analysis and Calorimetry, 2008. **91**(2): p. 503-509.
183. Galan, I., F.P. Glasser, and C. Andrade, *Calcium carbonate decomposition.* Journal of Thermal Analysis and Calorimetry, 2012. **111**(2): p. 1197-1202.
184. Wagner, N.J., et al., *Characterization of unburned carbon present in coarse gasification ash.* Fuel, 2008. **87**(6): p. 683-691.
185. Lee, B.Y., *Effect of Tianium Dioxide nanoparticles on early age and long term properties of cementitious materials*, in *School of Civil & Environmental Engineering*. 2012, Georgia Institute of Technology USA.
186. Zhang, J. and G.W. Scherer, *Comparison of methods for arresting hydration of cement.* Cement and Concrete Research, 2011. **41**(10): p. 1024-1036.
187. Longuet, P., L. Burglen, and A. Zelwer, *The liquid phase of hydrated cement.* Rev. Matér. Constr. Trav. Publics, 1973. **676**: p. 35-41.
188. Zhu, X., et al., *Characterisation of pore structure development of alkali-activated slag cement during early hydration using electrical responses.* Cement and Concrete Composites, 2018. **89**: p. 139-149.
189. Kang, X., et al., *Dissolution and precipitation behaviours of graphene oxide / tricalcium silicate composites.* Composites Part B: Engineering, 2020. **186**.
190. Scrivener, K., et al., *Advances in understanding cement hydration mechanisms.* Cement and Concrete Research, 2019. **124**.
191. Richardson, I.G., C.R. Wilding, and G.W. Groves, *The hydration of blast furnace slag cements.* Advanced in cement research, 1989. **2**(8): p. 147-157.
192. Roy, A., *Sulfur speciation in granulated blast furnace slag: An X-ray absorption spectroscopic investigation.* Cement and Concrete Research, 2009. **39**(8): p. 659-663.
193. Arai, Y., B.A. Powell, and D.I. Kaplan, *Sulfur speciation in untreated and alkali treated ground-granulated blast furnace slag.* Sci Total Environ, 2017. **589**: p. 117-121.
194. Giergiczny, Z., *Fly ash and slag.* Cement and Concrete Research, 2019. **124**.
195. Skibsted, J. and R. Snellings, *Reactivity of supplementary cementitious materials (SCMs) in cement blends.* Cement and Concrete Research, 2019. **124**.
196. Cong, X. and R.J. Kirkpatrick, *^{17}O and ^{29}Si MAS NMR study of β-C_2S hydration and the structure of calcium-silicate-hydrates.* Cement and Concrete Research, 1993. **23**: p. 1065-1077.
197. Tajuelo Rodriguez, E., et al., *Composition, silicate anion structure and morphology of calcium silicate hydrates (C-S-H) synthesised by silica-lime reaction and by controlled hydration of tricalcium silicate (C_3S).* Advances in Applied Ceramics, 2015. **114**(7): p. 362-371.
198. Collepardi, M. and B. Marchese, *Morphology and surface properties of hydrated tricalcium silicate pastes.* cement and Concrete Research, 1972. **2**: p. 57-65.
199. Fonseca, P.C. and H.M. Jennings, *The effect of drying on early-age morphology of C–S–H as observed in environmental SEM.* Cement and Concrete Research, 2010. **40**(12): p. 1673-1680.
200. Richardson, I.G. and G.W. Groves, *Microstructure and microanalysis of hardened ordinary Portland cement pastes.* Journal of Materials Science, 1993. **28**: p. 265-277.
201. Girao, A.V., et al., *morphology and nanostructure C–S–H in white Portland cement–fly ash hydrated at 85°C.* Advances in Applied Ceramics, 2007. **106**(6): p. 283-293.
202. Girão, A.V., et al., *Composition, morphology and nanostructure of C–S–H in white Portland cement pastes hydrated at 55 °C.* Cement and Concrete Research, 2007. **37**(12): p. 1571-1582.
203. Lothenbach, B., et al., *Effect of temperature on the pore solution, microstructure and hydration products of Portland cement pastes.* Cement and Concrete Research, 2007. **37**(4): p. 483-491.
204. Lothenbach, B. and A. Nonat, *Calcium silicate hydrates: Solid and liquid phase composition.* Cement and Concrete Research, 2015. **78**: p. 57-70.
205. Lothenbach, B. and E. Wieland, *A thermodynamic approach to the hydration of sulphate-resisting Portland cement.* Waste Manag, 2006. **26**(7): p. 706-19.

206. De Weerdt, K., et al., *Hydration mechanisms of ternary Portland cements containing limestone powder and fly ash.* Cement and Concrete Research, 2011. **41**(3): p. 279-291.
207. D., M., et al., *ESCA and SEM studies on early C_3S hydration.* Cement and Concrete Research, 1979. **9**: p. 473-482.
208. Jennings, H.M., B.J. Dalgleish, and P.L. Pratt, *Morphological development of hydrating tricalcium silicate as examined by electron microscopy techniques.* Journal of the American Ceramic Society, 1981. **64**(10): p. 567-572.
209. Wang, X.-Y., et al., *A multi-phase kinetic model to simulate hydration of slag–cement blends.* Cement and Concrete Composites, 2010. **32**(6): p. 468-477.
210. Ylm, R., U. J€aglid, and I. Panas, *Monitoring Early Hydration of Cement by Ex Situ and In Situ ATR-FTIR – a Comparative Study.* Journal of the American Ceramic Society, 2014. **97**(11): p. 3669–3675.
211. Rikard Ylmén, et al., *Early hydration and setting of Portland cement monitored by IR, SEM and Vicat techniques.* Cement and Concrete Research, 2009. **39**: p. 433-439.
212. Lodeiro, I.G., et al., *Effect of alkalis on fresh C–S–H gels. FTIR analysis.* Cement and Concrete Research, 2009. **39**: p. 147-153.
213. Balan, E. and J.T. Kloprogge, *Theoretical Aspects of Infrared and Raman Spectroscopies*, in *Infrared and Raman Spectroscopies of Clay Minerals*. 2017. p. 6-33.
214. Ciath, T.D., et al., *Microstructure of clacium silicate hydrates.* Cement and Concrete Research, 1971. **1**: p. 13-25.
215. Naber, C., et al., *Alite dissolution and C-S-H precipitation rates during hydration.* Cement and Concrete Research, 2018.
216. Bullard, J.W. and G.W. Scherer, *An Ideal Solid Solution Model for C-S-H.* J Am Ceram Soc, 2016. **99**(12): p. 4137-4145.
217. Nicoleau, L., *Accelerated growth of calcium silicate hydrates: Experiments and simulations.* Cement and Concrete Research, 2011. **41**(12): p. 1339-1348.
218. Scherer, G.W. and F. Bellmann, *Kinetic analysis of C-S-H growth on calcite.* Cement and Concrete Research, 2018. **103**: p. 226-235.
219. Qiu, L., *The nature of early age hydration products*, in *School of Civil Engineering*. 2008, University of Leeds: UK.
220. Wang, D., et al., *Effect of SiO_2 oligomers on water absorption of cementitious materials.* Cement and Concrete Research, 2016. **87**: p. 22-30.
221. Cong, X. and R.J. Kirkpatrick, *^{1}H — ^{29}Si CPMAS NMR study of the structure of calcium silicate hydrate.* Advanced in cement research, 1995. **7**(27): p. 103-111.
222. Lodeiro, I.G., et al., *Effect on fresh C-S-H gels of the simultaneous addition of alkali and aluminium.* Cement and Concrete Research, 2010. **40**: p. 27-32.
223. Alarcon-Ruiz, L., et al., *The use of thermal analysis in assessing the effect of temperature on a cement paste.* Cement and Concrete Research, 2005. **35**(3): p. 609-613.
224. Walkley, B., et al., *Phase evolution of Na_2O-Al_2O_3-SiO_2-H_2O gels in synthetic aluminosilicate binders.* Dalton Trans, 2016. **45**(13): p. 5521-35.
225. Walkley, B., et al., *Phase evolution of C-(N)-A-S-H/N-A-S-H gel blends investigated via alkali-activation of synthetic calcium aluminosilicate precursors.* Cement and Concrete Research, 2016. **89**: p. 120-135.
226. Walkley, B., et al., *Structural evolution of synthetic alkali-activated CaO-MgO-Na_2O-Al_2O_3 - SiO_2 materials is influenced by Mg content.* Cement and Concrete Research, 2017. **99**: p. 155-171.
227. Walkley, B., et al., *New Structural Model of Hydrous Sodium Aluminosilicate Gels and the Role of Charge-Balancing Extra-Framework Al.* The Journal of Physical Chemistry C, 2018. **122**(10): p. 5673-5685.
228. Gao, L., et al., *Revealing the chemistry of an anode-passivating electrolyte salt for high rate and stable sodium metal batteries.* Journal of Materials Chemistry A, 2018. **6**(25): p. 12012-12017.
229. Maekawa, H., et al., *Coordination of sodium ions in $NaAlO_2$-SiO_2 melts: a high temperature ^{23}Na NMR study.* Physics and Chemistry of Minerals, 1997. **24**: p. 53-65.

230. Newkirk, A.E. and I. Aliferis., *Drying and decomposition of sodium carbonate.pdf*>. Analytical Chemistry 1958. **30**(5): p. 982-984.
231. L'Hôpital, E., et al., *Influence of calcium to silica ratio on aluminium uptake in calcium silicate hydrate.* Cement and Concrete Research, 2016. **85**: p. 111-121.
232. Skibsted, J., E. Henderson, and H. Jakosen, *Characterization of calcium aluminate phases in cements by aluminum-27 MAS NMR spectroscopy.* Inorganic chemistry, 1993. **32**: p. 1013-1027.
233. Ke, X., *Improved Durability and Sustainability of Alkali-Activated Slag Cements*, in *Department of Materials Science and Engineering*. 2017, The University of Sheffield: UK.
234. Ukrainczyk, N., et al., *Dehydration of a layered double hydroxide—C_2AH_8.* Thermochimica Acta, 2007. **464**(1-2): p. 7-15.
235. Joseph, S., J. Skibsted, and Ö. Cizer, *A quantitative study of the C_3A hydration.* Cement and Concrete Research, 2019. **115**: p. 145-159.
236. Bussian, P., et al., *Speciation in solution silicate oligomers in aqueous solutions detected by mass spectrometry.* Angewandte Chemie International Edition, 2000. **39**(21): p. 3901-3905.
237. Pelster, S.A., W. Schrader, and F. Schüth, *Monitoring temporal evolution of silicate species during hydrolysis and condensation of silicates using mass spectrometry.* Journal of the American Chemical Society, 2006. **128**(13): p. 4310-4317.
238. Edrees, S.J., M.M. Shukur, and M.M. Obeid, *First-principle analysis of the structural, mechanical, optical and electronic properties of wollastonite monoclinic polymorph.* Computational Condensed Matter, 2018. **14**: p. 20-26.
239. Trevor L. Hughes, et al., *Determining cement composition by Fourier Transform Infrared Spectroscopy.* Advanced Cement Based Materials, 1994. **2**: p. 91-104.
240. Zhang, Z., et al., *Quantitative kinetic and structural analysis of geopolymers. Part 2. Thermodynamics of sodium silicate activation of metakaolin.* Thermochimica Acta, 2013. **565**: p. 163-171.
241. Zhang, Z., et al., *Quantitative kinetic and structural analysis of geopolymers. Part 1. The activation of metakaolin with sodium hydroxide.* Thermochimica Acta, 2012. **539**: p. 23-33.
242. Trevor L. Hughes, et al., *Determining cement composition by Fourier Transform Infrared Spectroscoy.* Advanced Cement Based Materials, 1995. **2**: p. 91-104.
243. Dent Glasser, L.S. and C.K. Lee, *Drying of sodium silicate solution.* Journal of Applied Chemistry and Biotechnology, 1971. **21**(5): p. 127-133.
244. Horgnies M., Chen J. J., and B. C., *Overview about the use of Fourier Transform Infrared Spectroscopy to study cementitious materials*, in *6th Int. Conf. on Computational Methods and Experiments in Materials Characterization,*, B. C.A. and K. A., Editors. 2013, WIT Transactions on Engineering Sciences: UK.
245. Kumar, A., et al., *The Atomic-Level Structure of Cementitious Calcium Silicate Hydrate.* The Journal of Physical Chemistry C, 2017. **121**(32): p. 17188-17196.
246. Özçelik, V.O., N. Garg, and C.E. White, *Symmetry-Induced Stability in Alkali-Doped Calcium Silicate Hydrate.* The Journal of Physical Chemistry C, 2019. **123**(22): p. 14081-14088.
247. Cong, X. and R.J. Kirkpatrick, *Effect of the temperature and relative humidity on the structure of C-S-H gel.* Cement and Concrete Research, 1995. **25**(6): p. 1237-1245.
248. Haas, J. and A. Nonat, *From C–S–H to C–A–S–H: Experimental study and thermodynamic modelling.* Cement and Concrete Research, 2015. **68**: p. 124-138.
249. Taylor, H.F., *Hydrated calcium silicates. Part I. Compound formation at ordinary temperatures.* Journal of the Chemical Society (Resumed), 1950: p. 3682-3690.
250. Nonat, A. and X. Lecoq, *The Structure, Stoichiometry and Properties of C-S-H Prepared by C_3S Hydration Under Controlled Condition.* 1998: p. 197-207.
251. Skibsted, J., M.T. Pedersen, and J. Holzinger, *Resolution of the Two Aluminum Sites in Ettringite by ^{27}Al MAS and MQMAS NMR at Very High Magnetic Field (22.3 T).* The Journal of Physical Chemistry C, 2017. **121**(7): p. 4011-4017.

Publications from the thesis

Journal publications

X. Zhu, I.G. Richardson, P. Purnell, "Morphology-structural change of C-S-H gel in blended cements", (Manuscript ready for submission).

X. Zhu, I.G. Richardson, P. Purnell, "Morphology-structural change of C-S-H gel during early-age hydration of alite", (Manuscript ready for submission).

X. Zhu, I.G. Richardson, P. Purnell, "Morphology-structural change of synthetic C-S-H in the presence of sodium and aluminium", (Manuscript ready for submission).

Conference publications

X. Zhu, I.G. Richardson, P. Purnell, "How anatase affects the hydration of wPC and its effect on C-S-H nanostructure", 39th Cement and Concrete Science Conference, Sep. 2019, Bath, UK.

X. Zhu, I.G. Richardson, P. Purnell, "Structural change of C-S-H gel during early-age hydration of alite", 40th Cement and Concrete Science Conference & 74th Rilem Week, Sep. 2020, Sheffield, UK (online).

Additional publications during the period of doctoral studies[9]

Journal publications

X. Zhu, M. Zhang, et al. "Setting behaviours and early-age microstructures of alkali-activated ground granulated blast furnace slag (GGBS) from different regions in China." Cement and Concrete Composites (2020): 103782.

X. Zhu, Q. Li, et al. "Characterisation of temporal variations of alkali-activated slag cement property using microstructure features and electrical responses" Construction and Building Materials 261 (2020): 119884.

X. Kang[1], **X. Zhu[1]**, et al. "Hydration of C_3A/gypsum composites in the presence of graphene oxide." Materials Today Communications 23 (2020): 100889.

X. Kang[1], **X. Zhu[1]**, et al. "Dissolution and precipitation behaviours of graphene oxide/tricalcium silicate composites." Composites Part B: Engineering 186 (2020): 107800.

X. Zhu & X. Kang. "Effect of graphene oxide (GO) on the hydration and dissolution of alite in a synthetic cement system." Journal of Materials Science,55(8) (2020), 3419-3433.

X. Zhu, M. Zhang, et al. "Understanding the aqueous phases of alkali-activated slag cement under water-bath curing" Advances in Cement Research, 2019: https://doi.org/10.1680/jadcr.18.00202

X. Zhu, Z. Zhang, et al. "Characterisation of pore structure development of alkali-activated slag cement during early hydration using electrical responses." Cement and Concrete Composites 89 (2018): 139-149.

X. Zhu, D. Tang, et al. "Effect of $Ca(OH)_2$ on shrinkage characteristics and microstructures of alkali-activated slag concrete." Construction and Building Materials 175 (2018): 467-482.

[9] These papers are performed during the author's MEng period in Chongqing University (as a master student) and Queen's University Belfast (as a visiting research associate), but published late due to the processing of peer-reviewing.